The Design and Production of the LHCb VELO High Voltage System and Analysis of the $B_d \to K^*\mu^+\mu^-$ Rare Decay

Barinjaka Rakotomiaramanana

Submitted in fulfilment of the requirements for the Degree of Doctor of Philosophy

Department of Physics and Astronomy
Faculty of Physical Sciences

December 2010

Abstract

LHCb is the dedicated flavour physics experiment of the LHC. The experiment is designed for probing new physics through measurements of CP violation and rare decays. This thesis includes simulation studies of the $B_d \rightarrow K^*\mu^+\mu^-$ decay. The LHCb vertex locator (VELO) is the highest precision tracking detector at the LHC and is used to identify primary and secondary vertices for the identification of the b and c hadrons. The VELO modules contain silicon strip detectors which must be operated under reverse bias voltage. This thesis presents the work performed on the design, production and characterisation of the VELO high voltage system. The VELO operates only 8 mm from the LHC beam in a high radiation environment. A future upgrade will require operation at up to 10^{16} $\mathrm{n_{eq}/cm^2}$. This thesis presents a characterisation of p-type silicon sensors before and after heavy irradiations.

The design of the HV system and the substantial programme of quality assurance tests performed on both the hardware and software parts of the VELO high voltage system are described. The tests cover normal operation and consideration of a range of failure scenarios. The hardware and software limits were tested. The stability of the output over time and the noise of the system were assessed. The performance is found to meet the specification, although problems at low voltage and low current operation are seen. An analysis of the current-voltage data during module production, and commissioning up to first LHC operation is given. No obvious signs of sensor degradation are seen. The VELO high voltage system complies with the safety and performance requirements in the environment where it is used and has been successfully operated throughout the first period of the LHC operations.

With its current design, LHCb expects to collect ≈ 10 $\mathrm{fb^{-1}}$ of data, running beyond this will require an upgrade of LHCb requiring more radiation hard silicon strip detectors. P-type silicon strip detectors are one possible candidate for the upgraded LHC. Tests performed on p-type detectors with four types of isolation techniques are detailed. The breakdown voltages and the full depletion voltage before irradiation are measured. Breakdown voltages above 1000 V are found from each type of isolation technique, except for an isolation scheme with individual p-stops. The average depletion voltage

is approximately 170 V. The current-voltage characteristics, breakdown voltage and the charge collection measurements of five irradiated p-type detectors are measured. Approximately 30% of the maximum charge is collected at a fluence of 10^{16} n_{eq}/cm^2 for a bias voltage of 1000 V. At a fluence of 2×10^{15} n_{eq}/cm^2, the detector with p-spray could be biased at a higher voltage before breakdown than the detector with common p-stops. This follows the expectation that the p-spray technology gives better results under irradiation. The n-on-p detectors are found to be promising candidates at the fluences expected at the high luminosity upgrade of the LHC (SLHC), albeit that at the highest fluences the charge collection efficiency is significantly reduced and they must be operated at high voltages and low temperatures.

The $B_d \to K^*\mu^+\mu^-$ decay is a rare Flavour Changing Neutral Current decay which proceeds via the b→s transition. This decay is one of the golden modes in LHCb due to its sensitivity to New Physics contributions beyond the Standard Model of particle physics from the measurement of observables, such as the forward backward asymmetry (A_{FB}) and its zero crossing point (S_0). The $B_d \to K^*\mu^+\mu^-$ event selection is described and is used to evaluate the signal and background yields. The estimated signal yield from the simulation is 4360^{+1160}_{-1040} events/2 fb^{-1}. The background rate is estimated to be 5300 ± 1800 events/2 fb^{-1}. A binned and unbinned method of extraction of A_{FB} and S_0 are discussed. The unbinned method gives direct access to the value of S_0, while the binned method may introduce a small bias to the mean value of S_0 due to assumptions of fitting the data close to the crossing point. It is estimated that the S_0 can be obtained with an accuracy of $\pm$ 1.1 GeV^2/c^4, $\pm$ 0.38 GeV^2/c^4 and $\pm$ 0.17 GeV^2/c^4 with data samples of 0.2 fb^{-1}, 2 fb^{-1} and 10 fb^{-1}, respectively. The effect of the VELO (and other tracking detectors) misalignments on the analysis is also studied. It is found that significant misalignments can have a large effect on event selection efficiency. However, at the current level of alignment obtained from the first LHC data the effect is already expected to give a less than 10% change. A method to study the effects of misalignments directly on A_{FB} is also demonstrated.

Contents

List of Figures

List of Tables

Preface

The LHCb experiment is one of the four main experiments of the Large Hadron Collider at the European Laboratory for Particle Physics (CERN) and started data taking at the end of 2009. LHCb is designed for precise measurements of CP violation and rare decays. The work presented in this thesis consists of three main topics: the high voltage system of the VELO; the qualification of p-type sensors for the LHC upgrade; and the analysis of the $B_d \to K^* \mu^+ \mu^-$ decay.

Chapter 1 presents a theoretical review of the Standard Model of particle physics which is relevant to the physics programme of the LHCb experiment. Particular emphasis is placed on the physics involved in $b \to s$ transitions, and the rare decay $B_d \to K^* \mu^+ \mu^-$. New Physics (NP) models, their sensitivity to the $b \to s$ transitions, and the current experimental constraints based on recent measurements are discussed.

Chapter 2 gives a description of the LHCb experiment and an overview of the other experiments of the Large Hadron Collider. A description of each sub-detector of LHCb is given. Particular emphasis is placed on the VELO, as part of the work in this thesis is focused in this sub-detector. The VELO is one of the tracking detectors of LHCb and provides the tracking coordinates close to the interaction point as well as the determination of primary and secondary vertices. The VELO silicon strip sensors must be operated under reversed bias.

The VELO high voltage system is responsible for supplying the bias voltage to the 88 silicon sensors which comprise the LHCb VELO. Chapter 3 details the design, the production and the quality assurance tests performed on both the hardware and software parts of the VELO high voltage system. Connectivity and stability tests, tests under failure modes as well as noise spectra measurements are presented. The reliability of the high voltage crate uninterruptible power supply (UPS), the hardware voltage and current limits are demonstrated. Current-voltage data taken during the module production and during the commissioning in December 2008, in June 2009 and in October 2009 are analysed.

With its current design, LHCb expects to collect approximately 10 fb^{-1} of data. Continuation of data taking beyond 10 fb^{-1} will require an upgrade of LHCb. More radiation hard silicon strip detectors are needed. Chapter 4 presents the studies of p-type silicon microstrip detectors, with different types of isolation techniques, relevant to the proposed upgrade of LHCb and of other LHC experiments. The aims and concept of the LHCb upgrade are briefly discussed. The results obtained from the characterisation of these p-type detectors before and after irradiation with neutrons and protons are presented. The general theory of silicon detectors, including the effects of radiation damage to silicon detectors, is also discussed. The current-voltage and capacitance-voltage characteristics of the unirradiated detectors allow the identification of their breakdown and full depletion voltages, respectively. Charge collection measurements are additionally performed on the detectors irradiated at fluences of 5×10^{14} $\text{n}_{\text{eq}}/\text{cm}^2$, 2×10^{15} $\text{n}_{\text{eq}}/\text{cm}^2$, 5×10^{15} $\text{n}_{\text{eq}}/\text{cm}^2$ and 10^{16} $\text{n}_{\text{eq}}/\text{cm}^2$.

The $B_d \to K^*\mu^+\mu^-$ decay is one of the golden modes in LHCb due to its sensitivity to New Physics contributions beyond the Standard Model of particle physics. The alignment of the tracking detectors is of crucial importance for the physics performance of the LHCb experiment. Chapter 5 is dedicated to the study of the $B_d \to K^*\mu^+\mu^-$ decay and the impact of the detector misalignment on this decay. The $B_d \to K^*\mu^+\mu^-$ event selection is described as well as the simulated data employed to evaluate the signal and background yields. The binned and unbinned methods to extract the forward backward asymmetry A_{FB} and its zero crossing point S_0 are presented. The value of S_0 is estimated using data samples of 0.2 fb^{-1}, 2 fb^{-1}, 10 fb^{-1} and 45.3 fb^{-1}. The effects of VELO misalignments, T-station misalignments and combined VELO and T-station misalignments on pattern recognition, event selection, and the B_d mass resolution are discussed. Their effects on A_{FB} and S_0 are also presented.

Chapter 6 gives a summary of the studies presented in this thesis and the corresponding results, with future prospects for continuation of the work presented in this thesis also outlined.

Acknowledgement

I would like to express my gratefulness to all the persons who have made possible and memorable with their help and support the four years of my PhD. This thesis was funded by the University of Glasgow. First, I would like to thank my primary supervisor Chris Parkes for his excellent supervision, help and guidance throughout these four years. At anytime, even under difficult situation, you have always found a way to motivate me. I would like also to thank my second supervisor Paul Soler. Thanks for your invaluable support and guidance on my physics analysis. Thanks to both of you for giving me the opportunity to be part of the Experimental Particle Physics Group of the University of Glasgow. Thanks also for reading many times each chapter of this thesis. Both your constructive comments have made possible this thesis to be in its current state.

Many thanks also to Lars Eklund, not only for answering all my questions during my high voltage and silicon detector works but also for being there for me during the tough period. I will never forget the first time I drank my first can of 'Irn Bru'. I would like to thank Prof. David Saxon and his wife for the memorable day that we spent together in visiting the Stirling Castle. Many thanks to Richard Bates for teaching me how to use the AlibaVa system and also for all your constructive comments and advice. Many thanks to Marco Gersabeck who kept me alive after my first whisky tasting in Edinburgh. Thanks for the great times we shared both as a flatmate and officemate in Glasgow. Your advice and comments were really helpful. I would like also to express my appreciation to Eduardo Rodrigues and Tomasz Szumlak for guiding me with my physics analysis. You were always there to give me advice on any of my coding issues. Many thanks also to Franciole, Laurence, Silvia and Michael. I really appreciated all the times we have shared during these four years. Many thanks to Andrew and Dima who were always ready to motivate the folks to go to Tennents on Friday evening. Thanks also for submitting my thesis. Thanks to Fred, Fiona, John, Aaron, Keith, Ken and everyone else.

I would like to thank Paula Collins. You have always been so supportive. Many thanks to Stefano de Capua for steering me on my way through PVSS. Many thanks to Massi, Themis, Jan, Abdi, Kazu, Karol and all the members of the LHCb VELO group. Many thanks to Dr. Ulrich Parzefall, Dr. Craig Buttar and Prof. Tony Doyle for examining this thesis. Finally, I would like to thank my whole family, especially, my wife Onja who provided her constant support to me.

Declaration

The work in this thesis is based on research carried out at the Experimental Particle Physics Group, the Department of Physics and Astronomy, University of Glasgow, Scotland and the European Organisation for Nuclear Research, Switzerland, Geneva. No part of this thesis has been submitted elsewhere for any other degree or qualification and it is all my own work unless referenced to the contrary in the text.

1 Theory Review

This chapter presents a theoretical review of the Standard Model (SM) which is relevant to the physics programme of the LHCb experiment. Particular emphasis is placed on the physics involved in $b \to s$ transitions, and the rare decay $B_d \to K^* \mu^+ \mu^-$. New Physics (NP) models, their sensitivity to the $b \to s$ transitions, and the current experimental constraints based on recent measurements are also discussed.

After an introduction to the SM in section 1.1, section 1.2 develops the theory of electroweak interactions. Section 1.3 introduces Charge-Parity (CP) violation and section 1.4 presents the theory of Quantum ChromoDynamics (QCD). Finally, section 1.5 is dedicated to the rare semi-leptonic B decays with particular emphasis given to $B_d \to K^* \mu^+ \mu^-$.

1.1 General Standard Model Theory

The SM [1–4] is the theory that provides an accurate description of elementary particles and their interactions. Extensively and successfully tested in the past decades, the SM still leaves important unanswered questions in high energy physics. Amongst these questions are the reason for the existence of three generations of quarks, the understanding of CP violation (see section 1.3), and the origin of the dark matter in the universe. The LHC experiments are designed to further our understanding of these issues by providing precise measurements of CP violation and rare decays in b-hadron decays, and searching for directly produced new physics particles. The LHC also aims to discover the final missing particle of the SM, the Higgs boson.

Within the SM description, matter is made of elementary particles which are in two types: *fermions* and *bosons*. The fermions are in two categories: *quarks* and *leptons*. They are half integer spin particles and obey the Pauli exclusion principle. Fermions are grouped in three generations with increasing mass [1]. As represented in Table 1.1, a generation of fermions contains a pair of *leptons* and *quarks*. The particles that

[1] This is true for the quarks and leptons. The masses, and mass ordering of the neutrinos are not yet known.

comprise the leptons are the electron e, the muon μ and the tau τ. Respectively, their corresponding neutrinos are denoted ν_e, ν_μ and ν_τ. The quarks come in six flavours: up (u) , down (d), charm (c), strange (s), top (t) and bottom (b). They are confined as constituents of the observed particles.

The quarks carry a type of charge called *colour* which can be of three different types: red, green and blue. Quarks are always bound in groups which constitue colourless objects, called *hadrons*. Hadrons which are composed of three quarks of different colour are called *baryons*, and those composed of a quark and antiquark are called *mesons*.

The bosons are the second type of elementary particles. They are integer spin particles and obey Bose-Einstein statistics. Bosons are the mediators of interactions between particles. These mediators are respectively the photon γ for the electromagnetic interactions, the gluons (A^α, α=1,...,8) for the strong interactions, and the $W^\pm$ and Z for the weak interactions

The SM is a quantum field theory based on the gauge theory of group $SU(3)_C \times SU(2)_L \times U(1)_Y$ [5]. This group is described as follows.

- $SU(3)_C$ group is the gauge group of the strong interactions which are described theoretically with QCD (see section 1.4). Proton-proton collisions at the LHC involve QCD processes.

- $SU(2)_L \times U(1)_Y$ is the group that describes the weak and electromagnetic interactions. In the SM, they are unified into the *electroweak* interaction (see section 1.2) with the corresponding boson energies below the electroweak unification scale, giving rise to the $SU(2)_L \times U(1)_Y$ symmetry. This breaking of the electroweak symmetry is explained by the introduction of a new scalar field, the Higgs field. The elementary particle's mass originates from its interaction with the Higgs field. However, the quantum of this field, the Higgs boson particle has not been observed yet. The main LHC physics programmes reside in the electroweak model such as studies of the Higgs mechanism, New Physics searches (eg. SUSY), CP violation and Flavour Changing Neutral Currents (FCNC) processes.

1.2 The Electroweak Interactions

The electroweak interaction theory developed by Glashow, Weinberg and Salam [1,2,7] unifies the electromagnetic and weak interactions. The weak interactions violate parity.

	Generation			
Fermions	I	II	III	Q
Quarks	u (up) 1.5 - 3.3 MeV/c^2	c (charm) ($1.27^{+0.07}_{-0.11}$) GeV/c^2	t (top) (171.3±1.1±1.2) GeV/c^2	$+\frac{2}{3}$
	d (down) 3.5 - 6.0 MeV/c^2	s (strange) (105^{+25}_{-35}) MeV/c^2	b (bottom) ($4.20\ ^{+0.17}_{-0.07}$) GeV/c^2	$-\frac{1}{3}$
Leptons	e (electron) 0.5109 MeV/c^2	μ (muon) 105.658 MeV/c^2	τ (tau) (1776.84±0.17) MeV/c^2	-1
	ν_e (e neutrino) < 2 eV/c^2	ν_μ (μ neutrino) < 0.19 MeV/c^2	ν_τ (τ neutrino) < 18.2 MeV/c^2	0

Table 1.1: *The three generations of fermions and their corresponding leptons and quarks pairs. Reproduced from [6].*

The interactions for fermions can then be constructed by assigning different interactions for the left-handed and right-handed components. The Dirac field ψ which represents a fermion can be expressed as a sum of a left-handed part, ψ_L, and a right-handed part ψ_R,

$$\psi = \psi_L + \psi_R, \tag{1.1}$$

where

$$\psi_L = P_L\psi \quad with \quad P_L = \frac{(1-\gamma_5)}{2}, \tag{1.2}$$

$$\psi_R = P_R\psi \quad with \quad P_R = \frac{(1+\gamma_5)}{2}, \tag{1.3}$$

$$\gamma_5 = i\gamma_0\gamma_1\gamma_2\gamma_3, \tag{1.4}$$

P_L and P_R are projection operators and γ_μ are the Dirac matrices [8]. Likewise the kinetic term of the Dirac Lagrangian and the interaction term of a fermion with the vector field are also expressed as the sum of two terms each involving only one helicity. However, the mass term mixes the two helicities. The origin of the mass term will be discussed in more detail in sections 1.2.1 and 1.2.2.

1.2.1 Leptonic Sector

In the Standard Model, the left-handed lepton states L are expressed by

$$L = \frac{(1-\gamma_5)}{2}\, l, \tag{1.5}$$

where $l = e, \nu_e, \mu, \nu_\mu, \tau, \nu_\tau$ and the right-handed states R are denoted by e_R, μ_R, τ_R. The left-handed charged leptons and left-handed neutrino are organized in doublets

$$\begin{pmatrix} \nu_e \\ e \end{pmatrix}_L, \quad \begin{pmatrix} \nu_\mu \\ \mu \end{pmatrix}_L, \quad \begin{pmatrix} \nu_\tau \\ \tau \end{pmatrix}_L, \tag{1.6}$$

that correspond to the three generations of leptons. Each doublet transforms in the spinor representation ($T = \frac{1}{2}$) of the weak isospin $SU(2)$ gauge symmetry. Hence, ν_l and l are eigenstates of the isospin projection T_z with eigenvalues $\frac{1}{2}$ and $-\frac{1}{2}$ respectively. The right-handed charged leptons do not participate in the weak interaction, while there is no right-handed neutrino in the SM. Experimental evidence has shown that neutrinos possess mass and there are oscillations between families [9], and hence the SM is known to require adaptation.

The gauge fields of the weak isospin SU(2) and the weak hypercharge U(1) symmetries are combined by means of the Higgs mechanism [10] to form the three massive vector bosons (W^+, W^-, Z^0) mediating the weak interaction, and one massless vector boson, the photon γ, responsible for the electromagnetic interaction. The gauge bosons introduced are

$$W^1_\mu, W^2_\mu, W^3_\mu \quad for \quad SU(2)_L, \tag{1.7}$$

$$B_\mu \quad for \quad U(1)_Y. \tag{1.8}$$

The lepton electric charge Q can be calculated by

$$Q = T_z + \frac{1}{2}Y, \tag{1.9}$$

where T_z and Y are the weak isospin projection and weak hypercharge respectively. The left-handed weak isospin doublets have $Y = -1$ and $Y = -2$ for the right-handed weak isospin singlet.

The Lagrangian that describes the interactions of the leptons, the vector bosons and the scalar boson (see below) can be written as

$$\mathcal{L} = \mathcal{L}_{leptons} + \mathcal{L}_{gauge}. \tag{1.10}$$

The first term of the Lagrangian $\mathcal{L}_{leptons}$ is given by

$$\mathcal{L}_{leptons} = \bar{L} i\gamma^\mu \left(\partial_\mu - \frac{1}{2} i g' B_\mu + \frac{1}{2} i g \tau_j W^j_\mu \right) L + \bar{R}\gamma^\mu \left(i\partial_\mu - g' B_\mu \right) R, \tag{1.11}$$

where g and τ_j are the coupling and generators of the gauge group $SU(2)_L$ respectively. The coupling of the gauge group $U(1)_Y$ is given by $\frac{g'}{2}$[‡].

The second term of the Lagrangian, $\mathcal{L}_{gauge}$, is given by

$$\mathcal{L}_{gauge} = -W^j_{\mu\nu}W^{j\mu\nu} - \frac{1}{4}B_{\mu\nu}B^{\mu\nu}, \tag{1.12}$$

where

$$W^j_{\mu\nu} = \partial_\mu W^j_\nu - \partial_\nu W^j_\mu + g\epsilon^{jkl}W^k_\mu W^l_\nu, \tag{1.13}$$

$$B_{\mu\nu} = \partial_\mu B_\nu - \partial_\nu B_\mu. \tag{1.14}$$

The Lagrangian in equation 1.10 is incomplete as the mass term is not included. As previously stated, there are three massive bosons and one massless boson that mediate the electroweak interaction and the mass originates from the Higgs mechanism [10]. The latter uses a symmetry breaking mechanism that keeps the gauge invariance of the group. One needs a doublet of complex scalar fields with hypercharge $Y = 1$, called the Higgs fields ϕ. The following interaction terms are added to the Lagrangian in eq. 1.10:

- The interaction of the Higgs field with fermions

$$\mathcal{L}_{Yukawa} = -G_e[(\bar{L}\phi)R - \bar{R}(\phi^\dagger L)], \tag{1.15}$$

  where G_e is the Fermi constant.

- The interaction of the Higgs field with bosons

$$\mathcal{D}\phi^\dagger\mathcal{D}\phi = \left|\left(\partial_\mu + \frac{1}{2}igW^j_\mu\tau_j + \frac{1}{2}ig'IB_\mu\right)\phi\right|^2, \tag{1.16}$$

  where I is the identity matrix.

- The Higgs field self-interaction

$$\mathcal{L}_H = V(\phi) = \mu^2\phi^\dagger\phi + \lambda(\phi^\dagger\phi), \tag{1.17}$$

$$< \phi >_0 = \begin{pmatrix} 0 \\ v/\sqrt{2} \end{pmatrix} \tag{1.18}$$

[‡]The factor $\frac{1}{2}$ has been chosen for simplicity.

with $\mu^2 < 0$ to allow the spontaneous symmetry breaking from which originates the masses. $< \phi >_0$ is the vacuum expectation value of ϕ.

By taking into account the Higgs field interactions, the mass of the fermions is obtained from the Yukawa interaction term as

$$m_l = \frac{G_e v}{\sqrt{2}}, \tag{1.19}$$

and the neutral gauge bosons are redefined as

$$\begin{pmatrix} B_\mu \\ W_\mu^3 \end{pmatrix} = \begin{pmatrix} \cos\theta_W & \sin\theta_W \\ \sin\theta_W & -\cos\theta_W \end{pmatrix} \begin{pmatrix} A_\mu \\ Z_\mu \end{pmatrix}, \tag{1.20}$$

where θ_W is the Weinberg angle, to ensure that photons remain massless. A_μ and Z_μ represent the massless photon and the neutral massive boson respectively.

The weak couplings g and g' are expressed in terms of elementary charge e and θ_W by

$$g = \frac{e}{\sin\theta_W}, \quad g' = \frac{e}{\cos\theta_W}, \tag{1.21}$$

which gives

$$\frac{g'}{g} = \tan\theta_W. \tag{1.22}$$

Hence,

$$Z_\mu = \frac{-g'B_\mu + gW_\mu^3}{\sqrt{g^2 + g'^2}}, \quad A_\mu = \frac{gB_\mu + g'W_\mu^3}{\sqrt{g^2 + g'^2}}, \tag{1.23}$$

and their masses are given by

$$m_{Z_\mu} = \frac{gv}{2\cos\theta_W}, \quad m_{A_\mu} = 0. \tag{1.24}$$

Similarly, the charged gauge bosons, W_μ^1 and W_μ^2 are rewritten as

$$\begin{pmatrix} W_\mu^+ \\ W_\mu^- \end{pmatrix} = \frac{1}{\sqrt{2}} \begin{pmatrix} 1 & -i \\ 1 & i \end{pmatrix} \begin{pmatrix} W_\mu^1 \\ W_\mu^2 \end{pmatrix}, \tag{1.25}$$

where $W_\mu^\pm$ are the massive charge bosons. Hence,

$$W_\mu^\pm = \frac{W_\mu^1 \mp W_\mu^2}{\sqrt{2}}, \tag{1.26}$$

and their masses are given by

$$m_{W_\mu^\pm} = \frac{gv}{2}. \tag{1.27}$$

Therefore, the Lagrangian in equation 1.10 can be rewritten in terms of the new vector bosons $W_\mu^\pm$, Z_μ and A_μ by substituting the gauge bosons defined in equation 1.7 and 1.8 with their new expressions deduced from eq. 1.20 and 1.25.

The fermionic currents are

$$J_\pm^\mu = \pm\bar{L}\gamma_\mu\tau_\pm L, \tag{1.28}$$

$$J_3^\mu = \bar{L}\gamma_\mu\tau_3 L, \tag{1.29}$$

$$J_{em}^\mu = \bar{R}\gamma_\mu R - \frac{1}{2}\bar{L}\gamma_\mu\left(1-\tau_3\right)L, \tag{1.30}$$

where $\tau_\pm = \frac{1}{2}\left(\tau_1 \pm i\tau_2\right)$.

1.2.2 Quark Sector

Similar to the leptons, the quarks are organized in left-handed doublets

$$\begin{pmatrix} u \\ d \end{pmatrix}_L, \quad \begin{pmatrix} c \\ s \end{pmatrix}_L, \quad \begin{pmatrix} t \\ b \end{pmatrix}_L, \tag{1.31}$$

and right-handed singlets u_R, d_R, c_R, b_R, t_R and s_R. Note that unlike the SM lepton sector all quarks have right-handed components. Each doublet corresponds to one family of quarks so that there are six quarks organized in three families. The three previously denoted doublets are the first, second and third family of quarks respectively. All quarks are massive and they acquire their mass through the spontaneous symmetry breaking of their couplings with the scalar fields. This procedure is called the Higgs mechanism (see section 1.2.1). More precisely, as quarks are fermions, their masses originate from the Yukawa interaction term. Unlike the neutrinos which are massless in the SM, the down-type quarks have masses. The complex conjugate of the field ϕ is

then included in the interaction Lagrangian where

$$\bar{\phi} = i\sigma_2\phi^*, \tag{1.32}$$

which is a field of $SU(2)_L$ with hypercharge $Y_{\bar{\phi}} = -1$.

Since the quark mass eigenstates are not the same as the weak eigenstates, mixing terms between the quarks are added in the interaction Lagrangian. Hence, the quark doublets are rewritten as

$$\begin{pmatrix} u \\ \tilde{d} \end{pmatrix}, \quad \begin{pmatrix} c \\ \tilde{s} \end{pmatrix}, \quad \begin{pmatrix} t \\ \tilde{b} \end{pmatrix}, \tag{1.33}$$

where $\tilde{d}, \tilde{b}, \tilde{s}$ are the interaction eigenstate.

To conveniently take into account these mixing terms, the mass matrix is assumed to be diagonal and the interaction states are taken as mixtures of the mass states. In addition, to allow transitions between different families of quarks the Cabibbo angle θ_c [11] was introduced. Considering the mixing between the first and second generations of quarks, the mass eigenstates are

$$\begin{pmatrix} \tilde{d} \\ \tilde{s} \end{pmatrix} = \begin{pmatrix} d\ \cos\theta_c + s\ \sin\theta_c \\ -d\ \sin\theta_c + s\ \cos\theta_c \end{pmatrix}, \tag{1.34}$$

whereas by adding the mixing with the third generation, the mass eigenstates are

$$\begin{pmatrix} \tilde{d} \\ \tilde{s} \\ \tilde{b} \end{pmatrix} = \mathbf{V_{CKM}} \begin{pmatrix} d \\ s \\ b \end{pmatrix}, \tag{1.35}$$

with

$$\mathbf{V_{CKM}} = \begin{pmatrix} V_{ud} & V_{us} & V_{ub} \\ V_{cd} & V_{cs} & V_{cb} \\ V_{td} & V_{ts} & V_{tb} \end{pmatrix}, \tag{1.36}$$

where V_{CKM} is the Cabibbo-Kobayashi-Maskawa unitary matrix and V_{ij} represents the matrix coupling elements between up-type quarks (i) and down-type quarks (j). Recent experimental values of all the CKM matrix elements V_{ij} can be found in [6].

1.3 CP Violation

CP violation is one of the requirements for the matter and anti-matter asymmetry in the universe [12]. Occurring via Electroweak interactions (see section 1.2), CP violation is included through the elements of the CKM matrix [11,13–15] in the SM. These elements parametrize the weak charged current interactions. The accurate determination of the CKM matrix elements is currently a central goal of particle physics, and is particularly addressed by the LHCb experiment. Measurements related to the CKM matrix provide sensitivity to the effects of new physics beyond the SM.

As introduced in section 1.2.1, the CKM matrix is a 3×3 unitary complex matrix. The postulated unitarity of V_{CKM}

$$V_{CKM}^{\dagger} V_{CKM} = V_{CKM} V_{CKM}^{\dagger} = \mathbb{1}, \tag{1.37}$$

implies six orthogonality conditions

$$\sum_{k=1}^{3} V_{kj}^{*} V_{kj} = 0 \quad (i, j = 1, 2, 3 \ \textit{and} \ i \neq j), \tag{1.38}$$

and three normalization conditions

$$\sum_{k=1}^{3} |V_{kj}|^2 = 1 \quad (j = 1, 2, 3), \tag{1.39}$$

on its complex elements, which reduces to nine the number of free parameters defining the matrix. By global phase rotations of the quark fields [16], five of these free parameters can be removed. Hence, the CKM matrix is completely defined in terms of four independent parameters, three mixing angles and one complex phase, where the latter accounts for CP violation.

The six orthogonality relations deduced from equation 1.38, which parametrize the CKM matrix can be represented as triangles in the complex plane. The most commonly used unitarity triangle, sketched in figure 1.1, arises from

$$V_{ud} V_{ub}^{*} + V_{cd} V_{cb}^{*} + V_{td} V_{tb}^{*} = 0, \tag{1.40}$$

with

$$\alpha = arg\left(-\frac{V_{tb}^{*} V_{td}}{V_{ub}^{*} V_{ud}}\right), \quad \beta = arg\left(-\frac{V_{cb}^{*} V_{cd}}{V_{tb}^{*} V_{td}}\right), \quad \gamma = arg\left(-\frac{V_{ub}^{*} V_{ud}}{V_{cb}^{*} V_{cd}}\right). \tag{1.41}$$

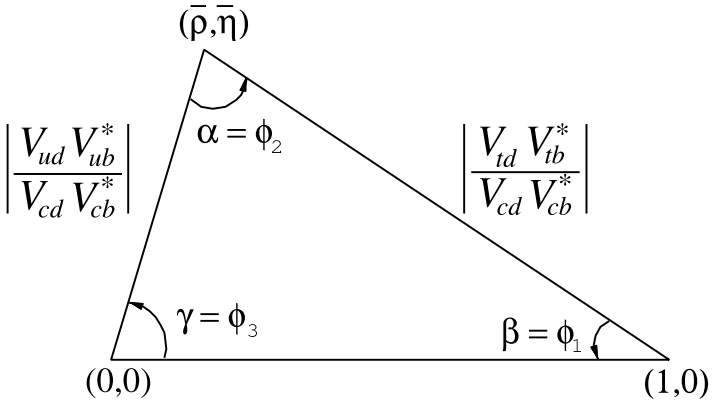

Figure 1.1: *The unitarity triangle. Reproduced from [6]*

Measurements of the angles of this triangle will be major elements of the LHCb programme, notably the angle γ which is the least well known. However, this thesis will concentrate on rare decay measurements and this is not discussed further. More details on LHCb γ prospects are given in [17,18].

1.4 Quantum Chromodynamics

QCD is the theory of strong interactions. It is based on the gauge symmetry $SU(3)_C$, which is a non-Abelian Lie group, where the subscript C stands for colour. Local transformations of this group keep the Lagrangian invariant. The strong colour charge interactions are mediated by 8 gauge bosons called gluons such that there are 8 generators in $SU(3)_C$.

By applying the gauge principle, the QCD Lagrangian is written as

$$\mathcal{L}_{\mathcal{QCD}} = \sum_q \bar{q}(x)\left(i\not{D} - m_q\right) q(x) - \frac{1}{4} G^{\alpha}_{\mu\nu} G^{\mu\nu}_{\alpha}, \tag{1.42}$$

where $G^{\alpha}_{\mu\nu}$ denotes the QCD strength tensor with

$$G^{\alpha}_{\mu\nu} = \partial_\mu A^{\alpha}_{\nu}(x) - \partial_\nu A^{\alpha}_{\mu}(x) + g_s f^{\alpha\beta\gamma} A_{\mu\beta} A_{\nu\gamma}, \tag{1.43}$$

and $f^{\alpha\beta\gamma}$ are the structure constants, A^{α}_{μ} are the gluon fields with α=1,...,8.

The coupling of the strong interactions α_s written as

$$\alpha_s = \frac{g_s^2}{4\pi}, \tag{1.44}$$

depends on the energy scale by means of the effective coupling such that

$$\frac{\partial \alpha_s(Q^2)}{\partial ln(Q^2)} = \beta\left(\alpha_s(Q^2)\right), \tag{1.45}$$

where Q denotes the momenta scale and β the expansion in α with

$$\beta(\alpha) = -\beta_0\alpha^2 + \mathcal{O}(\alpha^3) + ... \tag{1.46}$$

The renormalisation in equation 1.45 includes corrections of higher order, which add loop diagrams in the calculation. The QCD calculation is divided into two categories:

- The perturbative QCD regime which characterizes the short distance processes and energies above the QCD scale characteristic [19].
- The non-perturbative QCD regime which characterizes the long distance processes and low energy scales [20].

QCD is of great importance in the physics of LHC as it describes the production mechanism and the decays of hadrons. While LHCb extracts mainly results on the processes which occur via weak interactions, one has to consider also the strong interactions which occur in between the hadron's components.

1.5 Rare Semi-leptonic B Decays

Rare decays of b-hadrons provide another avenue to study new physics effects. $b \to s$ quark transitions are not allowed in the SM Lagrangian and are induced by the GIM[2] amplitudes [21] at the loop level. Hence, these decays are relatively rare, and can be affected by the presence of new physics in loops.

Rare B decays occur via flavour changing neutral currents (FCNC). The rare B decays of interest in this thesis are those which proceed via $b \to s$ and $b \to d$ transitions such as $B_d \to K^*\mu^+\mu^-$, $B_d \to K^*e^+e^-$, $B^+ \to K^+\mu^+\mu^-$, $B^+ \to K^+e^+e^-$, $B_s \to \phi\mu^+\mu^-$. A particular emphasis is placed on $B_d \to K^*\mu^+\mu^-$ in this section, which is the decay studied in this thesis.

After motivating the study of FCNC rare decays in section 1.5.1 and the search of NP in section 1.5.2, section 1.5.3 presents the Operator Product Expansion, which is necessary to understand the combined effects of the strong and weak interactions. The remaining sections are then more focussed on $B_d \to K^*\mu^+\mu^-$. Section 1.5.4 provides

[2]GIM stands for Glashow, Iliopoulos, and Maiani.

the relevant operators and the Wilson coefficients. Section 1.5.5 presents a number of observables with significant NP sensitivity, which are experimentally accessible with the much higher statistics available at LHCb. Finally in section 1.5.6, the results of the Babar, Belle and CDF experiments are discussed.

1.5.1 Motivation

The study of FCNC in particle physics has played a key role in high energy physics since the experimental discovery of the weak neutral current in 1973 by the Gargamelle experiment at CERN [22], the direct observation of the neutral charge carrier, the Z boson, by the UA1 and UA2 collaborations at CERN in 1983 [23] and its precise measurement at LEP in 1989 [24].

In the SM, FCNC are forbidden at tree level and only occur at higher orders, via box or penguin diagrams. New particles can form the same loop diagram and may modify the SM amplitude. FCNC are of two types classified based on the number of quark transitions in the event. FCNC with $\Delta F = 2$ are observed in $K^0 - \bar{K^0}$, $B^0 - \bar{B^0}$ and $D^0 - \bar{D^0}$ mixings [25–27]. Those with $\Delta F = 1$, like $b \to s$ transition, are observed in $B_d \to K^* \mu^+ \mu^-$, which is the decay studied in this thesis.

The $B_d \to K^* \mu^+ \mu^-$ [28–30] is a promising decay to search for new physics in LHCb. The four body final state, as $K^* \to K^+ \pi^-$, provides full angular information that is complementary to that obtained from studying $b \to s\gamma$ decays [31]. New particles can form the same loop diagram and may modify the SM amplitude. Hence, the angular distribution of the decay may be affected. $B_d \to K^* \mu^+ \mu^-$ offers a number of observables that are sensitive to additional new physics parameters beyond the SM, such as the forward backward asymmetry and its zero crossing point as well as the Wilson coefficients (see section 1.5.4).

1.5.2 New Physics Searches

Although the SM describes successfully most of the elementary particle interactions, it is not a complete theory. Astrophysical evidence has shown that the SM is incomplete, for instance it does not contain a theoretical explanation of the existence of dark matter in the universe, and as discussed in section 1.1 many unanswered questions remain.

The SM is interpreted as an effective theory valid at low energies. Therefore one needs to go to higher energies, which are only achievable in particle accelerators. The energy expected to be reached at the LHC could potentially reveal some hidden processes that

have not been observed previously. Thus, the LHC experiments are good probes for new physics phenomena [32].

Many theoretical extensions of the SM have been proposed. The most promising prediction is Supersymmetry (SUSY) [33], which introduces a number of new particles. So far, no direct evidences of any new particles have been observed in any experiment.

The $B_d \to K^*\mu^+\mu^-$ decay is a good place to look for indirect observation of new physics. As FCNC occur via penguin and box diagrams in the SM, any new particles would add additional loop diagrams at the same level as the SM. The presence of new particles inside the loops would affect observables as discussed in section 1.5.5. NP effects can be detected at mass scales well above those which can be probed directly. Its contribution can be introduced in different ways:

- Modification of the Wilson coefficient values due to the existence of new particles contributing with new loop diagrams.
- Appearance of new complex phases which arise from Wilson coefficients.
- Creation of new operators.
- New FCNC transitions would affect the CKM unitarity triangles.

1.5.3 The Operator Product Expansion

Since the quarks are bound in hadron states, the effects of QCD and the weak interaction are inextricably linked. The Operator Product Expansion (OPE) [34] was proposed to understand the effects of the weak and strong interactions together. It allows the factorization of the electroweak and perturbative QCD effects from the non-perturbative QCD. By applying the OPE formalism, the amplitude of a process from an initial state I to a final state F can be written as

$$A(I \to F) = \langle F|\mathcal{H}_{eff}|I\rangle = \sum_i C_i(\mu)\langle F|\mathcal{O}_i(\mu)|I\rangle, \tag{1.47}$$

where $\mathcal{H}_{eff}$ is the effective Hamiltonian. C_i are the Wilson coefficients and they encode the short distance part of the interaction. $\mathcal{O}_i$ are the Wilson operators and they describe the long distance part of the interaction. The renormalization scale μ is chosen to be of $\mathcal{O}(1GeV)$ for B-decays.

The Effective Hamiltonian of a semi-leptonic $b \to sll$ decay is written as

$$\mathcal{H}_{eff}(b \to sll) = \mathcal{H}_{eff}(b \to s\gamma) - \frac{G_F}{\sqrt{2}} V_{ts}^* V_{tb} \left[C_{9V}(\mu)Q_{9V}(\mu) + C_{10A}(\mu)Q_{10A}(\mu)\right], \tag{1.48}$$

where the effective Hamiltonian of the $b \to s\gamma$ is given by [35]

$$\mathcal{H}_{eff}(b \to s\gamma) = -\frac{G_F}{\sqrt{2}} V_{ts}^* V_{tb} \left[\left(\sum_{i=1}^{6} C_i(\mu) Q_i(\mu) \right) + C_{7\gamma}(\mu) Q_{7\gamma}(\mu) + C_{8G}(\mu) Q_{8G}(\mu) \right]. \tag{1.49}$$

By considering the amplitude A of the weak decay, the expression in equation 1.47 is rewritten as

$$A(I \to F) = \frac{G_F}{\sqrt{2}} V_{CKM} \sum_i C_i(\mu) \langle F | \mathcal{O}_i(\mu) | I \rangle, \tag{1.50}$$

which gives a general parametrisation of new physics in a model independent way, and can constrain some parameters with measurements as discussed in the next section.

1.5.4 Wilson Coefficients and Operators

As defined in section 1.5.3, the Wilson coefficients, C_i, are process independent coupling constants in the basis of effective vertices described by the local operator $\mathcal{O}_i$. The coefficients C_i encode the short distance physics and have been calculated perturbatively to Next-to-Next-to-Leading Order [36, 37]. The Wilson coefficients relevant to this study are C_7, C_9 and C_{10}, and the relevant operators are $\mathcal{O}_{7\gamma}$, $\mathcal{O}_{9V}$ and $\mathcal{O}_{10A}$, where

$$\begin{aligned} \mathcal{O}_{7\gamma} &= \frac{e}{16\pi^2} \bar{s}_\alpha \sigma_{\mu\nu} (m_b P_R) b_\alpha F^{\mu\nu}, \\ \mathcal{O}_{9V} &= \frac{e}{16\pi^2} (\bar{s}_\alpha \gamma^\mu P_L b_\alpha)(\bar{l} \gamma_\mu l), \\ \mathcal{O}_{10A} &= \frac{e}{16\pi^2} (\bar{s}_\alpha \gamma^\mu P_L b_\alpha)(\bar{l} \gamma_\mu \gamma_5 l), \end{aligned} \tag{1.51}$$

The mixing is taken into account by the effective Wilson coefficients, C_7^{eff} and C_9^{eff}. In the SM, C_7^{eff} and C_9^{eff} are defined as linear combinations of the original coefficients; at leading order they are given by [38]

$$\begin{aligned} C_7^{eff} &= C_7 - C_3/3 - 4C_4/9 - 20C_5/3 - 80C_6/9, \\ C_9^{eff} &= C_9 + Y(q^2), \end{aligned} \tag{1.52}$$

where $Y(q^2)$ represents the perturbative corrections to the Wilson operators $\mathcal{O}_1$ - $\mathcal{O}_6$. Detailed expressions for the Wilson operators can be found in [39].

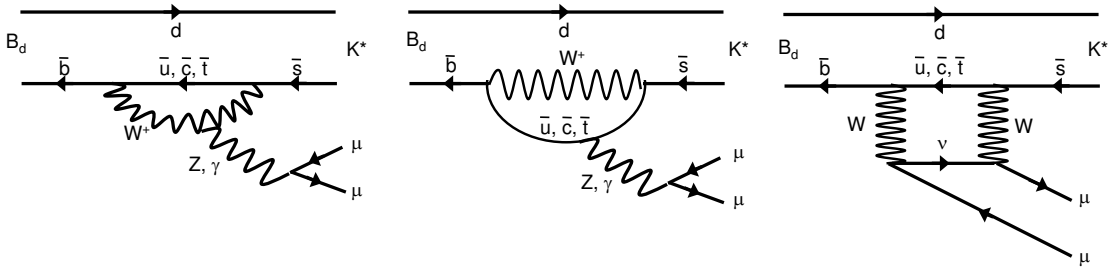

Figure 1.2: *Feynman diagrams for $B_d \to K^*\mu^+\mu^-$ in the SM. Reproduced from [40].*

1.5.5 Observables in $B_d \to K^*\mu^+\mu^-$

The $B_d \to K^*\mu^+\mu^-$ decay is a rare Flavour-Changing Neutral Current (FCNC) decay which proceeds via $b \to s$ quark transitions at the loop level. It has a branching ratio of $1.10^{+0.29}_{-0.26} \times 10^{-6}$ [6] and is sensitive to NP contributions through additional particles that may occur in the loop. Figure 1.2 shows the dominant SM Feynman diagrams for $B_d \to K^*\mu^+\mu^-$. The middle and left diagrams are loop diagrams; both present a γ and Z emission going into two muons. The right diagram is a box diagram, which presents double W exchange and the emission of two muons.

The $B_d \to K^*\mu^+\mu^-$ decay provides a significant number of observables such as the forward backward asymmetry, the dimuon invariant mass as well as the Wilson coefficients, which can be used to test the SM and to find any signs of new physics phenomena. This section reviews the observables that are experimentally easy to measure. The differential branching ratio is defined in section 1.5.5.1, the forward backward asymmetry in section 1.5.5.3, and the K^* longitudinal polarization F_L and the observable S_5 in section 1.5.5.4.

1.5.5.1 Differential Branching Ratio

The differential branching ratio is given by

$$\frac{d^2\Gamma}{dq^2 d\cos\theta_l} = \frac{3}{8}\left[(1+\cos^2\theta_l)H_T(q^2) + 2\cos\theta_l H_A(q^2) + 2\sin^2\theta_l H_L(q^2)\right], \qquad (1.53)$$

where q is the dimuon invariant mass, θ_l is the angle between the B_d ($\bar{B}_d$) and the $\mu^+(\mu^-)$ vectors in the dimuon rest frame, as illustrated in figure 1.3.

The functions H_T,H_A and H_L are quadratic combinations of transversity amplitudes which are given in terms of Wilson coefficients and hadronic form factors [41]. The latter contain information from the non-perturbative part of the Hamiltonian. The

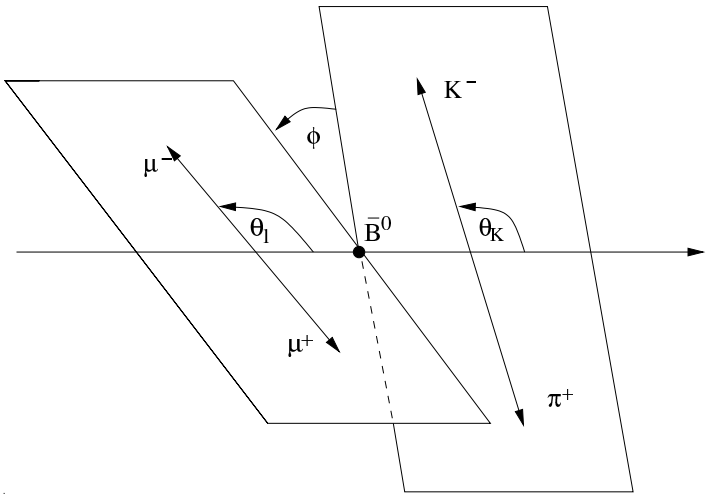

Figure 1.3: *Representation of the angles θ_l, θ_{K^*} and ϕ for $\bar{B}_d \to \bar{K}^*\mu^+\mu^-$. Reproduced from [40].*

expression of the differential branching ratio in equation 1.53 is written such that the Wilson coefficients can be extracted independently of q^2.

1.5.5.2 Dimuon Distribution

Figure 1.4 shows the differential branching ratio as a function of the squared dimuon mass distribution for the SM and various Supersymmetry models. The shaded area represents the SM prediction and the hadronic uncertainties. The solid and shaded lines represent respectively the Supergravity (SUGRA) and Mass Insertion Approximation (MIA)-SUSY models [42]. The two peaks are due to the J/Ψ and $\Psi(2S)$ resonances.

As shown in figure 1.4 the curve representing the SM is clearly separated from those of the Supersymmetry models, which reflects the overall rate differences between the models. In LHCb the absolute branching ratio is difficult to measure due to the significant uncertainties on the luminosity measurement. However, these uncertainties cancel out by using instead the ratios between the distributions, like the forward backward asymmetry distribution (see next section).

1.5.5.3 Forward Backward Asymmetry

The forward backward asymmetry (FBA) A_{FB} is of great interest in the $B_d \to K^*\mu^+\mu^-$ decay. It is a powerful tool to test the SM and search for NP. A_{FB} is defined as the difference between the number of forward-going events ($\theta_l < \pi/2$) and backward-going events

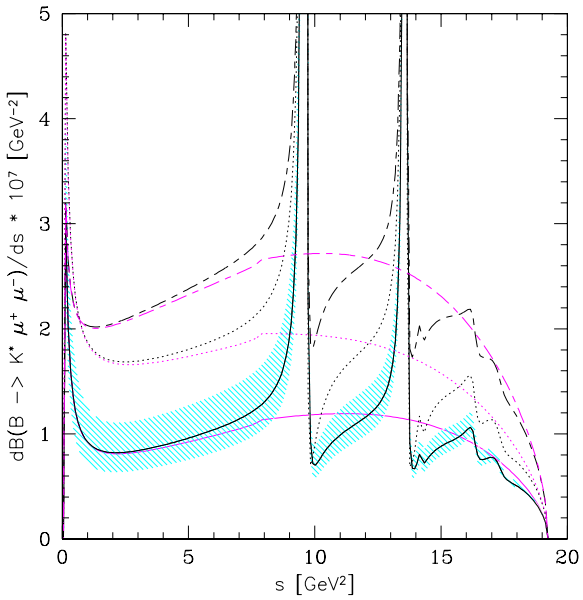

Figure 1.4: *Differential branching ratio as a function of the squared dimuon mass distribution for the SM and various Supersymmetry models. The solid line is the SM, the dotted and dashed lines corresponds respectively to SUGRA and MIA-SUSY models. The purple line represents short distance contributions and the shaded area represents form factor related uncertainties. Reproduced from [43].*

$(\theta_l > \pi/2)$ divided by the total number of events:

$$A_{FB}(q^2) = \frac{\int_0^1 d\cos\theta_l \frac{d^2\Gamma}{d\cos\theta_l dq^2} - \int_{-1}^0 d\cos\theta_l \frac{d^2\Gamma}{d\cos\theta_l dq^2}}{\int_{-1}^1 d\cos\theta_l \frac{d^2\Gamma}{d\cos\theta_l dq^2}}. \tag{1.54}$$

The point where the value of A_{FB} is zero, is referred to as the zero crossing point. The measurement of the zero-crossing point $\hat{s_0}$ of the FBA provides a clean measurement of the ratio of the Wilson coefficients C_9 and C_7. At leading-Log approximation within the Large-Energy- Effective-Theory the zero-crossing is predicted from [42]

$$\Re\{C_9^{eff}\} = -\frac{2\hat{m}_b}{\hat{s}_0} C_7^{eff} \frac{1-\hat{s}_0}{1+M_{K^*}^2-\hat{s}_0}. \tag{1.55}$$

where $\hat{s}_0 = q_0^2/M_{B_d}^2$ and $\hat{m}_b = m_b/M_{B_d}$. Measurement of this is discussed further in chapter 5.

1.5.5.4 F_L and S_5

In addition several other observables with NP sensitivity have been suggested for this channel, notably F_L and S_5. The K^* longitudinal polarization F_L is defined as the asymmetry between longitudinal decaying K^* with respect to the total decaying K^*:

$$F_L(q^2) = \int_{-1/2}^{1/2} d\cos\theta_K \frac{d^2\Gamma}{dq^2 d\cos\theta_K} \Bigg/ \int_{-1}^{1} dcos\theta_K \frac{d^2\Gamma}{dq^2 d\cos\theta_K} \tag{1.56}$$

where θ_K is the angle between the kaon and the B in the rest frame of the K^* (see figure 1.3). F_L is also written as [44]

$$F_L(q^2) = \frac{1}{9}\left(16 \int_{-1/2}^{1/2} d\cos\theta_K \frac{d^2(\Gamma+\bar{\Gamma})}{dq^2 d\cos\theta_K} \Bigg/ \frac{d(\Gamma+\bar{\Gamma})}{dq^2} - 11\right). \tag{1.57}$$

S_5 is a double asymmetry, being a forward backward asymmetry for the K decay with respect to K^* and an asymmetry in the angle between the K-π and dimuon planes:

$$S_5(q^2) = \frac{\int_{-\pi/2}^{\pi/2} d\phi\, FB_{K^*}(q^2,\phi) - \int_{\pi/2}^{3\pi/2} d\phi\, FB_{K^*}(q^2,\phi)}{\int_0^{2\pi}\int_{-1}^{1} d\cos\theta_K d\phi \frac{d^3\Gamma}{dq^2 d\cos\theta_K d\phi}}, \tag{1.58}$$

with

$$FB_{K^*}(q^2,\phi) = \int_{-1}^{0} d\cos\theta_K \frac{d^3\Gamma}{dq^2 d\cos\theta_K d\phi} - \int_{0}^{1} d\cos\theta_K \frac{d^3\Gamma}{dq^2 d\cos\theta_K d\phi} \tag{1.59}$$

where ϕ is the angle between the normal to the $K-\pi$ plane and the normal to the dimuon plane (see figure 1.3). S_5 can be expressed as [44]

$$S_5 = \frac{4}{3}\left(\int_0^{\pi/2} + \int_{3\pi/2}^{2\pi} - \int_{\pi/2}^{3\pi/2}\right) d\phi \left(\int_0^1 - \int_{-1}^0\right) d\cos\theta_K \frac{d^3(\Gamma-\bar{\Gamma})}{dq^2 d\cos\theta_K d\phi} \Bigg/ \frac{d(\Gamma+\bar{\Gamma})}{dq^2}, \tag{1.60}$$

New physics can enter through the Wilson coefficients (see section 1.5.4). Similarly to the zero crossing point $\hat{s}_0$ of the A_{FB} distribution, the zero crossing point of S_5,

$q_0^2(S_5)$ is also sensitive to NP contribution and is given by

$$q_0^2(S_5) = \frac{-m_B m_b(C_7^{eff} + C_7^{\prime eff})}{C_9^{eff} + \hat{m}_b(C_7^{eff} + C_7^{\prime eff})}, \tag{1.61}$$

where m_B and m_b are respectively the B meson and bottom quark masses. The primed coefficients $C_7^{\prime eff}$ have opposite chirality to the unprimed ones C_7^{eff}. As discussed in [44], A_{FB}, F_L and S_5 may be extracted by counting signal events as a function of only one or two decay angles. This makes them accessible with relatively small data samples. Further detailed definitions of other observables are given in [41].

1.5.6 Recent Experimental Results

The $B_d \to K^*\mu^+\mu^-$ decay is one of the most important modes that will be measured in LHCb. It was first detected by Belle [45] and thereafter by the Babar [46] and CDF [47] experiments. This section reviews recent experimental results from the Babar [48, 49], Belle [50] and CDF [51] experiments. The number of B-$\bar{B}$ events produced and the estimated branching ratios related to $B_d \to K^*\mu^+\mu^-$ from these experiments are presented in Table 1.2.

Experiment	B-$\bar{B}$ events	$B_d \to K^*\mu^+\mu^-$ events	BR($B_d \to K^*\mu^+\mu^-$)
Babar	384 million	64.4	$(1.35^{+0.40}_{-0.37} \pm 0.10)\times 10^{-6}$
Belle	657 million	246.7	$(10.7^{+1.1}_{-1.0} \pm 0.9)\times 10^{-7}$
CDF	[c]	101	$(1.06 \pm 0.14 \pm 0.09)\times 10^{-6}$

[c] This was obtained with 4.4 fb^{-1} from $p\bar{p}$ collisions at Tevatron.

Table 1.2: *Number of B-$\bar{B}$ and $B_d \to K^*\mu^+\mu^-$ events collected and measured branching ratios for $B_d \to K^*\mu^+\mu^-$.*

From these experiments, the following backgrounds have been identified:

- The main source of background arises from random combinations of leptons from semileptonic B and D decays. These decays were suppressed by the use of sophisticated selections using neutral networks [49].
- From $B \to J/\psi K^*$ and $B \to \psi(2S)K^*$ decays. Cuts on the dimuon invariant mass around the J/ψ and $\psi(2S)$ were applied to avoid contaminations from these decays.
- From B$\to$D($\to$ K$^*\pi$) π decays, where both pions are misidentified as leptons. These events were vetoed by assigning the pion mass to a muon candidate, and

requiring the invariant mass of the hypothetical $K^{(*)}\pi$ system to be outside the range 1.84-1.90 GeV/c^2.

- From $e^+e^- \to q\bar{q}$, with $q = u, d, c, s$, which were estimated using mass side bands and were subtracted.

The Babar Collaboration has made measurements of $B \to K^* l^+ l^-$ decays [48], where l is either muons or electrons. The branching fractions (see table 1.2), the direct CP asymmetry $A_{CP}^{K^{(*)}}$, the ratio of rates to dimuon and dielectron final states $R_{K^{(*)}}$, and the isospin asymmetry $A_I^{K^{(*)}}$ were measured. $A_I^{K^{(*)}}$ is the isospin asymmetry between the neutral B decays and the charged B decays, which are related by changing the d to u quark, and is given by

$$A_I^{K^{(*)}} = \frac{\Gamma(B^0 \to K^{(*)0} l^+ l^-) - r\Gamma(B^\pm \to K^{(*)\pm} l^+ l^-)}{\Gamma(B^0 \to K^{(*)0} l^+ l^-) + r\Gamma(B^\pm \to K^{(*)\pm} l^+ l^-)}, \tag{1.62}$$

where r is the ratio of the B^0 and B^+ lifetimes. The measurements were made within two ranges of q^2: the low and high q^2 regions, which are respectively defined as $0.1 < q^2 < 7.02$ GeV^2/c^4 and $q^2 > 10.24$ GeV^2/c^4. The measured $A_{CP}^{K^{(*)}}$ and $R_{K^{(*)}}$ are both in agreement with the SM prediction for the low and high q^2 regions. For $A_I^{K^{(*)}}$, no significant asymmetry was found for the high and combined q^2 regions. However, in the low q^2 region asymmetry of $A_I^{K^{(*)}\mu^+\mu^-} \approx -0.26^{+0.50}_{-0.34} \pm 0.05$ and $A_I^{K^{(*)}e^+e^-} \approx -0.66^{+0.19}_{-0.17} \pm 0.02$ were measured. Combining these two results, the value is found to differ from the negigible asymmetry of the SM at 2.7σ.

Babar have also measured the A_{FB} and F_L [49]. The results are only quoted with two bins of q^2 and have no significant tension with the SM. However, the A_{FB} spectrum is shifted towards the positive side of the SM expectation.

The Belle Collaboration has reported the highest statistics measurements of $B \to K^* l^+ l^-$ decays [50]. The branching fractions (see table 1.2), the differential branching fractions, the isospin asymmetries, the K* longitudinal polarisation were measured and are in agreement with the SM. The Collaboration has also measured the forward backward asymmetry. The $A_{FB}(q^2)$ spectrum was found to be shifted towards the positive side of the SM expectation, exceeding the SM by 2.7σ. The statistically less significant shift seen in Babar is in the same sense.

The CDF Collaboration has also recently presented measurements of $B \to K^{(*)}\mu^+\mu^-$ and first observation of the $B \to \phi\mu^+\mu^-$ decays [51]. Measurements of the differential branching ratio and the forward backward asymmetry as a function of q^2, and the K^* longitudinal polarization from the kaon angle in the K^{*0} rest frame are presented. These

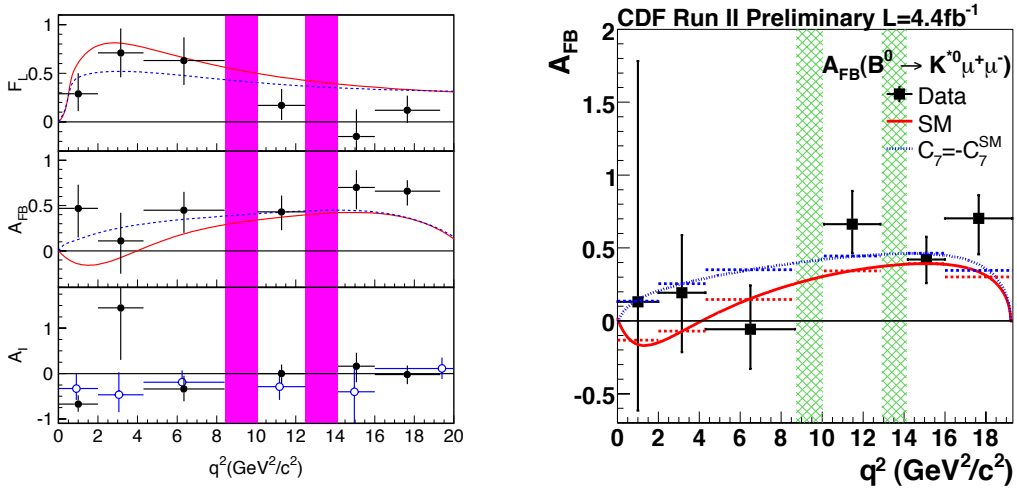

Figure 1.5: *Forward backward asymmetry distribution of the $B_d \to K^*\mu^+\mu^-$ from the Belle (middle left) and CDF (right) experiments. The two shaded regions correspond to the two veto regions of the J/ψ and $\psi(2S)$ resonances. The K^* longitudinal polarization F_L (top left) and the isospin asymmetry A_I (bottom left) distributions are also shown. Reproduced from [50, 51].*

are the first measurements at a hadron collider. All these measurements including the A_{FB} are consistent with the SM and the B-factories measurements.

Figure 1.5 presents recent distributions obtained from the Belle and CDF experiments. The forward backward asymmetry distributions are shown from both experiments. Note that they both use the opposite sign convention of that used in this thesis and defined in equation 1.54. In addition, from the Belle experiment, the K^* longitudinal polarization F_L and the isospin asymmetry distributions are also shown. As previously stated and within the error of the measurements, the A_{FB} distributions from CDF and Belle are in agreement.

1.5.7 Summary

This chapter provided an introduction to the SM theory of elementary particles discussing the electroweak and QCD components of the theory. Particular emphasis was placed on the rare B decay $B_d \to K^*\mu^+\mu^-$, which is one of the golden modes in the LHCb experiment. The $B_d \to K^*\mu^+\mu^-$ decay is an important channel for indirect measurement of any new physics phenomena, and observables that will be measured at LHCb were discussed. Recent experimental results from the B-factories and the Tevatron on the measurements of various observables, which are significant for $B_d \to K^*\mu^+\mu^-$ were also presented.

2 The LHCb detector

The Large Hadron Collider (LHC) is the main project of the European Organization for Nuclear Research (CERN). The LHC restarted in November 2009. The LHCb detector is one of the four main experiments of the LHC. LHCb is primarily designed to search for signs of new physics through b-hadron decays.

This chapter gives a description of the LHCb detector. Section 2.1 presents the LHC project. The LHCb experiment and each of its sub-detectors are described in section 2.2.

2.1 The LHC Accelerator

The Large Hadron Collider (LHC) [52, 53] is a proton-proton collider built at the European Organization for Nuclear Research (CERN) [54]. The LHC has a circular shape with a 27 km circumference and is placed approximately 100 m underground across the French-Swiss border near Geneva. The LHC ring is installed in the tunnel where the Large Electron Positron (LEP) [55] collider was placed previously. The accelerator will collide protons with a centre of mass energy of up to 14 TeV and a bunch-crossing[1] frequency of 40 MHz at a maximum luminosity[2] of 10^{34} $\mathrm{cm}^{-2}\mathrm{s}^{-1}$. This section gives an overview of the LHC and its four main experiments.

The LHC infrastructure has a pre-accelerating system, injection system and a main ring (see figure 2.1). First, protons are produced from hydrogen atoms and then injected into the Linear Accelerator (LINAC2) [56], which gives them an energy of 50 MeV. The second accelerating process happens in the Proton Synchrotron Booster (PSB) [57] where the protons reach an energy of 1.4 GeV. Then the protons pass into the Proton Synchrotron (PS) [58] to gain an energy of 26 GeV. Before entering the LHC, the protons are accelerated to an energy of 450 GeV by the Super Proton Synchrotron

[1] A bunch refers to the distribution of particles during the accelerating process.

[2] The luminosity is the measure of particle flux. It is given by the product of the number of particles in each bunch divided by the beam cross-sectional area and divided by the time interval between collisions.

(SPS) [59]. Finally, the protons are injected in the LHC where they reach an energy of 7 TeV.

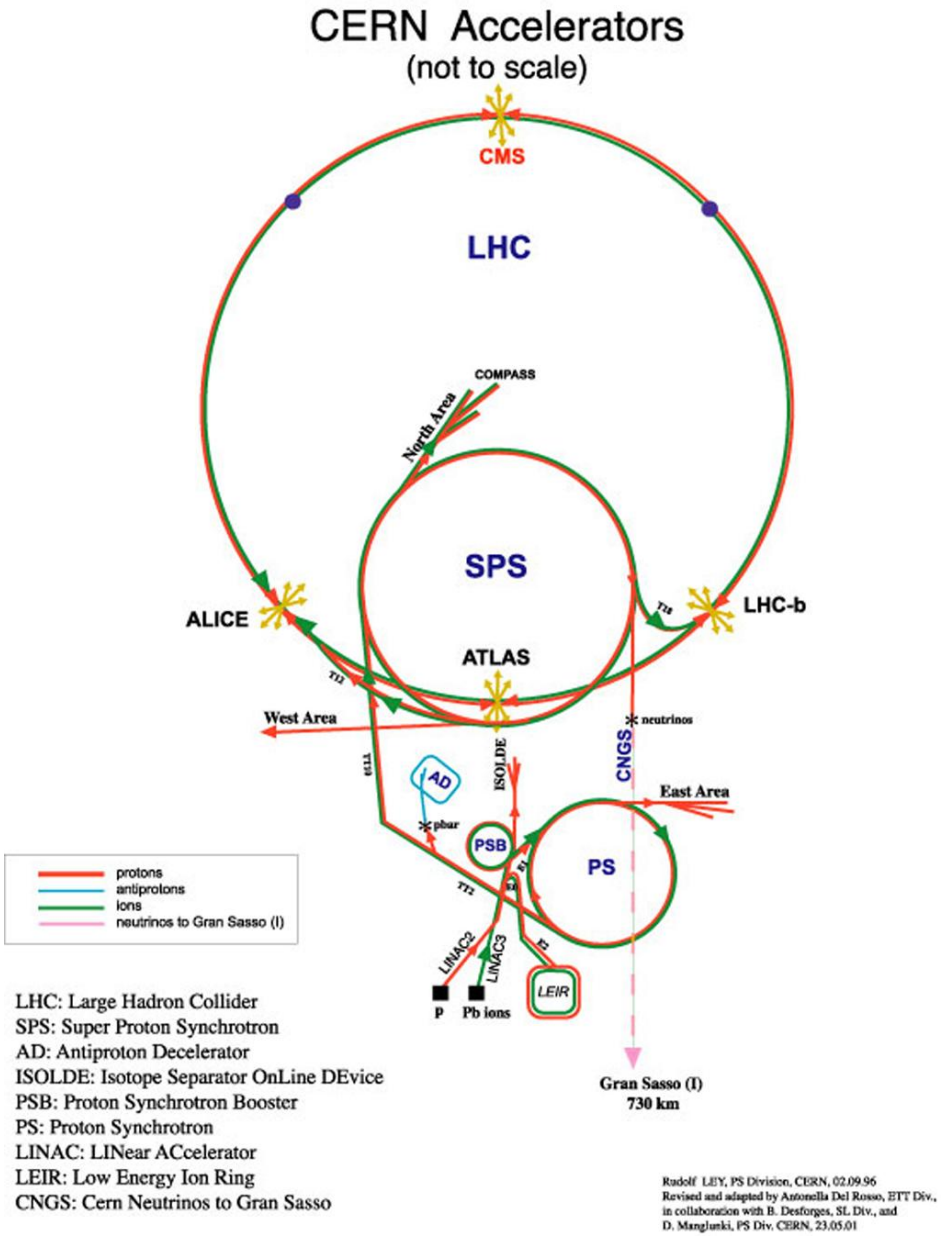

Figure 2.1: *Schematic overview of the accelerator system at CERN. Reproduced from [52].*

The LHC is made with two beam pipes in order to circulate protons in both directions. Furthermore, its superconducting dipole magnets provide 8.4 T to keep the protons trajectory inside the beam pipe. The LHC parameters are given in Table 2.1.

The proton-proton collisions take place in four interaction regions along the LHC, where the four experiments are located (see figure 2.2). The LHC detectors aim to make precision measurements of known standard model physics and search for new

Parameter	Value	Unit
Circumference of the Ring	27	km
Proton energy at injection	0.450	TeV
Proton energy at collision	7	TeV
Center of mass energy	14	TeV
Circulating beam current	0.582	A
Luminosity	10^{34} cm^{-2}s^{-1}	
Number of Bunches	2808	
Number of particles per bunch	1.5×10^{11}	
Time between beam crossings	25	ns
Beam size at IP8[a]	70.9	μm
Crossing angle at IP8	200	μrad
Bunch length	7.55	cm

[a]IP8 is the LHCb collision point

Table 2.1: *The main parameters of the LHC accelerators. Information taken from [52].*

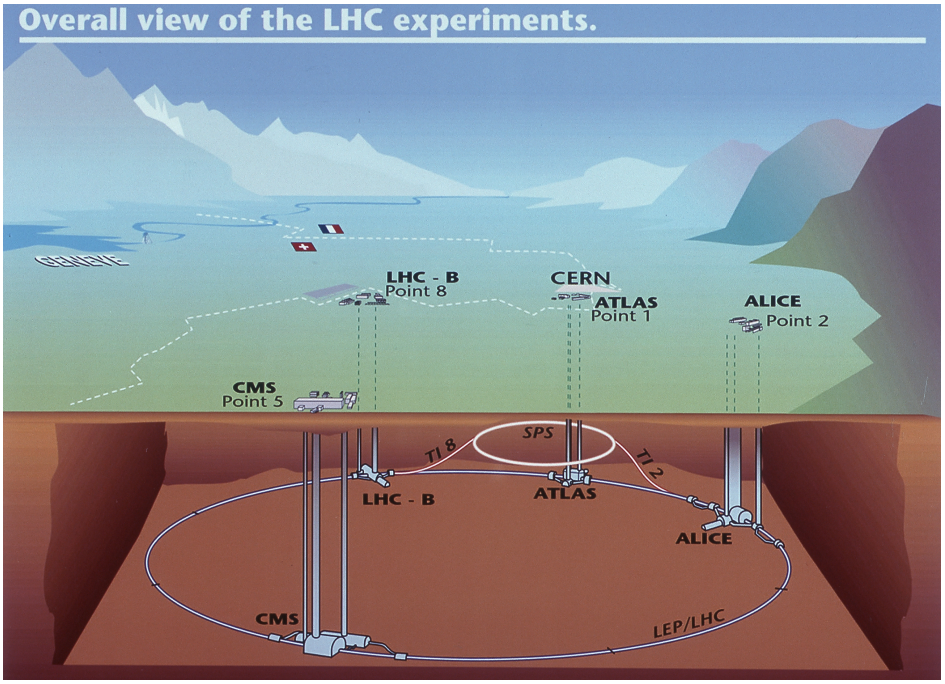

Figure 2.2: *Overview of the four main experiments at the LHC. Reproduced from [52].*

physics. The primary aims of the Toroidal LHC ApparatuS (ATLAS) [60] and the Compact Muon Solenoid (CMS) [61] detectors are to search for Higgs boson(s), Supersymmetry particles (SUSY) and signs of other directly produced phenomena that can be directly or indirectly inferred from data (e.g. extra dimensions). A Lead Ion Col-

lider Experiment (ALICE) [62] is focused on analyzing heavy-ion[3] (Pb-Pb) collisions to study the quark-gluon plasma. Finally, the Large Hadron Collider beauty experiment (LHCb) [63], which is the topic of this thesis, is designed for new physics searches through the study of b-physics.

2.2 The LHCb Experiment

The Large Hadron Collider beauty experiment (LHCb) is designed for precise measurements of CP violation and rare decays of hadrons containing b-quarks. It will also have significant research capabilities in other areas, notably in charm physics.

The LHCb detector, as shown in figure 2.3, is a forward-arm spectrometer and has an angular acceptance of ± 250 mrad in the yz plane[4] and ± 300 mrad in the xz plane and measures 20 m long in the beam direction (z). Figure 2.4 presents the production angles of the b mesons at the LHC. Both the b and the $\bar{b}$ are produced in the same hemisphere. The LHCb detector covers 34 % of the produced b-quarks in the proton-proton collisions.

The LHCb experiment will be operated at an instantaneous luminosity of 2×10^{32} cm^{-2}s^{-1}, which is a factor of 50 lower than the maximum luminosity of the LHC. At this luminosity there is most probably only one proton-proton collision per crossing. This has been chosen so that the trigger can accurately identify the primary production vertex and the decay vertex of the b-hadrons. Running at this reduced luminosity also reduces the radiation damage in the detector. This is an important issue for the Vertex Locator which is only 7 mm from the LHC beam. This reduced luminosity has been obtained by having a relatively defocused beam at the LHCb interaction point compared with ATLAS and CMS.

In the following sections each of the sub-detectors in the LHCb experiment is described. Section 2.2.1 describes the Vertex Locator in more detail, as much of the work in this thesis relates to this detector. Sections 2.2.2 to 2.2.6 are dedicated respectively to the Ring Imaging Cherenkov detector, the Magnet, the Tracking System, the Calorimeters and the Muon System. Section 2.2.7 and section 2.2.8 describe the experiment's Trigger System and Online System. The software and offline processing of the experiment is outlined in section 2.2.9.

[3] The LHC will collide lead nuclei at centre of mass energies of 5.5 TeV per colliding nucleon pair for a short period each year. [52]

[4] The LHCb coordinate system is a right handed system with positive z running along the beam-line away from the interaction point and positive y 'upward'. Positive x points toward the cavern access and away from the LHC cryogenics.

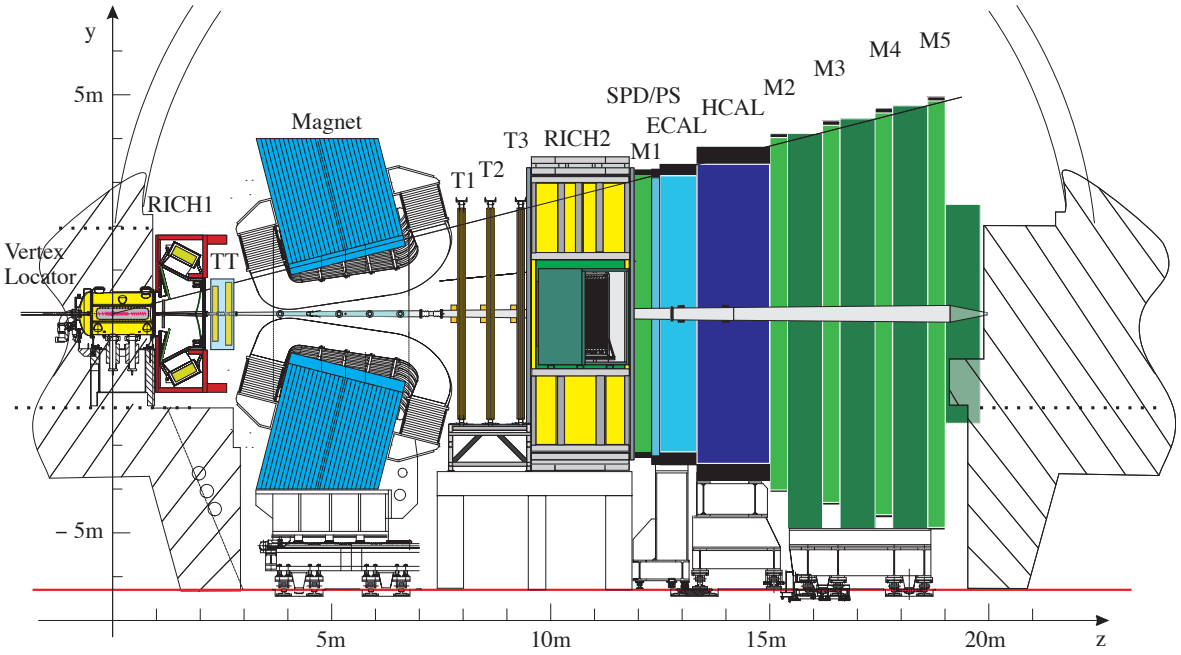

Figure 2.3: *The LHCb detector showing all sub-detectors. From left to right: the VErtex LOcator (VELO), the first Ring-Imaging Cherenkov Detector (RICH1), the Trigger Tracker (TT), the Magnet, three Tracking Stations (T1 - T3), RICH2, the Silicon Pad Detector and Pre-Shower (SPD/PS), the first Muon Station (M1), the Electron and Hadron CALorimeters (ECAL, HCAL) and finally the Muon Stations (M2 - M5). Reproduced from [63].*

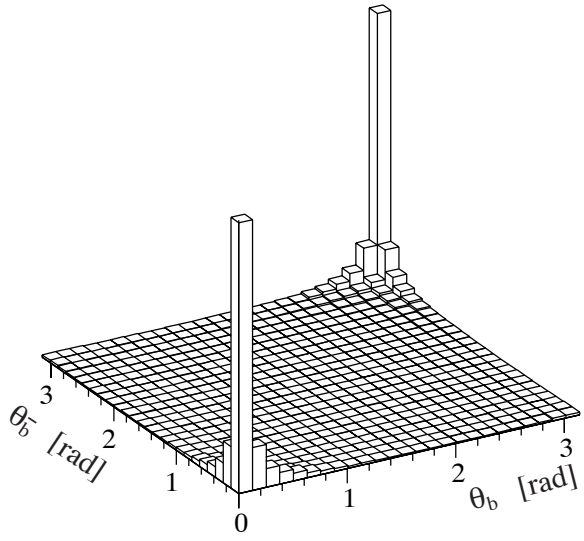

Figure 2.4: *Polar angle distribution of $b\bar{b}$ quarks produced in p-p collisions at the LHC. Reproduced from [64].*

2.2.1 The Vertex Locator

The Vertex Locator is the first tracking system of the LHCb detector. It is designed to provide precise measurements of track coordinates close to the interaction point, obtaining the position of the primary proton-proton collision vertex and the secondary decay vertices of b-hadrons. The determination of the position of the displaced secondary vertices with great precision is crucial in b and c-hadron decays both for their identification in triggering and for time dependent analyses.

The VELO, as shown in figure 2.5 left, is divided in two halves and the active elements are arranged in 21 stations along the beam direction. The first 2 stations located upstream of the VELO are the pile-up system. The pile-up veto system distinguishes between crossings with single and multiple visible interactions, thus only events with a single interaction are selected.

The VELO silicon sensors in each of the 21 stations have an inner radius of 7 mm. This distance is smaller than the aperture required during the LHC injection, hence the two VELO halves have been designed to be retractable. Therefore, as represented in figure 2.6, the VELO can be moved between open and closed positions. In the open position, as shown in figure 2.6 left, the halves are retracted by 30 mm each side. This position is necessary to prevent damage to the detectors during the LHC injection. Once stable beam collisions are obtained in the LHC, the VELO is moved to the closed position, as shown in figure 2.6 right. In this position the modules on each half overlap slightly which allow a complete coverage of azimuth angle and eases the alignment of the VELO [65]. Each VELO module has two different types of strip sensors placed back to back, R and ϕ sensors (see section 2.2.1.2).

In order to reduce the material traversed by a charged particle before it crosses the sensors, the VELO detectors are not placed outside a beam pipe but rather inside a vacuum. The detectors are located in a secondary vacuum separated from the LHC primary vacuum by a 300 μm thin aluminium sheet with a corrugated surface. This aluminium foil both protects the integrity of the LHC vacuum from outgassing by the modules and prevents electronic pickup from the beam on the sensors.

2.2.1.1 Requirements

Primary and secondary vertex reconstruction is fundamental to the b-physics aims of LHCb. The determination of these parameters provides an accurate measurement of the particle lifetime. This is used in the High Level Trigger for the selection of events with enriched b-hadron content and in the LHCb offline physics analysis. To

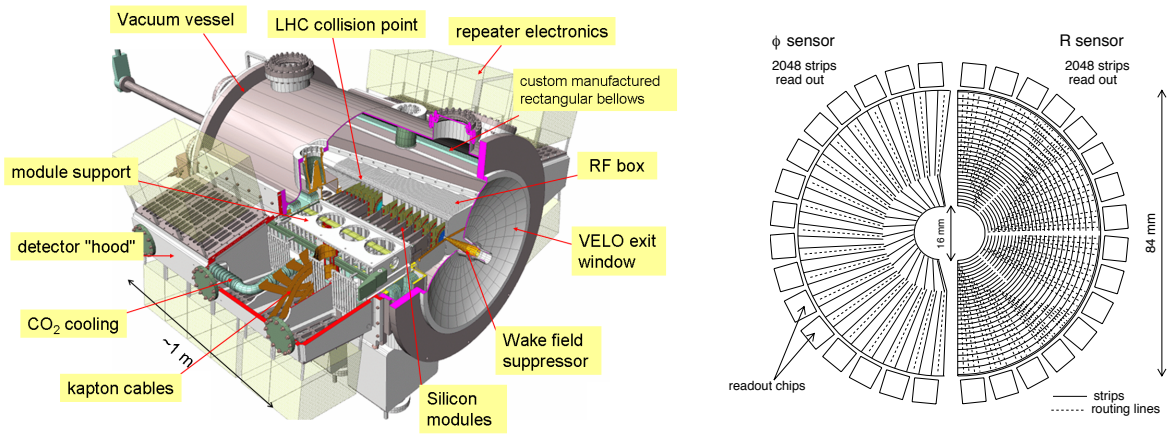

Figure 2.5: *(Left) Schematic of the LHCb Vertex Locator. Reproduced from [66]. (Right) Schematic comparison of the R and ϕ VELO Sensor layout. Reproduced from [67].*

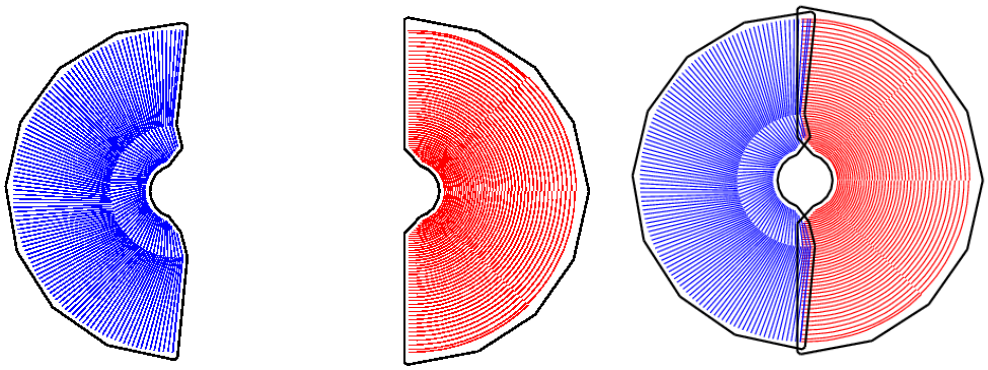

Figure 2.6: *Schematic view of the VELO detectors in (Left) the open position (Right) in the closed position. Reproduced from [66].*

fulfil efficiently its primary role during LHCb operation, the VELO is required to meet several conditions:

- The VELO aims for a Signal to Noise ratio greater than 14 to ensure an efficient trigger performance. The signal to noise value is equal to the most probable signal value from a cluster of strips when an ionizing particle traverses the sensor divided by the root mean square of the noise value of an individual channel.

- An accurate cluster spatial resolution is required. The achieved value is about 10 μm for perpendicular tracks and improves to 4 μm at the optimal track angle of $\approx 10°$.

- The VELO has to measure at least three space points for particles with pseudo-

rapidities in the range $1.6 < \eta < 4.9$ and primary vertex position in the range $|z| < 10.6$ cm. Hence, the angular acceptance of the downstream detector is covered.

- The VELO modules are designed to operate in an extreme radiation environment with non-uniform particle fluences. The expected fluence after an integrated luminosity of 2 $\text{fb}^{-1\dagger}$ in the innermost region of the silicon sensor is 1.3×10^{14} 1 MeV neutron equivalents $(\text{n}_{\text{eq}})/\text{cm}^2$. The irradiation is highly non-uniform and decreases to 5×10^{12} $\text{n}_{\text{eq}}/\text{cm}^2$ at the outer edge of the silicon. The modules are required to be able to be fully depleted for at least 3 years of nominal LHCb operation.

- The VELO uses a cooling system to remove the heat generated in the readout chips and to maintain the sensor temperature between -10°C and 0°C which limits the effects due to radiation damage.

2.2.1.2 The VELO Sensors and Modules

2.2.1.2.1 The Sensors

The VELO sensors are located as close as 7 mm from the LHC beam axis. The severe radiation induced damage at this region required the development of radiation tolerant technology. The VELO sensors[5] are silicon strip sensors made with n^+-implants in n-bulk technology with p-spray for strip isolation (see figure 2.7). Alternative techniques of strip isolation are described in more details in chapter 4.

The fabrication process of this type of sensor requires double sided processing [68] with guard-rings on the back to prevent high electric field strengths at the edge of the sensors which lead to avalanche breakdown. After type inversion[6] [69], the junction grows from the front n^+ side where the signal is picked up. The n^+-*on*-n detector does not guarantee that it will be fully depleted but it is more beneficial when operated under depleted after type inversion. An explanation of the theory of silicon detectors is presented in chapter 4.

The VELO sensors use (r,ϕ) geometric coordinates, with R and ϕ type measuring sensors. The two types of sensors have the same semi-circular shape and are both

$^\dagger 2$ fb^{-1}corresponds to one nominal year of running in LHCb

[5]The LHCb sensors were manufactured by Micron Semiconductors Ltd.

[6]The type inversion occurs such that irradiated at a certain dose, an n-type bulk material effectively turns into p-type.

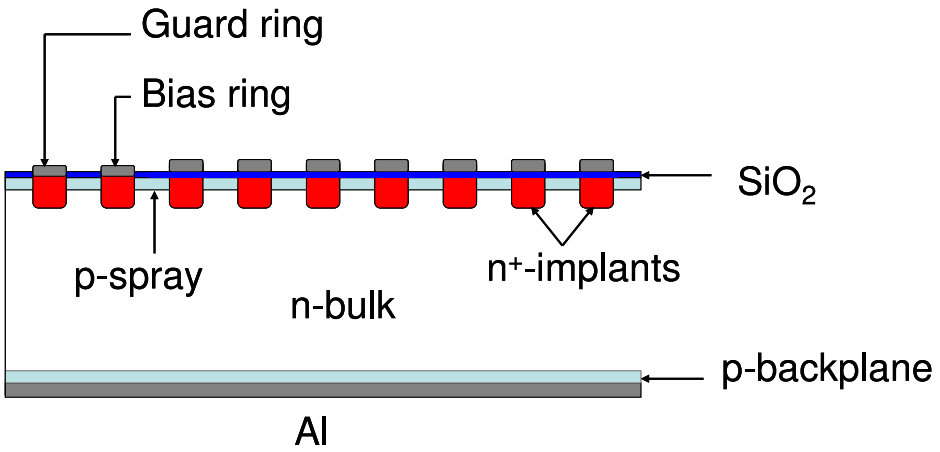

Figure 2.7: *Illustration of an unbiased n^+-on-n silicon detector.*

300 μm thick. Each one has 2048 strips. Figure 2.5 right, shows a schematic comparison between the R and ϕ VELO sensor layout. Their principal characteristics are summarized in Table 2.2.

The R sensor, as illustrated in figure 2.8, has strips arranged radially. Hence, It provides information on the radial distance from the beam axis of a traversing particle. As shown in figure 2.8 left, the R sensor is divided in four regions such that an angle of 45° in ϕ is covered by each strip. The strip pitch[7] varies between 40 μm and 101.6 μm.

The other type of sensor, called ϕ sensors, has strips arranged approximately azimuthally. It provides information on the azimuthal coordinate around the beam axis. The ϕ sensor strips are divided into inner and outer regions. This division reduces the overall strip length, hence, the strip occupancy as well as its capacitance. The strip pitch in the inner region varies between 35.5 μm and 78.3 μm, while in the outer region it varies between 39.3 μm and 96.6 μm. The inner and the outer strips make a small angle with respect to the radial line, called a stereo angle. The inner strips make a 20° angle with respect to a radial line at the start of the strip (8 mm from the beam). The outer strips are -10° from the radial line at the start of the strip (17 mm from the beam).

The modules are arranged so that the ϕ sensor on the subsequent module is flipped by 180°. Hence, two subsequent ϕ sensors have strips with opposite stereo angles. These angles improve the pattern recognition for tracking.

[7]The strip pitch corresponds to the distance between the current strip implant to its neighbouring strip.

	R-sensor	ϕ-sensor
Number of sensors	42+4(VETO)	42
Readout channels per sensor	2048	2048
Sensor thickness	300 μm	300 μm
Smallest pitch	40 μm	38 μm
Length of shortest strip	3.8 mm	5.9 mm
Length of longest strip	33.8 mm	24.9 mm
Inner radius of active area	8.2 mm	8.2 mm
Outer radius of active area	42 mm	42 mm
Angular coverage	182°	182°
Stereo angle	-	10°-20°
Double metal layer	yes	yes
Average occupancy	1.1 %	1.1/0.7 % inner/outer

Table 2.2: *The main characteristics of the VELO sensors. Information taken from [66]*

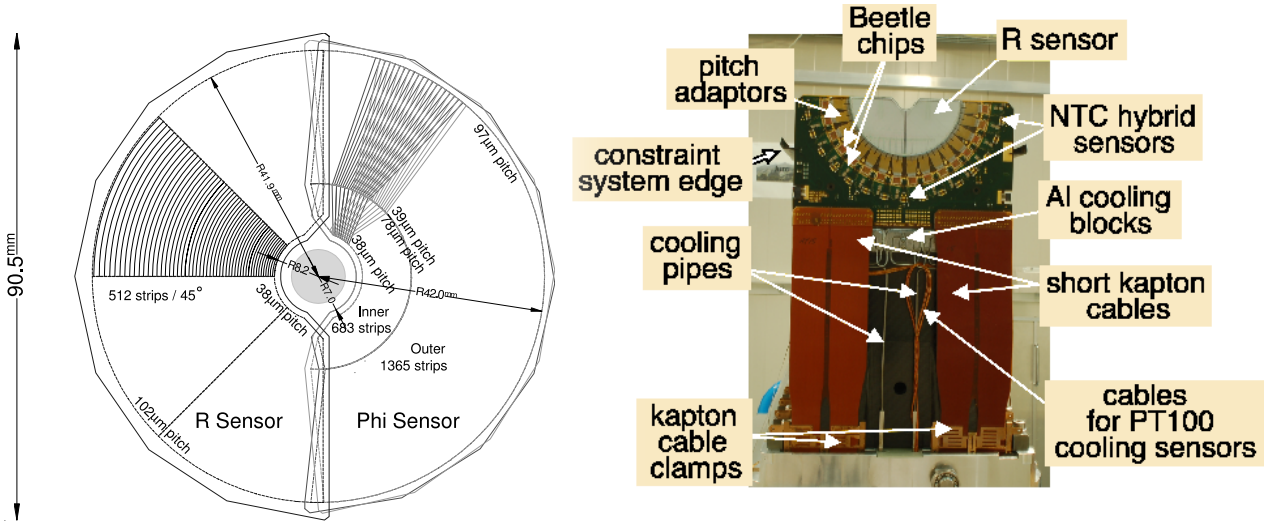

Figure 2.8: *(Left) Schematic illustrating the r-ϕ geometry used for the VELO sensors and their main characteristics. (Right) Photograph of a VELO module. Reproduced from [66].*

2.2.1.2.2 The Modules

A VELO module consists of an R and ϕ sensor, glued back-to-back, mounted together on an electronics hybrid. This is supported on a carbon-fibre paddle [70]. Figure 2.8 right shows an annotated picture of a VELO module. The front-end electronics on each module consist of 32 Beetle readout chips [71]. The sensors are connected to the electronics on the hybrid with wire bonds. Various readout circuit components are also mounted on the hybrid. Kapton cables are connected onto the hybrid to route signals in and out of the modules. These cables are also used to supply low voltage

power, control signals to the electronics and high voltage to bias the sensors. The hybrid is equipped with cooling blocks in order to compensate the heat generated from the electronics and to maintain the sensor temperature below -5°C. Four Negative Coefficient Thermistors (NTCs) mounted on the hybrid are used to monitor the sensor and module temperatures.

2.2.1.2.3 Electrical Readout Chain

A charged particle traversing the sensor produces electron-hole pairs in the silicon. These are drifted under the bias voltage and the electrons are collected on the n^+-strips implants. This signal is read out from the strips by Beetle front-end chips. Each single chip reads out 128 channels using four readout ports with 32 readout channels per port. Hence, each R or ϕ sensor is equipped with 16 Beetle front-end chips.

The VELO electrical readout chain is illustrated in figure 2.9. The analogue signal, which has been collected from the strips, is integrated through a pre-amplifier. The integrated signal is then transferred to a shaper which formats the pulse in order to obtain the appropriate response. The signal then passes into an analogue pipeline to match the trigger latency (see section 2.2.7). The data is brought off the chip at a frequency of 40 MHz.

After being collected by the Beetle chip, the signals are routed out to the repeater boards via two sets of kapton cables. Then they are driven by line drivers to the TELL1 boards [72] via 60 m analogue cables. The repeater boards also host other signals: the clock and fast command signals supplied by the control boards, configuration signals from control boards and temperature monitoring signals to the temperature boards. The TELL1 is an FPGA[8] based acquisition system. Within the TELL1, the signals that arrive from the analogue cables are digitised and then undergo different stages of processing such as pedestal subtraction, common mode subtraction and clustering. The output of the TELL1 processing is the raw VELO data. The analysis of these data for the VELO performance and monitoring is performed using a software package called VETRA [73].

2.2.1.3 The Vacuum System

The LHC beam circulates inside a beam pipe at very low pressure, of the order of 10^{-8} mbar. In the VELO the primary vacuum is at this pressure and the secondary

[8]FPGA stands for Field Programmable Gate Array. It is an integrated circuit containing a large number of logic blocks that one can program.

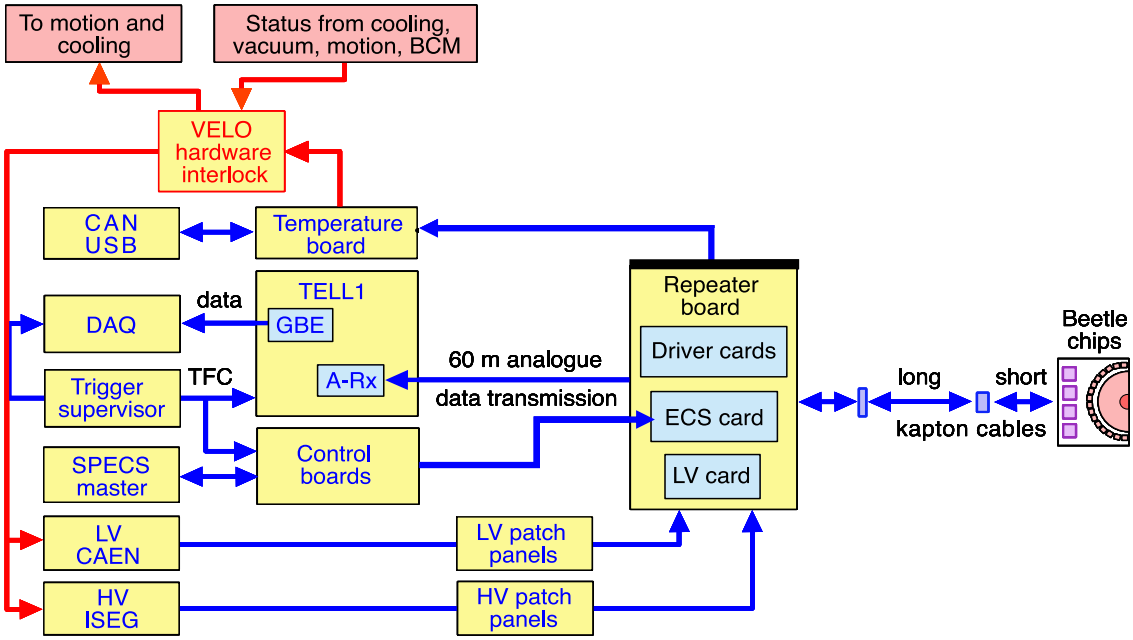

Figure 2.9: *Schematic of the VELO electrical readout chain. Reproduced from [66].*

vacuum containing the detector has a pressure below 10^{-4} mbar. The use of a secondary vacuum prevents any contamination to the primary vacuum from outgassing of the modules.

Operating the VELO under vacuum implies that the primary and secondary vacuum are kept at pressure close to each other. A pressure difference of 20 mbar between the primary and secondary vacuum can cause a considerable damage to the RF-foil. Hence, during venting and evacuation of the VELO vacuum system a special procedure is followed so that the pressure difference between the beam and detector vacuum will never exceed 5 mbar overpressure in the detector vacuum and 2 mbar overpressure in the beam vacuum.

2.2.1.4 The Cooling System

The operation of the VELO requires the use of an active cooling system in order to transfer the heat generated by the front-end electronics outside the system. Moreover, the silicon sensors must be operated at low temperatures to reduce the radiation damage. A power of approximately 20 W is consumed by one VELO module during operation. Under vacuum, this power would raise the temperature and damage the electronic components. The cooling system ensures that the heat generated by the electronics is extracted and keeps the silicon sensor temperature below -5°C. The cooling system uses a CO_2 liquid coolant. The cooling liquid is dissipated through 5 cooling blocks attached to each VELO module.

2.2.1.5 The Motion System

During the beam injection and damping, the VELO modules have to be moved away from the interaction region by 30 mm. After stable beam conditions are obtained, the detectors will be placed into an optimized position. The motion system can be adjusted within 5 mm in x and y to that position, as the beam position may change from fill to fill. The VELO has a motion mechanism that is used to bring the detector to its required position with a precision of approximately 10 μm. The motion system is remotely controlled by a Programmable Logic Controller (PLC). The VELO modules can be moved independently in x, and together in y. The motion system has a series of stops that prevents the system from moving beyond mechanical limits.

2.2.1.6 The Low Voltage and High Voltage Supplies

In order to operate the VELO modules, low voltage and high voltage systems were developed. They are installed in a radiation and magnetic field free zone in the LHCb cavern, called the counting house. The counting house is separated from the LHCb experimental zone by a thick concrete wall. Both high voltage and low voltage systems have hardware interlocks to prevent damage and provide safety in case of malfunctions.

The high voltage system supplies reverse bias to the VELO silicon sensors. The sensors are supplied a reverse bias voltage between 100 V and 500 V. As the sensor is irradiated, the voltage supplied will have to increase. The LHCb VELO high voltage system is described in detail in chapter 3.

The low voltage system supplies voltage to the analogue and digital part of the front-end chips, to the line drivers and to the digital circuitry of the control boards for the control signals (see section 2.2.1.2.3). Further details can be found in [66, 67].

2.2.2 The Ring Imaging Cherenkov Detector

The Ring Imaging Cherenkov (RICH) detector is designed to provide good particle identification [63, 64] between pions, kaons and protons. Particle identification is necessary to differentiate between CP-violating decays with identical topologies. The RICH system is composed of two detectors, RICH1 and RICH2 [66, 74]. Schematic views of RICH1 and RICH2 are presented in figure 2.10.

Cherenkov detectors are used to distinguish charged hadrons with different mass. Electromagnetic (Cherenkov) radiation is emitted when charged particles traverse a material with velocity v exceeding the local phase velocity of light in that material.

	RICH1		RICH2
	Aerogel	C_4F_{10}	CF_4
n	1.03	1.0014	1.0005
θ_{max} (mrad)	242	53	23
p range (mrad)	1-15	10-60	50-150

Table 2.3: *The values of the radiator characteristics used in RICH1 and RICH2. n is the refractive index, θ_{max} is the saturation angle (when β=1) and p the working momentum range. Information taken from [66].*

The radiation is emitted in a cone with an angle θ_C. The relation between the angle of emission θ_C and the particle velocity v is as follows

$$\cos\theta_C = \frac{1}{\beta n}, \tag{2.1}$$

where n is the refractive index of the material transversed and $\beta = v/c$. The velocity of the particle can be determined by measuring the angle θ_C, and when the momentum is known from the tracking system, the particle mass can be extracted. The RICH system uses three different materials with different refractive indices to cover the whole spectrum. The main parameters of the RICH radiator materials are listed in Table 2.3.

The RICH1 detector is placed between the VELO and the trigger tracker. It is designed to identify low momenta particles with Aerogel and C_4F_{10} radiators. Aerogel facilitates the identification of pions and kaons with a momentum range $1 < p < 15$ GeV/c, whereas the C_4F_{10} gas allows the identification of pions and kaons with momentum range $10 < p < 60$ GeV/c.

The RICH2 detector is placed between the T-stations and calorimeters. It uses CF_4 gas as a radiator material. CF_4 gas allows the detector to identify pions and kaons with momentum in the range $50 < p < 150$ GeV/c.

The Cherenkov light emitted in the radiators will be collected on a plane of photodetectors. They consist of Hybrid Photon Detectors (HPD), which combine a vacuum photo-cathode and a pixel sensor [75] to have single photon resolution.

2.2.3 The Magnet

The LHCb detector has a dipole magnet which bends charged particles. The analysis of particle tracks before and after the magnet provides the measurement of their momenta. The measured momentum values up to 200 GeV/c are obtained with a resolution of $\delta p/p \approx 0.4$ %. An integrated magnetic field of 4 Tm is provided to achieve this

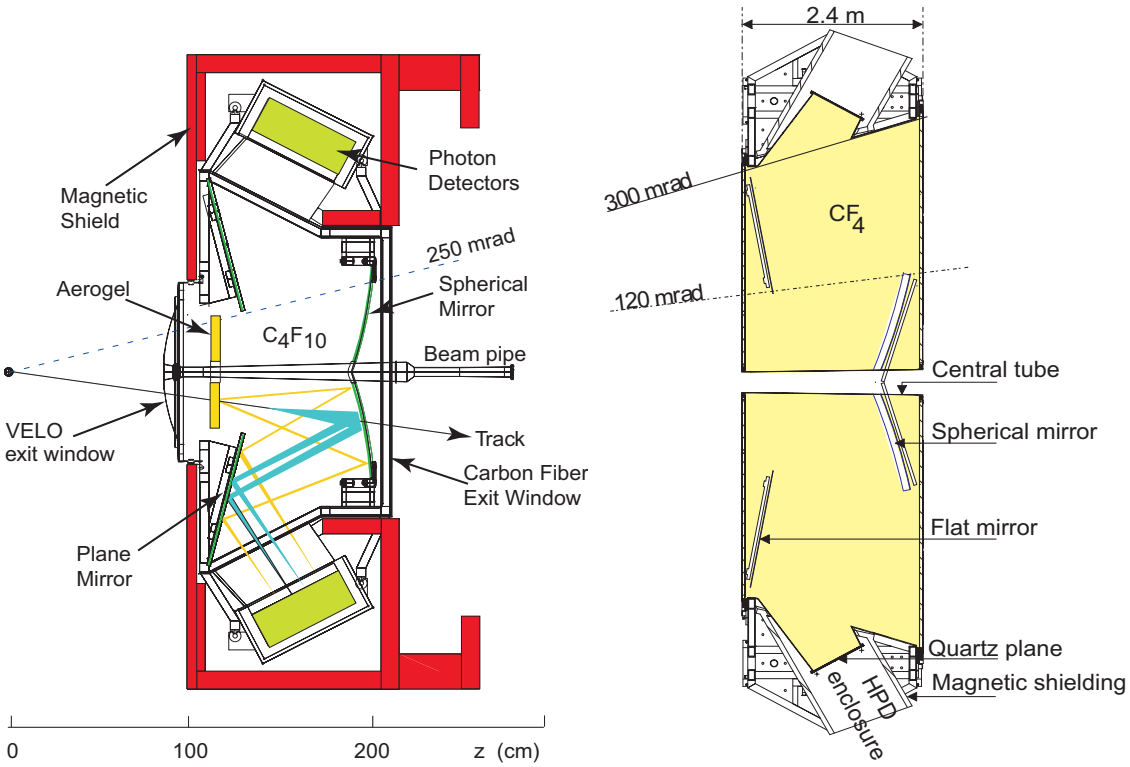

Figure 2.10: *Schematic view of the RICH detectors. (Left) RICH1 detector. (Right) RICH2 detector. Reproduced from [66].*

precision. Moreover, the field has to be uniform along the transverse direction. The magnet, as shown in figure 2.11, is a conventional (non-superconducting) warm dipole. During LHCb data taking, the magnetic field can be reversed regularly in order to study systematic asymmetries that could fake CP violation effects.

2.2.4 The Tracking System

The LHCb tracking system [66, 76, 77] will determine particle tracks in the region between the two RICH detectors and will measure particle momenta. It is composed of 4 stations arranged along the beam direction, the Tracker Turicensis (TT) stations and the 3 T stations (T1, T2, T3). The information from the 4 tracking stations are combined with those obtained from the VELO and the RICH system in order to perform a complete reconstruction of a particle trajectory and track association.

2.2.4.1 Tracker Turicensis

The TT stations are located between RICH1 and the Magnet. It consists of 4 silicon detector layers arranged in two pairs, (x,u) and (v,x). Figure 2.12 left illustrates the layout of a silicon detector layer on the TT stations. Each pair is composed of one layer

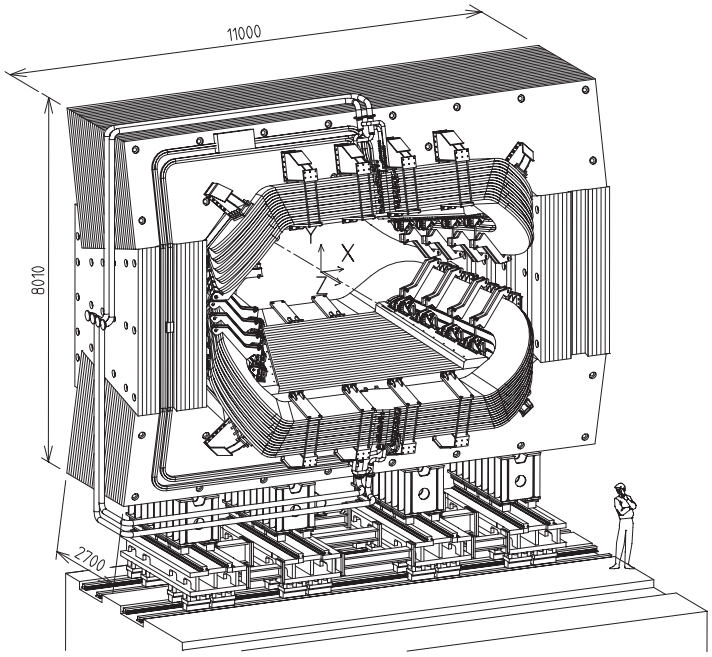

Figure 2.11: *Schematic view of the LHCb detector magnet. Reproduced from [66].*

equipped with vertical readout strips (x) and one layer equipped with readout strips rotated by a stereo angle $\pm 5°$ with respect to the vertical direction. The u direction corresponds to a positive rotation ($+5°$) and v corresponds to a negative rotation (-5°). This arrangement prevents ambiguities between the measured hits in order to measure the transverse component of the particle momenta.

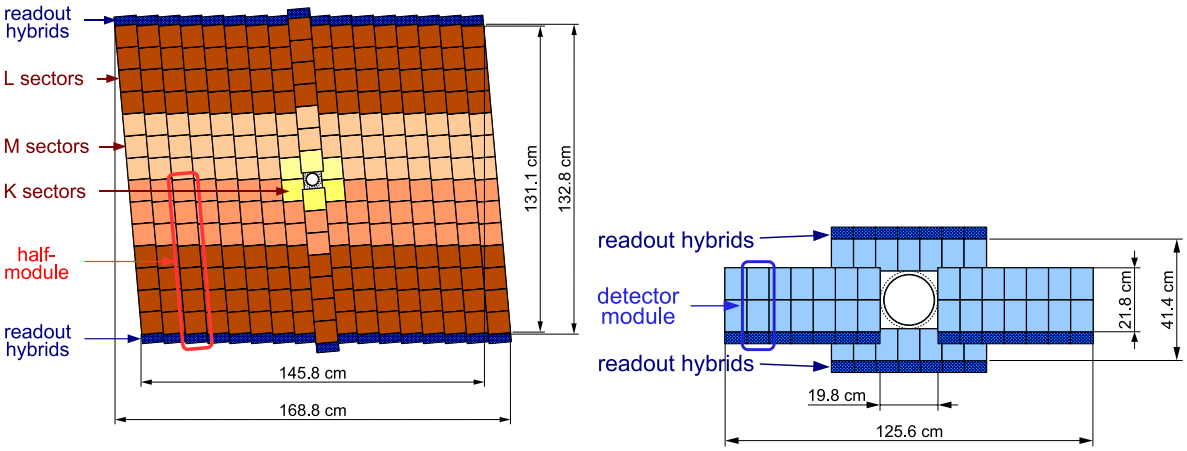

Figure 2.12: *Schematic view of a v Tracker Turicensis layer (left) and an x IT layer (right). Reproduced from [63].*

2.2.4.2 Inner and Outer Tracker

The Tracker stations consist of T1, T2 and T3 stations. Each station is divided into the Inner Tracker (IT), closest to the beam pipe and the Outer Tracker (OT).

The IT [76], as shown in figure 2.12 right, is constructed with silicon micro-strip detectors. It is designed to perform measurements in the inner region of the tracking system. Each station design is similar to that of the TT stations (see section 2.2.4.1). The spatial resolution of the IT is approximately 50 μm with 1 % occupancy per channel.

The OT [77] is composed of straw drift-tube modules with diameter of 5 mm and pitch of 6 mm each. The OT uses a mixture of Argon (70 %) and CO_2 (30 %) to ensure fast drift time (approximately 50 ns) and spatial resolution of approximately 200 μm.

2.2.5 The Calorimeters

The calorimetric system in LHCb is designed to identify hadrons, electrons and photons [66, 78]. Their energy and position are also measured by the calorimeters. This information is used by the first level trigger system to select events with high transverse energy, which are typical for B-decays, as well as for energy reconstruction used in further analyses. The calorimetric system is located between the first and second muon system. It is made of separate layers of active and passive (absorber) materials.

The energy of an incident particle is lost after a cascade of interactions with the absorber material of the calorimeter. During this process, showers of secondary particles are produced. The total energy of all showers absorbed in the active material is measured, which corresponds to the initial energy of the incident particle. The calorimetry system consists of the Scintillator Pad Detector (SPD), Pre-shower (PS), Electromagnetic Calorimeter (ECAL) and Hadronic Calorimeter (HCAL). The following sections give a brief description of this system.

2.2.5.1 Scintillator Pad Detector and Pre-shower

The SPD is made of 15 mm thick scintillator pads. It will distinguish between electrons and photons[9]. The PS is positioned after the SPD. They are separated by a 12 mm lead wall, called the lead converter that induces electromagnetic showers. The PS is also made of scintillator pads. It will measure the position of the induced showers in order to separate electrons and hadrons.

[9]The photon will traverse the scintillator without creating any signal.

2.2.5.2 Electromagnetic Calorimeter

The ECAL will be used to measure the energy of the electrons and photons. It has a modular design and is composed of alternating layers of 2 mm of lead and 4 mm of scintillator. Each ECAL module is constructed with 66 layers of lead and 66 layers of scintillator that corresponds to a total radiation length of 25 X_0. The energy resolution of the ECAL is given by

$$\frac{\sigma(E)}{E} = \frac{10\%}{\sqrt{E}} \oplus 1\%, \tag{2.2}$$

where E is the energy in GeV.

2.2.5.3 Hadronic Calorimeter

The HCAL is designed to measure the energy of the charged hadrons. Its structure alternates 16 mm thick of iron plates and 4 mm thick of scintillator tiles. The energy resolution of HCAL is

$$\frac{\sigma(E)}{E} = \frac{80\%}{\sqrt{E}} \oplus 10\%, \tag{2.3}$$

where E is the energy in GeV.

2.2.6 The Muon System

Muons with high transverse momentum (p_T) are present in the final states of a number of important B-decay channels. The penetrative power of these muons makes them simple to use in the trigger system.

The LHCb muon system is composed of 5 detector stations [66, 79]. The first muon station, M1, is placed before the SPD. M1 provides the transverse momentum for the first level trigger system. The other four, M2-M5, are located behind the HCAL, separated by 80 cm thick iron plates. The iron plates prevent any electron or hadron contamination, such that only muons with an energy above 6 GeV reach the M5 station.

Each muon station is built from multi-wire proportional chambers (MWPCs). The MWPCs provide a full response within the bunch crossing period of 25 ns. Therefore, hits are assigned unambiguously to their corresponding bunch. Since the particle flux is inversely proportional to the distance from the beam pipe, the muon stations are divided into regions of different granularity. The innermost region of M1 exceeds the capabilities of MWPCs detectors. Hence, gas-filled pad detectors using electron

multiplier (GEM) foils are employed in that region of the detector [80]. The MWPC and GEM chambers are arranged such that a projective geometry with respect to the interaction point is kept throughout the stations.

2.2.7 The Trigger System

The event rate of visible interactions is 10 MHz at a luminosity of 2×10^{32} cm^{-2}s^{-1}. This frequency is 4 times lower than that of the nominal LHC bunch crossing (40 MHz) due to the bunch structure and the LHCb luminosity. The trigger system [66, 81] reduces this event rate to 2 kHz. This reduction is performed in two trigger levels: level 0 trigger (L0) and high level trigger (HLT).

2.2.7.1 Level 0 Trigger

The L0 trigger is designed to reduce the event rate to 1 MHz. The frequency of 1 MHz allows an entire read out of the LHCb detector while retaining as many interesting events with b-hadrons as possible.

The L0 examines the overall event multiplicity from the pile-up detectors and the event's energy from the calorimeters and momentum from the muon system. A fast reconstruction is performed of the highest transverse energy (E_T) clusters in the calorimeters typical of hadrons, electrons and photons, and of the two muon candidates with the highest transverse momentum (p_T) in the muon chambers. This event processing is illustrated in figure 2.13.

The L0 is typically at least 80 % efficient for events containing a muon from a B-decay, 50 % efficient for events containing a hadron from a B-decay, and 30 % efficient with electrons from a B-decay.

2.2.7.2 High Level Trigger

The High Level Trigger consists of C++ programs that run on every CPU of the Event Filter Farm (EFF). The EFF is expected to have up to 2000 computing nodes (CPUs). The HLT can in principle have access to information from all sub-detectors to perform the event selection. Thus, it could execute off-line selection algorithms. The HLT is subdivided in two stages, HLT1 and HLT2.

The HLT1 is the first stage of the HLT. It aims to refine the L0 decision by reconstruction of particles in the VELO and T-stations that correspond to L0 objects. HLT1 is composed of 'alley' algorithms in order to reduce the event rate to approximately 30 kHz. Each alley addresses one of the trigger types of the L0 trigger. About 15 % of

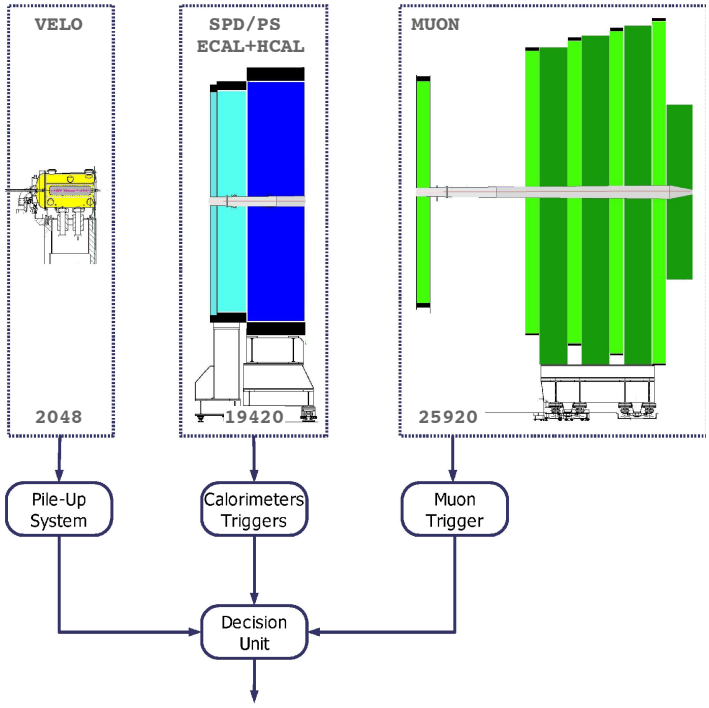

Figure 2.13: *Schematic of the Level 0 trigger system. Reproduced from [66].*

events are accepted by multiple L0 triggers, hence they will be passed through multiple HLT alleys.

The HLT2 executes exclusive and inclusive triggers. The exclusive trigger will reconstruct specific B final states, whereas the inclusive trigger will reconstruct partial B decays such as ϕX, $J/\psi X$, $D^{*}X$, $\mu^{\pm}X$, $\mu^{\pm}hX$, $\mu^{+}\mu^{-}X$, where h indicates a charged hadron and X any additional tracks. The final trigger operates the logical OR of the exclusive and inclusive selections. The HTL2 output rate will be approximately 2 kHz, the rate at which events will be written to disk.

2.2.8 The Online System

The Online system [66,82,83] is composed of three main sub-systems, Data Acquisition (DAQ), Timing Fast Control (TFC) and Experiment Control System (ECS). It ensures the data is transferred from the front-end electronics to permanent storage under known and controlled conditions. It includes also configuration and monitoring of operational parameters such as temperatures or pressures.

2.2.8.1 Data Acquisition System

The DAQ system will deliver the data that has events selected by the trigger system to the Event Filter Farm. The data is primarily collected, then transported from the

front-end electronics to permanent storage. The DAQ system is designed such that it can cope with high event rates, various data rates and different event sizes. The average event size in LHCb is approximately 150 kB.

LHCb uses two types of motherboards for data collection, digitization and pre-processing. The UKL1 boards are utilized on the RICH DAQ system, whereas the TELL1 boards [83] are employed on all the other sub-detectors of LHCb.

The two motherboards, UKL1 and TELL1, are controlled by a readout supervisor. The readout supervisor transmits the trigger signal and IP address to which the boards have to send the data. The IP address corresponds to a specific machine in the EFF which runs a software algorithm that reconstructs events based on the data received. The events are then processed by the HLT system. Only events that pass the trigger system selection are recorded.

2.2.8.2 Timing and Fast Control System

The TFC system drives the data acquisition system. It provides the clock signals to the DAQ boards and front-end electronics. In addition, the LO trigger decision to the boards originates from the TFC system.

The TFC system organizes the addresses to where the data is sent to the EFF. The events are transferred in multiple packs in LHCb which reduces the used bandwidth. The size of these packs are defined by the TFC system.

2.2.8.3 Experimental Control System

The ECS is in charge of the control and monitoring of LHCb experiment. It is used to configure different parts of the experiment. The performance of various components of LHCb is monitored by the ECS, such as in the VELO case the current drawn by the silicon sensors, the temperature of the hybrid and the vacuum pressure. The ECS has the capability to react in case of emergencies in the global system.

The ECS software has been built using PVSS II. PVSS is a commercial Supervisory Control And Data Acquisition (SCADA) system. It provides the infrastructure required to construct the ECS, such as graphical libraries. This toolkit is used to create operational panels, and alarm components. Figure 2.14 presents an overview of the structure of the LHCb ECS system. The use of this system for the VELO HV system is discussed in chapter 3.

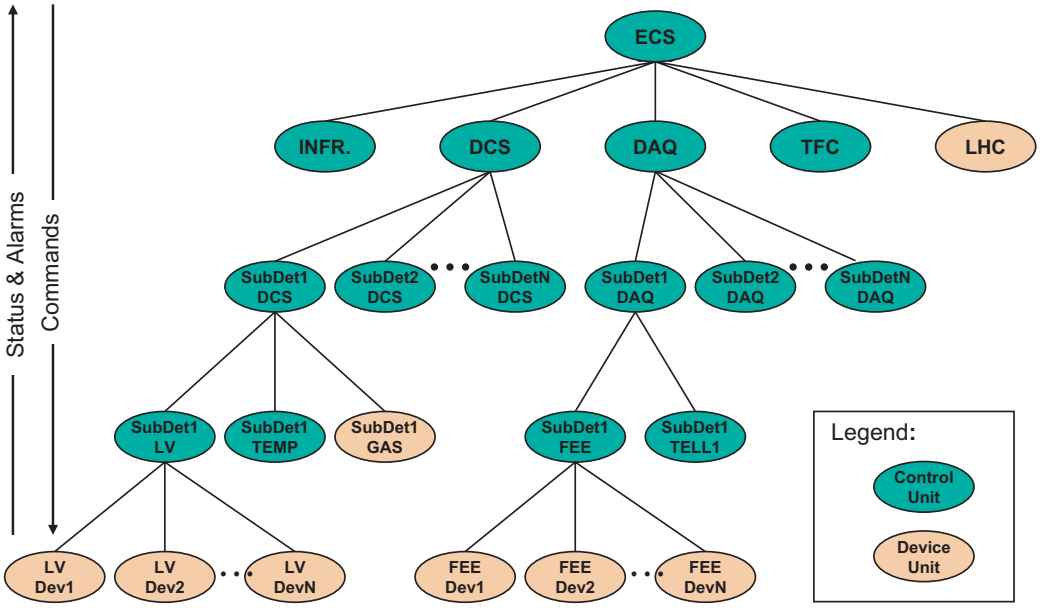

Figure 2.14: *Overview of the ECS architecture. Reproduced from [66].*

2.2.9 Software and Offline Processing

The LHCb software is based on the Gaudi framework [84]. It is structured as a set of various projects in order to produce simulated data, reconstructed real data, and to perform offline analysis. The production of simulated data and data reconstruction is mainly performed by projects called Gauss, Boole and Brunel. A project called, DaVinci provides tools necessary to perform offline analysis.

- **Gauss** performs the event generation for Monte Carlo simulation. There are two phases of processing: the generator and simulation phases. During the generator phase, proton-proton collisions are created and the decays of the particles produced (e.g. using EvtGen [85] for B-decays). The simulation phase makes use of the GEANT4 [86] toolkit to track the particles in the detector and simulates the physics processes occurring through the detector.

- **Boole** is responsible for the digitisation of simulated events. The digitisation consists of transforming the energy deposits calculated by GAUSS into signals.

- **Brunel** is used for event reconstruction from real data from the LHCb Data acquisition [66] system or from the simulated data output of Boole. During this phase, information from all sub-detectors is regrouped. Detector hits or calorimeter clusters are combined by the pattern recognition algorithms. A first particle identification is performed.

- **DaVinci** is the physics analysis software used in LHCb. DaVinci combines several packages of algorithms that perform various analysis tasks such as vertex and particle reconstruction, and event selections of specific decays. It uses the data output of Brunel, then reconstructs particles to their 'mother' particle and applies selections to separate signal and background. DaVinci is used for the selection of $B_d \to K^*\mu^+\mu^-$ which is the channel studied in this thesis (see chapter 5).

2.3 Summary

This chapter provided a description of the LHCb detector and its six sub-detectors. Since part of the work on this thesis, presented in chapter 4, is on the VELO high voltage system, the VELO system was extensively described. The trigger and the online system were also presented. The main projects that comprise the LHCb software were described as they were used for the production and analysis of the $B_d \to K^*\mu^+\mu^-$ events discussed in chapter 5.

3 The High Voltage System of the LHCb Vertex Locator

3.1 Introduction

The High Voltage system (HV) supplies the bias voltage to the 88 silicon sensors which comprise the LHCb Vertex Locator (VELO) and pile-up systems. The requirements of the high voltage system are presented in section 3.2. Section 3.3 describes the design and construction details of the high voltage system. Section 3.4 is dedicated to the characterisation tests that were performed on the high voltage system. In section 3.5 the commissioning of the system is described and current and voltage measurements mode with the system are used to characterise the VELO modules. A summary is provided in section 3.6.

3.2 System Requirements

The VELO high voltage system has been designed to provide a fail-safe, simple to use and secure system that complies with the requirements of the silicon modules. The high voltage system requirements are as follows:

- Supply sufficient voltage to fully deplete the VELO when it is irradiated to the expected dose and in the expected annealing scenario. The VELO system is specified for 500 V operation at a few mA. The high voltage power supply module chosen supplies up to 700 V at 4 mA. All components of the system have been tested to 500 V.

- Ensure the safety of the VELO modules and its operators. The system implements a current trip limit in both hardware and software. The operation of the system can also be inhibited through an interlock system [87].

- Provide a low noise level in order to maintain the high signal to noise ratio obtained from the VELO silicon modules.
- Protect the VELO against high voltage discharges in the vacuum. The electronics hybrid of the VELO sensors implements guard traces around the high voltage bias line to prevent discharges. The high voltage system also provides the voltage for these guard traces.
- The system must be remotely controllable and integrated in to the LHCb online software control system.
- No components requiring regular maintenance can be in the radiation zone of the experiment, and spare components must already be installed or easily swappable.

3.3 Design of the High Voltage System

This section describes the design and construction details of the HV system. The hardware components of the HV system are described in section 3.3.1, and the HV system control software in section 3.3.2.

3.3.1 Hardware

The high voltage system is the part of the VELO which is responsible for providing the bias voltage to the 84 VELO sensors and 4 Pile-Up sensors. As depicted in figure 3.1, the main hardware components of the VELO high voltage system are: the power supply crate, the high voltage modules, the counting house patch panels, the detector patch panels, and all connecting cables. This section describes each one in detail.

The high voltage system hardware design results from various considerations. To minimize the volume of routed cables, multicore cables are used to bridge long distances. However the final sensor locations means one needs individual cables for each sensor. Hence, patch panels are required to provide the correct connectivity between power supplies and cables, and between single core cables and multicore cables. Two types of patch panels are used. The first type called the counting house patch panel is placed in the electronics counting house. It connects the HV guard lines (see section 3.3.1.4) and maps the channels from the power supplies output to the long distance cables. The second type is called the detector patch panel and is located close to the VELO tank. It distributes HV channels onto the individual detector cables. The short cables that connect the power supplies to the counting house patch panels will be the

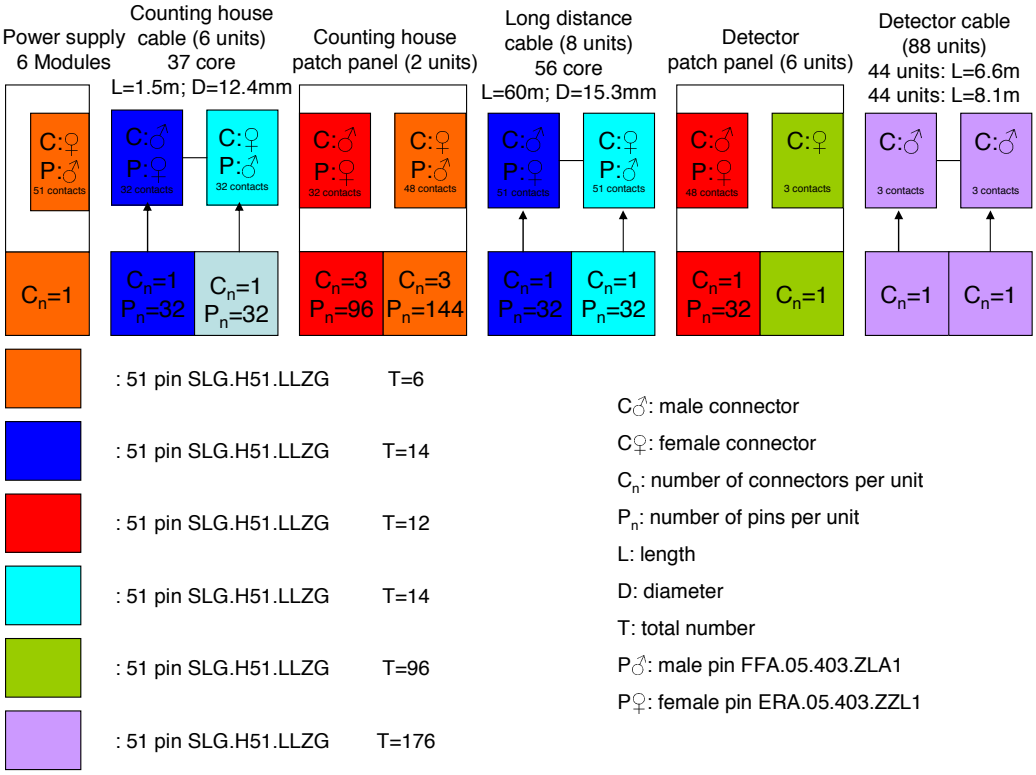

Figure 3.1: *Summary of cabling scheme for the high voltage system. The cables lengthes, the types of connectors and the pins employed are shown for each part of the high voltage sytem.*

most frequently manipulated. Hence, they have to be easy to replace. The spare long distance cables and detector cables were installed, for ease of exchange, as they are very difficult to replace during an experimental maintenance shutdown.

3.3.1.1 Power Supply

The VELO sensors are silicon micro-strip detectors based on n^+-on-n technology. To be efficiently operated, the sensors have to be sufficiently depleted. Test beam results [88] have shown that the n^+-on-n VELO sensors remain 99 % efficient in cluster finding as long as they are biased at 60 % of the full depletion voltage at fluences up to 2.5 $\times 10^{14}$ $\mathrm{n_{eq}/cm^2}$. The depletion is provided by supplying reverse bias to the sensors. The full depletion voltage increases proportionally with the irradiation [69]. A description of silicon strip detector behaviour under irradiation can be found in chapter 4. The VELO sensors are required to be operated at up to 500 V and a few mA. These requirements are justified in the following sections 3.3.1.1.1 and 3.3.1.1.2. The Iseg EHQ F607n-F power supply which supplies up to 700 V at 4 mA, was chosen.

3.3.1.1.1 Expected Leakage Current from a VELO Sensor

As detailed in chapter 4, the leakage current drawn from a silicon detector, such as the VELO sensors, ideally consists mainly of a diffusion current before irradiation. Additional radiation induced leakage current ΔI has to be taken into account once the sensors are irradiated. This is composed of the bulk generation current and the surface generation current. As demonstrated in [89], this radiation induced leakage current is proportional to the fluence and is independent of the type of sensor. It is given by

$$\Delta I = \alpha \Phi_{eq} V, \tag{3.1}$$

where α is the damage rate, Φ_{eq} is the fluence in 1 MeV $\mathrm{n_{eq}/cm^2}$ and V is the volume of a sensor. The value of the damage rate α depends on the sensor's temperature and the annealing time. In the VELO, the radiation across each sensor changes as a function of the distance from the beam. Φ_{eq} has the same value at each point at the same radius R and is inversely proportional to R^2, there is also a weak dependence on z position of the sensor [67] which we neglect here. Φ_{eq} is then rewritten as

$$\Phi_{eq}(R) = \left(\frac{R_I}{R}\right)^2 F, \tag{3.2}$$

where F is the fluence at the inner radius R_I. The radiation induced leakage current for a VELO sensor ΔI is then given by integrating over the radial distance from the beam

$$\Delta I = \int_{R_I}^{R_o} dI(R) = \int_{R_I}^{R_o} \alpha \Phi_{eq}(R) dV = \int_{R_I}^{R_o} \alpha K \frac{dR}{R}, \tag{3.3}$$

$$\Delta I = \alpha K \left(lnR_0 - lnR_I\right), \tag{3.4}$$

where R_I is the inner radius of the VELO sensor (8.2 mm), R_O is the outer radius of the VELO sensor (42 mm). K is a constant given by

$$K = \pi t F R_I^2, \tag{3.5}$$

where t is the thickness of the sensors of 300 μm.

As stated in chapter 2, the expected fluence after 2 $\mathrm{fb^{-1}}$, a nominal year of running in LHCb, is $\approx 1.3 \times 10^{14}$ 1 MeV $\mathrm{n_{eq}/cm^2}$. For the following calculation, a maximal fluence F of $10^{15}\times$ 1 MeV $\mathrm{n_{eq}/cm^2}$ is used, as seen in section 3.3.1.1.2, this is above what can be withstood from voltage consideration. Since LHCb will have a shutdown

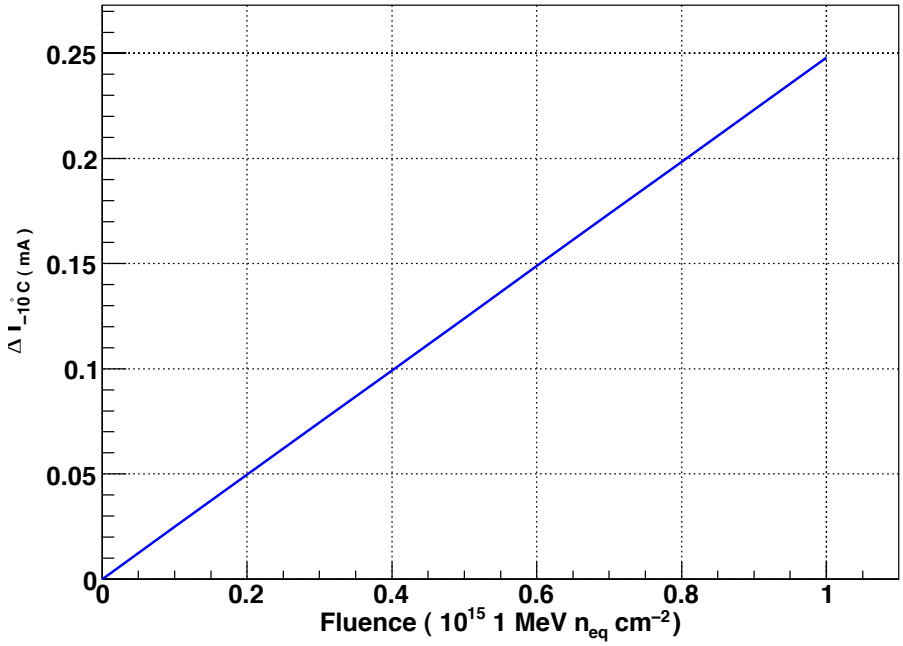

Figure 3.2: *Expected radiation induced leakage currents as a function of the fluence at the inner radius of the sensor.*

each year, four weeks of annealing at 20°C has been assumed. This annealing period is needed as the current significantly reduces as a result. The corresponding damage rate is $\alpha \approx 4 \times 10^{-17}$ A/cm at 20°C [89]. The corresponding current at 20°C is given, by using equation 3.4, as

$$\Delta I_{20°C} \approx 3.92\, mA. \tag{3.6}$$

Since the VELO will be operated at a temperature of approximately -10°C, one has to apply a temperature correction to obtain the current at the operating temperature $\Delta I_{-10°C}$. By applying the temperature correction function (equation 3.18 in section 3.5.1) at -10°C, the value of the radiation induced leakage current is

$$\Delta I_{-10°C} \approx 0.251\, mA. \tag{3.7}$$

This calculation is valid at the maximum fluence of LHCb. However, at high fluences ($> 10^{15}$ 1 MeV $\mathrm{n_{eq}/cm^2}$), recent literature [90] suggests the current behaviour with fluence deviates from the simple linear proportionality.

Figure 3.2 shows the expected radiation induced leakage current for a VELO sensor for fluences at the inner radius of up to 10^{15} 1 MeV $\mathrm{n_{eq}/cm^2}$. Since the Iseg power supply provides a maximum of 4 mA and the expected radiation induced leakage current at this high fluence is approximately 0.251 mA, it is clear that the Iseg power supplies

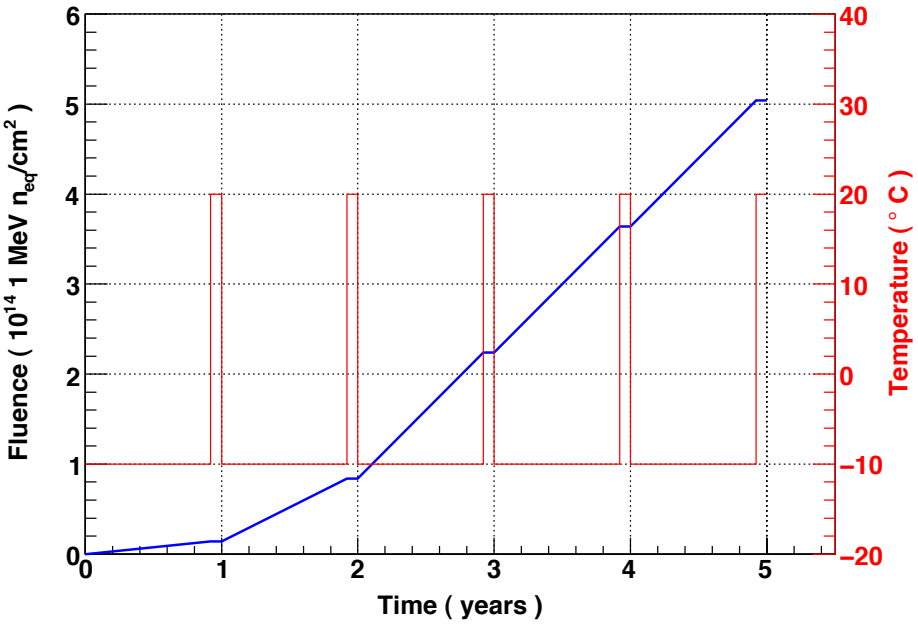

Figure 3.3: *The highest expected fluence in the VELO (blue line) and the sensors' temperature (red line) as a function of time.*

fulfill the current requirement of the VELO sensors.

3.3.1.1.2 Bias Voltage Required for a VELO Sensor

The choice of bias voltage is essential to fully deplete the sensors. The depletion voltage V_{dep} is given by

$$V_{dep} = \frac{|N_{eff}|d^2 q_0}{2\epsilon\epsilon_0}, \tag{3.8}$$

where q_0,ϵ_0 and ϵ are respectively the elementary charge, the vacuum permittivity and the relative permittivity of the silicon. d is the thickness of the depletion region of the sensors. At full depletion, d corresponds to the thickness W of the sensors of 300 μm. N_{eff} is the effective doping concentration, the difference in density of the donors and acceptors.

Before irradiation, the resistivity of the silicon ρ is inversely proportional to the doping concentration and the full depletion of the sensors is easily reached at relatively low voltages ($\approx$ 100V).

In contrast, radiation induces changes to the effective doping concentration and introduces defects into the bulk material of the sensors. As the radiation increases, fully depleting the sensors requires higher bias voltages. As shown in equation 3.8, the de-

pletion voltage will proportionally change with the change of the doping concentration ΔN_{eff}. For a given temperature T, ΔN_{eff} can be expressed by [91]

$$\Delta N_{eff}(\phi_{eq}, t) = N_a(\phi_{eq}, t) + N_c(\phi_{eq}) + N_Y(\phi_{eq}, t), \tag{3.9}$$

where t is the time. N_a and N_Y are respectively the short term and the reverse annealing terms. N_c is the stable damage component.

The short term annealing, also called beneficial annealing, induces an increase of the acceptors concentration. Thus, for the VELO sensors, it implies a reduction of their effective doping concentration, and hence the depletion voltage, until type inversion is reached. N_a can be modelled by

$$N_a(\phi_{eq}, t) = \frac{g_a \phi_{eq}}{k_a} \left(1 - exp(-k_a t)\right), \tag{3.10}$$

with

$$k_a = \frac{1}{\tau_a} = k_{0a}\, exp\left(-\frac{E_a}{k_B T}\right), \tag{3.11}$$

where g_a is the average acceptor introduction rate. E_a and τ_a are respectively the activation energy and the time constant. k_{0a} is the frequency factor.

The stable damage component N_c is independent of annealing. It is given by

$$N_c(t) = N_{c0}\left(1 - exp(-c\phi_{eq} t)\right) + g_c \phi_{eq} t, \tag{3.12}$$

where N_{c0} is the final value of the 'incomplete donor removal'. c is the number of donors removed per unit volume per unit flux.

The reverse annealing N_Y has a behaviour opposite to the short term annealing. It corresponds to the exponential increase of the effective doping concentration in long term operation of the sensors, until saturation is reached. The reverse annealing term is difficult to describe mathematically since it is a complicated process. Its expression is obtained by fitting experimental data. The following approximation of the reverse annealing term is denoted the 'first order process' [92]. This is used for the following calculation of the reverse annealing term, in which the expression of N_Y is given by

$$N_Y(t) = g_Y \phi_{eq} t - \frac{g_Y \phi_{eq}}{k_Y}\left(1 - exp(k_Y t)\right), \tag{3.13}$$

with

$$k_Y = \frac{1}{\tau_Y} = k_{0Y}\, exp\left(-\frac{E_Y}{k_B T}\right), \tag{3.14}$$

Parameters	Value
g_a	1.4×10^{-2} cm^{-1}
E_a	1.086 eV
k_{0a}	2.38×10^{13} s^{-1}
$N_{eff,0}$	1.26×10^{12} cm^{-3}
N_{c0}	$N_{eff,0}$
c	$\frac{10.9\times10^{-2}}{N_{eff,0}}$
g_c	5.30×10^{-3} cm^{-1}
g_Y	7.50×10^{-2} cm^{-1}
k_{0Y}	7.40×10^{14} s^{-1}
E_Y	0.662 eV

Table 3.1: *The values of the parameters used for the calculation of the required depletion voltage for the VELO sensor.*

where g_Y is the average acceptor introduction rate. E_Y and τ_Y are respectively the activation energy and the time constant. k_{0Y} is the frequency factor. The amplitude of the reverse annealing N_{Y0} is given by

$$N_{Y0} = g_Y \phi_{eq}. \tag{3.15}$$

For the following calculation, the VELO sensors are considered to have an operating temperature of -10°C, and an LHCb shut down period of approximately four weeks per year is assumed at which the sensors will be brought up to 20°C. The values of the other parameters employed for this calculation are summarised in table 3.1.

By using the equation 3.8 and 3.9, and the expressions of N_a, N_c and N_Y in equation 3.10, 3.12 and 3.13 respectively, the estimated depletion voltage V_{dep} for the VELO sensors as a function of time can be determined. The first five years of operation of LHCb are considered, and plausible assumptions made on the delivered integrated luminosity. In 2010, the first year of operation, an integrated luminosity of 0.2 fb^{-1},

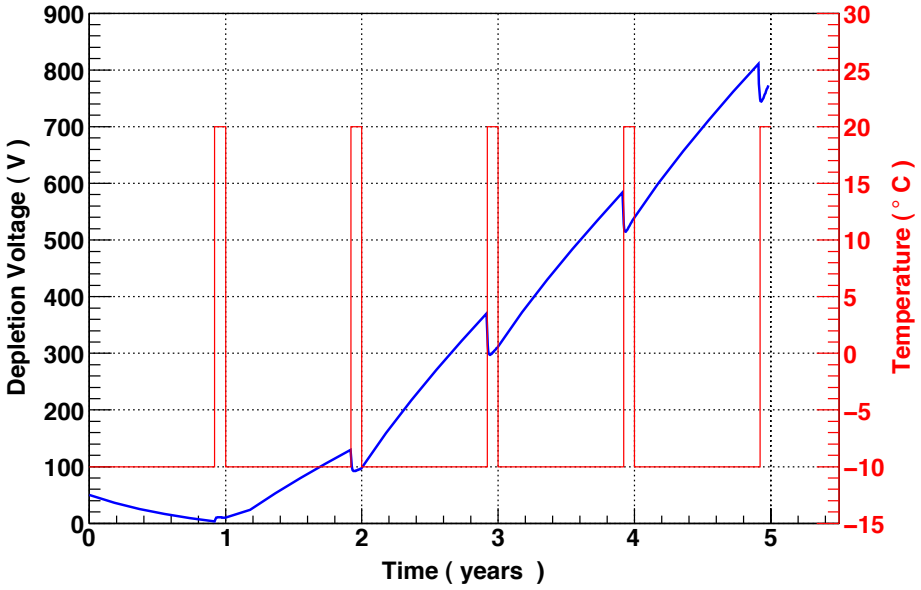

Figure 3.4: *Predicted depletion voltage (blue line) and sensor's temperature (red line) as a function of time.*

one tenth of a nomimal year is assumed. For the following year 1 fb^{-1} is assumed, with all subsequent years having 2 fb^{-1} of data. The equivalent maximal fluences are shown in figure 3.3.

As shown in figure 3.4, V_{dep} decreases due to type inversion during the first year of running. V_{dep} also decreases during each shutdown due to the beneficial annealing given by equation 3.10.

After $\approx$ 4.5 years of running (see figure 3.4) fully depleting the VELO sensors requires a bias voltage above the Iseg power supplies maximal bias voltage of 700 V. Due to the vacuum feedthrough, the sensors' bias voltages are actually limited to 500 V. Hence, during the last part of the third year and fourth year of running the sensors will be operated partially depleted (above a total fluence of $\approx 3.6 \times 10^{14}$ 1 MeV $\text{n}_{\text{eq}}/\text{cm}^2$). Test beam results [88] have shown that the VELO sensors remain 99 % efficient in cluster finding as long as they are biased at 60 % of the full depletion voltage. After 6-8 fb^{-1} data the sensors will be replaced.

Since the VELO sensors will be operated with bias voltages up to 500 V and the Iseg power supplies provide a maximum bias voltage of 700 V, the Iseg power supplies fulfill the bias voltage requirement of the VELO sensors.

Characteristics	Values
Maximum voltage	700 V
Maximum current	4 mA
Ripple and noise	< 20 mV at max load and $V > 50$ V
Voltage setting resolution	14 mV
Current setting resolution	80 mA
Voltage measurement resolution	14 mV
Current measurement resolution	80 mA
Range dV_{out}/dt	0.28 V/s to 70 V/s
Resolution of dV_{out}/dt	0.5 V/s

Table 3.2: *Performance of the Iseg EHQ F607-nF channel.*

3.3.1.1.3 The ISEG EHQ F607n-F

Each ISEG[1] EHQ F607n-F has 16 channels. A single channel is used for each sensor. This allows the voltage to be set separately and the current to be monitored for each sensor, and prevents any noise coupling between sensors. To completely supply voltage to 88 VELO sensors, six of these power supplies are required. From the power supply output, each HV channel consists of a HV bias and a HV return line. The specified channel performance is given in Table 3.2. Physically each unit fits within the 6U Eurocard format. On the front of each unit, there is a green LED and two potentiometers. The green LED indicates the status of the HV module, staying lit if no error occurs in any of the channels of that HV module. The potentiometers are used to control the maximum output current and voltage of the HV module. They have to be adjusted manually in order to set the desired values. The set value can be measured directly using the socket located below the potentiometer. To be operated, the HV modules require +24 V which is supplied by the crate (see section 3.3.1.1.4) and an external inhibit signal (see section 3.4.3.3) of +5 V. The inhibit signal is supplied individually to each channel, and provides a protection of the VELO sensors (as described in [93]). Within the module, each channel is floating with respect to each other and ground. Hence, the output voltage can be either positive or negative. The Iseg power supplies are remotely controllable through a CAN interface. A USB-CAN cable interconnects the control computer and the power supplies.

[1]ISEG Spezialelektronik GmbH, Bautzner Landstraβe 23 D-01454 Radeberg, OT Rossendorf, Germany.

3.3.1.1.4 The Crate ISEG ECH 238 UPS

The ISEG ECH 238 UPS is used to house and power the ISEG EHQ HV modules. It can accommodate up to eight 6U modules with a built in power supply of 700 W. The CAN controller of the crate allows the monitoring and the control of the HV modules. The Uninterruptible Power Supply (UPS) is a power reserve that is used when the normal power to the crate would be interrupted (see section 3.4.3.1). The UPS is required to prevent any sudden ramp down of the voltage in case of power cut. Such scenario can damage the front-end electronics of the VELO hybrid. When there is a power failure, the UPS sends a signal to the HV modules which will ramp down the voltages of all the channels in a controlled way. The ECH 238 crate UPS can last for at least one minute.

3.3.1.2 Grounding

The HV system grounding scheme follows the VELO grounding scheme. In the VELO, a local grounding point is defined to make its surrounding environment as stable as possible, to ensure low noise performance.

The VELO common grounding point is defined as the hybrid ground plane. Since the high voltage and low voltage power supplies are floating power supplies their respective return lines are linked together at this common grounding point. The HV return and hybrid ground are connected together, without a resistor, at the point R5 in figure 3.5. The hybrid ground is then connected to the LHCb grounding network via a kapton cable (at SAM2 in figure 3.5). The kapton cable is connected to the module base which is linked to the LHCb grounding network. The RF-foil is located at a distance of less than 1 mm from the sensors, hence it has to be at a potential as close as possible to the hybrid ground. The kapton cable provides the shortest possible path to the RF-foil.

The VELO mechanics are connected to the LHCb grounding network. The shields of the HV cables are connected to this grounding network at both ends of the cables. All crates and racks in the counting house are also connected to the LHCb grounding network.

3.3.1.3 Counting House Cable

This cable connects the Lemo Redel connector on the power supply to the counting house patch panel. The counting house cable input corresponds to the power supply output which consists of a HV bias and a HV return line for each HV channel (see section 3.3.1.1.3). The counting house cable just transfers the power supply channel

bias to the counting house patch panel. Hence, the number of cores required is 32 for each counting house cable. The high voltage system requires 6 units of the counting house cable of about 2 m in length each. Figure 3.9 details the wiring and pinning diagram of the counting house cable.

3.3.1.4 Counting House Patch Panel

To protect the VELO against high voltage discharges in the vacuum, the electronics hybrid of the VELO sensors implement guard traces around the high voltage bias line as shown in figure 3.5. Discharges on the HV line will induce noise which would feed into the front-end chip. The guard lines originate from the PCBs (see figure 3.6) that are housed within the counting house patch panels and are transmitted to the long distance cables.

Each counting house patch panel has three individual PCBs. In the current configuration of the HV system, the HV guard and the HV Bias are connected. Hence, at partial vacuum, any discharge will occur from the HV guard to the HV return line. The induced noise from the discharge between HV guard and HV bias has to travel all the way to the counting house patch panel where they are connected and then travels back to the hybrid. By the time the noise reaches the front-end chip, it would be attenuated as it is difficult to transmit high frequency signals through long distance cable.

Within the counting house PCBs, the HV guard can either be connected to HV bias or HV return or left floating. The connection is done via a jumper that provides the possibility of changing the configuration if system aspects would require so. Two counting house patch panels arrange and distribute the high voltage channels from the multi channel power supply to the 56 core long distance cables (see section 3.3.1.5). The wiring and pinning diagram from the counting house patch panel are depicted in figure 3.10 and 3.11.

3.3.1.5 Long Distance Cable

The long distance cable is used to connect the 51 pin connector of the two patch panels, 48 of these pins are used in the system. This is the longest cable since it has to breach the distance between the barracks and the experiment. Each channel in this cable is composed of a triplet: HV Bias, HV Guard and HV Return. The high voltage system requires 6 units of the long distance cable. In addition two spare long distance cables are installed as explained at the start of section 3.3.1. Figure 3.12 describes the wiring and pinning diagram of the long distance cable.

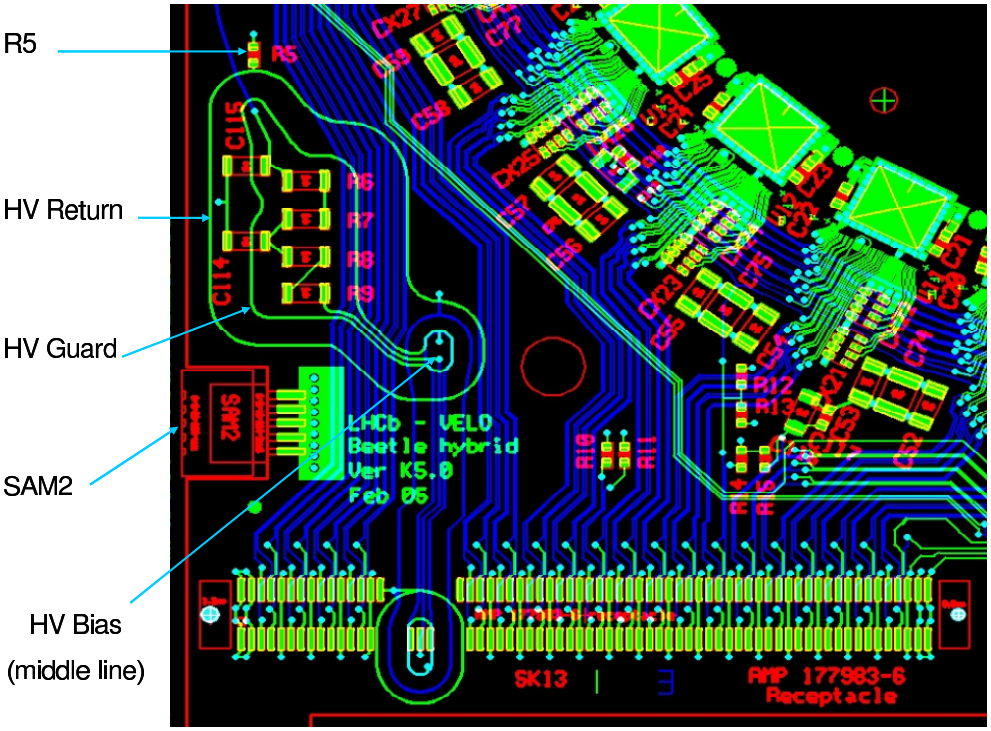

Figure 3.5: *Drawing of part of the hybrid showing the HV bias, the HV guard and the HV return. The resistance R5 and the connector SAM2 are also indicated. Reproduced from [94]*

3.3.1.6 Detector Patch Panel

The detector patch panels arrange and distribute the high voltage channels to each individual Repeater Board. They are located near the VELO tank. Figure 3.8 is a photo taken near the VELO tank. It shows where half of the detector patch panels and half of the detector cables are installed. The High Voltage system requires 6 units of the detector patch panel. Each detector patch panel possesses 16 outputs and is thus capable of providing HV to 16 repeater boards as depicted in figure 3.13. The detector patch panel housing is a modified cast iron box purchased from FARNELL[2]. The modifications consist of cutaways for the body of the connectors, as shown in figure 3.7. They are screwed to the wall close to the VELO using the flanges on the box.

[2]FARNELL, LS12 2TU Canal Road Leeds, United Kingdom.

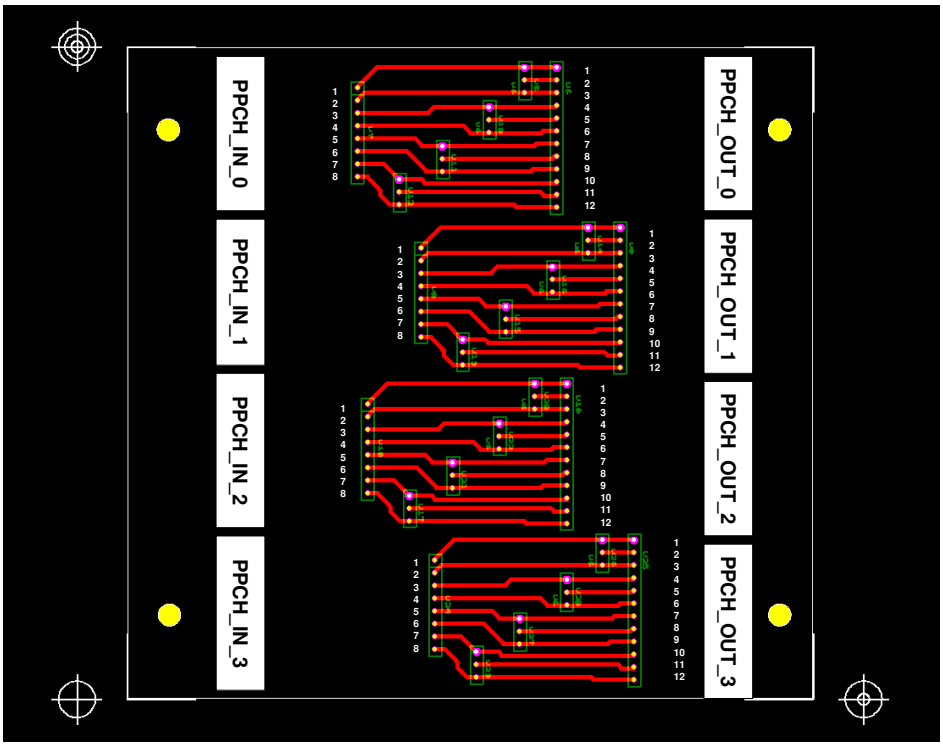

Figure 3.6: *Connector labels and pin numbers for PCB mounted in the counting house patch panel. Reproduced from [95].*

3.3.1.7 Detector Cable

The detector cable distributes each individual triplet (HV bias, HV guard and ground) from the detector patch panel output to its corresponding repeater board. The repeater board will then provide the HV guard line (see section 3.3.1.4) for the hybrid as well as the HV bias and the HV return to bias each sensor. The high voltage system requires 88 detectors cables units. The units come in two different lengths, one for the repeater board pointing upwards and one for the repeater boards pointing downwards. There are 44 of each unit required, which are installed near the VELO tank as shown in figure 3.8.

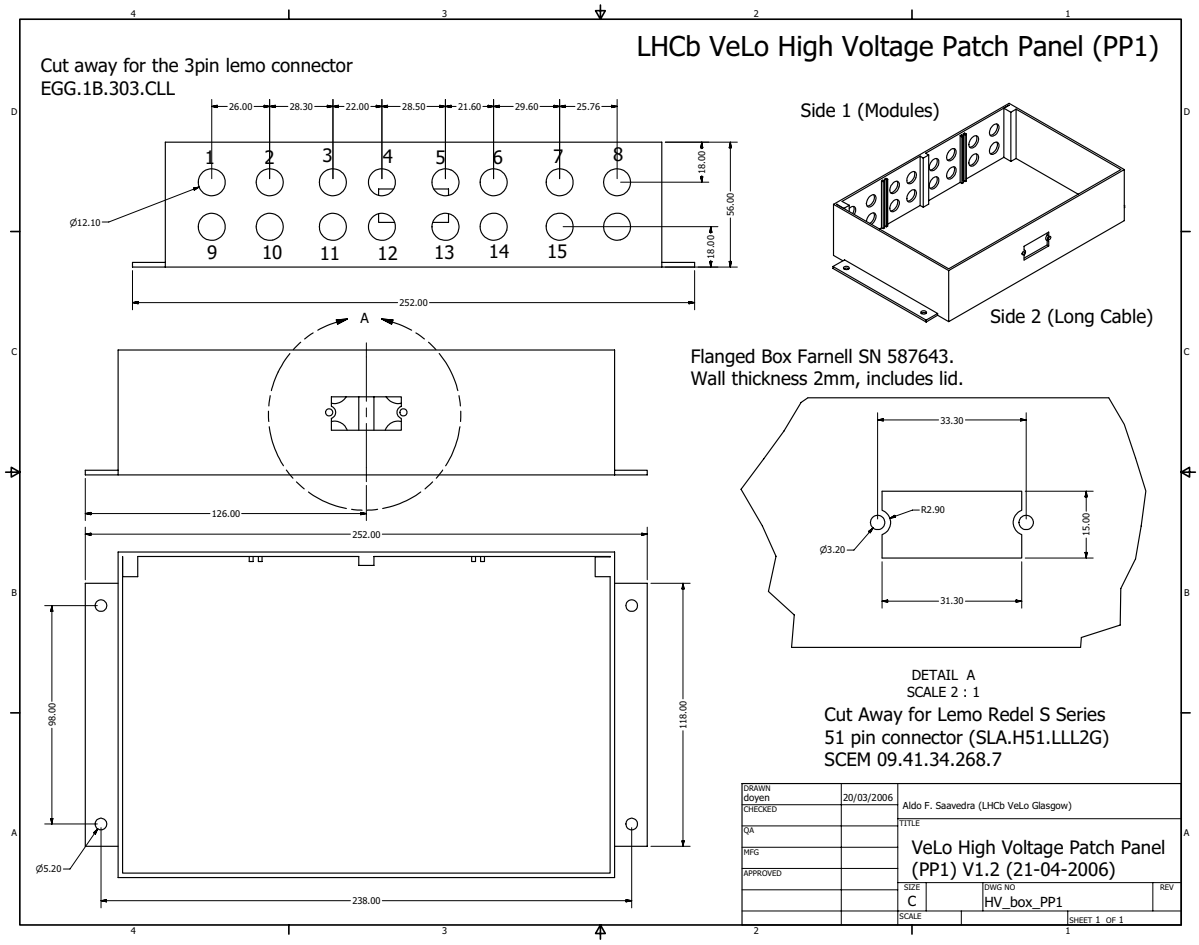

Figure 3.7: *Drawing of the detector patch panel box. Reproduced from [96].*

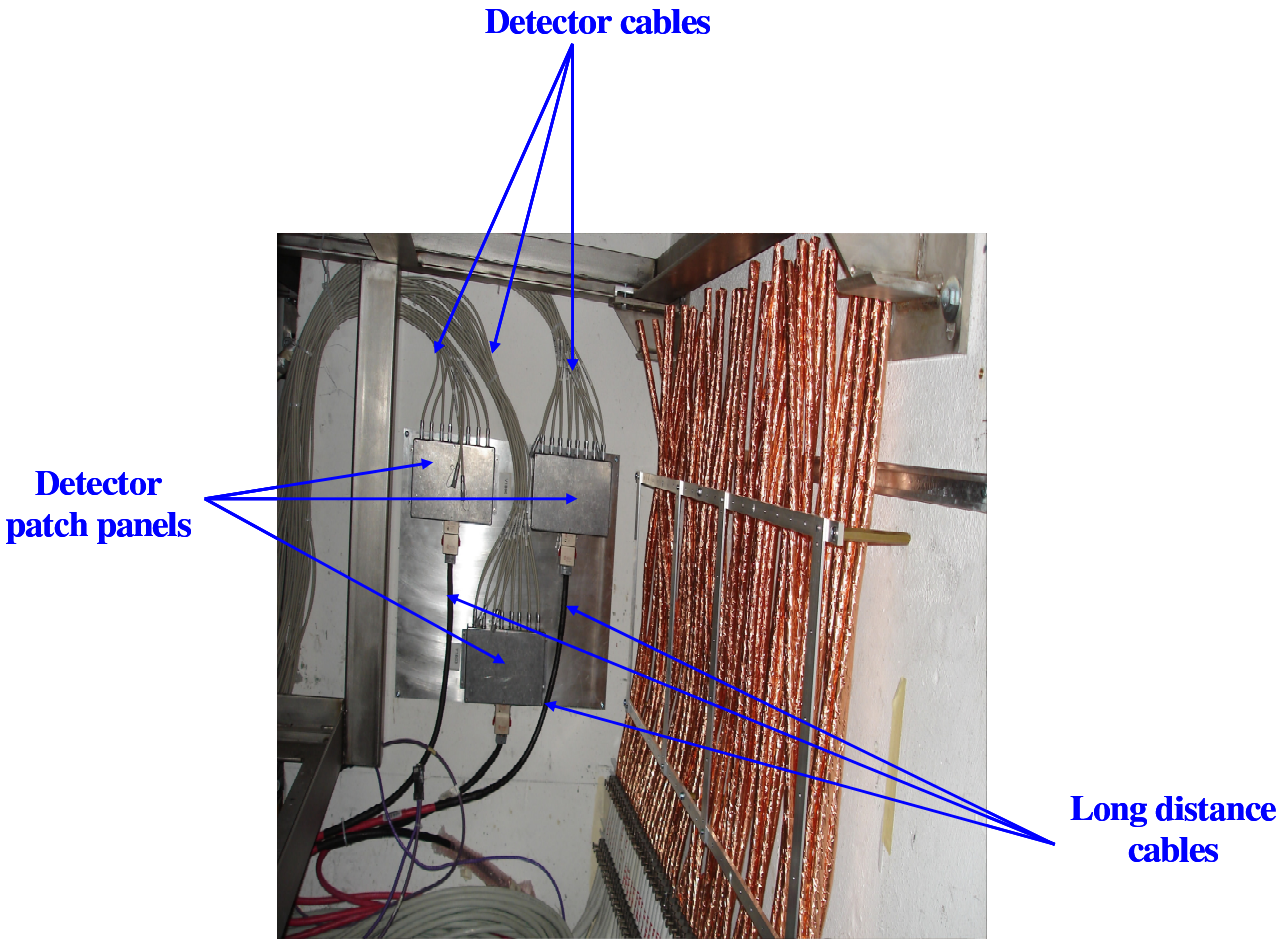

Figure 3.8: *Photograph of the area where half of the detector patch panels and half of the detector cables are installed. The long distance cable outputs to the detector patch panels are also indicated.*

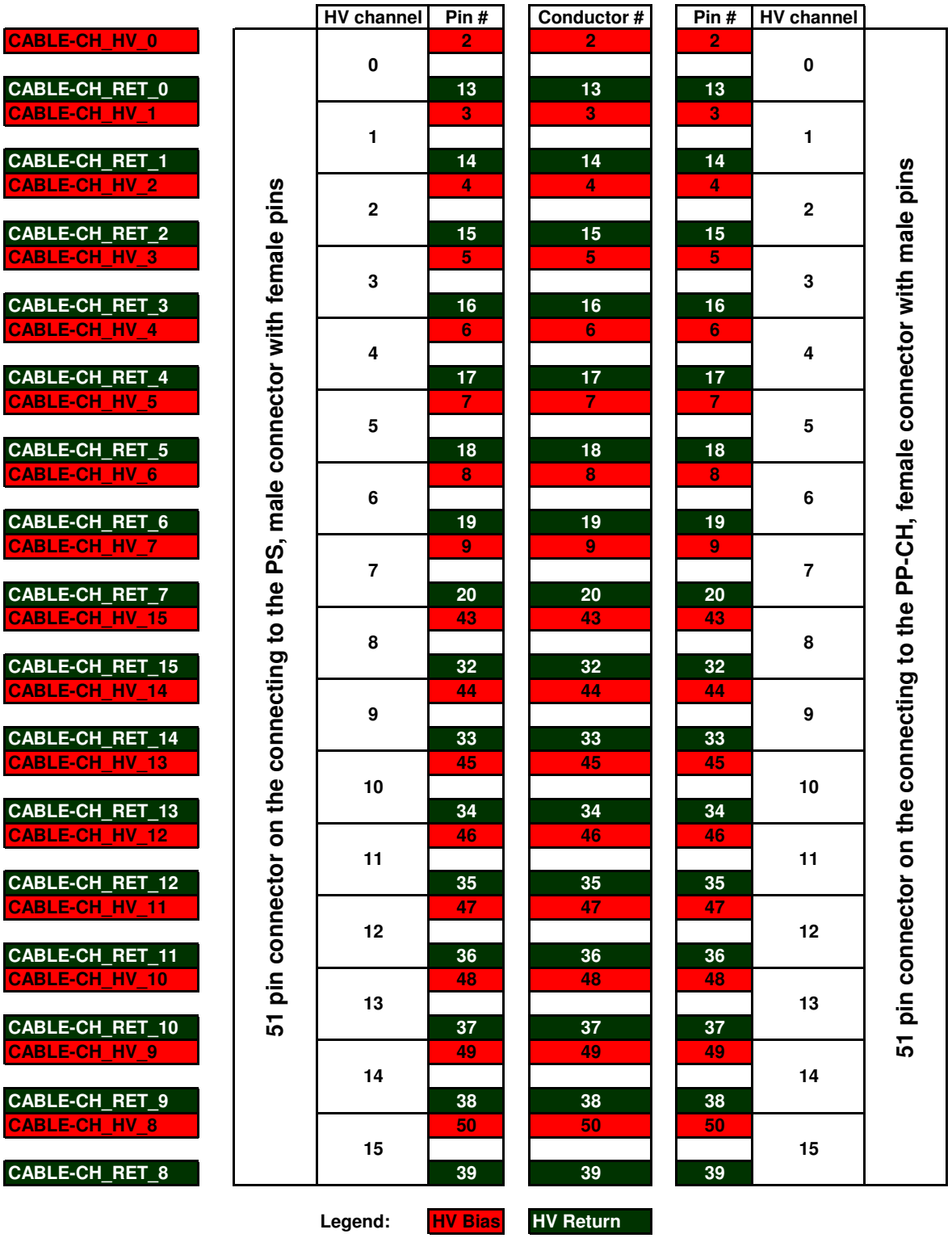

Figure 3.9: *Wiring and pinning diagram for the cable from the ISEG power supply to counting house patch panel.*

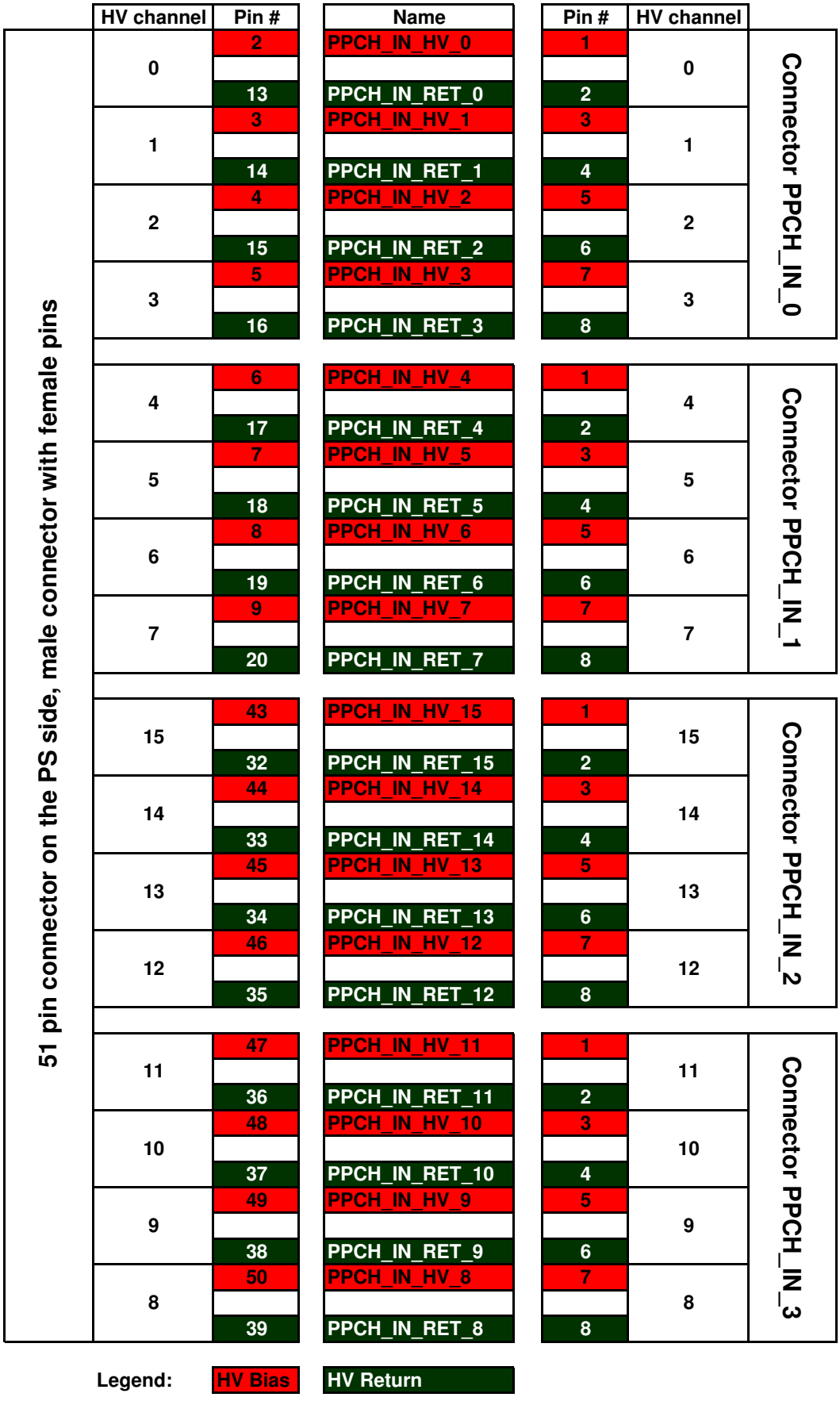

Figure 3.10: *Cabling scheme from panel connector to PCB input.*

	HV channel	Pin #	Name	Pin #	HV channel	
Connector PPCH_OUT_0	0	1	PPCH_OUT_HV_0	9	0	51 pin connector on the detector side, female connector with male pins
		2	PPCH_OUT_GUARD_0	8		
		3	PPCH_OUT_RET_0	7		
	1	4	PPCH_OUT_HV_1	12	1	
		5	PPCH_OUT_GUARD_1	11		
		6	PPCH_OUT_RET_1	10		
	2	7	PPCH_OUT_HV_2	15	2	
		8	PPCH_OUT_GUARD_2	14		
		9	PPCH_OUT_RET_2	13		
	3	10	PPCH_OUT_HV_3	18	3	
		11	PPCH_OUT_GUARD_3	17		
		12	PPCH_OUT_RET_3	16		
Connector PPCH_OUT_1	4	1	PPCH_OUT_HV_4	21	4	
		2	PPCH_OUT_GUARD_4	20		
		3	PPCH_OUT_RET_4	19		
	5	4	PPCH_OUT_HV_5	24	5	
		5	PPCH_OUT_GUARD_5	23		
		6	PPCH_OUT_RET_5	22		
	6	7	PPCH_OUT_HV_6	27	6	
		8	PPCH_OUT_GUARD_6	26		
		9	PPCH_OUT_RET_6	25		
	7	10	PPCH_OUT_HV_7	30	7	
		11	PPCH_OUT_GUARD_7	29		
		12	PPCH_OUT_RET_7	28		
Connector PPCH_OUT_2	15	1	PPCH_OUT_HV_15	6	15	
		2	PPCH_OUT_GUARD_15	5		
		3	PPCH_OUT_RET_15	4		
	14	4	PPCH_OUT_HV_14	51	14	
		5	PPCH_OUT_GUARD_14	50		
		6	PPCH_OUT_RET_14	49		
	13	7	PPCH_OUT_HV_13	48	13	
		8	PPCH_OUT_GUARD_13	47		
		9	PPCH_OUT_RET_13	46		
	12	10	PPCH_OUT_HV_12	45	12	
		11	PPCH_OUT_GUARD_12	44		
		12	PPCH_OUT_RET_12	43		
Connector PPCH_OUT_3	11	1	PPCH_OUT_HV_11	42	11	
		2	PPCH_OUT_GUARD_11	41		
		3	PPCH_OUT_RET_11	40		
	10	4	PPCH_OUT_HV_10	39	10	
		5	PPCH_OUT_GUARD_10	38		
		6	PPCH_OUT_RET_10	37		
	9	7	PPCH_OUT_HV_9	36	9	
		8	PPCH_OUT_GUARD_9	35		
		9	PPCH_OUT_RET_9	34		
	8	10	PPCH_OUT_HV_8	33	8	
		11	PPCH_OUT_GUARD_8	32		
		12	PPCH_OUT_RET_8	31		

Legend: HV Bias | HV Return | Guard

Figure 3.11: *Cabling scheme from PCB output to rear panel connector.*

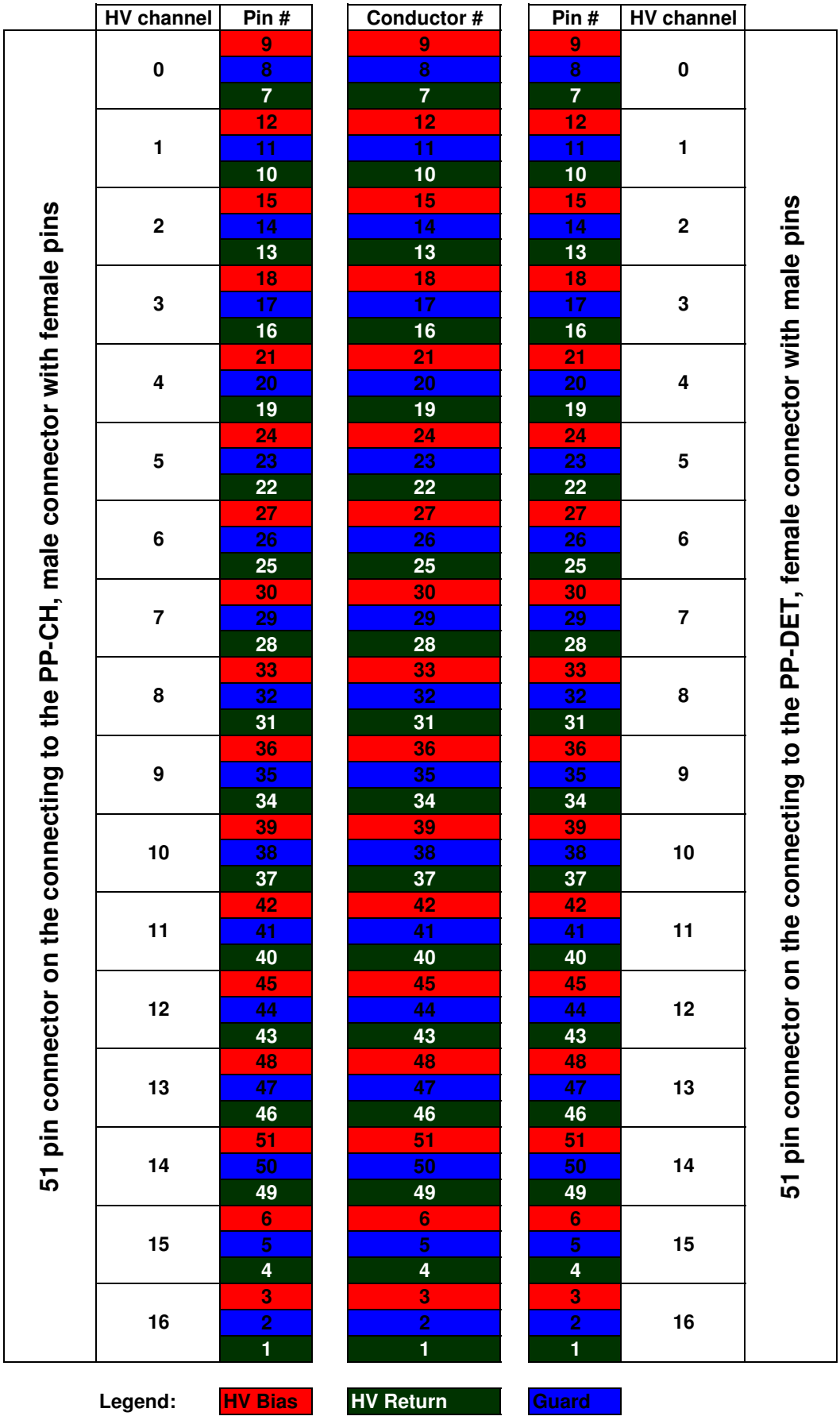

Figure 3.12: *Wiring and pinning diagram for the long distance cable between the counting house patch panel and the detector patch panel.*

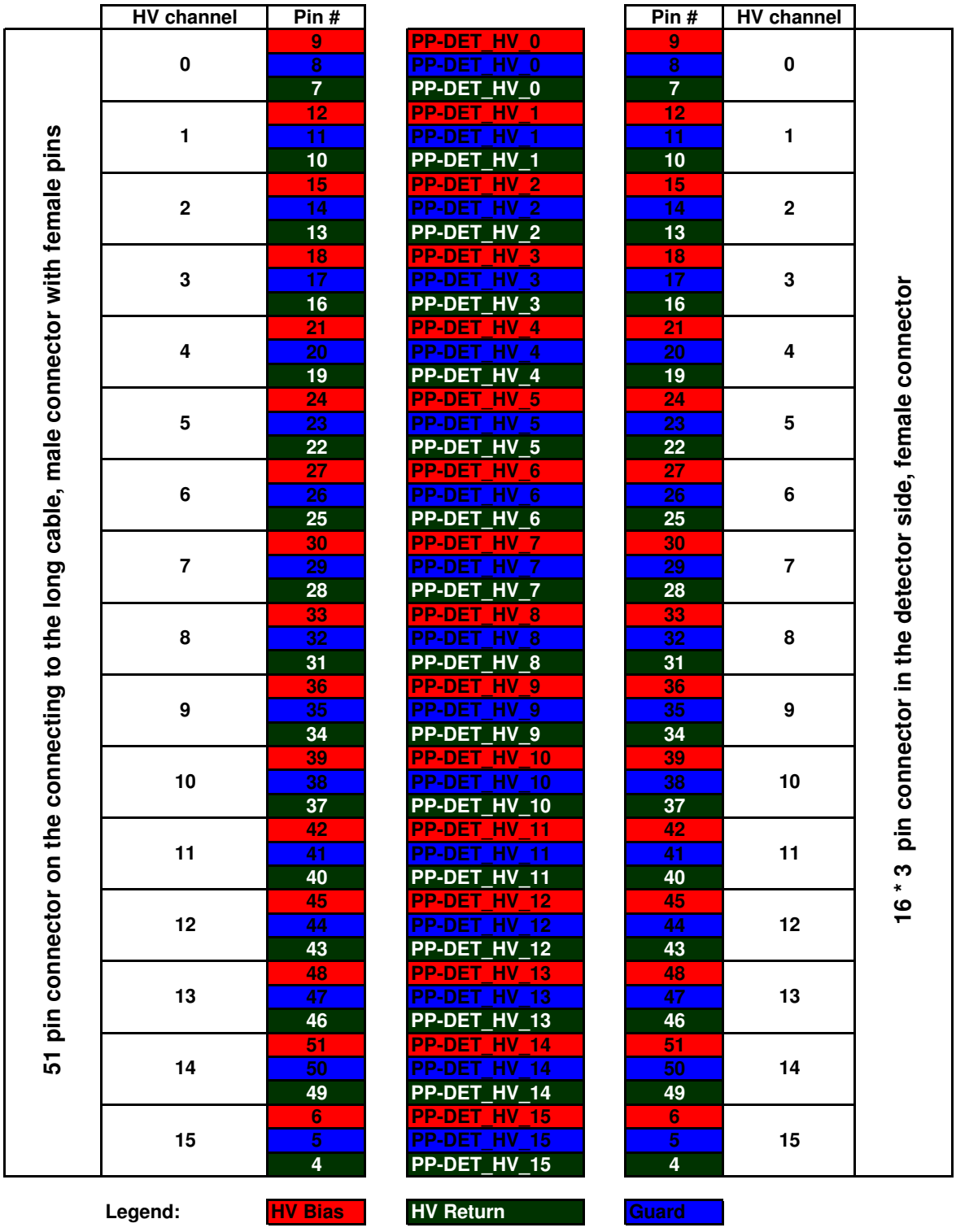

Figure 3.13: *Wiring and pinning diagram for the detector patch panel.*

3.3.1.8 Conclusion

The description of the hardware components of the VELO high voltage system was presented in this section. The role of each one of them was also discussed. It has been shown that the VELO high voltage system complies with the safety and the performance of the VELO as well as the environment where it is used. The HV components were assembled and tested with a substantial programme of quality assurance at the University of Glasgow. Then they were shipped and installed at CERN where they were verified in situ and approved to fulfill the specification. The results of these tests are presented in section 3.4. The high voltage system is now operational and used during the operation of the VELO.

3.3.2 Software

The high voltage system requires powerful, flexible and reliable software that is easy to maintain. Moreover, LHCb uses a distributed control system which allows inter-process communication between processes running on several different PCs. The software that was chosen to control the VELO high voltage system is PVSS [97]. The PVSS architecture for the HV system is presented in section 3.3.2.2. It has the following advantages:

- Powerful commercial product which supports distributed systems and includes tools for object-like device description, archiving, alarms, user-created panels and scripts.

- It is a Supervisory Control and Data Acquisition [98] (SCADA) framework and is used to connect to hardware (or software) devices, acquire the data they produce and use it for their supervision, i.e. to monitor their behaviour and to initialize, configure and operate them. Data structures have very flexible formats that can be exchanged between servers and clients; data can be sent on request or by subscription.

- Provides an object-like data structure called 'data points' created to model the complexity of devices and data structures in the experiments. Data points are instances of these objects and can easily be created in large numbers as needed by the application. One can create an object of data points type that can be instantiated for each hardware item (an example is an actual online value of the voltage in one channel).

- A PVSS 'manager' is available which permits exchange of data by a very simple mechanism between data points in PVSS and other processes running on different PCs.

- PVSS is the control system chosen for the LHC experiments. The Joint Controls Project [99] (JCOP) is part of the CERN IT/CO group and is a collaboration between the experiments and CERN support groups. JCOP has developed many commonly needed tools: a framework, interfaces to hardware devices, configuration tools, etc. PVSS 3.8 is used with the JCOP framework to control the ISEG high voltage power supply modules and crate. An ISEG Object linking and embedding Process Control (OPC) server provides interface between the high voltage power supplies and PVSS. An overview of the HV control system is given in section 3.3.2.1. Section 3.3.2.3 provides a description of the structure of the HV control software.

The LHC experiments will be operated as Finite State Machines (FSM) [100]. The FSM will then ensure that, for example, the high voltage state of a sub-detector is appropriate depending on operational mode. The crate and each high voltage channel will therefore be part of the VELO FSM architecture (see section 3.3.2.4). The HV errors and alarms (see section 3.3.2.5) are handled at the FSM level.

3.3.2.1 Overview of the High Voltage Control System

As shown in figure 3.14, the control of the high voltage system starts from a PC where PVSS is installed and on which the ISEG power supplies and crate are connected. Then, the ISEG modules command their individual channels to supply the desired voltage. Each bias voltage will pass through the counting house cable, then the counting house patch panels. The long distance cables distribute it to the detector patch panels, from which individual detector cables provide the voltage to the corresponding repeater board. Each repeater board then supplies the bias voltage to the corresponding VELO hybrid, hence to the corresponding sensor.

3.3.2.2 PVSS Architecture

The control systems that are built with PVSS are composed of communicating and independent processes. These processes are called 'Managers'. As shown in figure 3.15, the main PVSS managers are as follows. The central part is called the Event Manager (EM). It retains all data in a volatile memory, responds to notification of

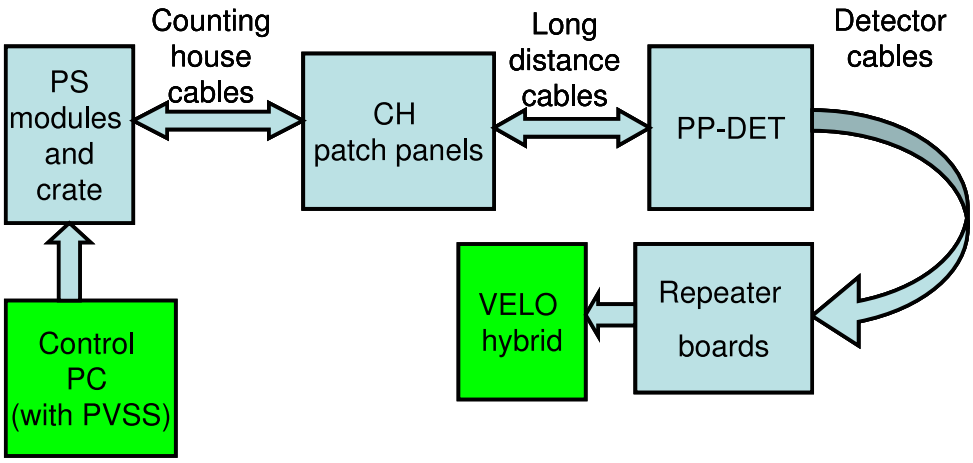

Figure 3.14: *Overview of the high voltage system control.*

data change and computes alarm conditions. Their values are held in structures called Data Points. The event manager of the VELO HV sytem is called the VELO Detector Control System High Voltage, also known as 'VEDCSHV project'. The database where non-volatile data such as system definitions, alert occurrences and latest values are stored, is managed by the Data Manager (DM). An Oracle database is used for the long term storage of data point values. The visualization of the data points values are ensured by User Interface (UI) managers such as synoptic panels, alarm screen (AES) and trend graphs (Trnd). The interconnection between individual PVSS systems that forms a distributed system is conducted by the Distribution Manager (DIM). The list of PVSS managers provided previously is not exhaustive. Managers could be created depending on its specific task (e.g. the ISEG HV Manager is an interface to the HV modules and crate).

3.3.2.3 Structure of the High Voltage Control Software

This section describes the structure of the HV control software (see figure 3.16). The VELO high voltage system is controlled remotely via PVSS. The PVSS VELO high voltage project VEDCSHV runs on an online[3] PC which is located in the counting house. The high voltage control software is able to control individual high voltage channels. Since the VELO has two halves, the part with $+x$ coordinates is referred to as the A-side and the one with $-x$ coordinates to as the C-side, based on the LHCb coordinate system (see chapter 2). The VEDCSHV project is divided into three sub-systems called 'VELO_HV' for controlling the whole VELO, 'VELOA_HV' for

[3]Online refers to the private network which is used at the LHCb experiment area. The network is protected behind a strong firewall.

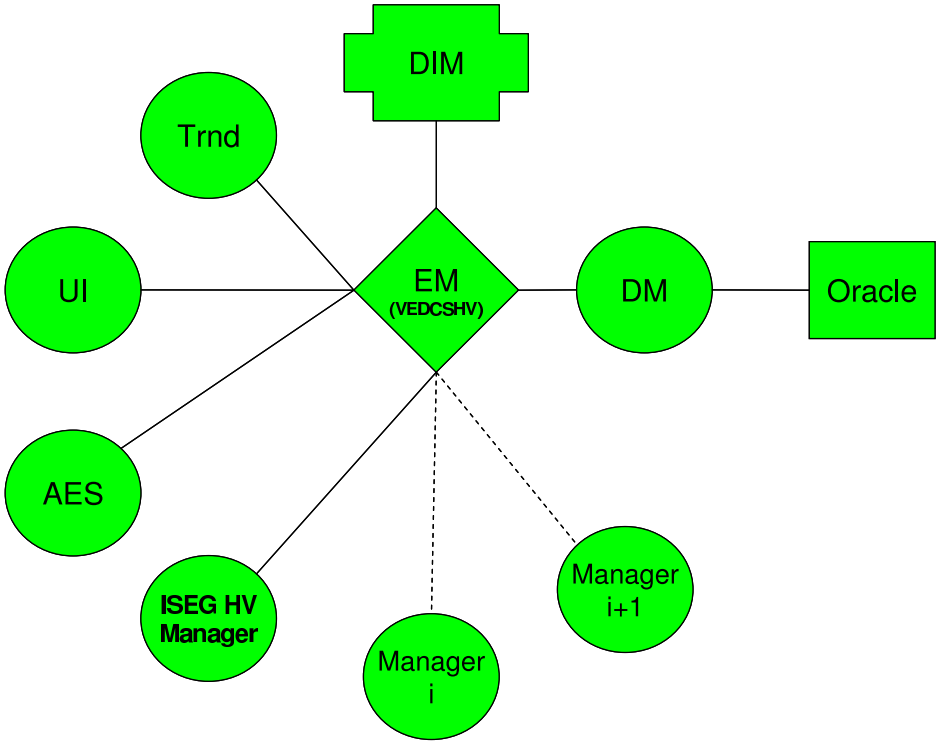

Figure 3.15: *Representation of the architecture of PVSS.*

controlling the A-side of the VELO, and 'VELOC_HV' for controlling the C-side of the VELO. The PVSS 'VEDCSHV FSM' was developed specifically for the VELO. This communicates to the PVSS ISEG framework. The PVSS ISEG framework is developed for all CERN users of ISEG power supplies. The PVSS ISEG framework communicates with the ISEG OPC Client[4]. The ISEG OPC Server is provided by the ISEG company. The version of the OPC Server used is 5.00.016[5]. The OPC server communicates with the power supply module via a USB hardware adapter. This USB hardware adapter is a USB-CAN interface produced by SYSTEC[6].

3.3.2.4 The VELO High Voltage Finite State Machine

The VELO FSM is constructed as a series of panels which are hierarchical and reactive. These panels allow the user to monitor and control the state of the system. The top level panel allows the control of all channels in the VELO. There are also panels one level down that permit control of the channels on the A-side or C-side. A number of the functionalities of the HV system can be applied to sets of 8 channels, known

[4]The OPC Client is the application which is interactively connected to the OPC server. It ensures the communication between PVSS and the OPC server.
[5]This version of the OPC server may change for future performance improvement.
[6]Systec Automation d.o.o. Katuri 17 52220 Labin, Croatia.

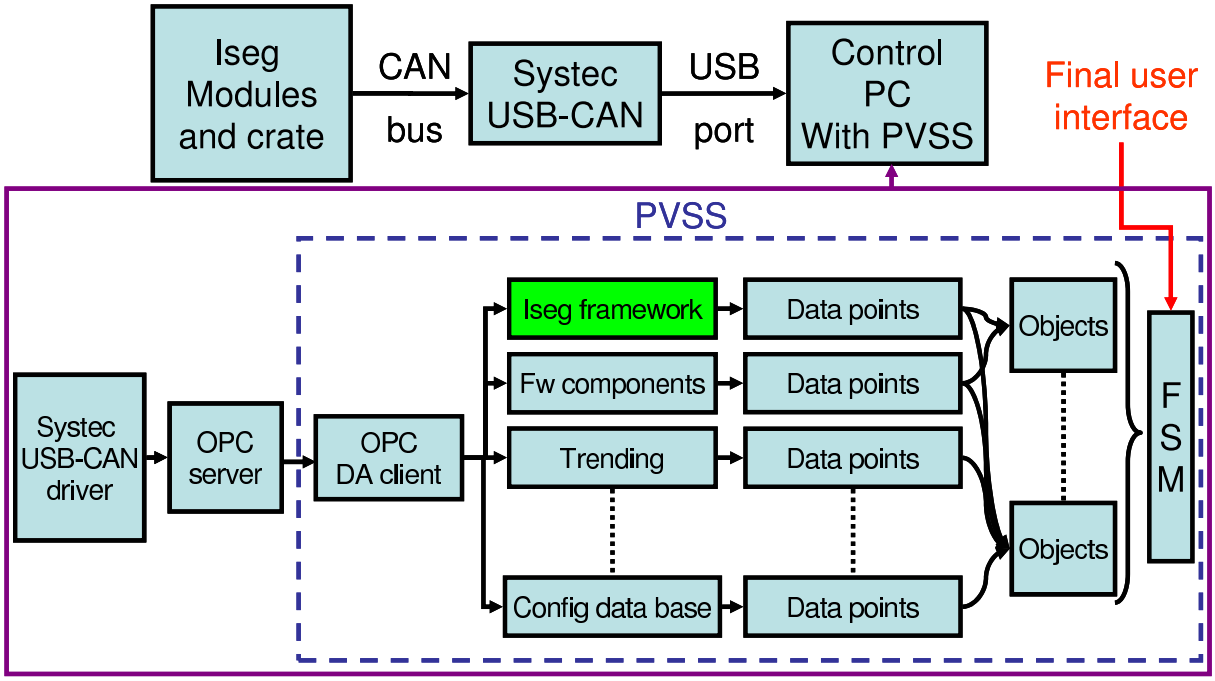

Figure 3.16: *Overview of the high voltage control software structure.*

as a 'board'. This is a natural division of the system as each power supply module controls two sets of 8 channels. Panels are also available which monitor and control individual channels. This section provides a brief overview of the functionalities of the system. The configuration of all channels (e.g. the voltages set, ramping speeds, software current limit) is known as a 'recipe'. The voltages and current limits can be set individually for each channel. The ramping speed can only be set per board. Applying this recipe starts this configuration, ramping up all channels. The recipes can only be edited from the top level panel. The recipe for all channels can be applied from the top level panel. The recipe can also be applied for A-side (or C-side), a single board or for a single channel. It is also possible to configure individual channels or whole boards by setting the individual parameters rather than applying a recipe. There are three default recipes, that all LHCb subdetectors must provide, that can be set:

- **GO_STANDBY1**: This is a first level for turning on all the channels. The voltage supplied to the VELO sensor at this level is 10 V.

- **GO_STANDBY2**: This is a second (higher) level for turning on all the channels. The voltage supplied to the VELO sensor at this level is 50 V.

- **GO_READY**: This is the standard physics setting for the detector. The voltage supplied to the VELO sensor at this level is 100 V. This is significantly above

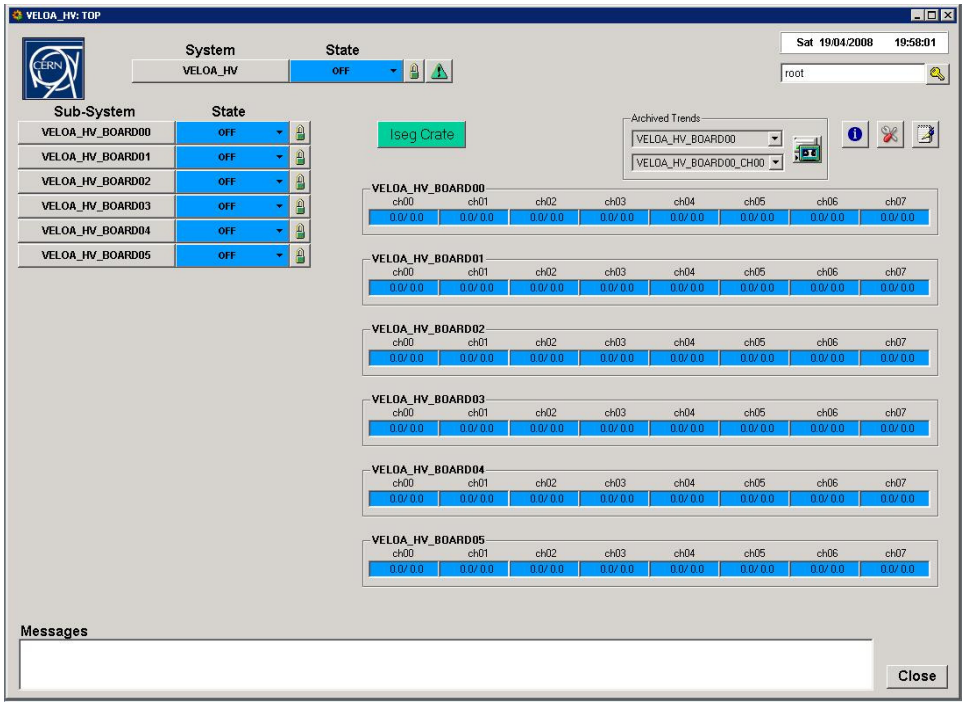

Figure 3.17: *Layout of the VELOA_HV panel. The VELOC_HV panel layout is similar to this panel.*

the depletion voltage of all sensors. Depending on the irradiation of the VELO sensors, this voltage may be increased.

There are four types of particularly important panels in the VELO HV FSM. The top level panel is called VELO_HV which provides control and monitoring of all HV channels in the VELO. The panels (see figure 3.17) that allow overall monitoring and control of all channels on the A-side (or C-side) are VELOA_HV (or VELOC_HV). These panels are accessible from the top level panel. The main panels for accessing information on one board (see figure 3.18) are 'VELO_A_HV_BOARDXY' or 'VELO_A_HV_BOARDXY' (where XY is the number of the board 00-05). The panels for individual channels (see figure 3.19) are 'VELO_A_HV_BOARDXY_CHVW' or 'VELO_A_HV_BOARDXY_CHVW' (where XY is the number of the board and VW is the number of the channel 00-07). These panels can either be accessed from the top level, the A-side (or C-side) panels or the main board panel. The organigram in figure 3.20 summarises the information and functionalities which have been discussed here, and provides a guide to determine at which level of the FSM they are available.

An IV scan can also be performed. This is obtained from the top level panel, and can be performed for either the whole VELO, A-side (or C-side), the whole board or an individual channel. This information can then be saved.

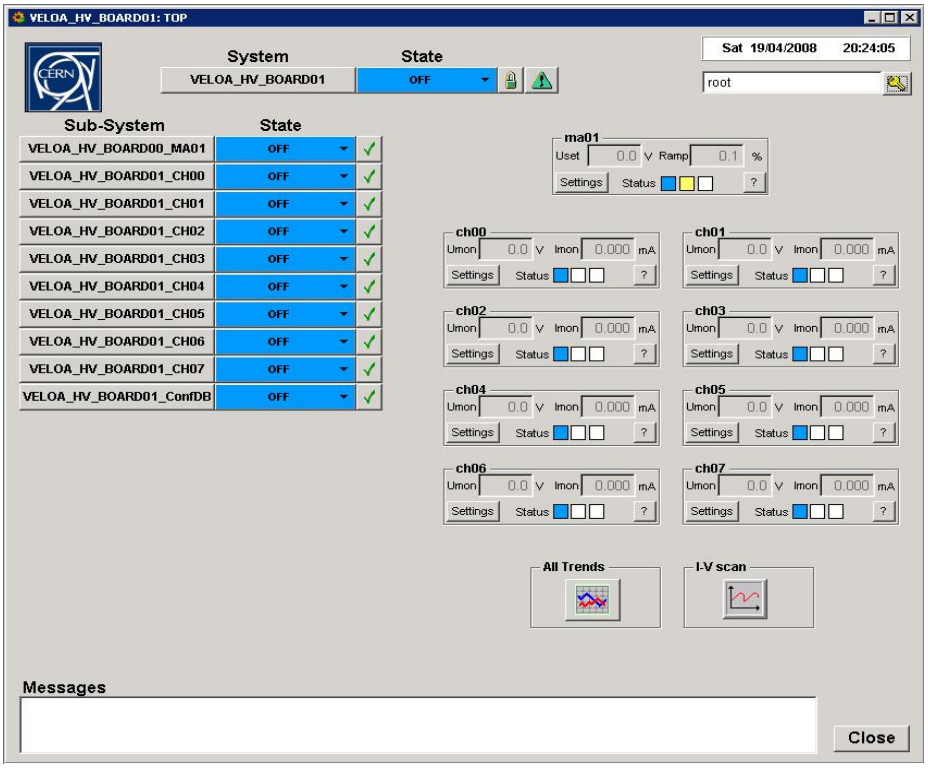

Figure 3.18: *Layout of the VELOA_HVBOARD01 panel. This board corresponds to the channels 8-15 of the Iseg module EHQ F607-nF Serial Number 474187 07/2006. All board panel layouts are similar to this panel.*

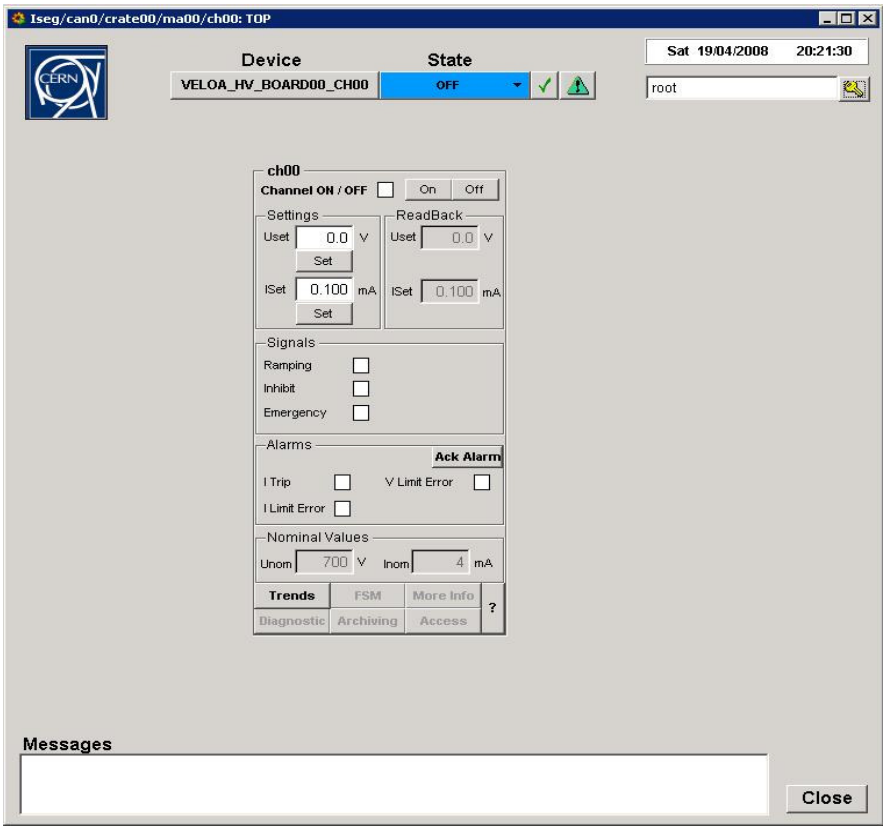

Figure 3.19: *Layout of the VELOA_HV_BOARD00_CH00 panel. The channel corresponds to the channel 0 of the Iseg module EHQ F607-nF with serial number 474187 07/2006. All channel panels are similar to this panel.*

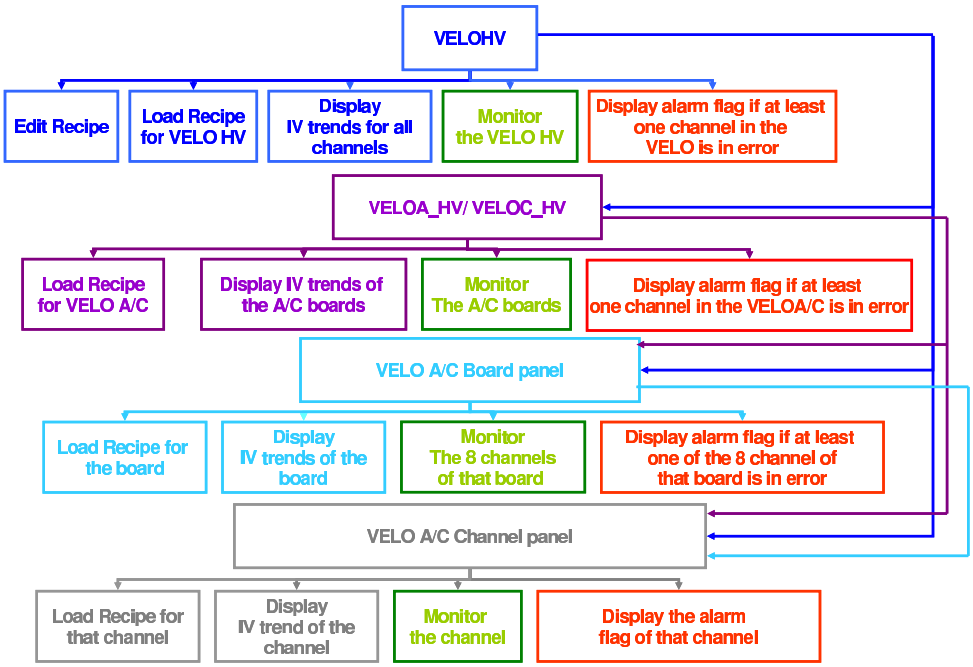

Figure 3.20: *Organigram showing the main VELO HV Finite State Machine structure.*

3.3.2.5 Alarm and Error Conditions

During the operation of the VELO, nominal operation boundary conditions have been defined to prevent any unexpected human mistake and to identify any abnormal behaviour of the sub-systems. For the VELO HV system, the main conditions are:

- Implementation of the current and voltage hardware limits (see section 3.4.3.5.1 and section 3.4.3.5.2). Their current values are currently set to 240 μA and 217 V respectively.
- Implementation of the current software limit (see section 3.4.3.5.3 and section 3.4.3.5.4) for all HV channels. The value is currently set to 105 μA.
- Implementation of a nominal ramping speed. The chosen value is approximately 1 V/s due to the behaviour of the HV modules at low currents (see section 3.4.3.5.4). The nominal ramping speed may be increased to 7 V/s once the sensors will draw higher current.

Furthermore, the HV FSM provides alarm monitoring of the general status of all HV channels, modules and crate. Any problem or error in the HV system will trigger an alarm which will be displayed on the HV PVSS panels. The main error conditions are as follows.

- **ITrip error** occurs when the current drawn reaches the current software limit.
- **ILimit error** occurs when one changes the current hardware limit while using the module.
- **VLimit error** occurs when one changes the voltage hardware limit while using the module.
- **Inhibit error** occurs when the interlock signal (see section 3.4.3.3)is interrupted.
- **Emergency off error** occurs when processes are interrupted. It causes channels to ramp down and then be switched off.
- **AC – line power error** is caused by an interruption of the normal crate power.
- **OPC server crash** is caused by a crash of the Iseg OPC server. The server will not respond and the process has to be restarted.

The error conditions cited above may prevent the HV system to restart if uncleared.

3.3.2.6 Conclusion

The description of the VELO high voltage control software was presented in this section. The implementation of its structure as a PVSS Finite State Machine was emphasized. The main error conditions that may occur during operation were also discussed. The VELO HV software conforms to the specification of the VELO.

3.4 Characterisation of the High Voltage System

This section presents the tests which were performed to the high voltage system hardware. Section 3.4.1 describes the tests of the high voltage modules under normal operation such as voltage ramping, and tests of the software and hardware limits. The tests dedicated to demonstrating the stability of the high voltage modules with time and assessing the noise of the system are detailed in Section 3.4.2. Section 3.4.3 shows the behaviour of the high voltage modules and crate under failure modes and includes a description of the two possible modes of operation of the high voltage module: current control mode, and current trip mode. The tests performed to the cables and patch panels are detailed in Section 3.4.4. Section 3.4.5 describes the tests which were performed at low voltages.

3.4.1 Normal Operation

This section describes the tests performed to verify the operation of the high voltage module under standard operating conditions. The tests verify that the voltage can be set correctly and can be ramped up or down on every channel.

3.4.1.1 Voltage Ramping up and Ramping down

The first test verifies that the full range of voltage can be applied to each channel of each high voltage module. Initially the voltage was ramped from 0 V to -500 V and then from -500 V back to 0 V. The control was performed through software and a ramping speed of 7 V/s was used. The voltage produced by the high voltage module was measured as a function of time with an oscilloscope. Two plots were produced for each channel: one for ramping up and one for ramping down, see figure 3.21. These two plots were produced for each channel of all 9 high voltage modules. No problems were observed.

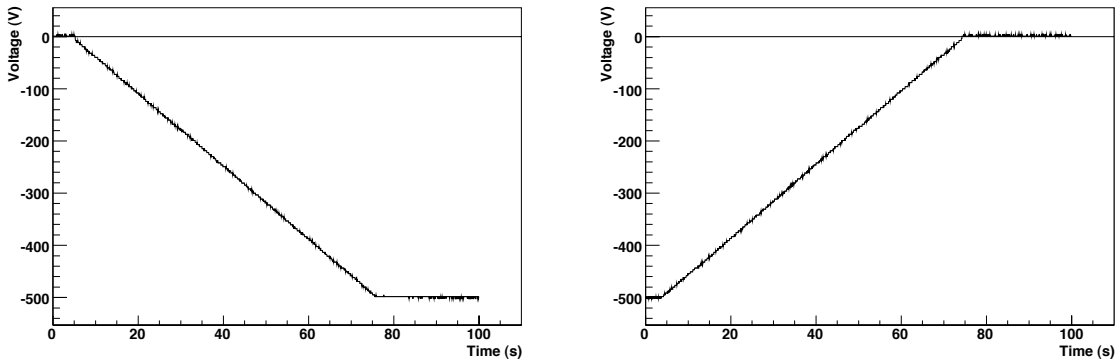

Figure 3.21: *Voltage measured on an oscilloscope during ramping of channel 15 of the high voltage module with serial number 474185 07/2006. The performance when ramping from 0* V *to -500* V *(left) and from -500* V *to 0* V *(right) is shown.*

3.4.1.2 Comparison of Channel Ramping up and down Gradients

Using the data from the previous test, the consistency of the ramping speeds in each channel of each module can be tested. Each power supply module has 16 channels. The gradient of ramping, up and down, is calculated for all 16 channels of each module. The nominal ramping speed set through the software is 7 V/s. The results of this check are shown in figure 3.22. The ramping speeds calculated during ramping up from 0 V to 500 V are slightly higher than the ramping speed set through software, while those for ramping down back to 0 V are mostly slightly less than the ramping speed set through software. The variance of the ramping speeds from channels of different modules is larger than that inside a single module. All channels of all modules performed acceptably and were within 1 % of the set value.

3.4.1.3 Firmware Error for Ramping down

The stress tests that were performed on the Iseg Modules revealed a bug in the firmware[7] that was installed in the modules. This error can cause a channel to 'instantaneously' change its voltage, rather than ramping at the required speed. The resulting voltage spike could potentially damage the VELO modules.

The error occurs if one (or more) channel(s) are being ramped and another channel is turned on. In this case the first channel(s) immediately jumps to its/their target voltage when the second channel is turned on, rather than continuing to ramp. The problem occurs for any channels in the same board of a power supply module: there

[7]The firmware version used was 2.04 for the modules.

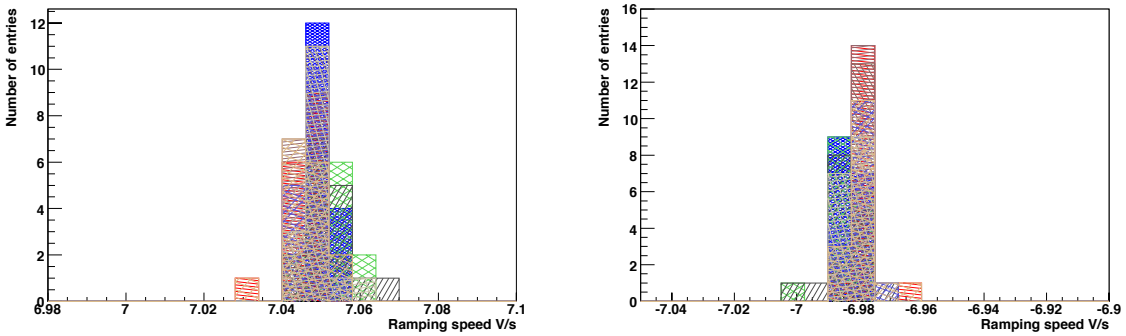

Figure 3.22: *Variation of the ramping speeds measured on each individual module by applying voltage (left) from 0* V *to -500* V *and (right) from -500* V *to 0* V*. One colour represents the group of 16 channels of one high voltage module, all 9 modules are shown but are not clearly visible as the plots are superimposed.*

are two boards in each power supply module, one for the first eight channels and one for the second eight. The problem occurs as a result of issuing the command to turn on a channel, i.e. it occurs even if that channel is already turned on. The problem only occurs if the channels are being ramped towards 0 V (e.g. from -500 V to -400 V), not if the channels are being ramped away from 0 V (e.g. from -400 V to -500 V).

The problem is caused by a firmware error and hence occurs whatever the method used to control the modules (standalone Iseg software or PVSS). After discussion with the company a new patch was released for the high voltage module firmware[8] which can be flashed into the FPGAs using the HV standalone control software. This firmware contains fixes for the previously stated problem and was tested. An upgrade of the firmware in all HV modules was performed in the 2008-2009 shutdown.

3.4.2 Stability of Operation

This section reports on tests to ensure that the output of the module is stable over time and does not have voltage spikes, and to measure the noise level at the output of the power supply and in the final setup. Significant voltage spikes could potentially damage the sensors, or at lower values would contribute to the noise thus degrading the performance of the VELO.

[8]The firmware version is 2.26.

3.4.2.1 Voltage Spikes

Two methods were used to check for any voltage spikes in the output of the power supply. The methods were applied both for constant output voltages over significant times and when ramping the voltage on the power supply.

3.4.2.1.1 First Method for Static Operation - Oscilloscope in Trigger Mode

The output of a channel was connected to an oscilloscope through a voltage divider which attenuates the input voltage by a factor of 20. The oscilloscope was set to trigger if a voltage spike occurred. During each test, a voltage of -100 V was applied which corresponds to -5 V displayed on the oscilloscope. The oscilloscope was put in the single trigger mode and the trigger level was set at -5.12 V so that if there was a voltage above -102.4 V the trace would be saved during the acquisition time. The oscilloscope was left armed for at least 12 hours. No spikes were observed during any of the tests.

3.4.2.1.2 Second Method for Static Operation - Oscilloscope in Persistency Mode

The oscilloscope was also used to test for voltage spikes using AC coupling and in persistency mode. The power supply channel output was connected directly to the oscilloscope and a voltage of -140 V was applied. The oscilloscope was in persistency mode, AC coupling was used, and the trigger level was set at 52 mV. The operation was performed for 12 hours. Figure 3.23 shows that the biggest spike observed is around 500 mV.

3.4.2.1.3 First Method during Ramping - Oscilloscope in Trigger Mode

In addition to checking for spikes during constant voltage operation, it is important to check that no significant spikes are obtained when turning the bias voltage on or off. Hence the previous tests were repeated while ramping the voltage. The power supply channel output was connected directly to the oscilloscope. During the test, the system was ramped from 0 V to 60 V, and repeated from 60 V to 120 V. The oscilloscope was put in DC mode and the trigger level was adjusted to find the minimum value such that a trace was not acquired.

The minimum value which did not provoke a trace acquisition was

$$Vset + 0.9 \text{ V}. \tag{3.16}$$

Figure 3.23: *Oscilloscope trace showing a test for voltage spikes. The trace was taken in persistency mode for 12 hours with -140* V *applied. The voltage scale is 500* mV/div*. The time scale is 500* ns/div*.*

Hence, we conclude that the power supply overshoots the set voltage and does not produce spikes at more than a 1 V level.

3.4.2.1.4 Second Method during Ramping - Oscilloscope in Persistency Mode

A check for voltage spikes was also performed using the oscilloscope in persistency mode. The power supply channel output was connected directly to the oscilloscope and the system was ramped in voltage from 0 V to -200 V. The oscilloscope was in persistency mode, AC coupling was used, and the trigger level was set at 100 mV. Figure 3.24A shows the oscilloscope trace when the voltage ramps up from 0 V to -200 V and figure 3.24B when it ramps down from -200 V to 0 V in persistency mode. The two figures show that there are no obvious significant spikes during ramping.

3.4.2.2 Noise Measurement

The tests in this section are intended to characterise the noise of the power supply module and of the full system. The first two tests characterise the noise and potential common mode noise in the power supply. The last two tests use the full assembled system and include a measurement of the bias voltage noise with a dummy load equivalent to connecting a module.

3.4.2.2.1 Noise at the Module Output

The oscilloscope was used to measure the power supply module noise. The power supply channel output was connected directly to the oscilloscope and the voltage applied was

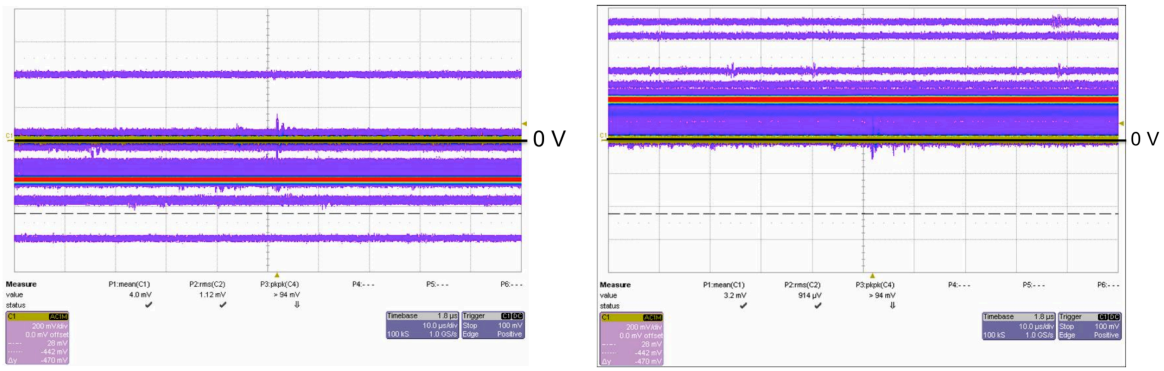

Figure 3.24: *Oscilloscope traces showing a test for voltage spikes during ramping of the voltage. The trace was taken in persistency mode. A- (left) The voltage was ramped from 0* V *to -200* V*. B- (right) The voltage was ramped from -200* V *to 0* V*. The voltage scale is 200* mV/div*. The time scale is 10* μs/div*.*

-100 V. The oscilloscope was used to measure the peak to peak voltage, RMS voltage and determine the frequency spectrum of the noise at the same time. The frequency spectrum was obtained by performing a Fast Fourier Transform of the output.

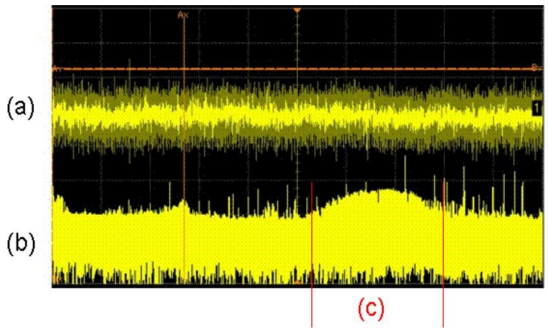

Figure 3.25: *Oscilloscope trace of the noise spectrum at the module output. (a) Indicates the noise level scan, the voltage scale is 100* mV/div*. (b) Shows the Fast Fourier Transform scan from 0* Hz *to 100* MHz *with (c) indicating a frequency range (50* MHz*-80* MHz*) in which a slight noise excess is observed.*

Figure 3.25 shows the oscilloscope traces obtained. The peak-to-peak voltage measured was approximately 100 mV and the RMS voltage is approximately 5 mV. The excess noise indicated by (c) in figure 3.25 from the Fast Fourier Transform is in the frequency range of 50 MHz to 80 MHz. While the noise levels are relatively low the frequency range does correspond to that of the VELO system, since the LHC beam crossing and front-end chip clocking frequency is 40 MHz.

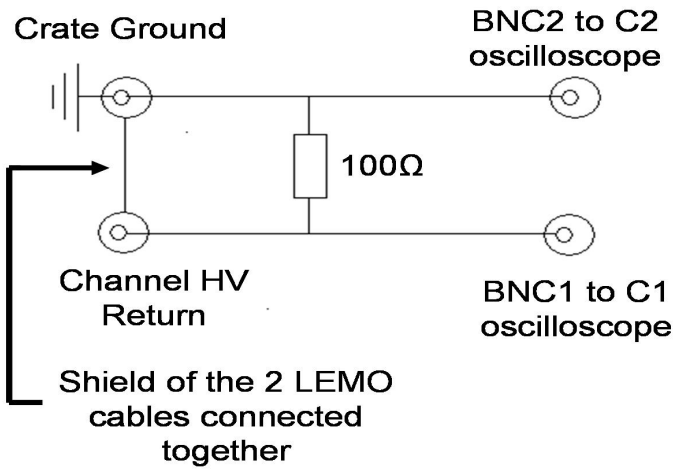

Figure 3.26: *Schematic of the common mode noise measurement setup.*

3.4.2.2.2 Common Mode Noise Measurement

A test was performed to measure the noise level produced by the potential difference between the ground of the power supply crate and the HV return of the channel. Figure 3.26 shows the schematic of the setup used to measure this common mode noise.

The channel HV return was connected directly to channel 1 of the oscilloscope and the ground of the crate to channel 2 of the same oscilloscope. The noise was displayed and measured on the oscilloscope by subtracting channel 2 from channel 1. The measurements on the oscilloscope have been performed at 0 V and -140 V on all channels. The peak-to-peak voltage has been measured as well as the RMS voltage and the frequency response by performing a Fast Fourier Transform at the same time.

Figure 3.27A is an oscilloscope screen image showing an example noise distribution. The peak-to-peak voltage measured was approximately equal to 63 mV and the RMS voltage approximately equal to 4.8 mV. The main excess noise peak indicated in figure 3.27A is at the frequency 54 MHz. The common mode noise measured between the crate ground and the HV return contains a non Gaussian component which is shown in figure 3.27B. The 'ringing' after the noise spike could be due to either the power supply module or the response of the oscilloscope.

3.4.2.2.3 Noise Measurement in the LHCb Pit without a Filter

A test was performed on the full high voltage system in the LHCb pit to measure the noise level at the end of the detector cable between the HV guard and the ground. This measurement was performed without any filter and hence corresponds to the noise that will be seen on the HV guard line under normal operation.

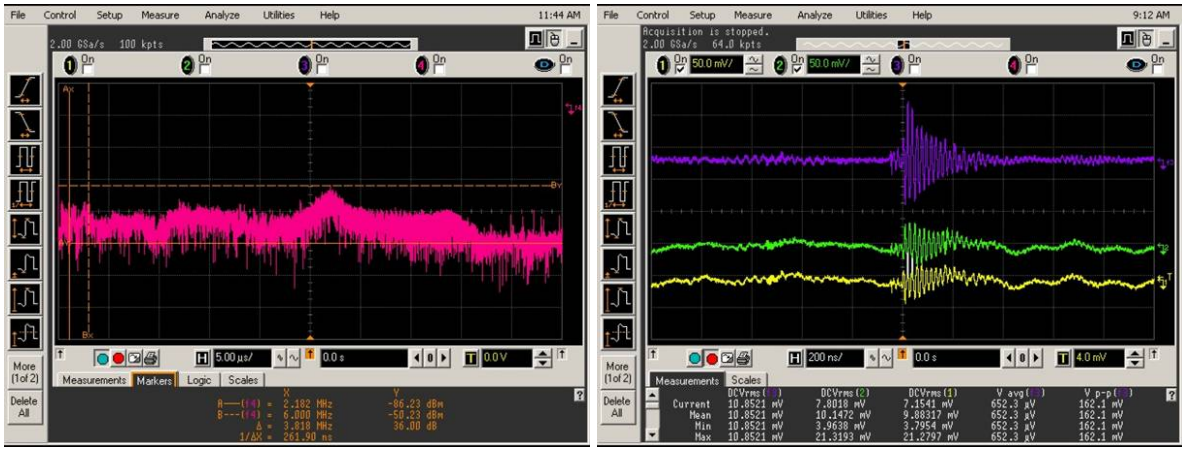

Figure 3.27: *Oscilloscope traces of the common mode noise measurement. A- (left) Fast Fourier Transform of the common mode noise. The frequency domain was from 0* Hz *to 100* MHz*. B- (right) The oscilloscope trace which shows the non Gaussian component of the noise. The time scale was 200* ns/div *and voltage scale 4* mV/div*.*

The guard line was connected directly to the oscilloscope and and the voltage applied was -100 V. The oscilloscope was used to measure the peak to peak voltage, RMS voltage and a Fast Fourier transform at the same time.

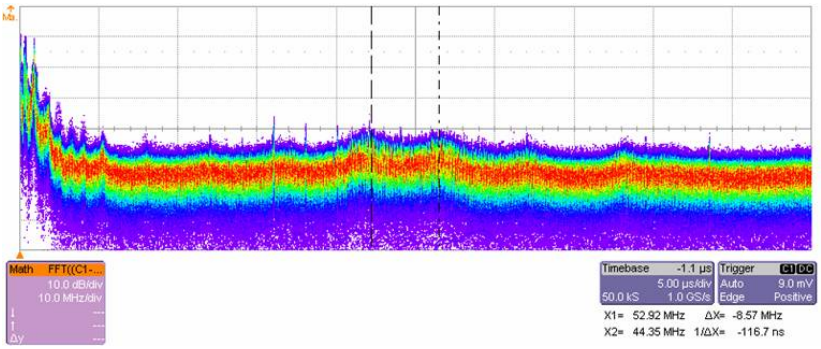

Figure 3.28: *Oscilloscope trace showing the noise measured at the detector cable output between HV guard and ground. The time scale was 5* μs/div*. The frequency domain was from 0* Hz *to 100* MHz*.*

Figure 3.28 is a screen image from the oscilloscope. The Peak to peak voltage measured was approximately 11.3 mV and the RMS voltage was approximately 2.3 mV. The excess noise peaks indicated in figure 3.28 are at the frequencies of 44 MHz and 53 MHz.

3.4.2.2.4 Noise Measurement in the LHCb Pit with a Filter

A measurement was performed of the noise level between the HV bias and ground in the LHCb pit under near realistic conditions. The hybrid of the VELO silicon module contains a low pass filter. A load emulating the hybrid was connected at the detector cable output. Figure 3.29 shows the schematic of the emulated hybrid.

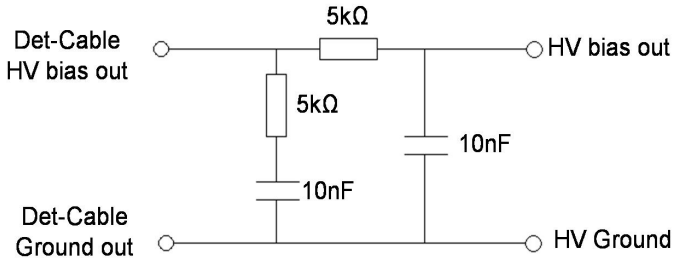

Figure 3.29: *Schematic of the load emulating the hybrid with HV filter.*

The bias line was connected directly to the oscilloscope and the Voltage applied was -100 V. The oscilloscope was used to measure the peak-to-peak voltage, RMS voltage and perform a Fast Fourier Transform at the same time.

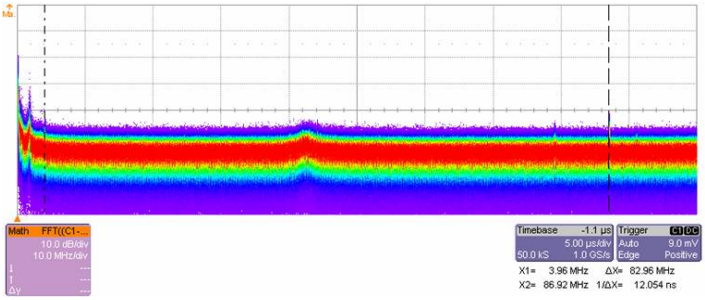

Figure 3.30: *Oscilloscope trace showing the frequency spectrum of the noise measured between HV bias and ground. The noise was measured at the output of an emulated hybrid which was connected to the detector cable. The frequency domain was from 0* Hz *to 100* MHz*.*

Figure 3.30 is a screen image from the oscilloscope. The peak to peak voltage measured was approximately 6.9 mV and the RMS voltage was approximately 1.2 mV. No significant excess noise was seen in the frequency spectrum (see figure 3.30)

3.4.3 Failure Modes

The previous section has reported on the behaviour of the system under normal operation. This section concentrates on the behaviour under failure modes. The system

response to a power failure or if the interlock signals are fired during operation is discussed. Tests of the current and voltage limits that can be set on the module (both in hardware and software) are reported.

3.4.3.1 Power Off

A test was performed to understand the behaviour of the system under a power cut. The high voltage module crate was purchased equipped with an uninterruptible power supply (UPS) which should initially maintain power to the system and then ramp down the channels.

A crate containing two high voltage modules was used for this test and a voltage of -500 V was applied to all channels. One of the channels was connected to the oscilloscope, through a voltage divider. The main power to the power supply crate was then turned off to simulate a power cut.

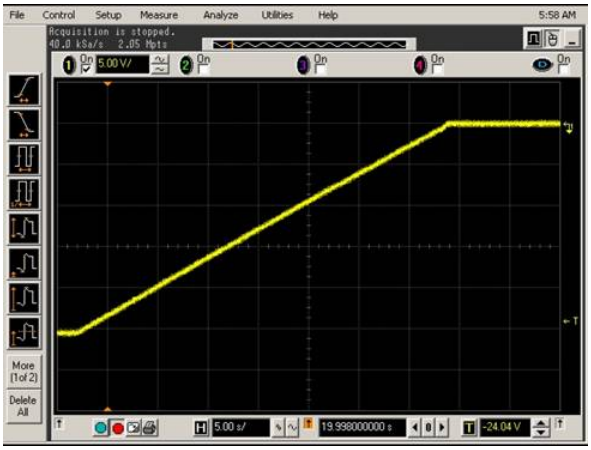

Figure 3.31: *Oscilloscope trace shows the output voltage of the module when a power cut occurs. The time scale is 5* s/div.

The voltage of -500 V is maintained on the channels for approximately 10 s, as seen in figure 3.31. It then takes approximately 40 s to ramp down from -500 V to 0 V. After a further 10 s the modules switch off completely. This behaviour of the UPS system provides a safer operation of the system than the sudden cut of voltage that would otherwise occur.

3.4.3.2 Brown-Out

Another potential failure mode of the system is a temporary interruption of the power supply or 'Brown-out'. Measurements were made to determine the HV power supply module response with short interruptions.

A crate containing seven high voltage modules and with a voltage of -140 V applied to all channels was used. One of the channels was connected directly to the oscilloscope which was in the single trigger mode and AC coupling. The trigger level was set at 40 mV.

Figure 3.32: *Oscilloscope trace of the output voltage during a brown-out when it is in persistency mode. The voltage scale is 500* mV/div*. The time scale is 500* ns/div*.*

The main power to the crate was switched off and on again to simulate a brown-out of short duration, for example 2 s. Figure 3.32 shows that a brown-out causes a spike in the voltage observed, but that the highest spike observed was approximately 1V.

If the brown-out duration exceeds 10 s the power supply module will already have started to ramp down the voltages on the channels. In this case, the channels continue to ramp to 0 V and are turned off, as in the case of a longer term power cut.

3.4.3.3 Interlock Signals

The VELO interlock system is a safety system that takes a number of inputs and will inhibit the operation of the VELO if a problem occurs, e.g. if a temperature alarm occurs from the temperature sensors on the modules. The interlock system provides an input signal to the power supply modules, if these signals are fired the power supply operation should be inhibited. A separate interlock signal is required for every channel of the power supply module. The measurements made in this section test the behaviour of the system when the interlock signals are fired.

In order to test the interlock system for the high voltage modules a box was constructed which supplies the required DC voltage of 5 V. The box has 8 switches allowing control of the individual interlock signal to a set of 8 channels of one module.

3.4.3.3.1 Interlock Signals Fired

The response of the system was investigated when all the interlock signals are fired. A crate containing 9 high voltage modules with the voltage set to -500 V on all channels was used for this test. When all the interlock signals are fired the voltages are shut down, without ramping, and an inhibit error alarm occurs via software. Applying the interlock signal again to all channels and clearing the error alarm via the PVSS software, the inhibit behaviour was reset and all channels were operational again and could be ramped up on demand as required.

In addition it is important to verify that the interlock works for each individual channel of the system. Using the interlock test box the check was performed and a voltage of -500 V was applied to all channels. The HV interlock signals were removed one by one to individual channels. The corresponding channel was checked to see that the voltage was interrupted. The checks were performed to verify all the other channels in the module were still on and had -500 V measured.

This test has shown that each channel can be inhibited individually without affecting the remaining channels.

3.4.3.3.2 Voltage Spikes when Interlock Signals Fired

The behaviour of the system was investigated when the interlock signals were fired for only some of the channels on a power supply module. The aim was to investigate if voltage spikes could occur on other channels on the module. The interlock signals are provided to the 16 channels on a power supply module via two 9 D-sub connectors in the rear panel of the module. Each connector controls 8 channels.

A crate containing 9 high voltage modules was used and -140 V was applied to all channels. The voltage and current hardware limits were set respectively to 700 V and 4 mA. A channel was chosen for monitoring and the interlock of other channels was fired. The channel for which the interlock was fired was connected directly to one channel of an oscilloscope and used as the trigger, with the trigger level set at -138 V. The monitored channel was connected to another channel of the same oscilloscope.

The interlock signals for one half of the power supply module were then fired (eight channels), while a channel on the other eight was monitored. Figure 3.33 shows that the behaviour of the monitored channel is not affected by firing half of the interlock signals.

This test was repeated interrupting the interlock signal for one channel and monitoring the behaviour of its neighbour. Again, this test has shown that firing the interlock

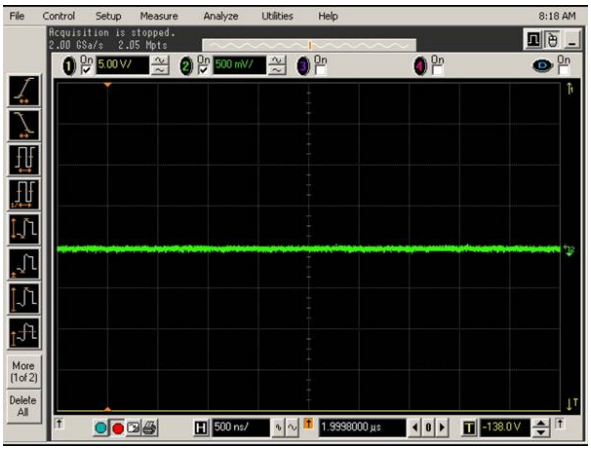

Figure 3.33: *Oscilloscope trace of a test for voltage spikes when the interlock signals are disabled. Half of the interlock signals of one HV module were fired and another channel monitored. The Voltage scale is 500* mV/div*. The time scale is 500* ns/div*.*

signal to one channel does not affect the voltage supplied to its neighbouring channel.

3.4.3.4 Speed of Voltage Cut

Measurements were made to determine the time taken for the voltage to be cut after the interlock signal was fired. During this measurement the channel was connected to the oscilloscope, through a voltage divider and a voltage of -500 V was applied. The oscilloscope was in single trigger mode. The trigger level was set at -24 V which corresponds to -485 V after compensation for the voltage divider.

Figure 3.34: *Oscilloscope trace of the output voltage when the interlock signals were removed. The time scale is 10* ms/div*.*

The interlock signals were then fired. Figure 3.34 shows that it takes approximately 90 ms for the module to ramp from -500 V to 0 V when the HV inhibit is fired.

This sudden interruption of bias voltage to the sensors could cause a voltage spike at the input of the AC-coupled front-end chips. Accidental power interruptions have occurred during test beam operation from voltages of over 100 V and no damage has been observed. However, a test has not been performed from 500 V.

3.4.3.5 Voltage and Current Limits

Limits on the maximum voltage and current that can be applied can be set for the power supply module. This section discusses the testing of these limits.

The power supply module can supply up to 500 V but its maximum voltage can be restricted through altering a potentiometer. The initial operation of the VELO sensors will be at around 100 V, but after radiation damage this voltage is expected to be increased up to a maximum of 500 V(see section 3.3.1.1). Hence, for safety, this potentiometer will be adjusted to limit the applied voltage.

Similarly, the power supply module can supply up to 4 mA. However, these current levels will only be required when the sensors are heavily irradiated. Hence, in early operation the current limit should, for safety, be set considerably lower. The power supply can be set in modes to either 'trip' when the maximum current is reached or to limit the supplied current in 'control' mode.

The maximum voltage and current are adjusted by the potentiometers, labeled Vmax and Imax, next to the two LEMO connectors on the front panel of the module [101]. The potentiometers affect the setting values in the module's microprocessor. The values set by the potentiometers are converted via an ADC-converter and are processed by this microprocessor. The microprocessor limits the maximum value of current or voltage that will be applied. The potentiometer position limits the voltage or current for all channels on the module.

It is possible to measure the hardware current or voltage limit that has been set on the potentiometer through the LEMO connector: the maximal value of Imax (4 mA) and Vmax (700 V) corresponds to 2.5 V measured from the LEMO connector. The linearity of the measured 0 - 2.5 V signal to the current and voltage limits set are discussed below.

In addition to the 'hardware' limit on the current a software limit can be applied to each channel individually. This is an additional safety feature. As the current-voltage characteristics of the sensors differ significantly (see section 3.5.2) the variability for each channel is also a useful feature.

The power supply module can be operated in two modes: current control or current

trip. In the current control mode the maximum current delivered by the system is limited to the value that has been set. In the current trip mode, a maximum safe current is set and the voltage is cut if this value is reached. For the VELO system we recommend using the current trip mode, using this limit as a safety system. The trip value should be set to a value above that which would be reached in normal operation. The mode of operation is controlled through the software by the 'kill enable' bit that can be configured to the values 0 and 1. If the kill enable is set to 0 the mode of operation is current control and if it is 1 the mode is current trip. The choice of mode applies to both 'hardware' and 'software' current limits. The following tests aim to check that the limits function and the accuracy with which the hardware can be set.

3.4.3.5.1 Voltage 'Hardware' Limit

The performance of the voltage limit was tested over the full voltage range of the power supply and was found to function correctly.

The linearity between the voltage measured on the LEMO connector (0 to 2.5 V) and the voltage limit applied (0 to 700 V) was tested. The potentiometer was changed over the full range and thus the voltage measured from the LEMO connector changed accordingly. For each setting the hardware voltage limit was measured. The measured hardware limits as a function of the voltage measured on the LEMO connector are shown in figure 3.35A as the blue line. The pink line in figure 3.35A is given by assuming a linear relationship, where 2.5 V corresponds to 700 V. The deviation of the measured behaviour from linear is shown in figure 3.35. The hardware limit has been tested from 84 V up to 700 V. The discrepancy from linear behaviour should be considered when determining the maximum voltage to set.

3.4.3.5.2 Current 'Hardware' Limit

The corresponding tests considered in the previous section for the voltage limit were also applied to the current limit. The current limit was provoked by connecting a resistance of 100 kΩ to the output of the power supply module and ramping the applied voltage. The hardware current limit has been tested from 120 μA up to 4 mA.

Figure 3.36A shows the measured current limits as a function of the measured voltage on the Imax LEMO connector as the blue line. The pink line in figure 3.36A is obtained by assuming a linear relationship where 2.5 V corresponds to 4 mA output on the power supply. Figure 3.36B shows that the discrepancy from the linear behaviour is small.

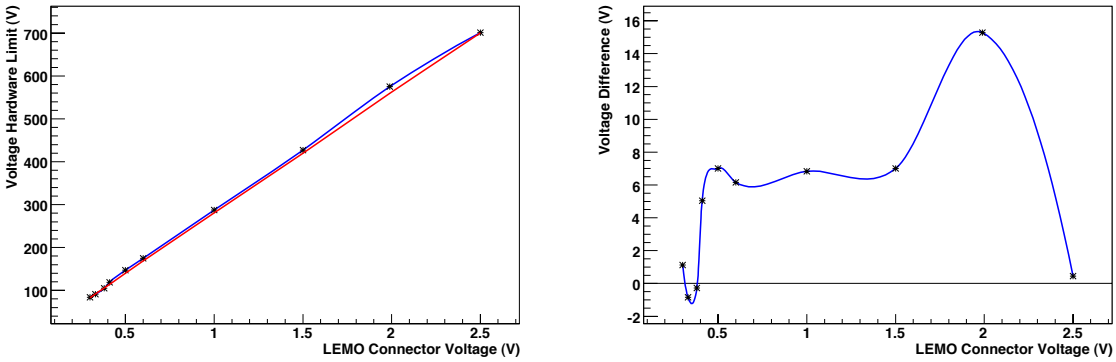

Figure 3.35: *A- (left) Hardware voltage limits as a function of voltages measured from the LEMO connector. B- (right) Discrepancy between the measured hardware voltage limits and linear behaviour for the voltages measured from the LEMO connector.*

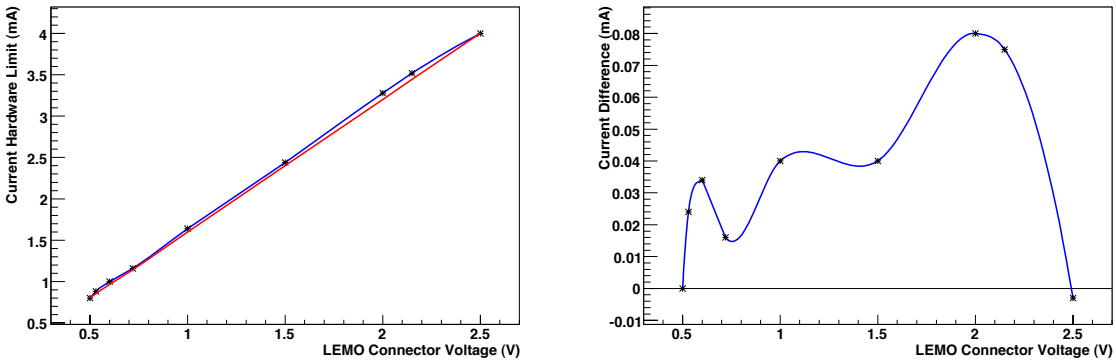

Figure 3.36: *A- (left) Hardware current limits as a function of voltages measured from the LEMO connector. B- (right) Discrepancy between the measured hardware current limits and linear behaviour for the voltages measured from the LEMO connector.*

3.4.3.5.3 Current Software Limit up to 4 mA

In addition to the 'hardware' limit that can be set through the potentiometer, software limits on the current can also be set. This test aims to verify that the current software limit of the individual channel works.

The current limit was provoked by applying various voltages to a resistance of 100 kΩ. The software limit was tested from 120 μA up to 4 mA. The test were performed both in current control mode and in current trip mode. When the software current limit is reached a trip error alarm is displayed in the software, and the current is either limited to the limit value (control mode) or the voltage to this channel turned off (trip mode). The HV power supplies are always used in trip mode to maximize the VELO modules protection. After repairing the error, the alarm can be cleared and the channel returned to normal operation. All channels have been tested and for each one the current software limits work correctly.

3.4.3.5.4 Current Limit below 120 μA

In the sections above the current limit was only considered above 120μA. Tests were also performed at lower values. Again the current limit was provoked by applying various voltages to a resistance of 100 kΩ. The results show that a ramping speed of 7 V/s (i.e. 1 % of full output per second) always provokes a trip for a current software limit below 40 μA even if nothing is connected to the module. If the ramping speed is reduced, e.g. to 1 V/s, or the current software limit is set higher this problem is prevented. While it is not expected that the hardware limit would be set below 40 μA, one need to be aware of this behaviour for setting the software limits.

3.4.3.5.5 Voltage Cut in Current Trip Mode

The current trip was designed to shut off the module immediately if activated. The firmware of the modules does not offer the possibility to 'ramp down' the channels in the case of trips. This ramp down period would have to be short for safety purposes but could be longer than the current behaviour which is equivalent to that reported in section 3.4.3.4, where the potential danger of a sudden voltage cut to the modules is considered. An upgrade of the modules' firmware[9] was performed during the 2008-2009 shutdown.

[9]The firmware 2.26 was flashed on the HV modules during the 2008-2009 shutdown

3.4.4 Cables and Patch Panels Testing

The cables and patch panels of the high voltage system have been tested, including all spare components. Connectivity tests were performed by the Glasgow team prior to installation on the following components: the counting house cable which links the power supply modules to the patch panel in the counting house; the counting house patch panels; the patch panel close to the detector. A full chain test of these components was then performed up to 500 V, using a prototype long distance cable. The leakage current measured was consistent to zero within the resolution of the measurement.

The connectivity of the long distance cables that link the counting house and detector patch panels were tested after the in-situ installation of the connectors. One of the connectors was subsequently damaged during the installation of the low voltage system and this connector was replaced and retested.

The detector cables that link the detector patch panels and the HV connectors on the VELO repeater boards were assembled in the two required lengths and tested by LEMO S.A.[10].

The connectivity and leakage current at 500 V was tested on all channels of the full assembled HV system in the pit, including the spare detector and long distance cables. The description of these tests is given in [102].

3.4.5 Low Voltage Behaviour and Current Fluctuations

3.4.5.1 Low Voltage Behaviour

The high voltage system of the VELO will typically be operated at voltages in excess of 100 V. However, during tests it can be useful to apply low voltages to the system, for example, when testing connectivity. During these tests of the system it was observed that the behaviour of the power supply modules at low voltages (below 10 V) was not as expected. This behaviour is reported in this section.

The requested value of the high voltage was compared with the voltage obtained as read back from the system and displayed in the software and cross-checked with a DVM. Figure 3.37A shows the result obtained when setting voltages from 0 V to 28 V via the PVSS software in steps of 0.5 V. The PVSS measurements (blue points) and the DVM measurements (pink points) are all averages over several measurements. Both measurements are consistent (indeed the blue points are largely obscured by the pink points on this scale) and their differences are presented in figure 3.37B.

[10]LEMO S.A., CH-1024 Ecublens, Switzerland

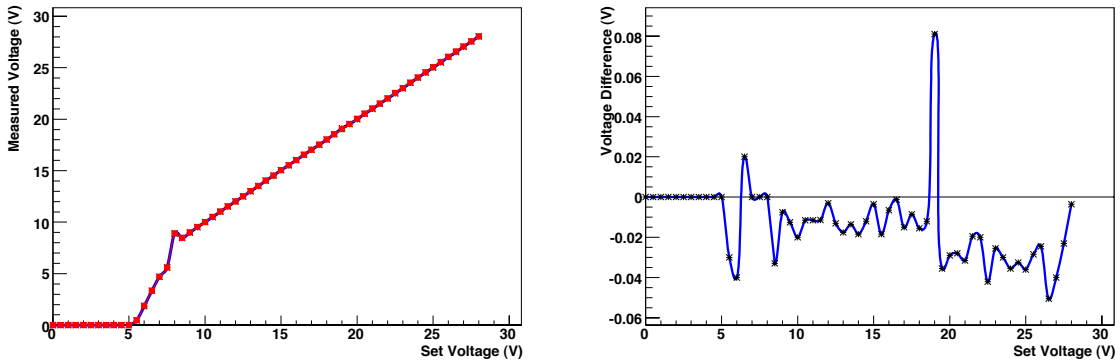

Figure 3.37: *Comparison of the requested and measured voltages at low voltages. A- (left) Voltage measured as a function of the set voltage. The blue points, largely obscured, are for PVSS software measurements and the pink points are for DVM measurements. B- (right) Difference between the PVSS and DVM measurements as a function of the requested voltage. These results are for channel 5 of the module with serial number: 474189 07/2006.*

It is clear from figure 3.37 that the behaviour above 9 V is as expected, the measured voltage in software and through the DVM both agree with the voltage that has been requested. This confirms the normal operating behaviour that was reported in section 3.4.1.

However, below 9 V the voltage applied does not correspond to the voltage that has been set. Further measurements have been taken from channels of several high voltage modules to understand its behaviour in this non linear part of the graph. Figure 3.38 reports the behaviour of four channels. These results are representative of the larger sample of measurements that were made. The following conclusions are drawn:

- The high voltage module operates correctly for voltage settings above 9 V.
- Setting a voltage below 5 V, results in no voltage being applied.
- For requested voltages between 5 V and 6.5 V the voltage applied is less than the voltage set.
- For requested voltages between 6.5 V and 9 V the voltage applied is typically higher than that which has been set. The highest voltage set is approximately 10 V.

The behaviour of all channels on a single module is not the same, see figure 3.38C and 3.38D. It was not clear that the variation in behaviour between channels on different

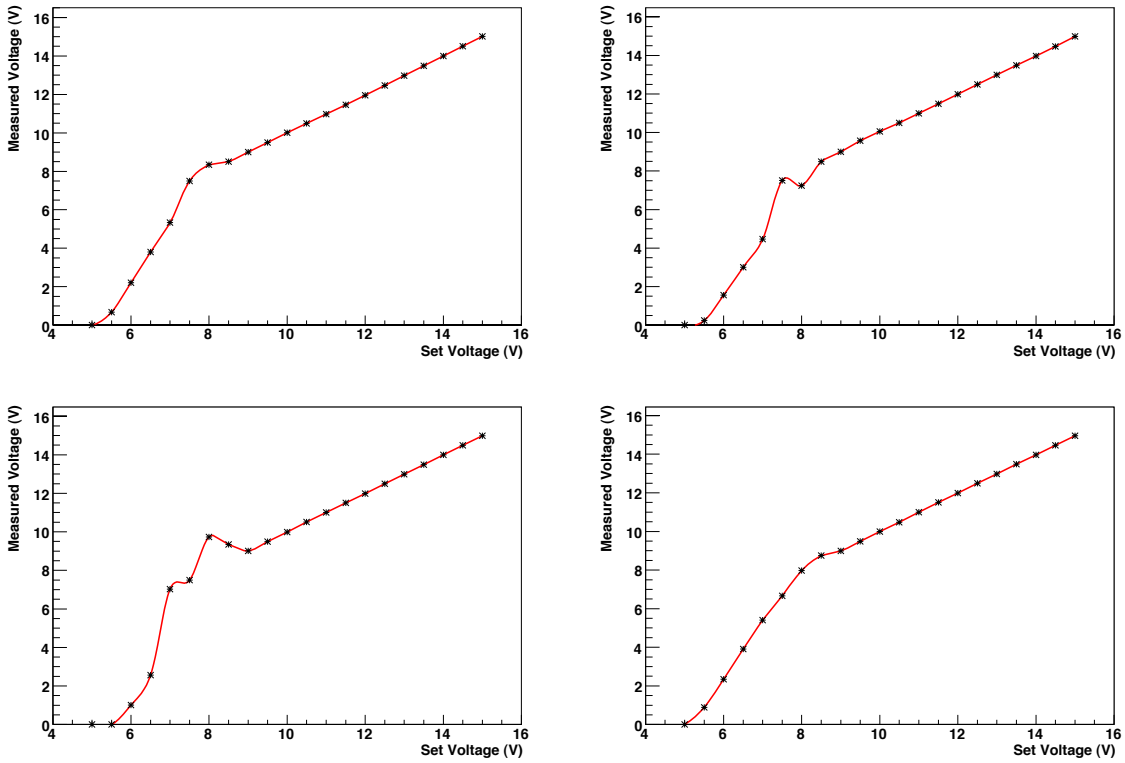

Figure 3.38: *Measured voltage as a function of set voltage for low voltages. A- (top left) channel 1 of the module with SN: 474195 07/2006 B- (top right) channel 10 of the module with SN: 474193 07/2006 C- (bottom left) channel 15 of the module with SN: 474191 07/2006 D- (bottom right) channel 2 of the module with SN: 474191 07/2006*

modules (e.g. figure 3.38A, 3.38B, 3.38C) is any larger than between channels on the same module.

The difference between the values set and the voltage measured in this low voltage region are thought to be due to the noise of the ADC and of the voltage dividers in the power supply module in this region. In discussion with the power supply company, the modules were claimed to typically be calibrated above 1 % of the maximum voltage, i.e. above 7 V. However, the company has seen problems with the calibration and suggest that the true calibration may be only achieved above 1.5 % (11 V) to 2 % (14 V). From the test results stated previously, only using the system above 10 V is advised.

3.4.5.2 Current Reading Fluctuation

The accuracy of the current reading of the ISEG module has been tested. The ISEG manual [101] states that the current measurement resolution is 80 nA and the accuracy of the measurement is given as

$$0.005\%\ I + 0.01\%\ Imax, \tag{3.17}$$

where I is the supplied current and $Imax$ is 4 mA (the maximum current the power supply can produce), so for low currents the precision is 0.4 μA r.m.s. The fluctuations in measured current values with stable loads have been observed. This was tested for all channels of the high voltage system without any load applied at 100 V. The test was repeated for a few number of channels per module with a 100 MΩ resistance and operated at 100 V. The results of both tests are in agreement.

Fluctuations of 4 μA peak-to-peak amplitude were observed on power supply module 474187 07/2006. This is considerably worse than observed on the other modules, which all showed similar behaviour and similar to that expected from the manual. The peak-to-peak amplitude of the fluctuation observed is always less than 1 μA, for all the modules used in the VELO system. The fluctuations are caused by a measurement error, they are not actual variations in the supplied current this has been checked with an oscilloscope and a DVM. The voltage was set and measured using the Iseg standalone control software IsegHVControl version 1.57. In addition, a comparison has been made by using PVSS, using the Iseg OPC server 5.00.006.

As typical currents drawn by the unirradiated modules are less than 5 μA at 250 V, a fluctuation of 1 μA is of relevance for early operation: the currents after irradiation will be considerably higher. Indeed, the current reading provides useful information on the level of irradiation. The level of the observed fluctuations has been reported to Iseg. The accuracy of the measurement of 'current-voltage' (IV) curves on the VELO modules has been improved by implementing an averaging procedure in the PVSS FSM. The current values are recorded ten times and the average value used in the IV plots produced.

3.4.6 Conclusion

The tests that were performed to characterise the HV system were presented in this section. The HV system was tested under normal operation, during voltage ramps and under failure modes. Noise spectra were measured and quantified. The tests were performed both in the laboratory and at the LHCb Pit. The tests have given the following main results.

The HV system will not add extra noise to the front-end electronics. There was a small excess of noise observed in the range of 50 MHz to 80 MHz at the module output and also at 44 MHz and 53 MHz at the end of the detector cable installed in the LHCb

Pit. When connecting a load emulating the hybrid, this excess of noise is suppressed to a negligible level.

The HV power supplies are stable and supply accurate voltages. The voltages measured at the channel outputs are approximately within 1 % of the set values for all channels. No spikes were observed during long term test of the HV power supply at a defined voltage. No spikes were seen when the interlock signals were fired individually and globally. No noise spikes were observed during ramping and stable operation. However, spikes up to 1 V were observed during short power glitches (brown-out). In case of a power-cut, the crate UPS will temporary power the modules while all channels will be ramped down to 0 V with a ramping speed of 12 V/s. Once triggered the ramp down will continue even if the normal power is back. The crate UPS power can last at most 1 minute.

The HV power supplies will always be operated in current trip mode. Under this mode, the channel that triggers a trip alarm shuts off directly.

The HV system has a reliable protection both in hardware and software for the VELO modules. All HV channels can be inhibited individually or globally by firing the interlock signal of corresponding channel(s). The interlock signals may be fired if the temperature of the module would be out of range or the cooling system would fail or the beam condition monitored would be unsatisfactory. Firing the interlock signal causes the corresponding channel(s) to ramp down at a ramping speed of approximately 5 kV/s. The hardware voltage and current limits of the modules can be changed as desired. Furthermore, current trip limits can also be set at the HV software level which cannot exceed the hardware current limits.

Despite the fact that the HV system has generally shown good performance, two points have to be considered when operating the HV system. The tests have revealed current reading fluctuations. The highest fluctuation observed was 4 μA peak-to-peak amplitude. This was only observed in one of the modules. Upon the observation, that module was replaced by one of the spare modules. The other modules current reading fluctuations were always less than 1 μA peak-to-peak amplitude. Investigations have indicated that the fluctuations are caused by a measurement error as they are not actual variation in the supplied current. The tests have also shown that the HV modules do not supply the correct voltages below 9 V. Hence, using the HV system above 10 V is advised.

3.5 Commissioning Experience and Current-Voltage Performance of the VELO Sensors in-situ

The commissioning of the high voltage system has passed through several stages. The components of the HV system were characterised individually at the University of Glasgow. A full chain test was done at the University of Glasgow using a 1.5 m cable of the same type as the long distance cables.

The 60 m long distance cables were installed in the LHCb Pit then had their connectors fitted, and were then tested. After all components were installed, characterisation tests were repeated to ensure no degradation of their performance had occurred. The results of all the tests were presented in section 3.4.

It is important to regularly retest the system and this will be done annually during shutdowns. Due to the limited space where all the components were installed, a long distance cable connector was broken during the installation of the low voltage system. This was repaired and retested. There were also problems in the software. The OPC server version that was used to operate the HV modules and crate was not compatible with the Windows 2003 server used in the LHCb Pit. At Glasgow the tests have been performed with Windows XP, where the OPC server was working properly. A new OPC server version was released by the Iseg company that solved this incompatibility.

The system was tested and complies with the electrical safety regulations at the LHCb Pit. Current-Voltage data were taken at different periods of the commissioning to monitor the behaviour of each sensor. The resulting characteristics are presented in section 3.5.2. Since the data were not taken at the same temperature, temperature corrections (see section 3.5.1) were applied to the measured current values.

3.5.1 Temperature Correction

To investigate if there was any degradation in the current voltage behaviour of the VELO sensors, current-voltage data were compared. The comparison was made on current-voltage data that were taken at the time of module production, during their commissioning and around the time of the beam absorber collision data[11], and up to the start of the LHC run in autumn 2009. Since measurements of the same module were made at different temperatures, one has to consider the leakage current dependence on the sensor's temperature. The leakage current measured from the detector is a

[11] Data were taken from the collision of a beam of protons with a beam absorber during LHC synchronisation test of the anti-clockwise beam. [103]

combination of the bulk and the surface currents. The bonding scheme of the VELO modules makes it impossible to distinguish these two current contributions. Moreover, their temperature dependences are different. The bulk leakage current is due to thermal excitation from the valence band to the conduction band (see chapter 4) under an electric field at the p-n junction of the sensor. If the bulk current would be dominant, the following equation can be used to scale the measured leakage current values:

$$I\left(T_{ref}\right) = I(T).\left(\frac{T_{ref}}{T}\right)^{2}.exp\left(-\frac{E_g}{2k_B}\left[\frac{1}{T_{ref}}-\frac{1}{T}\right]\right), \tag{3.18}$$

where T is the measurement temperature in K, T_{ref} is the reference temperature and k_B is the Boltzmann constant. E_g is the silicon band gap of 1.12 eV. In practice this corresponds to approximately a doubling of current every 8°C. No such simple scaling occurs for the surface current, so this adjustment will not work in all cases.

3.5.2 Current-Voltage Characteristics

The high voltage system has been used to study the stability of the VELO sensors by studying the current-voltage characteristics. The comparison was made between the current-voltage characteristics taken during the module production ($\approx$ 20°C) and during commissioning in December 2008 ($\approx$ 25°C for most of the A-side sensors[12] and $\approx$ 10°C for C-side sensors), in June 2009[13] ($\approx$ 20°C) and in October 2009 ($\approx$ -25°C). Since these measurements were taken at different temperatures, the leakage current values were scaled to 20°C. The temperature correction was applied using equation 3.18 in section 3.5.1. The comparison was made at the nominal operating voltage of 100 V. As explained in section 3.4.5.2, the Iseg power supply suffers from reading fluctuations at low current. Hence differences below 1 μA may be due to reading errors.

The high leakage current sensors were identified for each data. Their comparisons are provided in section 3.5.2.1. Section 3.5.2.2 presents the change of sensors' leakage currents when cooling. The evolution of the sensors' leakage currents at room temperature is given in section 3.5.2.3.

[12]The temperatures of the pile-up sensors P02R and P03R in December 2008 were $\approx$ 10°C.
[13]The June 2009 data does not contain data for the pile-up sensors.

Data	Percentage of high leakage current sensors (I $>$ 5 μA)	
	Without temperature correction	With temperature correction
Production	19 %	19 %
December 2008	20 %	25 %
June 2009	23 %	15 %
October 2009	15 %	-

Table 3.3: *Comparison of the percentages of high leakage current sensors from the measurement at the module production, and the measurements during commissioning in December 2008, in June 2009, and in October 2009.*

3.5.2.1 Comparison of the Observed High Leakage Current Sensors from all Data

To perform the sensors' leakage currents comparison over time, the sensors are grouped in two categories: those below 5 μA leakage current and those above. The high leakage current sensors are then divided in three sub-categories in table 3.4.

Figure 3.39 shows the comparison of the R and ϕ sensors' leakage currents between the production data, the December 2008 data, the June 2009 data, and the October 2009 data. No temperature scaling was applied to any of the data.

Table 3.3 summarises the comparison of the percentages of high leakage current sensors from each of these four measurements with and without temperature correction. The October 2009 data was not scaled, hence this entry is not included in table 3.3. Furthermore, the measured leakage currents are close to the resolution of the Iseg power supply and there might be surface current contribution which cannot be scaled. The scaling of the current with temperature cannot be done to the -25°C data because it is likely that the measured current has a surface current component that dominates at low temperature. It is clear from figure 3.39 and table 3.3 there is no significant change in the fraction of high leakage current sensors.

Table 3.4 provides the full list of the observed high leakage current sensors, without applying any temperature correction to any of the data and by scaling both December 2008 and June 2009 data to 20°C. The high leakage current sensors are broadly in

agreement with that observed at production, there are more ϕ sensors with high leakage currents than R.

3.5.2.2 Change of Leakage Current When Cooling

Since the October data ($\approx$ -25°C) cannot be scaled to 20°C, to identify the change of leakage current when cooling, all data were compared without temperature scaling. The sensors' leakage currents are expected to decrease exponentially with temperature. Hence, an increase of leakage current on cooling would indicate an abnormal behaviour of the sensor.

As shown in figure 3.39, six sensors have an increase in current when cooling. These sensors are M23P, M24P, M26P, M36P, and the two pile-up sensors P00R and P02R which correspond to 54% of the high leakage current sensors.

These sensors are worrying and their future behaviour will have to be particularly followed. Their high leakage current behaviour might be due to stress in the modules as materials of different coefficients of expansion are cooled to lower temperature. The VELO modules are made with R and ϕ sensors glued back to back (see figure 2.8) on the carbon fibre supports and these materials may contract different amounts leading to stress in the module.

The pile-up modules contain only single sided R sensors, and required stiffening carbon fibre structures glued between the modules. Cooling could induce stress in these structures and the carbon fibre support, which may cause an increase of the sensors' leakage currents.

3.5.2.3 Evolution of the Sensors' Leakage Currents at Room Temperature

To identify the evolution of the sensors' leakage currents, the December 2008 data and the June 2009 data were scaled to 20°C and compared with the Production data (see figure 3.40). No clear trend was observed as a function of time at 20°C. Some sensors have increased their scaled current in December 2008, but this seems to be due to the temperature scaling behaviour. Hence for the following, no temperature scaling was applied to the data, this data was already shown in figure 3.39.

Since some changes of the classification of the high leakage current sensors were observed after applying the temperature correction to the December 2008 data and the June 2009 data (see table 3.4), three detailed comparisons were performed to estimate their leakage current increases (or decreases): the comparison between the Production data and the December 2008 data, the Production data and the June 2009 data, and

the December 2008 data and the June 2009 data.

Figure 3.41 shows the amount of leakage current increase (or decrease) between Production, December 2008 and June 2009. Only sensors with leakage currents and current increase (or decrease) above 5 μA were shown in these graphs.

From Production until June 2009, seven sensors present significant leakage current increases at room temperature with an average of ≈ 10 μA which correspond to 8% of the VELO sensors. Note that this increase is small compared with that expected from radiation damage (see section 3.3.1.1.1).

3.5.3 Conclusion

A detailed comparison of the current-voltage characteristics of the VELO sensors was presented in this section. The high leakage current sensors were identified for each dataset.

It was observed that the temperature correction function used to scale the sensors' leakage current cannot always be used due the measured current resolution of the Iseg power supply and the surface current contribution.

Cooling down has increased the leakage currents of some sensors. This behaviour could be due to the stress induced effects on cooling.

The evolution as a function of time for all data have shown no strong increase in the number of high leakage current sensors. No clear trend was observed as a function of time at 20°C. However, approximately 8% of the sensors (primarily ϕ sensors) do show non negligible leakage current increase compared to production. The increases are small enough not to affect their performance.

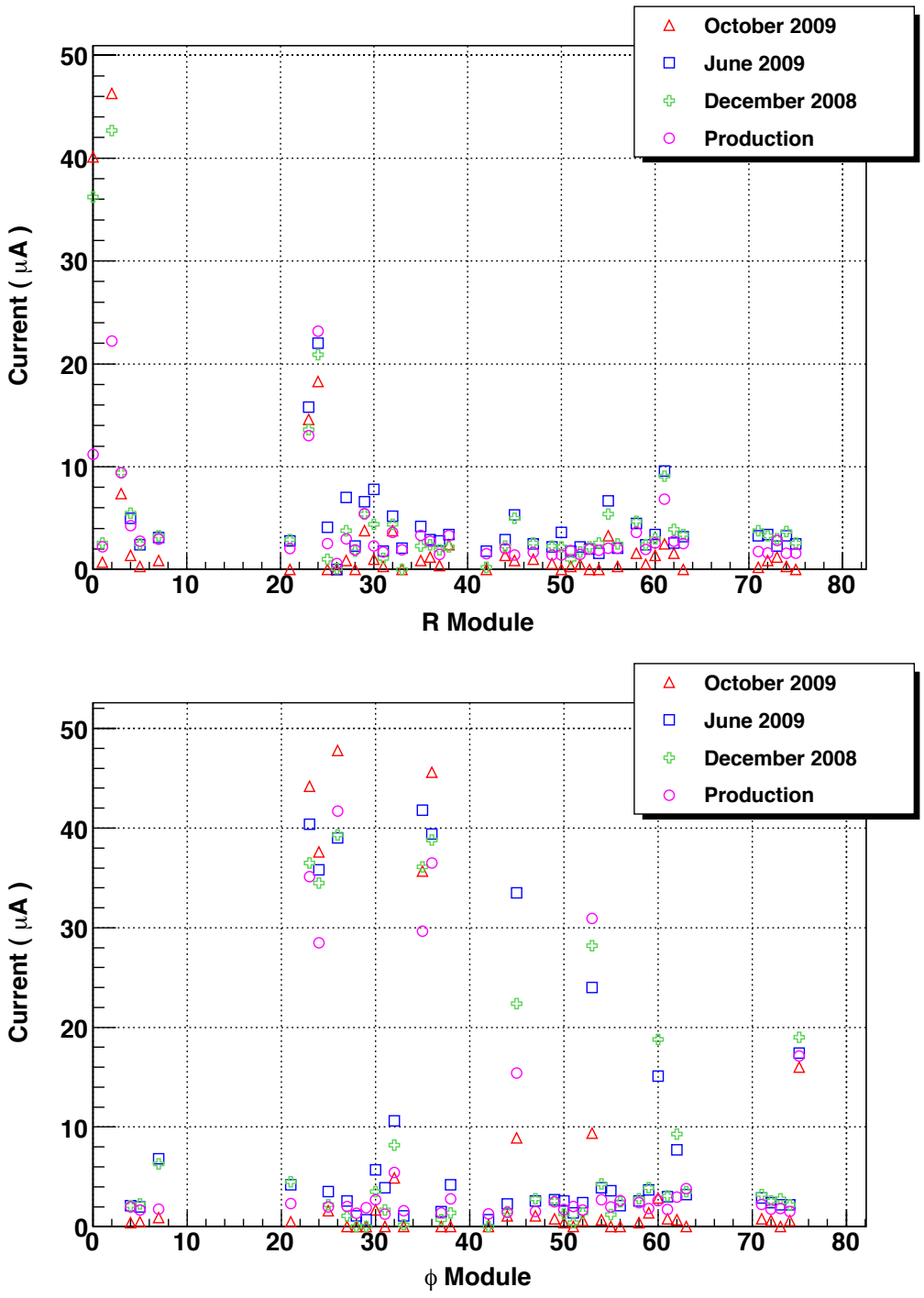

Figure 3.39: *Comparison of the sensors' leakage currents at 100 V between the data taken at the module production (pink rings) and data taken during commissioning in December 2008 (green crosses), in June 2009 (blue squares) and in October 2009 (red triangles). No temperature scaling was applied to any of the data. A-(top) R sensors. B-(bottom) ϕ sensors.*

Sensors	Data	5 μA < I < 15 μA	15 μA < I < 25 μA	I > 25 μA
R	Production	M29R, M61R, P03R, P00R, M23R	P02R, M24R,	
	December 08	M61R, P03R, M23R	M24R	P00R, P02R
	December 08 scaled to 20°C	M27R, M30R, M32R, M45R M29R, M55R	P03R	M23R, M24R P00R, P01R
	June 09	M29R, M55R, M27R, M30R M61R	M23R, M24R	
	June 09 scaled to 20°C	M61R, M23R, M24R		
	October 09	P03R, M23R	M24R	P00R, P02R
ϕ	Production	M32P	M45P, M75P	M24P, M35P, M53P, M23P, M36P, M26P
	December 08	M07P, M32P, M62P	M60P, M75P, M45P	M53P, M24P, M35P, M23P, M36P, M26P
	December 08 scaled to 20°C	M30P, M60P, M75P	M53P, M32P, M26P	M45P, M24P, M35P, M23P, M36P
	June 09	M07P, M62P, M32P, M60P	M75P, M53P	M45P, M24P, M26P, M36P, M23P, M35P
	June 09 scaled to 20°C	M32P, M60P, M75P	M53P, M45P M24P, M26P	M23P, M36P, M35P
	October 09	M45P, M53P	M75P	M35P, M24P, M23P, M36P, M26P

Table 3.4: *Comparison of the observed high leakage current sensors without applying any temperature scaling to any of the data and by scaling the December 2008 and the June 2009 data to 20°C. The order of the module numbers represents lowest to highest currents in that category.*

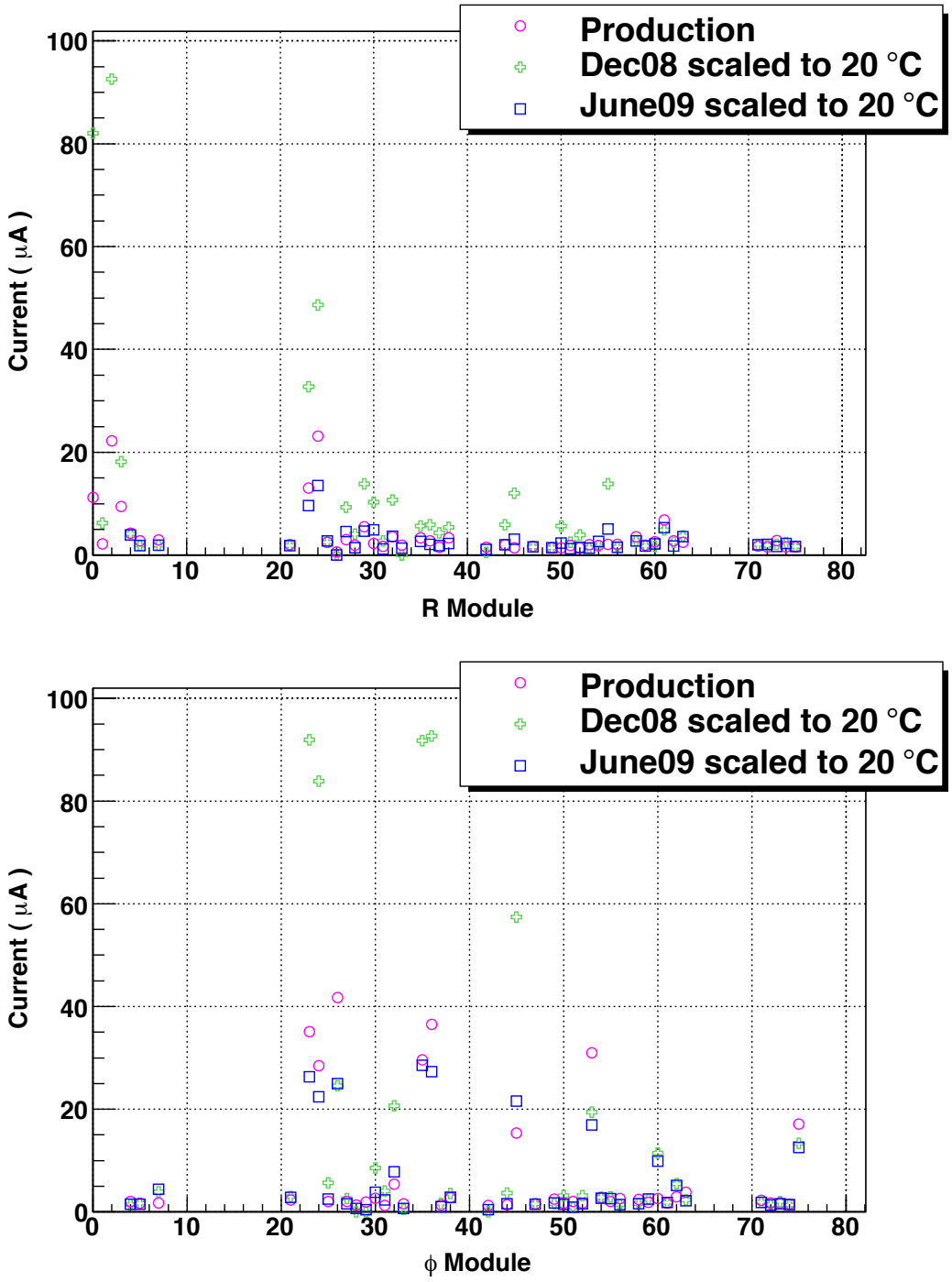

Figure 3.40: *Comparison of the sensors' leakage currents at 100* V *between the data taken at the module production (pink rings) and data taken during commissioning in December 2008 (green crosses), and in June 2009 (blue squares). Both December 2008 data and June 2009 data were scaled to 20°*C*. A-(top) R sensors. B-(bottom) ϕ sensors.*

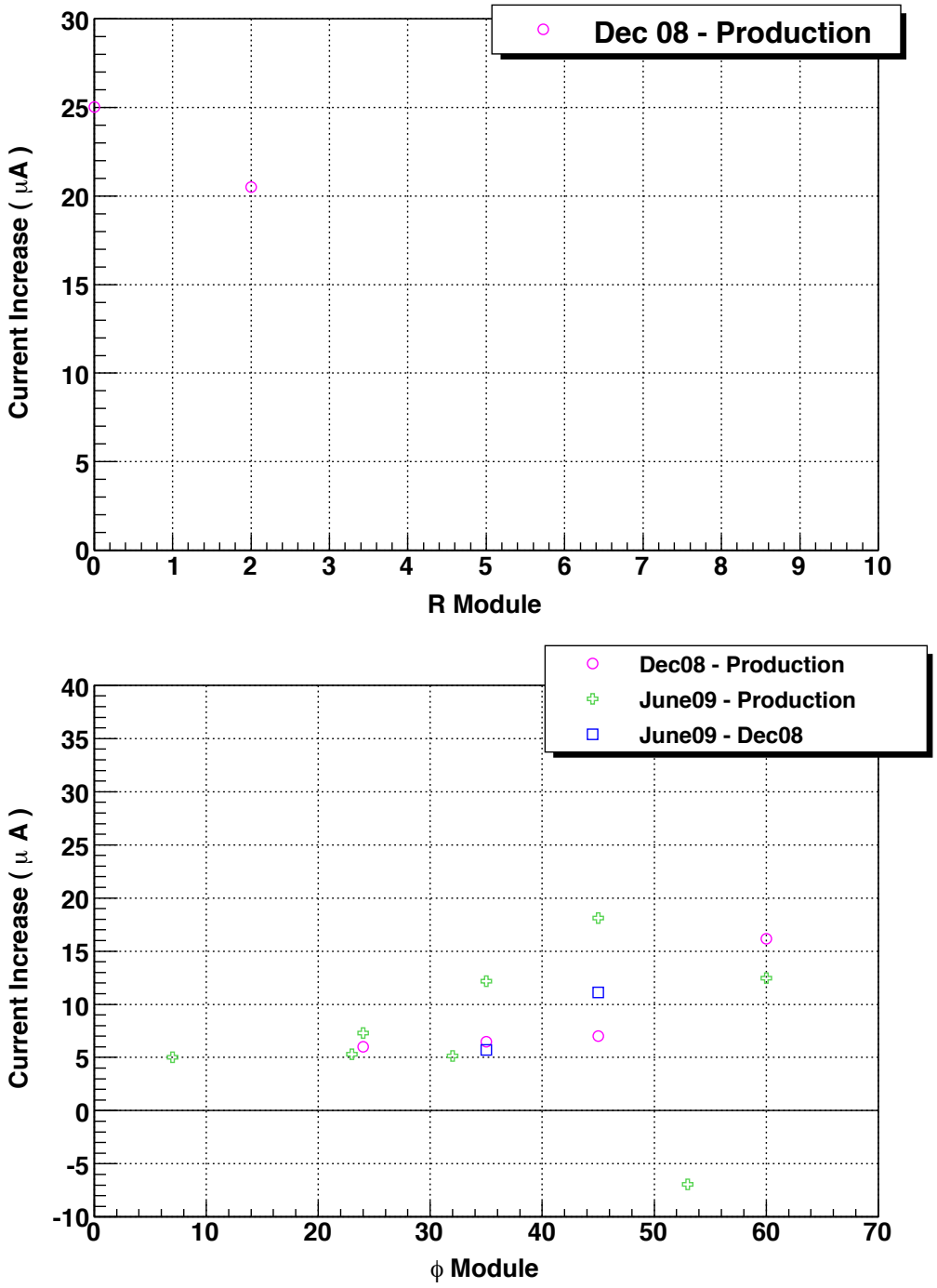

Figure 3.41: *The amount of leakage current increase (or decrease) for the sensors that have shown significant leakage current difference from the three comparisons performed without temperature scaling. Only sensors with leakage currents above 5 μA in any of the data. A-(top) R sensors. B-(bottom) ϕ sensors.*

3.6 Summary

This chapter has provided a detailed description of the VELO high voltage system, both the hardware and the software part have been presented. The hardware includes power supply modules, patch panels and cabling. The software is based on the PVSS control architecture. The designed system meets the LHCb VELO requirements.

The characterisation tests of the high voltage system were also presented and the high voltage system performance was demonstrated. The system noise is found to be sufficiently low, and a range of failure modes have been successfully tested. The tests revealed both hardware and software problems, which have been rectified, and the system is fully operational.

Comparisons of current-voltage characteristics of the VELO sensors were also presented. The leakage current of a number of sensors was found to increase on cooling to -25°C, contrary to expectation. This could be a consequence of stress in the modules and will be monitored. No significant degradation in sensor currents was observed over time.

4 Qualification of p-Type Silicon Strip Sensors for the LHC Upgrades

This chapter presents the qualification of p-type silicon microstrip sensors, with different types of isolation techniques, towards the proposed upgrades of LHCb and other LHC experiments. Characterisations of these detectors were performed before and after irradiations with neutrons and protons. The results obtained are presented in this chapter. Section 4.1 briefly introduces the concept of the LHCb upgrade. Section 4.2 provides the general theory of semiconductors relevant to silicon detectors which includes the effects of radiation on silicon detectors. The characterisation of the p-type silicon detectors studied is given in section 4.3, and their characterisation after irradiation in section 4.4.

4.1 Concept of LHCb Upgrade

LHCb is a heavy flavour physics experiment designed to make precision measurements of CP-violation and rare decays of B-hadrons. In five years of nominal operation LHCb expects to collect an accumulated data sample of 10 fb^{-1} which will allow LHCb to collect a much larger B meson sample than previously available. As presented in [104], continuing running LHCb beyond 10 fb^{-1} without an upgrade will not be overly profitable, since the statistical precision achieved will only increase slowly by running at constant peak luminosity.

LHCb is designed to operate at a LHC luminosity of 2×10^{32} $cm^{-2}s^{-1}$. The LHCb upgrade design luminosity would increase this by a factor of 10 to 2×10^{33} $cm^{-2}s^{-1}$. To fully profit from the increased luminosity in hadronic channels, the full detector has to be read out at 40 MHz event rate, as a displaced vertex trigger is needed. This will require replacement of most front end electronics and a more radiation hard vertex detector.

After five years of operation, either new physics beyond the standard model will have been discovered at the LHC experiments or new physics will be at a higher mass scale. If new particles are discovered, their flavour structure has to be studied to reveal their true nature. If no discoveries are made, precision measurements, sensitive to loop diagrams, are the only probe one has above the direct new particle production TeV scale. For Flavour Changing Neutral Current (FCNC) decays, like $B_d \to K^* \mu^+ \mu^-$ (see chapter 5), with an upgrade of LHCb, one could perform measurements that are highly sensitive to new physics effects. With its current design and luminosity LHCb expects to collect 7200 $B_d \to K^* \mu^+ \mu^-$ events per 2 fb^{-1}. However, with an upgraded LHCb, one expects to collect 360k $B_d \to K^* \mu^+ \mu^-$ events with 100 fb^{-1}.

The LHC has a design luminosity of 10^{34} cm^{-2}s^{-1} and hence no upgrade is required to operate the LHCb upgrade. In the longer term, an upgrade to LHC, the SLHC, is also planned. This will upgrade the luminosity of the LHC by around a factor of 10. The VELO, at a distance of only 8 mm from the beam, will receive a fluence of 10^{15} n$_{\rm eq}$/cm^2 per year, and must withstand 10^{16} n$_{\rm eq}$/cm^2 over the full lifetime. The ATLAS and CMS inner layers at the SLHC will operate at a higher luminosity but be further from the beam. They must also withstand around 10^{16} n$_{\rm eq}$/cm^2.

As part of the research and development towards LHC upgrades, n-on-p microstrip detectors with six different types of isolation techniques have been manufactured for ATLAS by Hamamatsu[1]. This thesis work is focused on characterisation of these detectors before irradiation with Current-Voltage and Capacitance-Voltage characteristics, and after neutron and proton irradiation at different fluences up to 10^{16} n$_{\rm eq}$/cm^2 by Current-Voltage characteristics and Charge Collection measurements. The aim is to find the most radiation hard isolation technique that would suit the LHC upgrade vertex detectors without degrading the detector performances.

The results in this section are also valuable for estimating the lifetime of the current VELO sensor (primarily n-on-n sensors) and the spare replacement sensors (primarily n-on-p). The current detectors will be replaced by the spare system if an accident occurs or after significant radiation damage.

[1]Solid State Division, 1126-1, Ichino-cho, Higashi-ku, Hamamatsu City, Shizuoka Pref., 430-8587, Japan.

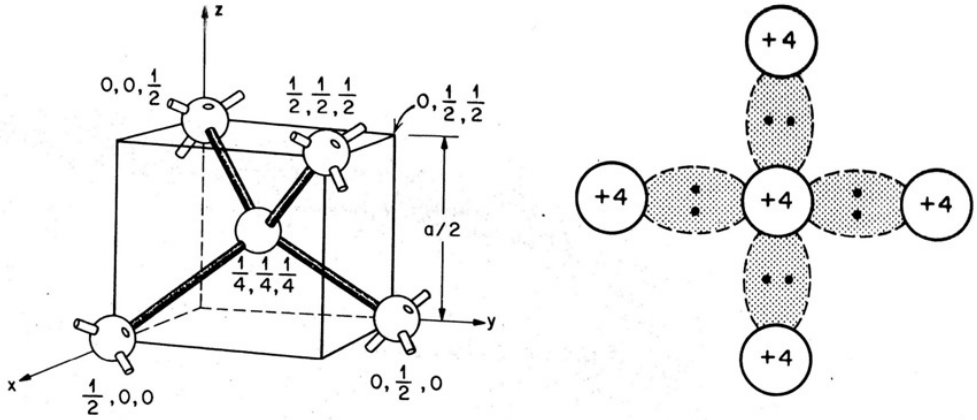

Figure 4.1: *Representation of the atomic structure of silicon. A-(left) The tetrahedral bonding structure. B-(right) The covalent bonding structure. Reproduced from [105].*

4.2 Silicon Detector Theory

4.2.1 General Theory of Semiconductors

Semiconductors are used in many applications especially in microelectronics. They are used for the production of many electronic components such as integrated circuits, diodes and transistors, as well as for tracking detectors for charge particles in high energy physics experiments.

Semiconductors have either a diamond structure like Silicon (Si) and Germanium (Ge), or Zinc blende structure like GaAs. As illustrated in figure 4.1, semiconductors have a tetrahedral bonding structure in which each atom shares its outermost electron, called a valence electron, with its four neighbours to form covalent bonds.

Both insulators and semiconductors have a bandgap structure which is the energy difference between the top of the valence band and the bottom of the conduction band. There is no bandgap in a conductor. As shown in figure 4.2, the bandgap E_g in an insulator is ≈ 9 eV and is ≈ 1 eV in a semiconductor ($E_g \approx 1.12$ eV in silicon).

With thermal excitation, an electron in the valence band may gain enough energy to jump to the conduction band leaving behind a hole. In an intrinsic semiconductor, i.e. one that contains almost no impurity, the electron concentration n and the hole concentration p are equal with

$$n = p = n_i, \tag{4.1}$$

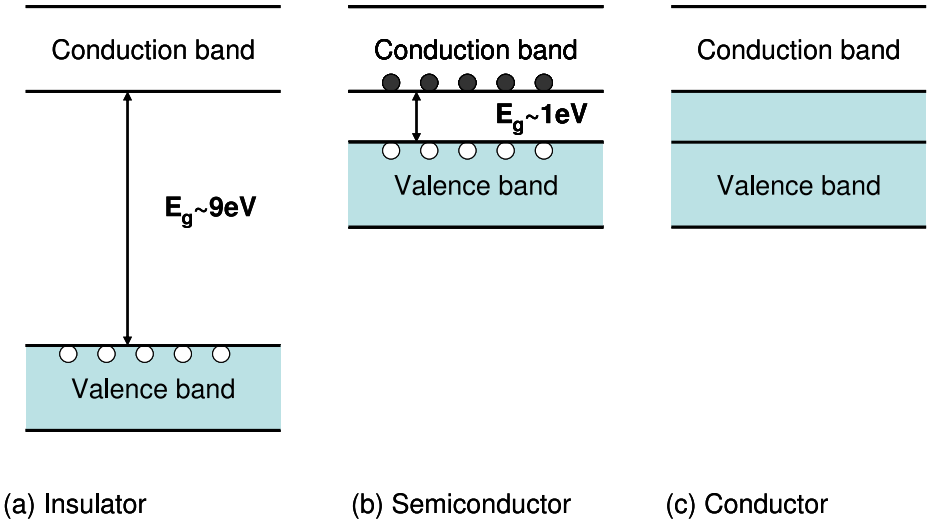

Figure 4.2: *Schematic of the band structures of the three types of materials. (a) Insulator, (b) semiconductor and (c) conductor.*

where n_i is the intrinsic carrier concentration. The value of n_i at a defined temperature can be found by considering the density of states available in the conduction band, and the Fermi-Dirac distribution f(E) which is the probability of a level at energy E to be occupied by an electron. The probability of occupation is 0.5 at the Fermi level E_F. For intrinsic silicon E_F is in the middle of the band gap.

Impurities with five valence electrons like Phosphorus are referred to as donors. Each donor adds an extra free electron that is not involved in the covalent bonds and becomes positively charged. If one has a concentration of N_d donors, such that $N_d \gg n_i$, then

$$N_d = n, \tag{4.2}$$

where n is the concentration of free electrons. This material is referred to as n-type material and the donors act as positive space charges.

Likewise, impurities with three valence electrons such as Boron are referred to as acceptors. Each acceptor creates an electron vacancy, i.e. hole, in the covalent bonds. This hole is virtually free as it may be filled by an electron from a neighbouring atom and the corresponding acceptor becomes negatively charged. For a concentration of N_a acceptors, and $N_a \gg n_i$, then

$$N_a = p, \tag{4.3}$$

where p is the concentration of free holes. The corresponding material is referred to as p-type material and the dopants act as negative space charges. The concentration of

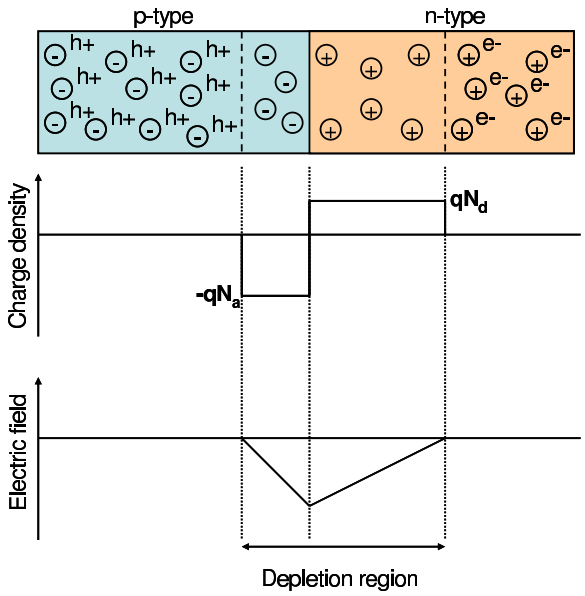

Figure 4.3: *Representation of a p-n junction at thermal equilibrium. The charge distribution and the electric field at the depletion region are shown.*

impurities introduced in a semiconductor material indicates its doping concentration. For p-type doped material, the doping concentration corresponds to the concentration of acceptors introduced to the material.

4.2.1.1 The p-n Junction

Joining a n-type material with a p-type material creates a 'p-n junction', the basic element of almost all electronic devices and tracking detectors in high energy physics. There is diffusion of holes from the p-type side into the n-type and electrons from the n-type to the p-type, driven by the difference in concentration. The recombination of these electrons and holes creates a depleted region with no free carrier concentration as illustrated in figure 4.3. The fixed space charges, indicated in figure 4.3, in the depleted region originate from dopants that have been compensated with the diffused electrons and holes. Hence, an electric field comes from the fixed space charges with the maximum strength being at the p-n junction. The field generates a built-in potential V_{bi} across the depletion region and causes carrier drift in the direction opposite to the diffusion. At thermal equilibrium and without external bias, the net current flow is zero.

Applying an external reverse bias V_R to the p-n junction, where a positive bias is applied to the n-type region and a negative bias to the p-type increases the width

of the depletion region. Since V_{bi} and V_R have the same polarity, electrons in the n-type region and holes in the p-type region will be attracted away from the edges of the depletion region, increasing the width of the region with uncompensated space charges. The total potential difference across the junction will be $(V_{bi} + V_R)$. The width of the depleted region x_d is given by [106]

$$x_d = \sqrt{\frac{2\epsilon_s(N_a + N_d)}{qN_aN_d}(V_{bi} + V_R)}, \tag{4.4}$$

with,

$$V_{bi} = \frac{kT}{q} ln \frac{N_aN_d}{n_i^2}, \tag{4.5}$$

where q is the elementary charge and ϵ_s the permittivity of the semiconductor material.

Since there are equal concentrations of positive and negative space charges at the depletion region, respectively Q and $-Q$, if the doping concentrations are different the depletion region will grow further into the lightly-doped region. For example, if $N_d \gg N_a$, under reverse bias the depletion will extend from the p-type into the n-type region, and the width of the depletion region is proportional to $\sqrt{V_R/N_a}$ with $V_R \gg V_{bi}$ ($V_{bi} \approx 0.6$ V for silicon). Since $C = dQ/dV$, the capacitance C of the depleted p-n junction per unit area depends on the width of the depletion region with

$$C = A\frac{\epsilon_s}{x_d}, \tag{4.6}$$

where A is the area of the semiconductor material.

Silicon detectors are operated in reverse bias mode. The depletion region corresponds to its active region. Hence, to deplete the full volume of the detector, a minimum reverse bias voltage V_{FD} has to be applied at the p-n junction. V_{FD} is called the 'full depletion voltage' and in this case x_d of equation 4.4 corresponds to the thickness of the detector.

Replacing the expression of x_d in equation 4.4 into equation 4.6, the capacitance-voltage characteristic CV or $1/C^2$ versus voltages is given by

$$\frac{1}{C^2} = \frac{2(N_a + N_d)}{qA^2\epsilon_s N_aN_d}(V_{bi} + V_R), \tag{4.7}$$

which is the standard relation used to determine the full depletion voltage V_{FD}. Results obtained by using this relation are presented in section 4.3.3.

4.2.1.2 Signal Generation

The generation of signal in silicon tracking detectors is discussed in this section. More details of the description of semiconductors and their application can be found in many text books such as [106] and [89].

Silicon detectors use the properties of the p-n junction (see section 4.2.1.1). Consider a p-on-n silicon strip detector, also called an n-type detector, as illustrated in figure 4.4, with heavily doped p-type implants (p^+) and an n-type lightly doped bulk. Typical doping concentrations for bulk and implants are respectively of order 10^{12} cm^{-3} and 10^{18} cm^{-3}. Under reverse bias, the depletion region grows from the p^+ side to the n-type side. When high energy particles traverse the detectors, they deposit energy that can excite electrons from the valence band to the conduction band, creating free electron-hole pairs. Charges created in the depletion region can be collected. There is no field in the non-depleted region. Hence, no signal is generated in that region.

Due to the electric field the electrons created at the depletion region are drifted to the n^+ implants and the holes to the p^+ implants. Since they are charged, as they drift through the detector their field will induce a measurable signal. The carriers generated may often be shared between multiple implants. Charge spread between several strips increases the resolution but decreases the signal to noise ratio. Charge sharing increases in thicker detectors and decreases with bias voltage. The integrated collected charges correspond to the energy deposited by the particles.

4.2.1.3 Electrical Breakdown

Electrical breakdown occurs when the field at the p-n junction is high enough to allow the creation of new electron-hole pairs from collisions between the free electron (hole) with the lattice atoms. The produced charge carriers then repeat this process. This phenomenon is known as avalanche multiplication or 'hard breakdown' and is characterised by a sudden transition to high leakage current under reverse-bias in silicon detectors. The reverse-bias voltage at which the avalanche multiplication starts is called the 'Breakdown Voltage'

The breakdown effect is temperature dependent since scattering occurs due to the thermal displacement of the atoms from the ideal lattice. It depends also on crystal defects, for instance lattice distortion near the surface. The breakdown effect is therefore dependent both on the design of the detector and the environment in which the detector is operated. It differs also from one detector to another since it depends on defects and imperfection within the detector. In particular, the exposure of the de-

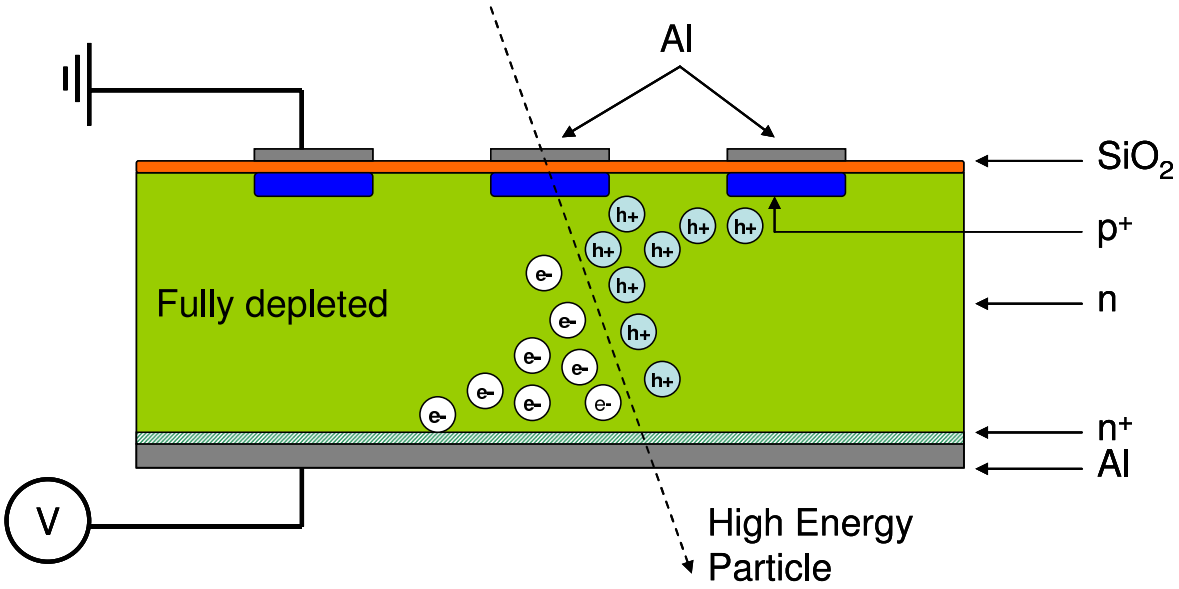

Figure 4.4: *Illustration of a fully depleted p-on-n microstrip detector traversed by high energy particles.*

tector to intense radiation may change both the surface and bulk material properties drastically. The breakdown voltages were identified for each detector characterised in this thesis (see section 4.3.2 and 4.4.2).

4.2.1.4 SiO_2 Protection and AC Coupling

Silicon micro strip detectors require a passivating layer to protect the silicon detector surface. SiO_2 is mostly used for this purpose as it establishes a well-controlled termination of the dangling bonds where the crystal lattice is truncated during fabrication.

Another layer of SiO_2 is grown between the implant and the aluminium strip which decouples the implant from the front-end electronics, called AC-coupling. This shielding of the readout electronics is a protection against leakage current from the sensor which can, for instance, lead to a pedestal[2] shift.

4.2.2 Radiation Damage

For the application of silicon detectors in high energy physics as position sensitive detectors, one has to take into account radiation damage due to high charged particle

[2]The pedestal refers to the level of the zero signal of each readout chip channel. Since the electronics on each readout chip channel are not perfectly identical, the pedestals may vary between channels.

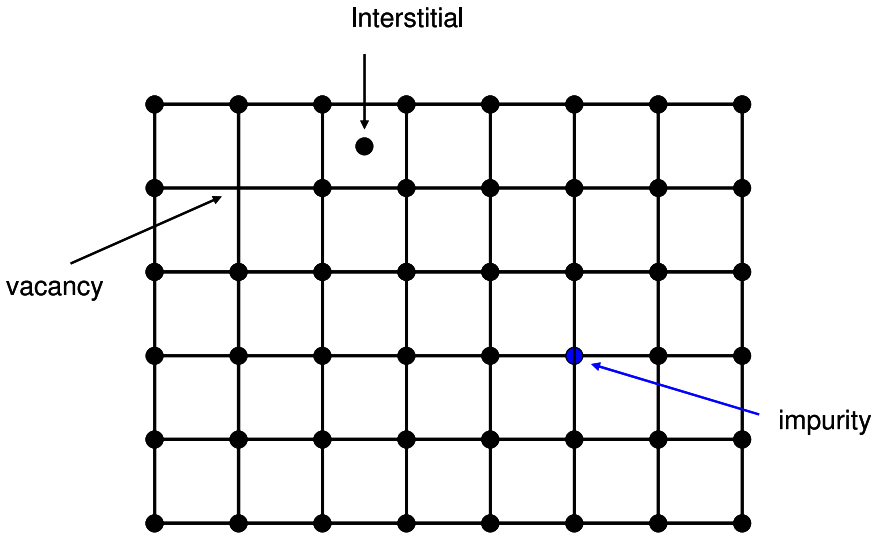

Figure 4.5: *Representation of different types of defects in the lattice.*

fluxes passing through the detectors. Radiation induces changes to the properties of the detector that manifest in changes of the sensor parameters like leakage current, depletion voltage and charge collection efficiency.

More specifically, macroscopic changes are due to microscopic changes within the silicon itself, which are dependent on the type of radiation. In this section, the radiation induced damage in both the bulk and the surface of a detector will be considered. A detailed description of radiation damage effects can be found in [89, 107].

4.2.2.1 Radiation Damage in the Bulk Material

When high energy particles traverse the detector, they excite electron-hole pairs and interact with the atoms via the electromagnetic and strong forces. The displaced atoms create interstitials and vacancies as shown in figure 4.5. These deviations from the crystal symmetry are called 'defects'. A localised empty site in the atom lattice is known as a 'point defect', whereas a group of a few adjacent point defects forms a 'defect cluster'.

By diffusion, they move and can then combine with impurity atoms like oxygen, phosphorus or carbon to create new levels, which change the initial silicon properties. The induced macroscopic effects are an increase of leakage current, change of depletion voltage and a decrease of charge collection efficiency.

Defects close to the Fermi level are constantly produced during radiation. At mid-bandgap their presence induces the creation of electron-hole pairs that increase the leakage currents. The leakage current is the radiation induced leakage current presented

in section 3.3.1.1.1, and its proportionality to the fluence is given by equation 3.1.

Defects can act as acceptors or donors and hence change the effective doping concentration. Radiation induces changes to the effective doping concentration. The full depletion voltage is proportional to the effective doping concentration. The change in effective doping concentration is due to the introduction of acceptor levels by radiation damage. Microscopic defects interact with each other, which can enhance or suppress this effect over time. This is called annealing. The annealing is highly temperature dependent and has two components, the short time (beneficial) annealing and the reverse annealing (see section 3.3.1.1.2). Therefore, with increasing radiation, an n-type bulk silicon becomes p-type after type inversion, whereas a p-type bulk silicon will become more p-type. Before type inversion the effective doping concentration of the n-type bulk silicon decreases due to the introduction of acceptor levels, hence the full depletion voltage decreases. It goes through the point of intrinsic silicon and the n-type becomes p-type and the depletion voltage goes up again. Further details can be found in [108]. On the other hand, for the p-type bulk the effective doping concentration increases with radiation which induces a full depletion voltage increase.

Due to radiation, defects may combine with impurities which create vacancies that act as traps for mobile charge carriers. Since electron-hole pairs are created when high energy particles traverse the detectors, part of the produced mobile charge carriers may be trapped and will not arrive to the collecting electrodes. Thus, radiation induced trapping causes a degradation of charge collection efficiency.

4.2.2.2 Strip Isolation

In general, a grown oxide contains charge which is left from manufacturing. In SiO_2, the charge is usually positive and is due to holes trapped in defect sites. The defect concentration is higher in the vicinity of the Si - SiO_2 interface which gives rise to the presence of more positive space charges at that region. Hence, the Si - SiO_2 interface is intrinsically positively charged. This will attract electrons to form an accumulation layer that will short the strips without isolation.

For n^+ read out detectors, specifically for n-on-p detectors, strip isolation is therefore needed. It prevents short-circuits between neighbouring strips due to the electron accumulation layer.

The isolation is achieved by depositing a p^+ layer surrounding each n^+-strip called 'p-stops'. The p^+ implants are necessary to break the electron accumulation layer at the Si - SiO_2 boundary. Another method of isolation, called 'p-spray', consists of an

uniform layer of p-dopants spread over the full detector area.

Combinations of the p-stop and p-spray technologies were used as isolation techniques and were manufactured in six types [109]. In this thesis, only p-type detectors manufactured with four of them were studied. Figure 4.6 presents the configuration of the four types of isolation techniques that were studied. Type 1 has no p-stop technology, in this case the mask was processed with p-spray technology to achieve the isolation. Type 3 has 'common p-stops', Type 4 'individual p-stops with DC field plate' and Type 6 has 'AC-field plate'.

Electrical characterisation of silicon pixel detectors has shown that detectors with p-spray isolation are more radiation hard than those with p-stops at a fluence of 4.3×10^{14} n_{eq}/cm^2 [110], which is equivalent to approximately three nominal years of operation of LHCb. Alternative isolation techniques utilize field plates made of polysilicon either integrated within the p-stop implant (DC field plate) or deposited on top of the insulator oxide (AC field plate) [111]. The p-stop with DC field plate was found to be more resistant against microdischarges at the p-stop edges [112]. For a detector with AC field plates, the polysilicon potential can be controlled externally to remove the electron accumulation by employing the Metal Oxide Semiconductor (MOS) effect [111]. In this study the AC field plates were left floating.

Two different layouts of p-stop isolation were used: individual and common p-stops. For the individual p-stops there is a p^+-implant around each n^+ strip. For the common p-stop, there is a continuous p^+-implant in between the strips. The common p-stop has the advantage of being compact and simple. However, the existence of the single electrically floating conductor around the detector could change the potentials at different points leading to high leakage currents or earlier breakdown. On the other hand the individual p-stop is more protected against such behaviour but requires further processing which increases the cost of the detector.

4.2.2.3 Radiation Damage in the Detector Surface

Radiation damage at the surface of the detector is caused by ionisation of penetrating particles in the SiO_2. Macroscopically, it manifests itself in several ways such as increases of the surface leakage current, the full depletion voltage and interstrip capacitance.

As discussed in section 4.2.2.2, SiO_2 has built-in positive space charges. The induced radiation damage to the surface leads to the creation of additional positive charges in the SiO_2 layer and the introduction of surface generation centres, which are respon-

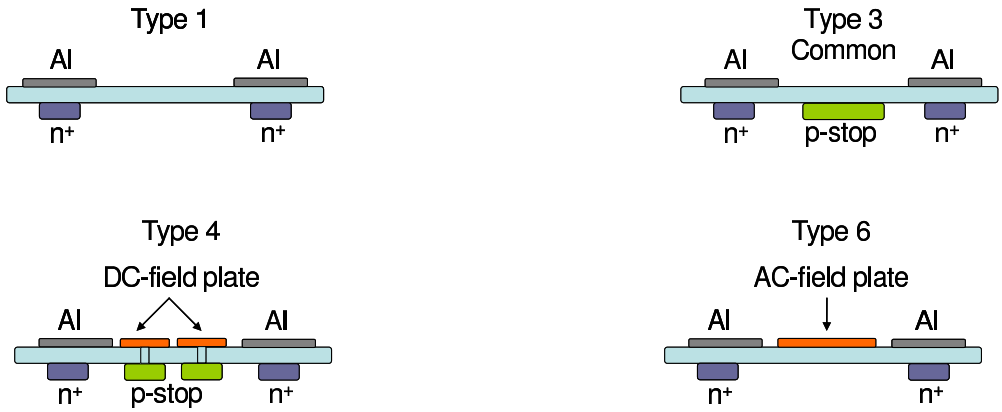

Figure 4.6: *Illustration of the four types of isolation studied.*

sible for the increase of the surface current. The accumulated positive oxide charges underneath the implants increases and attracts more free electrons. The space charge region extends and prevents the electric field from penetrating the detector bulk unless higher bias voltages are applied. Hence, the full depletion voltage increases. Another effect due to radiation damage is the increase of interstrip capacitances, and hence the detector noise, which also depends on the strip geometry and diminishes for narrower strips or wider pitches.

Radiation induced by ionising particles in silicon microstrip detectors depends crucially on the material properties such as the silicon orientation and the oxide quality. Since the oxide charge buildup saturates once the semi-permanent traps in the oxide are filled, it has been observed [113] that the initially increased surface current saturates at around 3-5 MRad with a value of $\Delta I_{ox}/area \approx 2\ \mu\mathrm{A/cm}^2$.

4.3 Study of Non-Irradiated p-Type Silicon Strip Sensors

4.3.1 The Sensors Tested

Each detector tested was a p-type silicon strip sensor, which has one of the four isolation techniques defined in section 4.2.2.2 labelled Type 1, Type 3, Type 4 and Type 6. As illustrated in figure 4.7, a p-type strip detector consists of p-type bulk and backplane, and n^+ readout strips with strip isolation (p-spray in that figure).

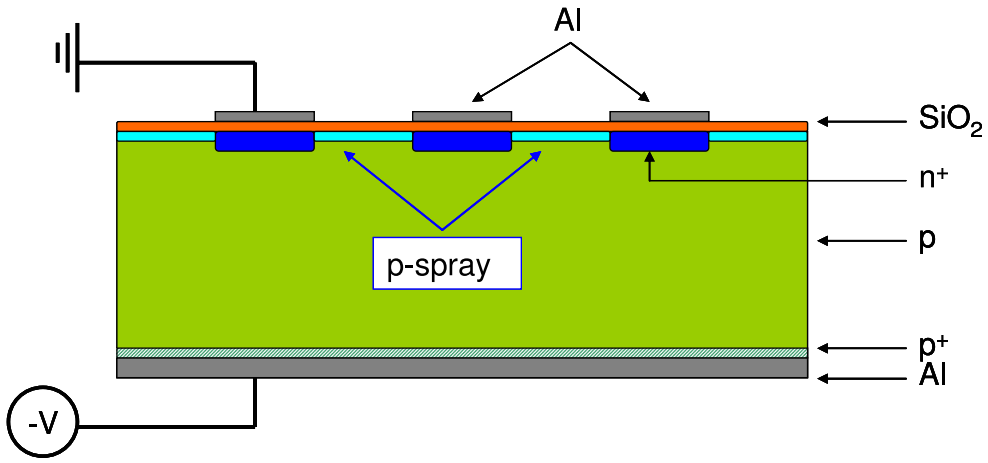

Figure 4.7: *Schematic of a p-type strip detector. Only the p-spray technology is shown in this figure to illustrate the presence of strip isolation.*

Ten non-irradiated detectors were tested in Glasgow by the author and a further nineteen non-irradiated p-type detectors tested at the University of Liverpool laboratory, were included in the analysis.

4.3.2 Pre-Irradiated Current-Voltage Characteristics and Breakdown Voltages

Before irradiation the current drawn by each p-type microstrip detector under different reverse bias voltages was measured, giving their Current-Voltage (IV) characteristics. The IV characteristic is a probe of any abnormal behaviour of the detector, and allows to determine its breakdown voltage (see section 4.2.1.3).

A Cascade Microtech probe station was used to take the IV characteristics of all detectors. Two needles of the probe station were used to make contact with the metal pads on the detector's surface. One needle made contact to the guard ring and another the strips via the bias rail so that all strips were at the same potential. Both needles were connected to the HV Ground of the HV power supply.

A metal chuck provided a contact to the backplane of the detector, which was connected to the HV bias of the power supply. Hence the measured current corresponds to the current drawn between the strips and the backplane. The required reverse bias voltage was supplied by a Keithley 237, which measured also the current flow for every applied voltage. Reverse-bias voltages up to 1000 V were applied to the detectors.

The combined Glasgow and Liverpool results were divided per type of isolation technique, and the breakdown voltages were identified for each of them. The detectors tested in Glasgow and Liverpool are labelled in Table 4.1.

Figures 4.8A, 4.9A, 4.10A and 4.11A present respectively the IV characteristics of the Type 1, Type 3, Type 4 and Type 6 detectors. No abnormal behaviour was observed on any of the detectors. Their IV characteristics show the rapid increase of current as the detectors deplete, and the curves flattened off after full depletion. Then, an exponential increase of current occurs when the detectors breakdown.

Table 4.1 presents the observed breakdown voltages and the calculated full depletion voltages (see section 4.3.3) of all detectors. The breakdown voltages were found as the voltage where the leakage current increased by 30 %. The nominal current increase before breakdown was in the order of 5%. A summary of the breakdown characteristics per type are presented in Table 4.2. For each Type the fraction of the detectors with breakdown voltage above 1000 V, the average breakdown voltage and the lowest breakdown voltage are shown.

All types present detectors with breakdown voltages above 1000 V except Type 4 which only consisted of two detectors. No significant difference between the four types was observed with the available statistics. Hence, the recommendation would be to go for Type 1 as it has the simplest design and lowest production cost.

4.3.3 Pre-Irradiated Current-Capacitance Measurements and Full Depletion Voltages

Like the IV measurements, the Capacitance-Voltage (CV) measurements were performed using the probe station needles in order to make contact to the metal pads of the detectors, and the chuck to the backplane contact. The needles position (see section 4.3.2) remained unchanged. The capacitances were therefore measured from the strips to the backplane. The Keithley 237 was again used to supply bias voltages to the detectors. An Agilent 4284 LCR meter was used for the capacitance measurements. To protect the LCR meter the bias voltages were limited up to 350 V in Glasgow. The frequency used for the capacitance measurement was 10 kHz.

For strip detectors the variation of the depletion behaviour is indicated by the change in the capacitance as a function of bias voltages. As indicated from equation 4.7, the relation between the capacitance and the bias voltage allows to determine the full depletion voltages, by plotting $1/C^2$ as a function of the applied voltages. The full depletion behaviour corresponds to the plateau in the capacitance curve.

Type	Detectors	Breakdown voltage	Full depletion voltage	Site
Type 1	BZ1-P07-0	960 V	$\approx$ 174 V	Glasgow
	BZ1-P07-1	980 V	$\approx$ 171 V	
	W01-BZ1-P07	800 V	$\approx$ 168 V	Liverpool
	W03-BZ1-P07	$>$ 1000 V	$\approx$ 166 V	
	W06-BZ1-P07	$>$ 1000 V	$\approx$ 170 V	
	W24-BZ1-P19	200 V	$\approx$ 168 V	
	W27-BZ1-P19	640 V	$\approx$ 156 V	
	W29-BZ1-P19	$>$ 1000 V	$\approx$ 152 V	
Type 3	BZ3-P09-0	$>$ 1000 V	$\approx$ 163 V	Glasgow
	BZ3-P09-1	$>$ 1000 V	$\approx$ 164 V	
	BZ3-P15-0	$>$ 1000 V	$\approx$ 182 V	
	BZ3-P01-0	850 V	$\approx$ 175 V	
	W01-BZ3-P03	670 V	$\approx$ 173 V	Liverpool
	W06-BZ3-P06	$>$ 1000 V	$\approx$ 180 V	
	W09-BZ3-P03	570 V	$\approx$ 177 V	
	W11-BZ3-P09	$>$ 1000 V	$\approx$ 180 V	
	W23-BZ3-P03	530 V	$\approx$ 162 V	
	W24-BZ3-P21	290 V	$\approx$ 163 V	
	W26-BZ3-P15	580 V	$\approx$ 175 V	
Type 4	BZ4-P10-1	580 V	$\approx$ 162 V	Glasgow
	BZ4-P10-0	470 V	$\approx$ 176 V	
Type 6	BZ6-P24-0	970 V	$\approx$ 175 V	Glasgow
	BZ6-P12-0	580 V	$\approx$ 209 V	
	W01-BZ6-P12	720 V	$\approx$ 195 V	Liverpool
	W06-BZ6-P12	400 V	$\approx$ 201 V	
	W09-BZ6-P12	720 V	$\approx$ 203 V	
	W23-BZ6-P24	$>$ 1000 V	$\approx$ 168 V	
	W24-BZ6-P24	950 V	$\approx$ 174 V	
	W26-BZ6-P24	$>$ 1000 V	$\approx$ 172 V	

Table 4.1: *Comparison of the breakdown voltages and full depletion voltages per type and per non-irradiated detector.*

	Breakdown Voltage above 1000 V	Average Breakdown Voltage	Lowest Breakdown Voltage
Type 1	3/8	820 V	200 V
Type 3	5/11	712 V	290 V
Type 4	0/2	525 V	470 V
Type 6	2/8	792 V	400 V

Table 4.2: *Breakdown characteristics per Type: fraction of the detectors with breakdown higher than 1000* V *and average breakdown voltage.*

As from the IV characteristics, all detectors CV measurements were combined and separated by their type of isolation. Figure 4.8B, 4.9B, 4.10B, 4.11B show respectively the CV characteristics of the Type 1, Type 3, Type 4 and Type 6 detectors. All detectors present the expected full depletion behaviour, which was limited by their breakdown voltages (or 350 V in the Glasgow setup).

The full depletion voltage of each detector was computed by determining the intersection of two linear fits of the data, before the full depletion behaviour and under full depletion. Based on the common observed behaviour of the CV characteristics of all detectors, two bias voltages intervals were chosen. The first bias voltage interval, before full depletion, was between 80 V and 150 V. The second bias interval, under full depletion, was between 200 V and 300 V. Table 4.1 presents the computed full depletion voltages of all detectors, which were classified by type. To illustrate this method, the linear fits of the CV characteristics of the two Type 4 detectors are shown in Figure 4.10B. The two blue lines correspond to the fits for BZ4-P10-1 and the black lines for that of BZ4-P10-0.

No depletion voltage dependence on the isolation technique was observed before irradiation, as expected. As discussed in section 3.3.1.1.2, the depletion voltage is proportional to the effective doping concentration which is inversely proportional to the resistivity of the silicon before irradiation. Hence, it depends on the quality of the wafer. The average full depletion voltages were approximately 165 V, 172 V, 169 V and 187 V for Type 1, Type 3, Type 4 and Type 6 respectively. Type 6 detectors have shown the highest full depletion voltage of 200 V which was not so much larger than the lowest full depletion voltage of 152 V for Type 1 detectors.

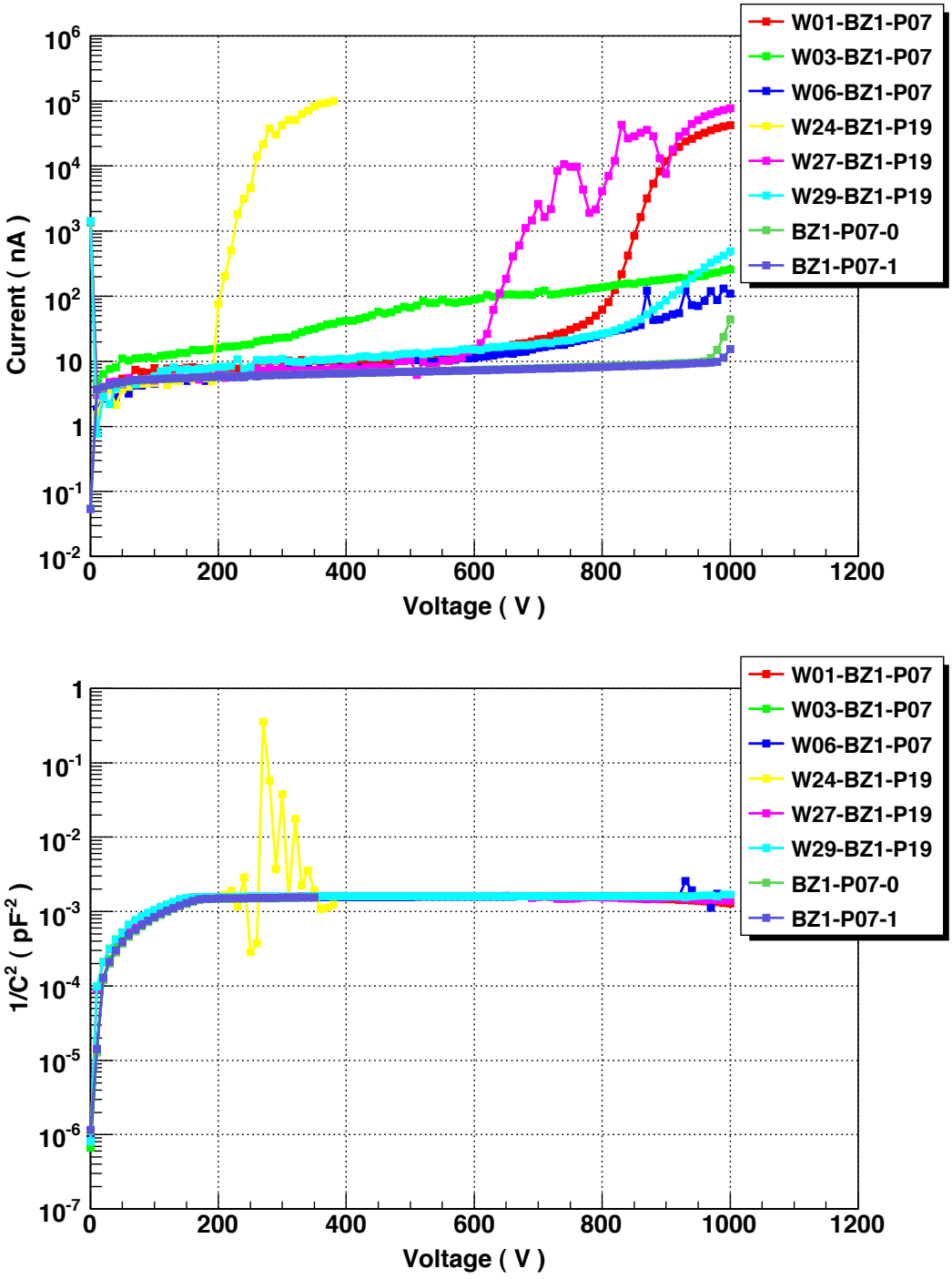

Figure 4.8: *Characteristics of the Type 1 detectors before irradiation. A-(top) Current-Voltage characteristics. B-(bottom) Capacitance-Voltage characteristics.*

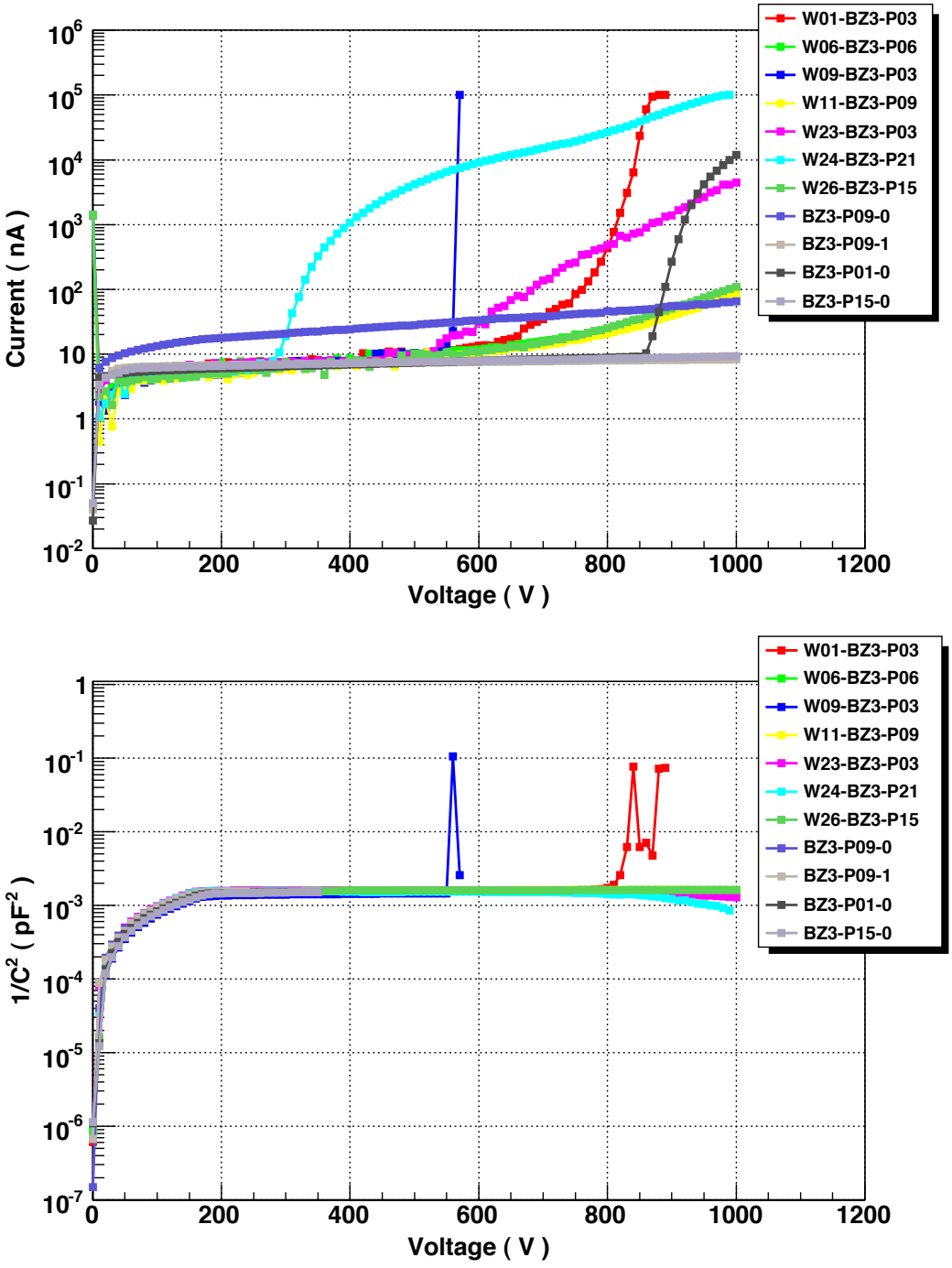

Figure 4.9: *Characteristics of the Type 3 detectors before irradiation. A-(top) Current-Voltage characteristics. B-(bottom) Capacitance-Voltage characteristics.*

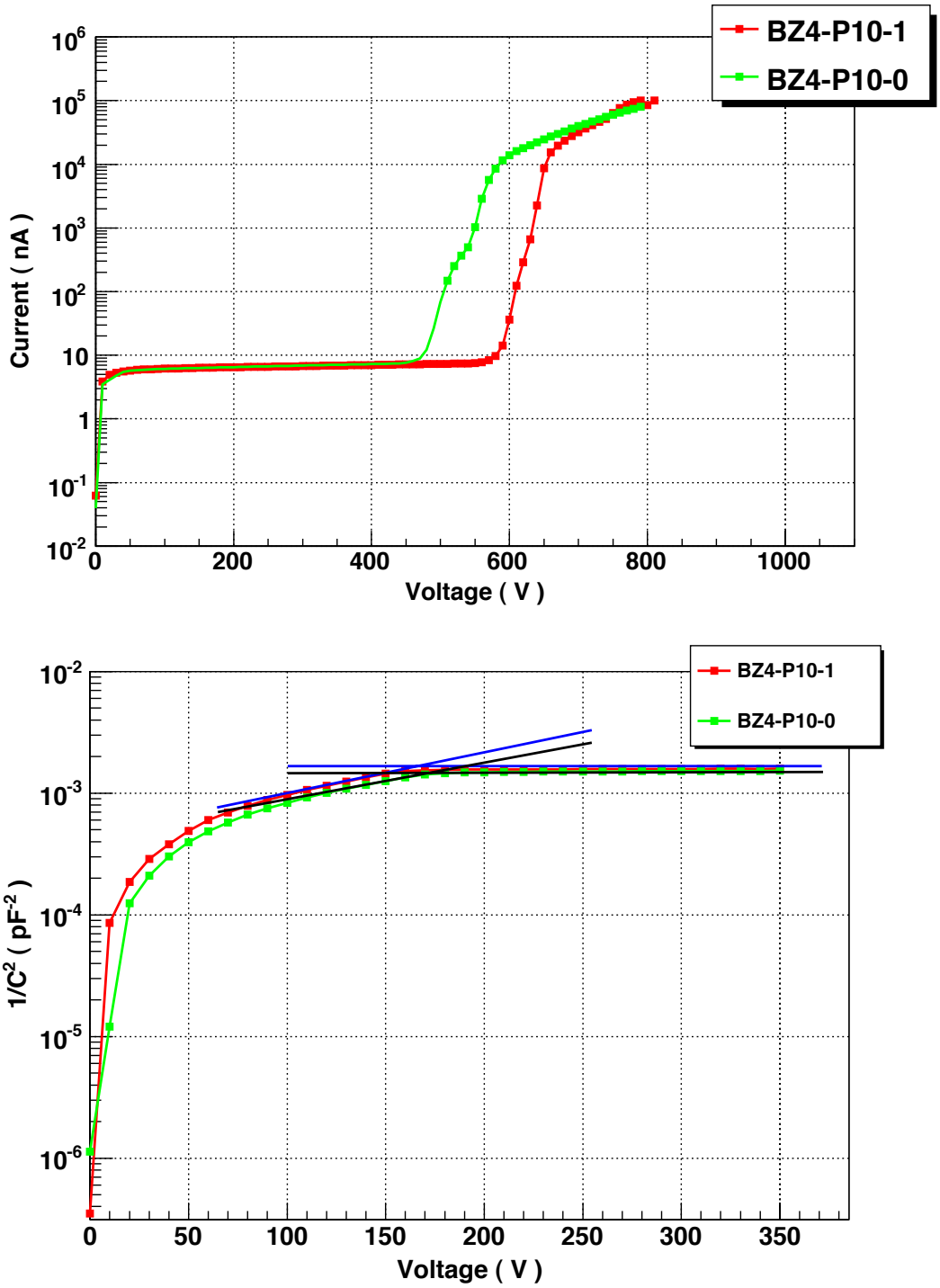

Figure 4.10: *Characteristics of the Type 4 detectors before irradiation. A-(top) Current-Voltage characteristics. B-(bottom) Capacitance-Voltage characteristics. The linear fits for the extraction of the full depletion voltages are shown. The blue and black lines correspond respectively to the fit of the CV characteristics of BZ4-P10-1 and BZ4-P10-0.*

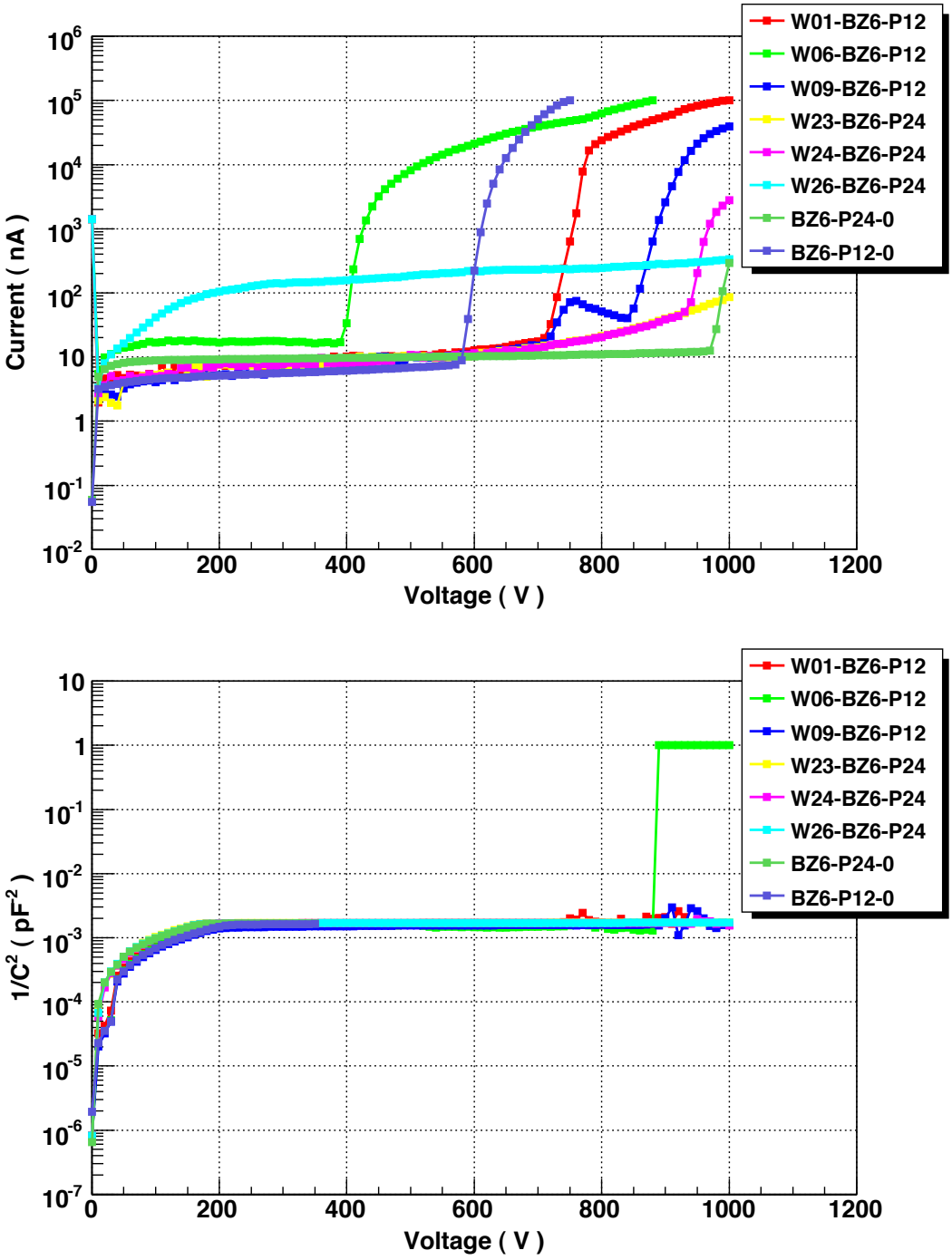

Figure 4.11: *Characteristics of the Type 6 detectors before irradiation. A-(top) Current-Voltage characteristics. B-(bottom) Capacitance-Voltage characteristics.*

4.3.4 Conclusion

This section has presented the IV and CV characterisation of the ten detectors tested in Glasgow. Additional IV-CV characteristics from 19 detectors tested in Liverpool were added in order to increase the statistics per isolation technique category. All detectors have shown normal behaviour and their breakdown voltages and full depletion voltages were identified for each of them. Breakdown voltages above 1000 V were observed from each type of isolation apart from the Type 4. As expected no dependence on the type of isolation technique was observed from the computed full depletion voltages of the detectors. The depletion voltage had an average of approximately 170 V.

From this we conclude that no significant difference in behaviour was observed between isolation technique for the unirradiated detectors. Hence, at this point, there would be a preference for Type 1 which has the simplest design and hence lowest production cost. Before irradiation, previous research and development studies investigating p-type wafers [114–117] have not observed any significant difference in performance of the detectors regardless of the type of isolation employed. The largest difference in isolation would only appear after irradiation, which changes the electrical properties of the detectors as discussed in section 4.2.2. The latter will be discussed further in the next section.

4.4 Study of Irradiated p-Type Silicon Strip Detectors

In addition to the characterisation of the p-type silicon strip detectors before irradiation, their characterisation after different doses of irradiation was performed. Five detectors were characterised after irradiation with either high energy protons or neutrons. The detectors were irradiated with neutrons at the Nuclear Research reactor of neutrons in Ljubljana and with protons in KEK Japan. Table 4.3 provides information on each of these five detectors, it includes their type of isolation, their respective fluence as well as the corresponding irradiated particle.

Their characterisation consisted of taking IV characteristics to determine their high voltage behaviour and their breakdown voltages after a certain dose of irradiation (see section 4.4.2), and measuring their charge collection efficiency by gradually increasing the supplied bias voltage (see section 4.4.4). For these purposes, an experimental setup was built at the detector development laboratory in Glasgow which is described in detail in section 4.4.1.

Fluence [n_{eq}/cm^2]	Type of isolation	Detector	Irradiated Particles
5×10^{14}	Type 3	W06-BZ3-P06	proton
2×10^{15}	Type 1	W13-BZ1-P07	neutron
	Type 3	W13-BZ3-P01	neutron
5×10^{15}	Type 4	W06-BZ4-P10	neutron
10^{16}	Type 3	W09-BZ3-P15	neutron

Table 4.3: *The five irradiated detectors characterised.*

4.4.1 Experimental Setup

To measure the charge collected by individual irradiated p-type microstrip detectors, an experimental setup was installed in the laboratory. As shown in figure 4.12, the setup used an Alibava system [118] as data acquisition system, a freezer to keep the detectors at low temperature ($\approx$ -20°C) and a data acquisition PC.

The Alibava system is a portable data acquisition system which consists of a mother board and a daughter board interlinked with a multicore data cable. The daughter board contains two Beetle chips [71], with 128 channels each and a sampling frequency of 40 MHz. It also holds the detector to be tested. The mother board processes the external trigger signal and the analogue data from the Beetle chips by means of an FPGA. It establishes the communication with the data acquisition PC via an USB port.

The setup was organised as follows. The p-type detector to be tested was mounted on the Alibava daughter board, as shown in figure 4.13. Each of its 104 strips are bonded to pitch adapters, which are also bonded to channels of the Beetle chip. The 14 remaining channels of the Beetle chip were left unbonded and were masked out during the data analysis. The whole daughter board is placed inside a freezer. The zoom of the installation is shown in the bottom left photograph of figure 4.12. As viewed from that photograph, a source of Beta particles, Strontium 90 (^{90}Sr), was placed perpendicularly to the daughter board so that the flux of Beta particles will traverse the detector under test. A scintillator connected to a photomultiplier tube (PMT) was placed underneath the detector to generate a trigger signal when Beta particles reach the scintillator.

The system composed of the scintillator connected to the photomultiplier tube, the ^{90}Sr source and the detector, provides the lower threshold of the Beta energy that will reach the scintillator. In addition, to avoid external photons biasing the results, the whole setup was properly protected against external light.

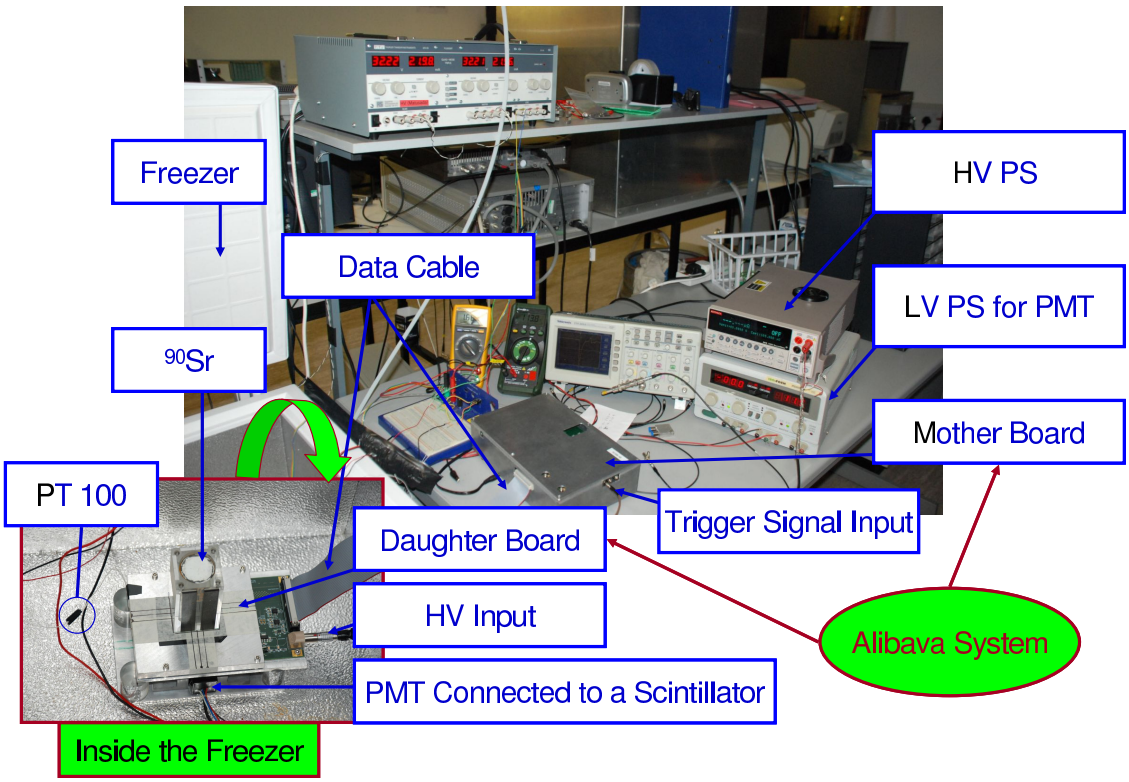

Figure 4.12: *Photographs of the experimental setup installed at the detector development laboratory for charge collection measurements.*

The high voltage was supplied by a Keithley 2410 through cables to the daughter board input by a LEMO connector. The multicore data cable connected between the Alibava daughter board and mother board transmits the data and supplies the required low voltage to the Beetle circuitry. An external low voltage power supply provides the 11.5 V required for the PMT.

The ^{90}Sr source was used as it produces Beta particles with a spectrum of energies up to 2.83 MeV. The high energy part of the spectrum approximates Minimum Ionising Particles (MIPs) [119]. These Beta particles generate on average 80 electron-pairs per micron along their path in the detector. Low energy particles emitted by the ^{90}Sr are stopped by the detector and do not generate a signal in the scintillator. In order to obtain a narrower beam of Beta particles, a collimator was placed between the ^{90}Sr and the detector. To ensure a good trigger signal and a flux of Beta particles traversing the detector, both the ^{90}Sr and the detector were properly aligned with the scintillator.

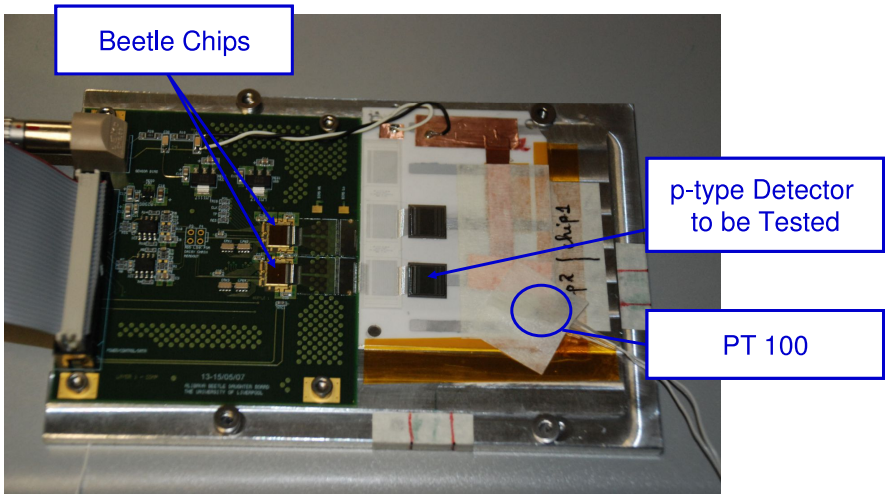

Figure 4.13: *Photograph of a daughter board part of the Alibava system which contains two Beetle chips. Two p-type detectors are shown but only one was connected to a Beetle chip.*

4.4.2 Post-Irradiated Current-Voltage Characteristics and Breakdown Voltages

To measure the IV characteristics of the five irradiated detectors, only part of the experimental setup described in section 4.4.1 was employed. It consisted of the Keithley 2410 to supply bias voltages and to measure the drawn current, the daughter board which holds the detector and provides the HV connection to the detector, and finally the freezer which has kept the detector at $\approx$ -20°C during measurements.

Figure 4.14 presents the IV characteristics of the five irradiated detectors tested. The current measurements were stopped once the breakdown voltages were reached. Since the IV measurement temperatures were not identical, the measured currents were scaled to -20°C using the temperature correction function of equation 3.18.

Table 4.4 presents the leakage current measurements at 500 V from these detectors before and after their respective irradiation dose. Before irradiation the currents were taken at $\approx$20°C. The measured current values after the irradiation of the detectors were scaled to -20°C instead of 20°C. These difficulties in scaling over large temperature difference was discussed in section 3.5.2.2 when studying the IV characteristics of the VELO sensors. As expected irradiation has induced an increase of leakage current on all five detectors, regardless of their type of isolation, which increases as a function of fluence (see section 3.3.1.1). Although the leakage currents were not scaled to the same temperature, the increases are obvious from the current of the order of nA before

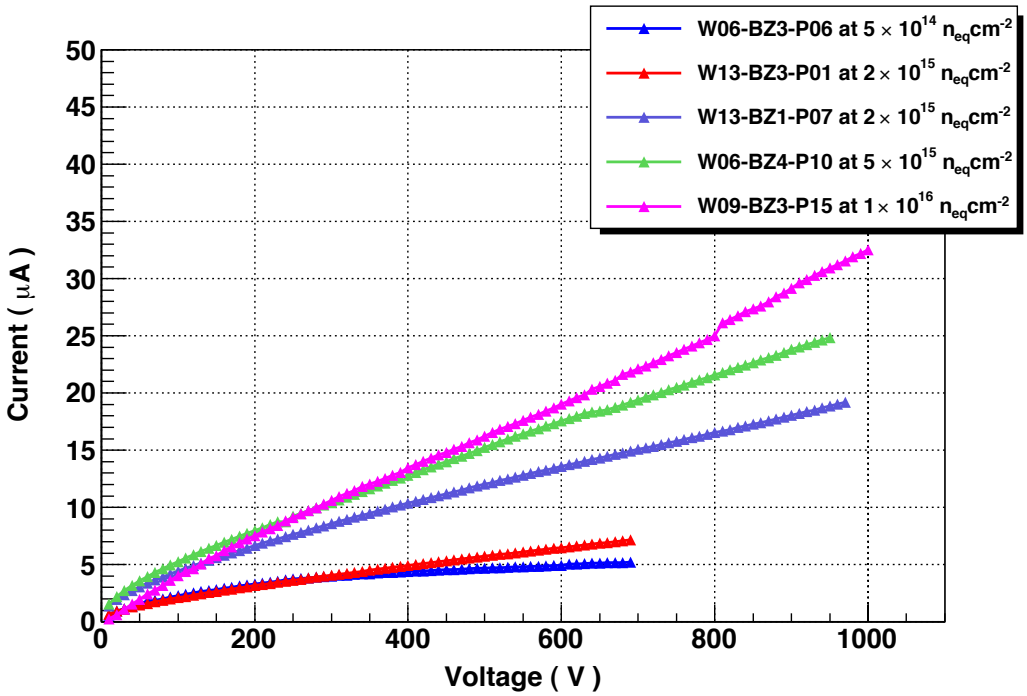

Figure 4.14: *Current-Voltage characteristics of the irradiated detectors of different Types. All data were scaled to -20°C.*

irradiation to the order of μA after irradiation. Using the theory described in section 3.3.1.1.1 and assuming a damage rate of $\approx 6\times10^{-17}$ A/cm, which corresponds to one day of annealing at 20°C and fluences within the sample fluences, the estimated currents were of the order of μA as observed in Table 4.4.

Table 4.5 is a summary of the breakdown voltages of each detector before and after being irradiated. Three of the five detectors have shown either unchanged or improved breakdown behaviour after irradiation. Radiation damage introduces additional acceptor levels in the bulk material and increases the oxide charge (see section 4.2.2). Since the maximum field decreases with the increase of the oxide charge density, the increase of the breakdown voltages can be explained by the compensation of the acceptor dopants by the oxide charge. For the two Type 3 detectors which have shown degraded breakdown behaviour, the bulk damage has predominantly led to this effect. The extra protection provided by the DC field plates (see section 4.2.2.2) seems to have no effect in these detectors.

4.4.3 Gain

The gain is defined as the ratio of the output to the input signal. In this case it relates the output in ADC units to the input in generated electron-hole pairs in the silicon.

Types	Fluences [n_{eq}/cm^2]	Detectors	I_{after}(-20°C) [μA]	I_{before}(20°C) [nA]
Type 1	2×10^{15}	W13-BZ1-P07	12.10	6.97
Type 3	5×10^{14}	W06-BZ3-P06	4.74	10.5
	2×10^{15}	W13-BZ3-P01	5.74	7.37
	10^{16}	W09-BZ3-P15	16.42	7.59
Type 4	5×10^{15}	W06-BZ4-P10	15.38	7.31

Table 4.4: *Leakage current measurements at 500* V *before (I_{before}) and after (I_{after}) irradiation.*

Types	Fluences [n_{eq}/cm^2]	Detectors	$V_{BD_{after}}$ [V]	$V_{BD_{before}}$ [V]
Type 1	2×10^{15}	W13-BZ1-P07	980	960
Type 3	5×10^{14}	W06-BZ3-P06	700	$>$ 1000
	2×10^{15}	W13-BZ3-P01	700	850
	10^{16}	W09-BZ3-P15	$>$ 1000	$>$1000
Type 4	5×10^{15}	W06-BZ4-P10	960	580

Table 4.5: *Breakdown voltages before ($V_{BD_{before}}$) and after ($V_{BD_{after}}$) irradiation of the detectors tested.*

It was used to normalise the charge collected from each detector at a defined bias voltage. As a reference, a p-type non irradiated detector was tested and the charges collected were measured at nine bias voltages from 100 V to 500 V in steps of 50 V. Measurements were also performed at room temperature.

At each bias voltage, a charge distribution was obtained whose peak corresponds to the amount of charge deposited into the silicon detector. The peak value was extracted by fitting a Landau convoluted with a Gaussian function to that distribution. The obtained peak values were then plotted as a function of the applied bias voltages to determine the amount of charge collected at full depletion. The green interlinked circles in figure 4.20 is the curve obtained for the p-type non-irradiated detector. As shown in that figure, at voltages above 300 V the peak ADC value is constant at $\approx$ 80 ADCs within the measurement precision.

Since characterisation of the irradiated detectors was performed at low temperature ($\approx$ -15°C), further comparison measurements of the collected charge were performed with the p-type non-irradiated detector at 400 V and at two different temperatures, -16°C and +24°C. It was found that the gain had increased by $\approx$ 6% from +24°C to -16°C. The gain variation introduces a small error, due to the temperature variations of $\pm$3°C between the measured detectors. The peak ADC of $\approx$ 87.6 ADCs at -16°C,

was considered as 100% charge collection efficiency, and used to normalise the results presented in section 4.4.4.

4.4.4 Charge Collection Efficiency

The charge collected from each of the five irradiated detectors was measured using the experimental setup described in section 4.4.1. Various bias voltages were applied to each irradiated detector. Their minimum operating bias voltages were identified which correspond to the minimum voltage below which the Signal to Noise ratio would become too small so that one cannot separate the signal from noise.

Figure 4.15, 4.16, 4.17, 4.18 and 4.19 present the charge collected from the irradiated detectors. The results are given for detectors irradiated at 5×10^{14} n_{eq}/cm^2, 2×10^{15} n_{eq}/cm^2, 5×10^{15} n_{eq}/cm^2 and 10^{16} n_{eq}/cm^2. The detectors were biased at up to their breakdown voltages or a maximum of 1000 V. P-type Type 1, Type 3 and Type 4 detectors were analysed.

As expected, the charge collected increases as a function of the applied bias voltage. Conversely, at the same bias voltage the amount of charge collected decreases with increasing fluence. The reduction of collected charge is due to increasing radiation induced defects into the silicon bulk, which act as trapping centres for mobile charge carriers as discussed in section 4.2.2.1. Moreover, with increasing fluence, the shape of the charge distribution may diverge from the expected Landau distribution. The most irradiated detectors are operated under-depleted. This reduces the signal and hence increases the relative contribution of the noise. The large current in these detectors after irradiation also gives rise to a high noise. Good Landau fits could not be obtained at 100 V at 2×10^{15} n_{eq}/cm^2, at 300 V and below at 5×10^{15} n_{eq}/cm^2, and under 1000 V at 10^{16} n_{eq}/cm^2.

Each of the collected charge distributions was fitted with a Landau convoluted with a Gaussian function in order to extract the signal height which corresponds to the peak[3] of the fitted distribution. For each detector, the obtained signal height was plotted as a function of the bias voltages and combined in the same graph for comparison (see figure 4.20). Unlike the charge collection curve of the non-irradiated detector, those of the irradiated detectors do not plateau under any bias voltage, which indicates that the irradiated detectors were not operated fully depleted. The supplied bias voltages were limited by the breakdown of the detectors.

[3]The peak of the fitted distribution corresponds to the most probable value (MPV) of the Landau distribution.

The charge collection efficiency (CCE) of each of the five irradiated detectors was obtained by dividing the peak of each measurable signal as shown in figure 4.20 by the peak ADCs of 87.6 (see section 4.4.3) which corresponds to a charge collection efficiency of 100 %. The obtained CCE as a function of bias voltages CCE(V) are presented in figure 4.21. The highest signals collected are respectively $\approx$ 70 % and $\approx$ 55 % at fluences of 5×10^{14} n_{eq}/cm^2 and 2×10^{15} n_{eq}/cm^2. For both fluences of 5×10^{15} n_{eq}/cm^2 and 10^{16} n_{eq}/cm^2, the highest signal collected was $\approx$ 30%. When considering the maximal bias voltages that were able to be applied to the detectors, these results are in agreements within the experimental errors with those obtained in [120, 121]. The latter were similar studies of the charge collection efficiency of the same batches of p-type detectors irradiated at fluences up to 10^{16} n_{eq}/cm^2.

By comparing the Type 1 and Type 3 detectors, both irradiated at 2×10^{15} n_{eq}/cm^2, one observes $\approx$ 15 % more charge collected from the Type 1 p-type detector. The difference is explained by the higher breakdown voltage of the Type 1 detector (980 V) compared to that of the Type 3 detector (700 V). This follows the expectation that the p-spray technology presents better resistance against radiation damage, hence better performance, as discussed in section 4.2.2.2.

At higher fluences CCE of up to 30 % has been shown, which is consistent with the results observed in [121] for bias voltages of up to 1000 V. However, in that reference, bias voltages up to 1700 V were able to be applied to the detectors, which has resulted in higher CCE of $\approx$ 55 % for a fluence of 10^{16} n_{eq}/cm^2.

4.4.5 Conclusion

This section has presented the characterisation of the five irradiated p-type detectors. The IV characteristics were shown and the breakdown voltages were identified for each of them. The experimental setup used for charge collection measurements was described as well as the technique to analyse the obtained data. The results have shown that the minimum required operating bias voltage increases as a function of the fluence. Only 30 % of the charge was collected for fluences of 5×10^{15} n_{eq}/cm^2 and 10^{16} n_{eq}/cm^2 for bias voltages up to 900 V and 1000 V respectively. At a fluence of 2×10^{15} n_{eq}/cm^2, a Type 1 detector could be biased at a higher voltage before breakdown than a Type 3 detector. As a result, the collected charge at the highest applied voltages was 15 % higher in the Type 1 than the Type 3 detector. This difference may be due to the variation of breakdown behaviour between the detectors due to the isolation technique. The n-on-p detectors are promising candidates at SLHC fluences, albeit that at the

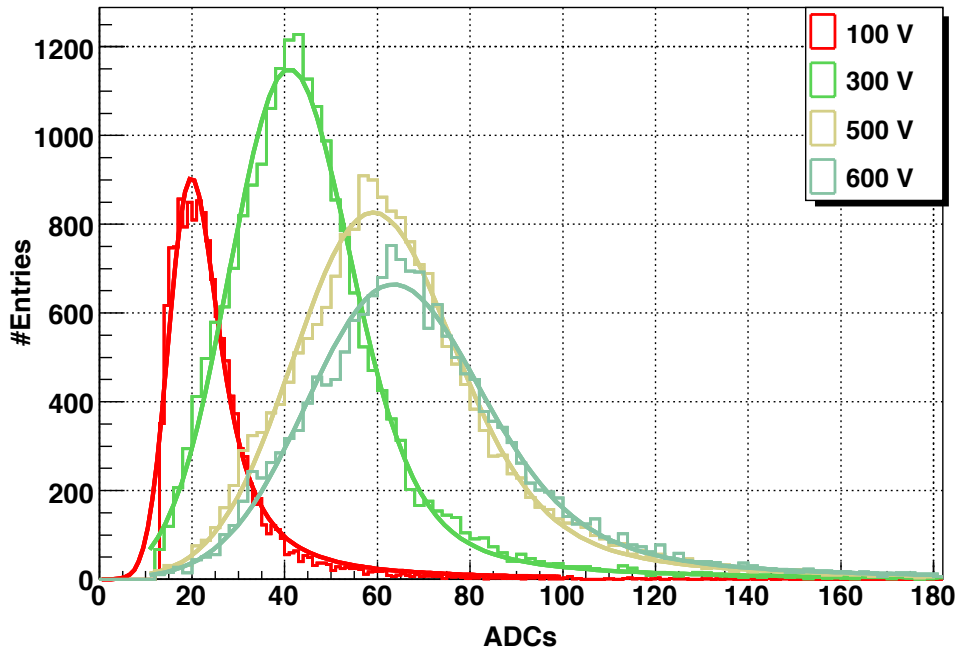

Figure 4.15: *Charge collected from the p-type Type 3 detector W06-BZ3-P06 irradiated at* 5×10^{14} $\mathrm{n_{eq}/cm^2}$ *under bias voltages of* 100 V, 300 V, 500 V *and* 600 V.

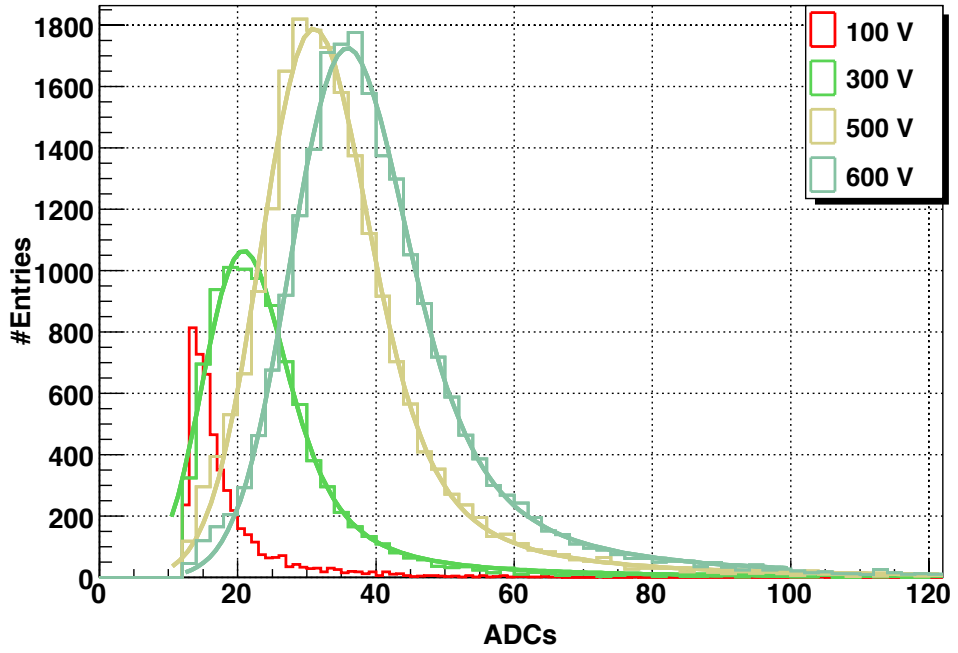

Figure 4.16: *Charge collected from the p-type Type 3 detector W13-BZ3-P01 irradiated at* 2×10^{15} $\mathrm{n_{eq}/cm^2}$ *under bias voltages of* 100 V, 300 V, 500 V *and* 600 V.

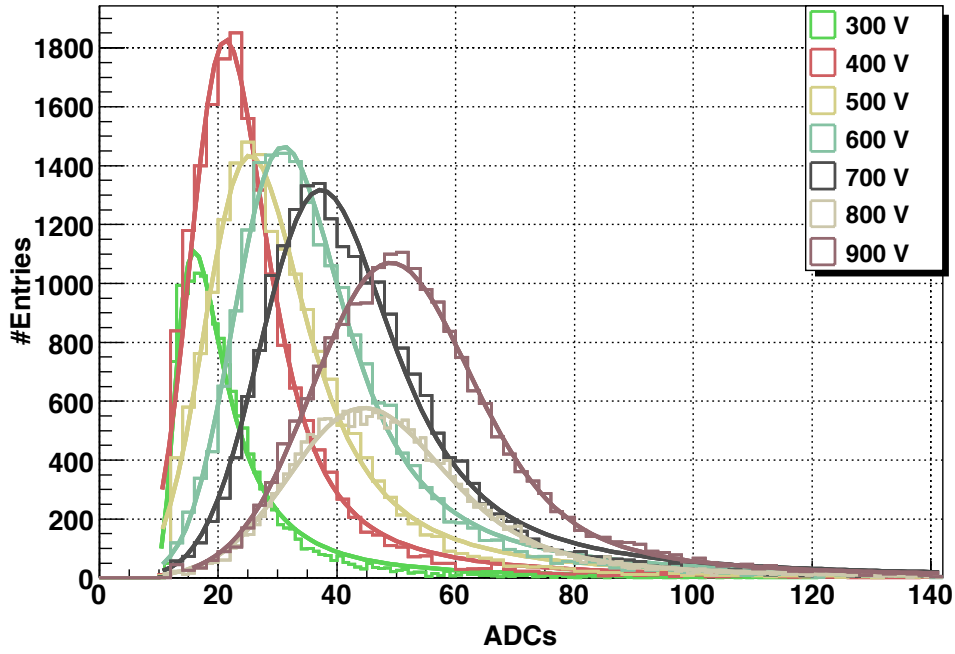

Figure 4.17: *Charge collected from the p-type Type 1 detector W13-BZ1-P07 irradiated at 2×10^{15} n_{eq}/cm^2 under bias voltages of 300 V, 400 V, 500 V, 600 V, 700 V, 800 Vand 900 V.*

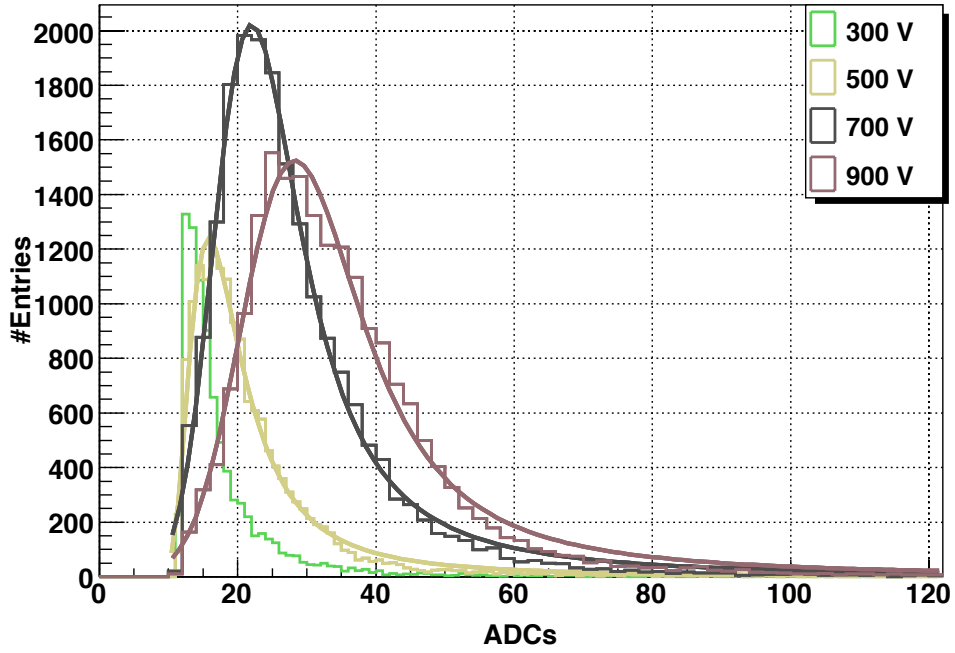

Figure 4.18: *Charge collected from the p-type Type 4 detector W06-BZ4-P10 irradiated at 5×10^{15} n_{eq}/cm^2 under bias voltages of 300 V, 500 V, 700 V, and 900 V.*

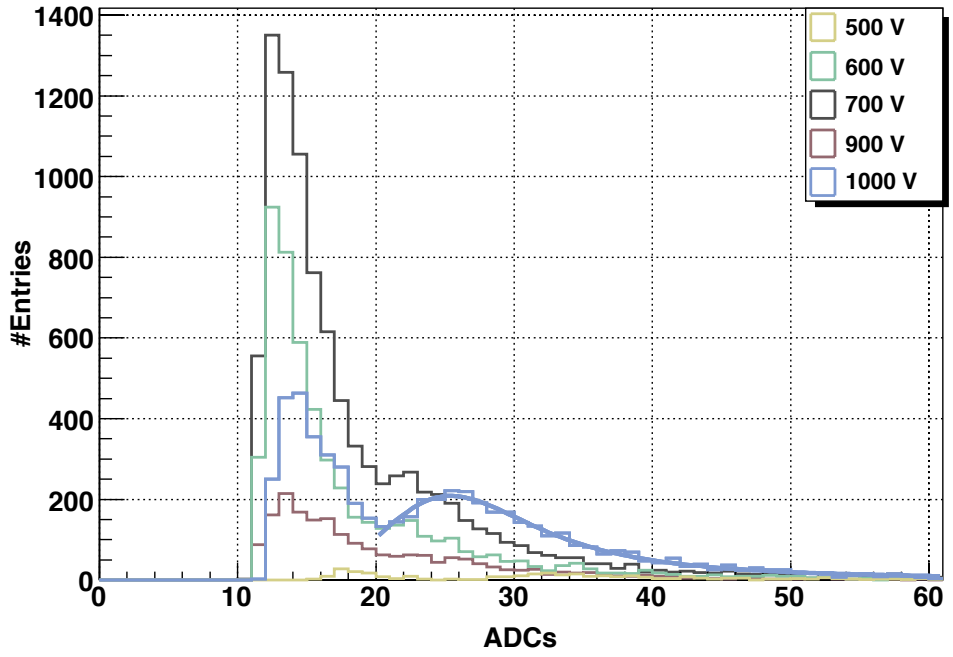

Figure 4.19: *Charge collected from the p-type Type 3 detector W09-BZ3-P15 irradiated at 10^{16} n_{eq}/cm^2 under bias voltages of 500 V, 600 V, 700 V, 900 V and 1000 V.*

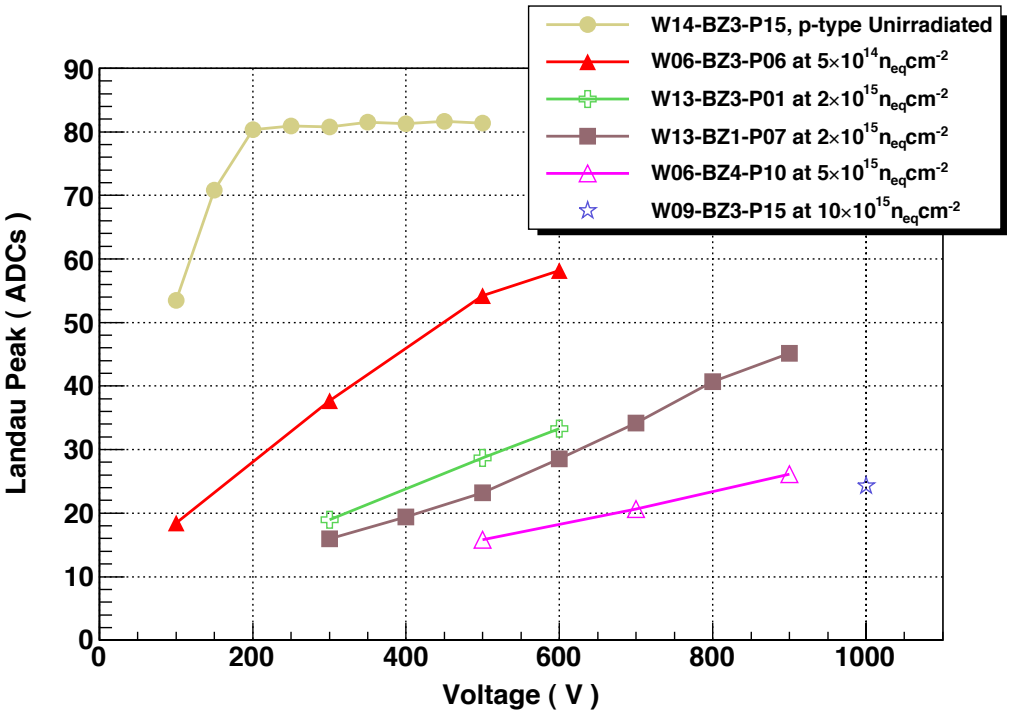

Figure 4.20: *Comparison of the charges collected from the irradiated p-type detectors and the non-irradiated p-type detector as function of bias voltages.*

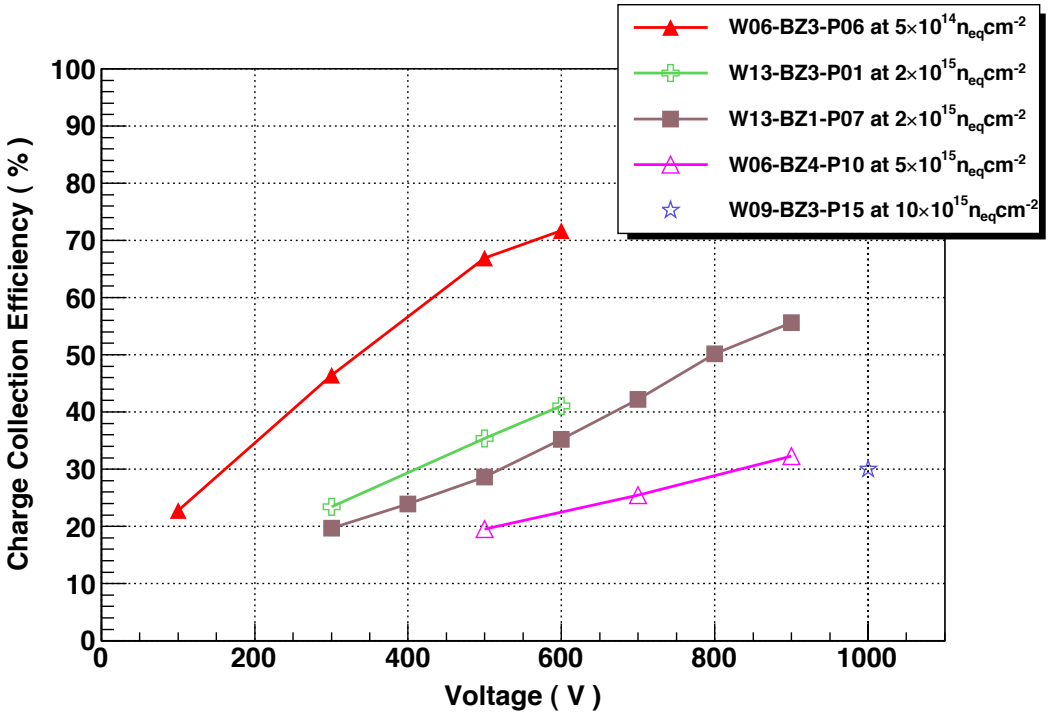

Figure 4.21: *Comparison of the Charge Collection Efficiencies of the irradiated p-type detectors as function of bias voltages.*

highest fluences the CCE is significantly reduced and they must be operated at high voltages and low temperatures.

4.5 Summary

This chapter has presented the characterisation of p-type detectors with four different isolation techniques before and after irradiation up to 10^{16} n_{eq}/cm^2. Before irradiation, their IV and CV characteristics were taken and analysed to identify their breakdown and full depletion voltages. In total results from 29 detectors were shown. No abnormal behaviour was observed in any of the detectors regardless of the isolation technique employed. A breakdown voltage above 1000 V was observed within three of the four categories of isolation employed. The full depletion voltages of the detectors were not significantly different between isolation techniques with an average of 170 V.

After irradiation, five detectors were characterised. Their IV characteristics were taken and the breakdown voltages as well as the radiation damage rate were identified. The charges collected were measured and the charge collection efficiencies were compared. It has been shown that $\approx$ 30 % of charge was collected at a fluence of 10^{16} n_{eq}/cm^2 for a bias voltage of 1000 V. At a fluence of 2×10^{15} n_{eq}/cm^2 the Type 1

detector could be biased to a higher voltage than the Type 3 detector, potentially due to the p-spray isolation technique, as a result it collected ≈ 15 % more charge.

We have shown that the n-on-p detectors are a promising candidate for the LHCb upgrade as they provide a reasonable collected charge at fluences up to 10^{16} n_{eq}/cm^2. Moreover they can be operated not fully depleted.

As discussed in section 3.3.1.1.2, the current VELO sensors will be replaced after approximately 6-8 fb^{-1}, which could be expected after around five years of operation. The current modules are n-on-n with one n-on-p module. The replacement modules, currently finishing production, are n-on-p. The results here show that after 7 fb^{-1} and a fluence of 5×10^{14} n_{eq}/cm^2, a collected charge of $\approx 65\%$ could be expected from n-on-p sensors. The simulation of the required full depletion of the VELO sensors, presented in section 3.3.1.1.2, under these conditions has demonstrated that they will be operated under-depleted. The full depletion voltage was estimated to be of the order of 800 V. Although the CCE is reduced, as the n-on-p detectors have n^+-type readout their resolution should be maintained.

5 Analysis of $B_d \to K^*\mu^+\mu^-$

This chapter is dedicated to the study of the $B_d \to K^*\mu^+\mu^-$ decay in LHCb. The $B_d \to K^*\mu^+\mu^-$ event selection and the extraction of the Forward Backward Asymmetry are presented in section 5.1 and 5.2 respectively. The impact of detector misalignments on the analysis of this channel is given in section 5.3.

5.1 $B_d \to K^*\mu^+\mu^-$ Selection

This section presents the $B_d \to K^*\mu^+\mu^-$ cut-based event selection. The Monte Carlo data samples and their simulation are briefly discussed in section 5.1.1, followed by the presentation of the description of the event selection processes in section 5.1.2. The expected signal and background yields are discussed in section 5.1.3. Finally, section 5.1.4 summarises the development of this selection algorithm using the Python scripting language.

5.1.1 Data Samples Simulation

The studies of the $B_d \to K^*\mu^+\mu^-$ channel presented in this thesis are based on Monte Carlo simulations. The MC simulation aims to provide a realistic description of the detector performance and physics processes, which permit an evaluation of the ability of the experiment to measure this decay. As discussed in chapter 2, the production of MC data is performed by three LHCb software packages based on the Gaudi framework called, Gauss [122], Boole [123] and Brunel [124].

As part of the Gauss package, PYTHIA [125] generates the particles produced in proton-proton collisions and EvtGen [85] simulates the b-hadron decays. Then GEANT4 [86] simulates the energy deposition from the passage of the particles through the detector material.

The Boole package models the detector response which consists of simulating both the signal produced by the energy deposited by the particles in the sensitive parts of the detectors and the response of the readout electronics to these signals. At the output

of Boole the simulation and real data are stored in the same format.

At this stage, the next step is the reconstruction, which is performed by the Brunel package. This stage is the same for simulation and data. It consists of the reconstruction of the charged particle tracks, the Cherenkov rings and the calorimeter clusters, using the raw data acquired by the DAQ system or simulated by Boole. The output of the reconstruction is saved in data summary tape files (DST) which will be the input of the offline analysis. The analysis software is called DaVinci [126] and is discussed further in the next section.

In this study, the data samples correspond to $B_d \to K^*\mu^+\mu^-$ simulated data using this complete LHCb data simulation. As the simulation software is always developing in order to achieve improved descriptions of the detectors, two MC reconstructed data versions were employed. The first version called 'DC06' was simulated using Gauss v25r7, and reconstructed using Boole v12r0 and Brunel v32r2. The DC06 reconstructed data were employed for the study of the impact of detector misalignments to the $B_d \to K^*\mu^+\mu^-$ decay (see section 5.3). The second data set called 'MC09' was simulated using a more recent version of the LHCb simulation software: Gauss v37r2, Boole v18r1 and Brunel v34r7. The MC09 reconstructed data were used for the extraction of the Forward Backward Asymmetry distribution (see section 5.2).

5.1.2 Event Selection

The $B_d \to K^*\mu^+\mu^-$ event selection was performed using the DaVinci LHCb software package. DaVinci provides the necessary tools in order to perform vertex reconstruction from primary and secondary vertices and allows selection cuts to be applied. 'Mother' particles can be reconstructed by combining the information from the measured charged particles. For $B_d \to K^*\mu^+\mu^-$, the final state particles consist of two muons of opposite charges, with the presence of K^+ and π^- from the K* decay. The information from the K^+ and π^- was combined to ensure that their invariant mass was consistent with a K^*. Subsequently, the B_d was reconstructed from the K* and the two muons $\mu^+\mu^-$. The reconstructed B_d mass value was required to be close to the expected B_d mass. Similarly in the $\bar{B_d} \to \bar{K^*}\mu^+\mu^-$, the $\bar{K^*}$ decays into K^- and π^+ and the $\bar{B_d}$ is obtained from the $\bar{K^*}$ and the two muons.

The selection of the $B_d \to K^*\mu^+\mu^-$ events comprises a set of selection criteria, also known as cuts, which are applied in sequence to the information obtained from the final state reconstructed four charged particles as well as to the reconstructed B$_d$ and K*. The four charged particle tracks $K^\pm$, $\pi^\pm$ and $\mu^\pm$ were identified using the LHCb particle

identification information. For a given particle hypothesis, an overall log-likelihood ($\ln\mathcal{L}$) value is obtained from different sub-detectors, which is to be compared with the π hypothesis with the difference in likelihood $\Delta ln\mathcal{L}$ for its identification. For example, the muon tracks were identified by imposing

$$\Delta ln\mathcal{L}_{\mu\pi} = ln\mathcal{L}_{\mu} - ln\mathcal{L}_{\pi} > -5, \tag{5.1}$$

Where the log-likelihood uses information on hits in the muon chambers; the K and π separation relies on the RICH detectors. Details on the particle identification algorithms are available in [127]. Cuts on the track χ^2/ndof of these four reconstructed charged tracks are used to ensure fake tracks are removed.

Tracks from B-decays typically have high momentum compared with tracks produced at the primary vertex and hence track p, p_T cuts are applied. Tracks from the primary vertex are rejected by requiring that the $K^{\pm}$, $\pi^{\pm}$ and $\mu^{\pm}$ tracks have significant impact parameter[1] (IP) χ^2. As the B_d flies a few mm before decaying, the tracks from the B-decay should have significant IP χ^2. As some events have more than one primary vertex (PV), the check was performed with respect to all PVs found in the event.

Selection cuts were also applied to the reconstructed K^* and di-muon pair. The reconstructed K^* and di-muon decay vertices were required to be well separated (Flight Distance FD[2]) from the PV, by FD and FD χ^2 cuts. The tracks were required to make a good quality vertex through a vertex χ^2 cut. As already mentioned in section 1.5.6, cuts on the di-muon invariant mass around the J/ψ and $\psi(2S)$ resonances were applied to reject the background from $B \to J/\psi K^*$ and $B \to \psi(2S)K^*$.

The B_d is reconstructed from the K^* and di-muon pair, and a vertex-χ^2 applied. Flight distance and Flight distance χ^2 cuts are applied to the B_d decay vertex separation from the PV, and the B_d origin is checked to be compatible with the PV through an impact parameter selection. In order to reduce fake reconstructed B_d, a cut on the B_d pointing angle θ was applied. The angle θ is defined as the angle between the flight direction and the momentum vector direction of the B_d.

The list of the selection cuts applied to all particles in the $B_d \to K^*\mu^+\mu^-$ decay and their respective values are presented in Table 5.1. The $B_d \to K^*\mu^+\mu^-$ selection had already been designed within the LHCb collaboration prior to this study [128] and was used by the author. However, the author translated the selection to the new Python format and tested and determined the performance of this (see section 5.1.4). In the

[1]The impact parameter of a track is the closest approach between the track's trajectory and the primary vertex. The IP χ^2 is obtained by the square of the ratio between the IP and its error.
[2]The FD is positive if the secondary vertex is at a greater z than the primary vertex.

following section, the selection efficiency, the signal and background yields are given.

5.1.3 Selection Efficiency, Signal and Background Yields

The selection efficiency ϵ_{Sel} is computed using [40]

$$\epsilon_{Sel} = 0.87 \times \left(\frac{N_{Selected}}{N_{Total}} \right) \times 0.1747, \tag{5.2}$$

where 87 % is the trigger efficiency measured on simulation for selected events, $N_{Selected}$ and N_{Total} are, respectively, the number of events that have passed the selection and the total number of simulated data. 0.1747 is the fraction of generated B hadrons decaying within the angular acceptance of LHCb.

A total of 60000 $B_d \to K^*\mu^+\mu^-$ DC06 (see section 5.1.1) signal events were primarily used for the study. The selection cuts employed to evaluate the selection efficiency are those listed in Table 5.1. In total 2708 events have passed the selection. Using equation 5.2, the selection efficiency is $\epsilon_{Sel} = 0.69 \pm 0.02$ %, which is broadly in agreement with the selection efficiency of 0.71 ± 0.02 % quoted in [40] using the same selection criteria. The difference may be due to the difference of software versions employed.

The signal yield is computed with

$$S_{yield} = N_{b\bar{b}} \times 2 \times f(b \to \bar{B}_d) \times \mathrm{BR}(B_d \to K^*\mu^+\mu^-) \times \mathrm{BR}(K^* \to K^\pm\pi^\mp) \times \epsilon_{Sel}, \tag{5.3}$$

where $N_{b\bar{b}}$ is the number of $b\bar{b}$ pairs produced per 2 fb^{-1}. $f(b \to \bar{B}_d)$ is the production fraction of B_d from b quarks. BR($B_d \to K^*\mu^+\mu^-$) and BR($K^* \to K^\pm\pi^\mp$) are, respectively, the branching ratios of $B_d \to K^*\mu^+\mu^-$ and $K^* \to K^\pm\pi^\mp$. The values of the parameters used for the calculation of the signal yield are listed in Table 5.2. These give a signal yield of 4060^{+1080}_{-970} events/2 fb^{-1}, which is in agreement with the obtained yield of 4200^{+1100}_{-1000} events/2 fb^{-1} [40]. Figure 5.1 shows the reconstructed B_d and K* mass distributions. The B_d mass distribution was fitted with a Gaussian function. The B_d mass obtained was $m^{rec}_{B_d} = 5279.0 \pm 0.3$ MeV/c^2 with a resolution of $\sigma = 15.5 \pm 0.3$ MeV/c^2. The K^* mass distribution, however, was fitted with a Breit-Wigner function and the K^* mass obtained was $m^{rec}_{K^*} = 895.4 \pm 0.6$ MeV/c^2 with a full width at half maximum $\Gamma = 45 \pm 1$ MeV/c^2. Both mass values are in good agreement with their input values in the simulation, which are $m^{input}_{B_d} = 5279.5$ MeV/c^2 and $m^{input}_{K^*} = 896$ MeV/c^2 for B_d and K^* respectively.

98788 events were selected from the 2006744 events in the MC09 data, by using the

$B_d \to K^*\mu^+\mu^-$ selection parameter		Cut value
B_d	$\|\Delta m\|$ (MeV/c^2)	< 50
	Flight Distance (mm)	> 0
	Flight Distance-χ^2	> 900
	Impact Parameter-χ^2	< 9
	$\cos\theta$	> 0.99995
	Vertex-χ^2	< 16
K^*	$\|\Delta m\|$(MeV/c^2)	< 100
	Flight Distance (mm)	$>$ -1.0
	Flight Distance-χ^2	> 1
	Impact Parameter-χ^2	> 0.25
	Vertex-χ^2	< 25
	p_T (GeV/c)	> 0.5
$\mu^+\mu^-$	Vertex-χ^2	< 25
	J/ψ mass rejection (MeV/c^2)	2900 - 3200
	$\psi(2S)$ mass rejection (MeV/c^2)	3650 - 3725
K	p (GeV/c)	> 1
	p_T (GeV/c)	> 0.2
	$\Delta\ln\mathcal{L}_{K\pi}$	$>$ -1.0
	$\Delta\ln\mathcal{L}_{Kp}$	$>$ -1.0
	Track-χ^2/ndof	< 2
	Impact Parameter-χ^2	> 16
π	p (GeV/c)	> 1
	p_T (GeV/c)	> 0.2
	$\Delta\ln\mathcal{L}_{K\pi}$	< 25
	Track-χ^2/ndof	< 2
	Impact Parameter-χ^2	> 16
$\mu^\pm$	p (GeV/c)	> 3
	p_T (GeV/c)	> 0
	$\Delta\ln\mathcal{L}_{\mu\pi}$	$>$ -5.0
	Track-χ^2/ndof	< 2
	Impact Parameter-χ^2	> 9

Table 5.1: *Selection cuts applied to the $B_d \to K^*\mu^+\mu^-$ decay.*

Parameter	Values
$N_{b\bar{b}}$	10^{12}
$f(b \to \bar{B}_d)$	0.399 ± 0.011
$\mathrm{BR}(B_d \to K^*\mu^+\mu^-)$	$1.10^{+0.29}_{-0.26} \times 10^{-6}$
$\mathrm{BR}(K^* \to K^\pm\pi^\pm)$	0.67

Table 5.2: *Values of the parameters employed for the calculation of the signal yield.*

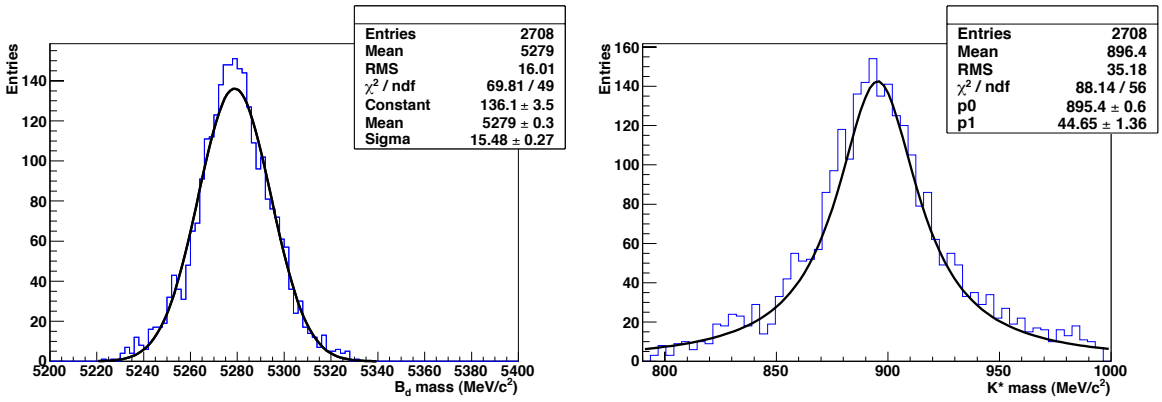

Figure 5.1: *Reconstructed B_d (left) and K^* (right) mass distributions from the DC06 data. A Gaussian fit for the B_d and Breit Weigner fit for the K^* are shown.*

same $B_d \to K^*\mu^+\mu^-$ selection as used with the DC06 data. Using equation 5.2, the corresponding selection efficiency is $\epsilon_{Sel} = 0.74 \pm 0.01$ %, which gives a signal yield of 4360^{+1160}_{-1040} events/2 fb^{-1}. This is in agreement with the numbers given above for DC06 data.

The main source of background for $B_d \to K^*\mu^+\mu^-$ originates from events where both b and $\bar{b}$ quarks decay directly to two muons ($b \to \mu^-$, $\bar{b} \to \mu^+$). The background estimate presented in this thesis is from $b \to \mu^-$, $\bar{b} \to \mu^+$ MC09 simulated events. Contributions from other sources of background were studied in detail in [129]. In total 12 $b \to \mu^-$, $\bar{b} \to \mu^+$ events have passed the $B_d \to K^*\mu^+\mu^-$ selection from the 10226662 $b \to \mu^-$, $\bar{b} \to \mu^+$ events.

The background yield was estimated with

$$B_{yield} = 0.87 \times N_{b\bar{b}} \times BR(b \to \mu^-, \bar{b} \to \mu^-) \times \frac{N_{Selected}}{N_{Total}} \times 0.434, \tag{5.4}$$

where 87% is the trigger efficiency for events that have passed the selection. This is the same trigger efficiency as for signal events as the rare background events passing the selection have characteristics very similar to the signal. $BR(b \to \mu^-, \bar{b} \to \mu^+)$ of 0.012 is the branching ratio of the $b \to \mu^-, \bar{b} \to \mu^+$ events and 0.434 is the fraction of $b \to \mu^-, \bar{b} \to \mu^+$ events decaying within the angular acceptance of LHCb. The estimated background yield from $b \to \mu^-, \bar{b} \to \mu^+$ events is 5300 $\pm$ 1800 events/2 fb^{-1} for this MC09 sample to be compared with 7900 $\pm$ 810 events/2 fb^{-1} estimation for the DC06 sample [129]. The detector is more realistically described in MC09.

5.1.4 Cut-based $B_d \to K^*\mu^+\mu^-$ Selection using Python

The LHCb simulation software was recently improved to be more flexible and more user-friendly. It has required changes to the interface from which the selection algorithms are called. The interfaces have all been changed to a Gaudi Python style, which are written using the Python scripting language. A set of option files were previously employed to select events using the DaVinci framework. These were rewritten using the Python language, by the author, to comply with the most recent LHCb analysis conventions.

In this section the technical details of the design of the algorithm in Python will not be discussed. Instead, a comparison between the distributions obtained using the previous DaVinci options and the new Python based options will be shown. Detailed information on Python based physics analyses can be found in [130]. The $B_d \to$

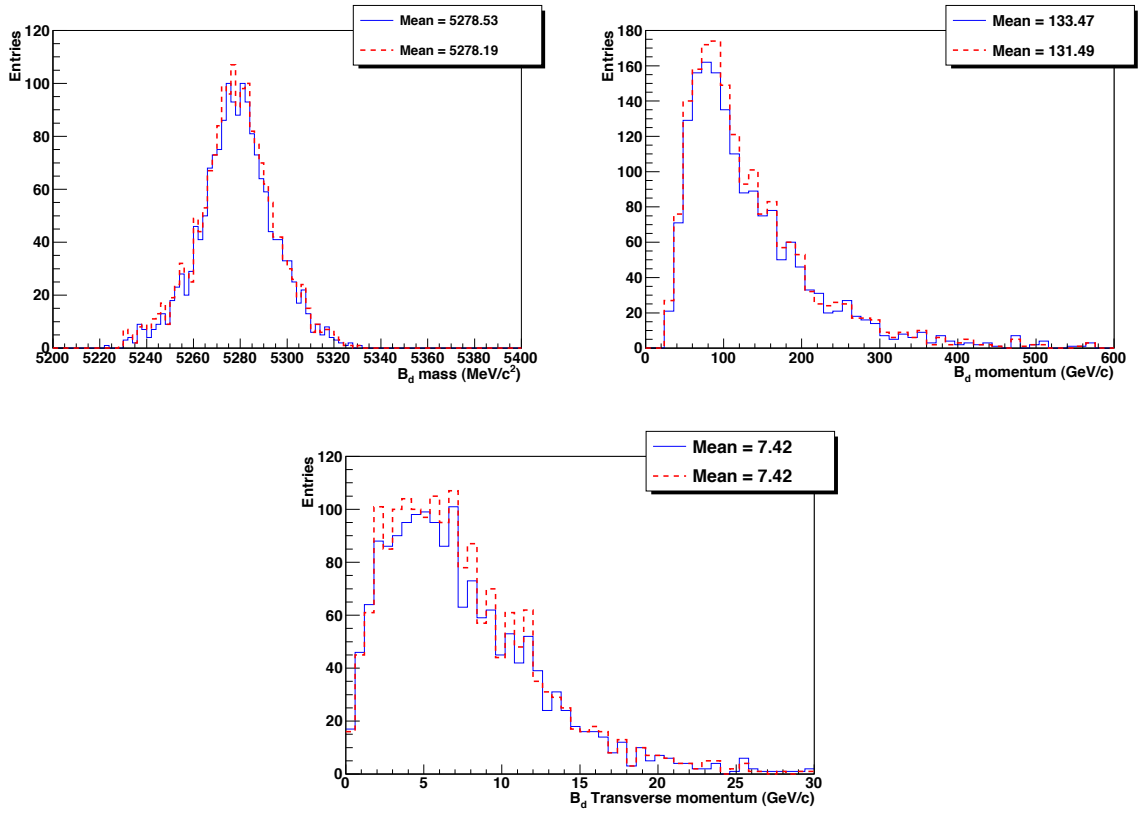

Figure 5.2: *Comparison of B_d distributions obtained with the $B_d \to K^*\mu^+\mu^-$ DaVinci options (red dashed lines) and the Python (blue solid lines) selections processing the DC06 data. A-(top left): The B_d mass distribution. B-(top right): The B_d momentum distribution. C-(bottom): The B_d transverse momentum distribution.*

$K^*\mu^+\mu^-$ selection criteria remained the same as those presented in Table 5.1, with minor differences required by the implementation.

Figure 5.2 and 5.3 present comparisons of distributions obtained with the $B_d \to K^*\mu^+\mu^-$ previous DaVinci options and the new Python selections used to process the DC06 data. The mass, momentum, and transverse momentum distribution are shown for both B_d and K^*. The invariant mass distribution is also shown for the $\mu^+\mu^-$. While, in general, the agreement is very good, small discrepancies were observed between the distributions obtained with the DaVinci options file and the Python selection. The Python version selects 6 ± 2 % less events than the DaVinci options. From this statistic, it is not clear if this difference is significant or not. However, the small change may be due to the implementation of the cuts or changes in the software between the options based release and the Python based release.

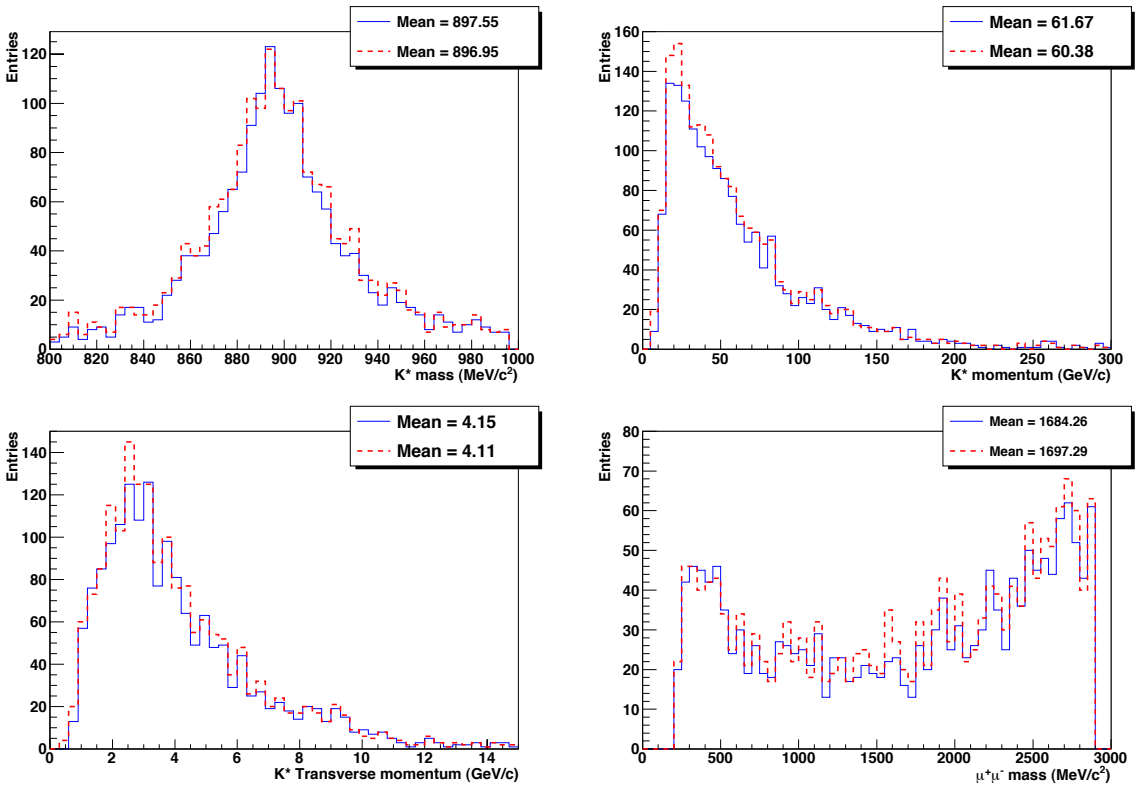

Figure 5.3: *Comparison of distributions obtained with the $B_d \to K^*\mu^+\mu^-$ DaVinci options file (red dashed lines) and the Python (blue solid lines) selections processing the DC06 data for K^* and $\mu^+\mu^-$. A-(top left): The K^* mass distribution. B-(top right): The K^* momentum distribution. C-(bottom left): The K^* transverse momentum distribution. D-(bottom right): The $\mu^+\mu^-$ invariant mass distribution.*

5.2 Extraction of the Forward Backward Asymmetry

As defined in section 1.5.5.3, the Forward Backward Asymmetry (A_{FB}) is the difference between the number of forward and backward events as a function of the dimuon mass squared. Two methods were employed to extract the A_{FB} distribution.

The first method, described in section 5.2.1, is a binned counting analysis. This method is a simple and easy method for the early extraction of the A_{FB}. It requires an interpolation in order to extract the zero crossing point S_0 of the A_{FB} distribution. Hence, the value of the chosen bin size is likely to bias S_0.

The second method, reported in section 5.2.2, is an unbinned non-parametric counting analysis. It provides a better access to the shape of the A_{FB} distribution. Furthermore the A_{FB} is directly given without any fit. However, it relies on the values of the smoothing parameters which act equivalently to the bin size for this method.

5.2.1 Binned Method

The binned method to extract the Forward Backward Asymmetry $A_{FB_{Total}}$ consists of dividing the di-muon mass squared in bins and computing the Forward Backward Asymmetry distributions for $B_d \to K^*\mu^+\mu^-$ and $\bar{B_d} \to \bar{K^*}\mu^+\mu^-$ decays denoted $A_{FB_{B_d \to K^*\mu^+\mu^-}}$ and $A_{FB_{\bar{B_d} \to \bar{K^*}\mu^+\mu^-}}$ respectively in each bin, according to the definitions in section 1.5.5.3 using equation 1.54. Then $A_{FB_{Total}}$ is given by

$$A_{FB_{Total}}(q^2) = A_{FB_{B_d \to K^*\mu^+\mu^-}}(q^2) + A_{FB_{\bar{B_d} \to \bar{K^*}\mu^+\mu^-}}(q^2), \tag{5.5}$$

This method was employed by the Babar and Belle experiments as well as in previous LHCb studies [129, 131].

As already mentioned at the start of this section, the binned method is distinct for its simplicity. The bin sizes can be varied to adapt to statistics but it is relatively insensitive to the shape of the A_{FB} distribution. One needs to make an interpolation to extract the zero crossing point of the A_{FB}.

5.2.2 Unbinned Method

An alternative to the binned method discussed in section 5.2.1 is an unbinned non-parametric method to obtain the A_{FB} distribution in the $B_d \to K^*\mu^+\mu^-$ analysis. This method has already been used and tuned to extract the A_{FB} from simplified toy Monte Carlo $B_d \to K^*\mu^+\mu^-$ data generated by smearing simulated variables without

taking into account the full detector simulation (see section 5.1.1) [28]. In this study, the unbinned method was employed on fully reconstructed simulation events.

To evaluate A_{FB}, the $B_d \to K^*\mu^+\mu^-$ events were separated into forward and backward events according to the definition given in section 1.5.5.3. For each category of event the dimuon mass squared distribution was evaluated using a probability density function denoted $f_n^f(f_n^b)$ for a forward (backward) event with

$$f_n^{f/b}(q^2) = \frac{1}{nh}\sum_{i=1}^{n} K\left(\frac{q_i^2 - q^2}{h}\right), \tag{5.6}$$

where $K(x)$ are the Kernel functions and h the smoothness parameters [132].

The Kernel functions are taken as Gaussians. Hence this method is equivalent to replacing each event i with a Gaussian centred on the measured q_i^2 of that event, and with the Gaussian having a sigma of h. In this method, each event, which would be a single entry of the binned method, is replaced with the normalised Gaussian function $f_n^{f/b}(q^2)$.

The smoothing parameters h are equivalent to the bin width of the histograms. With histograms, as the number of events increases the bin width is decreased. Similarly, the h values are decreased as the number of events increases. Too high values (too low values) of h would overestimate (underestimate) the true distribution. Appropriate values of h are then required depending on the number of events. A detailed description of the method can be found in [133].

In the previous study of $B_d \to K^*\mu^+\mu^-$ to extract A_{FB} [28], the optimisation of the smoothing parameters h have already been performed with $N_{Reference} = 7000$ $B_d \to K^*\mu^+\mu^-$ events and a general method was proposed. The values of h are a function of q^2. In this thesis, the previously optimised values of h were used but they were scaled according to

$$h'(q^2) = h(q^2)\left(\frac{N_{Reference}}{N_{Selected}}\right)^{1/2}, \tag{5.7}$$

where $N_{Selected}$ is the number of selected $B_d \to K^*\mu^+\mu^-$ events from which the A_{FB} distribution is extracted. The scaled smoothing parameters h' were used for the extraction of the A_{FB} distribution using the unbinned method throughout this thesis.

The A_{FB} distribution with the unbinned method is then obtained with

$$A_{FB}(q^2) = \frac{N_{forward}\, f_n'^f(q^2) - N_{backward}\, f_n'^b(q^2)}{N_{forward}\, f_n'^f(q^2) + N_{backward}\, f_n'^b(q^2)}, \tag{5.8}$$

with

$$f_n'^{f/b}(q^2) = \frac{1}{nh'} \sum_{i=1}^{n} K\left(\frac{q_i^2 - q^2}{h'}\right), \tag{5.9}$$

where $N_{forward}(N_{backward})$ is the total number of forward (backward) events.

The main advantages of the unbinned method is that one does not need to bin the sample, it allows the shape of the distribution to be extracted more easily and that one does not need to interpolate to extract the zero crossing point S_0 of A_{FB}. S_0 is directly extracted from the obtained A_{FB} distribution.

5.2.3 Forward Backward Asymmetry Distribution and The Zero Crossing Point

The binned and unbinned methods to extract the A_{FB} distributions defined in section 5.2.1 and 5.2.2 were employed on the MC09 reconstructed simulation data (see section 5.1.1). The zero crossing point of the A_{FB} was also extracted with both methods and the obtained results were compared. Assuming an expected signal annual yield of 4360 events/2 fb^{-1}(see section 5.1.3), the MC09 $B_d \to K^*\mu^+\mu^-$ sample corresponds to 45.3 fb^{-1} of data.

Figure 5.4A presents the A_{FB} distributions obtained with the MC09 sample. The results shown as crosses were obtained with the binned method. The vertical size of the cross representing the A_{FB} statistical error and the horizontal size the q^2 bin width. The continuous lines represent the unbinned method. One observes good agreement between the binned and unbinned methods on this full MC09 data sample.

From the A_{FB} distribution obtained with the unbinned method, the zero crossing point S_0, was directly obtained from the curve. The extracted value of S_0 using the unbinned method is $S_0 = 4.19 \pm 0.08$ GeV^2/c^4, for the full MC09 data sample.

Figure 5.4B is the A_{FB} distribution obtained with the MC09 sample using the binned method. As shown in that figure, a linear fit was performed between the q^2 range 2 to 6 GeV^2/c^4 to extract the zero crossing point. The value obtained of S_0 is 4.12 $\pm$ 0.07 GeV^2/c^4. The two methods produce slightly different values for S_0, using the same data set. The theoretical prediction for S_0 from the Standard Model is $S_0 =$ 4.2 GeV^2/c^4 [134]. It seems that the binned method is introducing a small bias due to assumptions in the fit close to the zero crossing point. Hence, the unbinned method is more adequate to extract A_{FB} and S_0. However, the bias introduced by the binned method is small, so it could be used for the earlier extraction of A_{FB} from the real data obtained with the LHCb detector, due to its simplicity.

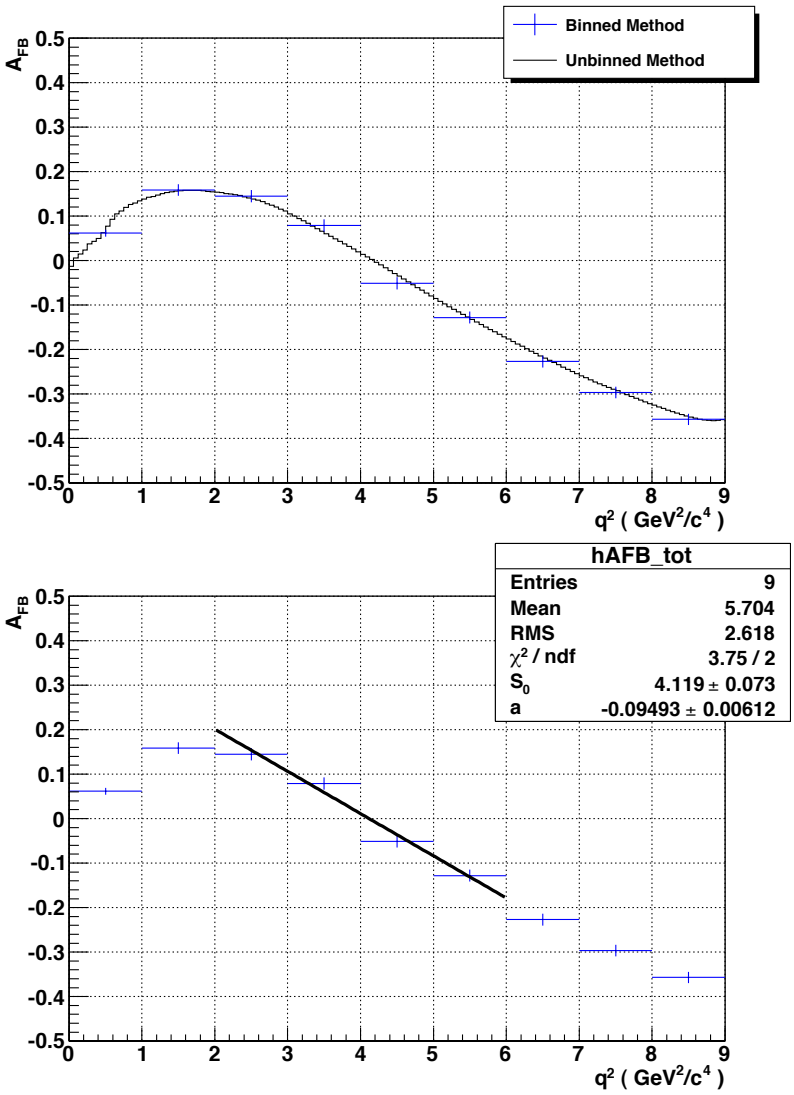

Figure 5.4: *A- (top): A_{FB} distributions extracted using the binned (crosses) and unbinned (continuous line) methods from the 45.3 fb^{-1} MC09 simulated sample. B- (bottom): A_{FB} distribution extracted using the binned method from the 45.3 fb^{-1} MC09 simulated sample. As shown, a linear fit was performed in the range of q^2 between 2 - 6 GeV^2/c^4 to extract the zero crossing point S_0 of A_{FB}.*

Using the unbinned method, the A_{FB} distribution and its zero crossing point were extracted from MC09 simulation samples of 0.2 fb^{-1}, 2 fb^{-1} and 10 fb^{-1}. The obtained A_{FB} distributions are presented in figure 5.5A, 5.5B and 5.5C, respectively. For the 0.2 fb^{-1} and 2 fb^{-1} results, the error bands were obtained from analysing 20 data sets, each of 0.2 fb^{-1} or 2 fb^{-1}. From each data set, an A_{FB} distribution was extracted. The 1σ error (green band) corresponds to the RMS of the entries of the 20 A_{FB} distributions. In addition the 2σ error (yellow band) is also presented. For the 10 fb^{-1} data, the error

Data sample	S_0 [GeV^2/c^4]
10 fb^{-1}	4.19 ± 0.17
2 fb^{-1}	4.19 ± 0.38
0.2 fb^{-1}	$4.0\ ^{+0.8}_{-1.4}$

Table 5.3: *The values of S_0 extracted from MC09 samples of 0.2* fb^{-1}*, 2* fb^{-1}*and 10* fb^{-1} *using the unbinned method.*

band was obtained by scaling the 1σ error computed with the 2 fb^{-1} data sample by the ratio of the square root of the number of events in both samples. The extracted values of the zero crossing point S_0 of A_{FB} are summarised in Table 5.3. The uncertainties given are the estimate for that data size. The central values are that for the full data sample (10 fb^{-1}) or the average of those for the 20 data samples (2 fb^{-1} or 0.2 fb^{-1}).

5.3 Detector Misalignments and their Impacts on $B_d \to K^*\mu^+\mu^-$

The alignment of the tracking detectors is of crucial importance for the physics performance of the LHCb experiment. Since the VELO is retracted and reinserted for each fill, and has a very high resolution, particular attention must be paid to its alignment [65,135]. Furthermore, the B-field will be regularly reversed in the detector which may misalign the ST and OT tracking detectors.

This section presents the impact of the tracking detector misalignments on $B_d \to K^*\mu^+\mu^-$. The implementation of the misalignments on the VELO and T (IT and OT) stations is given in section 5.3.1. Section 5.3.2 presents the impact of these detector misalignments on pattern recognition, event selection, the B_d mass resolution, the Forward Backward Asymmetry and its zero crossing point.

5.3.1 Implementation of Detector Misalignments

In this section the strategy of implementation of the misalignments on the VELO and T-stations are presented. This study was first developed for the analysis of the two body decays $B^0(s) \to h^+h'^-$ [136], and is extended here to the four body decay $B_d \to K^*\mu^+\mu^-$. The implementation of the misalignments follows those presented in [136]. Section 5.3.1.1 describes the misalignment scales employed. Section 5.3.1.2 presents the misalignment data samples.

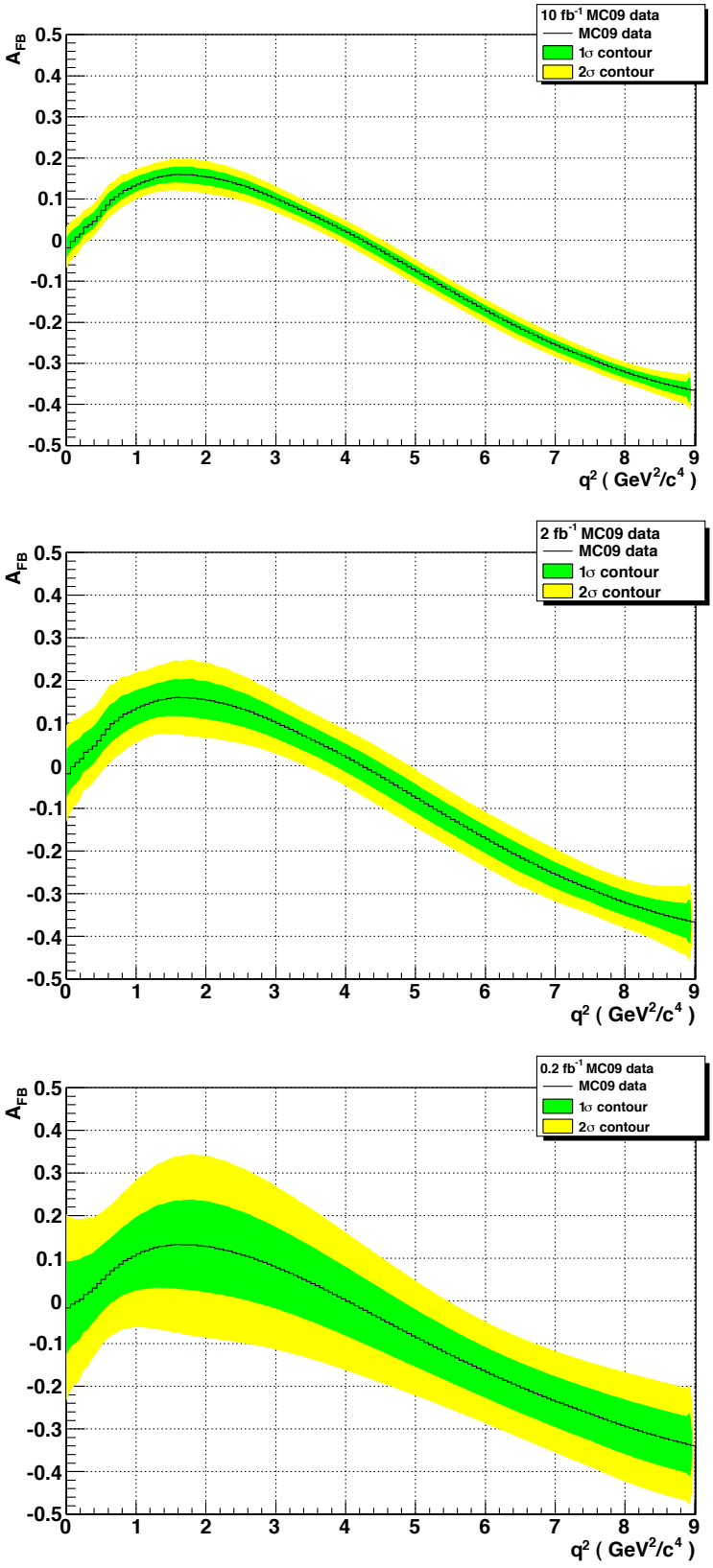

Figure 5.5: *A_{FB} distributions obtained from the MC09 simulated samples using the unbinned method. A- (top): A data sample of 10* fb^{-1}*. B- (middle): A data sample of 2* fb^{-1}*. C- (bottom): A data sample of 0.2* fb^{-1}*. The error bands* $\pm 1\sigma$ *(green) and* $\pm 2\sigma$ *(yellow) are shown. The calculation of these error bands is detailed in the text.*

Detector	Translations (μm)			Rotations (mrad)		
	Δ_x	Δ_y	Δ_z	R_x	R_y	R_z
VELO modules	3	3	10	1.00	1.00	0.20
VELO sensors	3	3	10	1.00	1.00	0.20
IT boxes	15	15	50	0.10	0.10	0.10
OT layers	50	0	100	0.05	0.05	0.05

Table 5.4: *Misalignment "1σ" scales for the VELO modules and sensors, the IT boxes and OT layers.*

5.3.1.1 Misalignment Scales

The misalignment effects were implemented as a function of a 'misalignment scale'. The scales were chosen to be approximately 1/3 of the detector single-hit resolution denoted '1σ'. The misalignments were then applied to each VELO module and sensor, each IT box and OT layer following a Gaussian distribution with a standard deviation corresponding to the 1σ values. Table 5.4 summarises the list of the 1σ misalignment scales employed.

For each sub-detector, ten sets of such 1σ misalignments were generated, to ensure sets of random misalignments. Similarly, this procedure was repeated with the creation of ten similar sets of the so-called '3σ' and '5σ' misalignment scales for the VELO, IT and OT, which were obtained by increasing the 1σ misalignment scale by a factor of 3 and 5 respectively.

Each of these ten misalignment sets were implemented and stored in dedicated (conditions) databases. In total nine databases were produced which correspond to the 1σ, 3σ and 5σ misalignments for the VELO, T (IT and OT) detectors and for both VELO and T detectors.

Since LHCb has been running for almost nine month at the time of writing, an estimation of the detector misalignments has now been obtained. The preliminary VELO resolution is close to that expected. Recent alignment results [137] have shown that the VELO module and sensor alignment are known better than 5 μm and the relative variation of two VELO halves from fill to fill are $\pm$5 μm and $\pm$3 μm along x and y, respectively. The IT and OT hit resolution are currently 54 μm and 250 μm, respectively. The IT is aligned to an accuracy of 16 μm in x and y. The OT alignment is at the 80 μm level in x and y. Hence, the current level of alignment of LHCb is at around 1.5σ of the scale shown in Table 5.4.

5.3.1.2 Data Samples

The study was performed with a $60k$ sample of $B_d \to K^*\mu^+\mu^-$ DC06 events. Three different scenarios are considered VELO misalignments, T-station misalignments, and combined VELO and T-station misalignments. From the $60k$ $B_d \to K^*\mu^+\mu^-$ events, 0σ (perfect alignment), 1σ, 3σ and 5σ of misaligned data were produced for each of these three scenarios. Each $60k$ misaligned sample consists in reality of ten sub-samples of $6k$ events, each of which was processed with a different one of the ten sets of a particular misalignment scenarios. This process of using ten different sets of misalignments was used in order to prevent the results being unrepresentative due to a particularly favourable (or unfavourable) sample misalignment scenario being used.

The $B_d \to K^*\mu^+\mu^-$ events were generated and digitized with a perfect geometry (Gauss generation program version v25r8 and Boole digitization program version v12r10). Starting always from the same digitized data samples, the misalignments were only introduced at reconstruction level, where pattern recognition, track fitting, primary vertexing and particle identification are performed. The version v32r2 of the Brunel reconstruction software was used. Physics analysis was later performed with the DaVinci program version v20r3.

5.3.2 Impact of Misalignments

In this section the effect of misalignments on the selection of the $B_d \to K^*\mu^+\mu^-$ decays is presented. After providing the effect on pattern recognition in section 5.3.2.1, the effect on event selection and on the B_d mass resolution are presented in section 5.3.2.2 and 5.3.2.3 respectively. Finally in section 5.3.2.4 the effect on the Forward Backward Asymmetry and its zero crossing point are given.

5.3.2.1 Effect on Pattern Recognition

The effects on pattern recognition are considered in this section. As misalignments were introduced at the reconstruction level, one has to quantify the ability of the pattern recognition algorithms in finding tracks. These algorithms are summarised in terms of the type of tracks they reconstruct:

- Those that find tracks in the VELO in the $r-z$ projection and in three dimensional space are called VeloR and VeloSpace, respectively [138].
- Those that find the long tracks[3], which are the so-called Forward and Matching

[3]Long tracks refer to the tracks that traverse the whole LHCb detector.

algorithms [139]. The Forward tracking algorithm extrapolates and combines tracks from the VELO up to the T-stations. On the other hand, the Matching tracking algorithm starts with seed tracks in the VELO and T-station, extrapolates them to the magnet region and then looks for matching in the tracks parameter space (xy position and slopes).

Table 5.5 presents the efficiencies[4] for the VeloR, VeloSpace, Forward and Matching pattern recognition with 0σ, 1σ, 3σ and 5σ misalignments of the VELO, the T-stations and both the VELO and T-stations. These results are, as expected, compatible with those reported in [136], as this study will be relatively independent of the physics data type used since the majority of tracks will be from the underlying event.

	Misalignment scenario	VeloR efficiency (%)	VeloSpace efficiency (%)	Forward efficiency (%)	Matching efficiency (%)
Velo Mis.	0σ	98.1 ± 0.1	97.1 ± 0.1	86.2 ± 0.2	81.5 ± 0.2
	1σ	98.1 ± 0.1	96.8 ± 0.1	85.9 ± 0.2	81.3 ± 0.2
	3σ	98.0 ± 0.1	93.9 ± 0.8	83.3 ± 0.6	78.7 ± 0.6
	5σ	97.7 ± 0.2	91.2 ± 1.7	80.4 ± 1.6	75.8 ± 1.5
T Mis.	0σ	98.1 ± 0.1	97.1 ± 0.1	86.2 ± 0.2	81.5 ± 0.2
	1σ	-	-	86.2 ± 0.2	81.4 ± 0.2
	3σ	-	-	86.0 ± 0.2	80.2 ± 0.4
	5σ	-	-	85.7 ± 0.3	77.7 ± 1.3
Velo+T Mis.	0σ	98.1 ± 0.1	97.1 ± 0.1	86.2 ± 0.2	81.5 ± 0.2
	1σ	98.1 ± 0.1	96.9 ± 0.1	85.9 ± 0.2	81.1 ± 0.2
	3σ	98.1 ± 0.1	94.4 ± 0.4	83.7 ± 0.5	77.7 ± 0.7
	5σ	97.9 ± 0.2	90.1 ± 1.7	78.7 ± 1.8	70.8 ± 1.9

Table 5.5: *VeloR, VeloSpace, Forward and Matching pattern recognition efficiencies for a perfectly aligned detector (0σ) and various misalignment scenarios (1σ, 3σ and 5σ) of the VELO, the T-stations, and both the VELO and T-stations.*

VELO Misalignments

One observes a degradation of 6.1 % for the VeloSpace track finding algorithm in the 5σ scenario. Moreover, there is a similar deterioration of the Forward and Matching

[4] All efficiencies quoted for these algorithms are averages obtained from the 10 sub-samples employed (see section 5.3.1.2).

efficiencies which are due to the worsening of the VELO part of the algorithm. These are indirect effects of the VELO misalignments.

T-station Misalignment

In the case of T misalignment, the only tracking algorithms that would be affected are the Forward and Matching. No significant efficiency degradation was observed for 1σ and 3σ. However a deterioration was observed for the 5σ scenario with these two long track finding algorithms: a loss of 4 % for the Matching, and only of 0.5 % for the Forward. This higher degradation of the Matching efficiency compared to that of the Forward is expected. As discussed at the start of this section, the Matching tracking algorithm uses the tracks parameter space (xy position and slopes) to confirm matching to long tracks. Since misalignments induce changes to the track parameter space, the Matching algorithm is more sensitive to T-station misalignments than the Forward algorithm.

VELO and T-station Misalignments

In the case of combined VELO and T-station misalignments, relative efficiency losses of 7 % and 11 % were observed for the long tracking algorithms Forward and Matching, respectively. These losses match the combined loss of efficiency due to the VELO and T-station misalignments independently, which indicates the effects of the VELO and T-station misalignments are uncorrelated, as previously observed in [136].

5.3.2.2 Effect on Event Selection

In this section the effects on event selection efficiencies and on the cut variables are analysed. Table 5.6 presents the number of $B_d \to K^*\mu^+\mu^-$ events that pass the cut based selection (see section 5.1.2) and the set of selection cuts shown in Table 5.1. The loss caused by VELO misalignment is more important than those caused by T-station misalignments. At the worst misalignment scenario of the 5σ combined VELO and T-station misalignments 99 % of the selected events are lost. This clearly demonstrates the importance of an accurate alignment. However, as discussed in section 5.3.1.1, this level of misalignment is not representative of the alignment performance obtained. Furthermore, this analysis is pessimistic as the uncertainties used are not retuned for the worse resolutions, hence χ^2 cuts become tighter than they would be in practice. These effects are more important than those observed for the study of the impact of detector misalignments on the selection of two body decays $B^0(s) \to h^+h'^-$ [136],

which presents event losses up to 80% for the worst misalignment case. Similarly to the study of the effect of misalignments on the pattern recognition in section 5.3.2.1, the corresponding effect from the VELO, T-stations, and the combined VELO and T-station misalignments were also studied.

The effects of detector misalignments on all selection cuts presented in Table 5.1 have been studied. Each of them has been studied separately. However, the same procedure was adopted for all. It consisted of implementing a very loose cut value on the selection variable to be studied while leaving all other cuts unchanged. The modified selection was then applied on each of the nine misaligned data samples (see section 5.3.1.2) and the non-misaligned one. From each of them the acceptance distribution $F_{acceptance}(X)$ was extracted, which is defined as

$$F_{acceptance}(X) = \frac{1}{N_{Total}(X)} \sum_{i=1}^{j} N_i(X) \qquad (j = 1, 2, ..., n), \tag{5.10}$$

where X represents the selection cut variable to be studied and j is the bin number of the acceptance distribution. $N_{Total}(X)$ is the total number of events selected with a very loose cut value of X initially applied. $N_i(X)$ is the number of events within the bin i of the distribution of X with the very loose cut value and n is the total number of bins in that distribution.

For each cut a graph of the acceptance distribution was produced. A vertical dashed line is also shown on these plots to indicate the value of the standard cut used. The intersection of the graph and cut line corresponds to the efficiency of the selection variable.

In total four of the selection cuts presented in Table 5.1 have shown significant sensitivity to detector misalignments. Table 5.7 presents the list of these four selection cuts. Figure 5.6 presents the distributions obtained from studying the effect of the different misalignment scenarios on the B_d Impact Parameter-χ^2 cut. The distributions from the VELO misaligned data, the T-station misaligned data and the combined VELO and T-station misaligned data are shown. For each of them 0σ, 1σ, 3σ and 5σ misalignments were considered. Similarly figures 5.7, 5.8 and 5.9 are the distributions obtained by studying the effects of the detector misalignments on the other significantly affected variables.

The most sensitive variable to VELO misalignment is the B_d Impact Parameter-χ^2. The acceptance decreases down to 60 % at the standard cut value with 5σ misalignments, which gives a relative loss of ≈ 30 %.

On the other hand the Kaon, Pion and Muon Track-χ^2/ndof are sensitive to T-station misalignments. Each of these variables encounters a relative loss of efficiency of ≈ 30 % from 5σ misalignments at the standard cut value.

Misalignment scenario	Number of selected events		
	VELO Mis.	T Mis.	VELO+T Mis.
0σ	2708 (100%)	2708 (100%)	2708 (100%)
1σ	2589 (95%)	2657 (98%)	2527 (93%)
3σ	1259 (46%)	2083 (77%)	660 (24%)
5σ	381 (14%)	1068 (40%)	30 (1%)

Table 5.6: *Number of selected events after running the $B_d \to K^*\mu^+\mu^-$ selection for the different misalignment scenarios.*

5.3.2.3 Effect on the B_d Mass Resolution

In addition, the effects of detector misalignments on the B_d mass resolution have also been studied. For each of the misaligned data defined in section 5.3.1.2 the B_d mass resolution was extracted by means of a Gaussian fit of the obtained B_d mass distribution. The resulting B_d mass resolution from the misaligned data is presented in Table 5.8. Only a small degradation is seen. As the current knowledge of alignment is around the 1σ scenario no significant effect is expected on the B_d mass resolution.

5.3.2.4 Effect on the Forward Backward Asymmetry Distribution and the Zero Crossing Point

The effects of detector misalignments on the Forward Backward Asymmetry distribution have also been analysed. The misaligned data defined in section 5.3.1.2 were again

	Cut variable
B_d	Impact Parameter-χ^2
K	Track-χ^2/ndof
π	Track-χ^2/ndof
$\mu^\pm$	Track-χ^2/ndof

Table 5.7: *The most sensitive variables to tracking detector misalignments.*

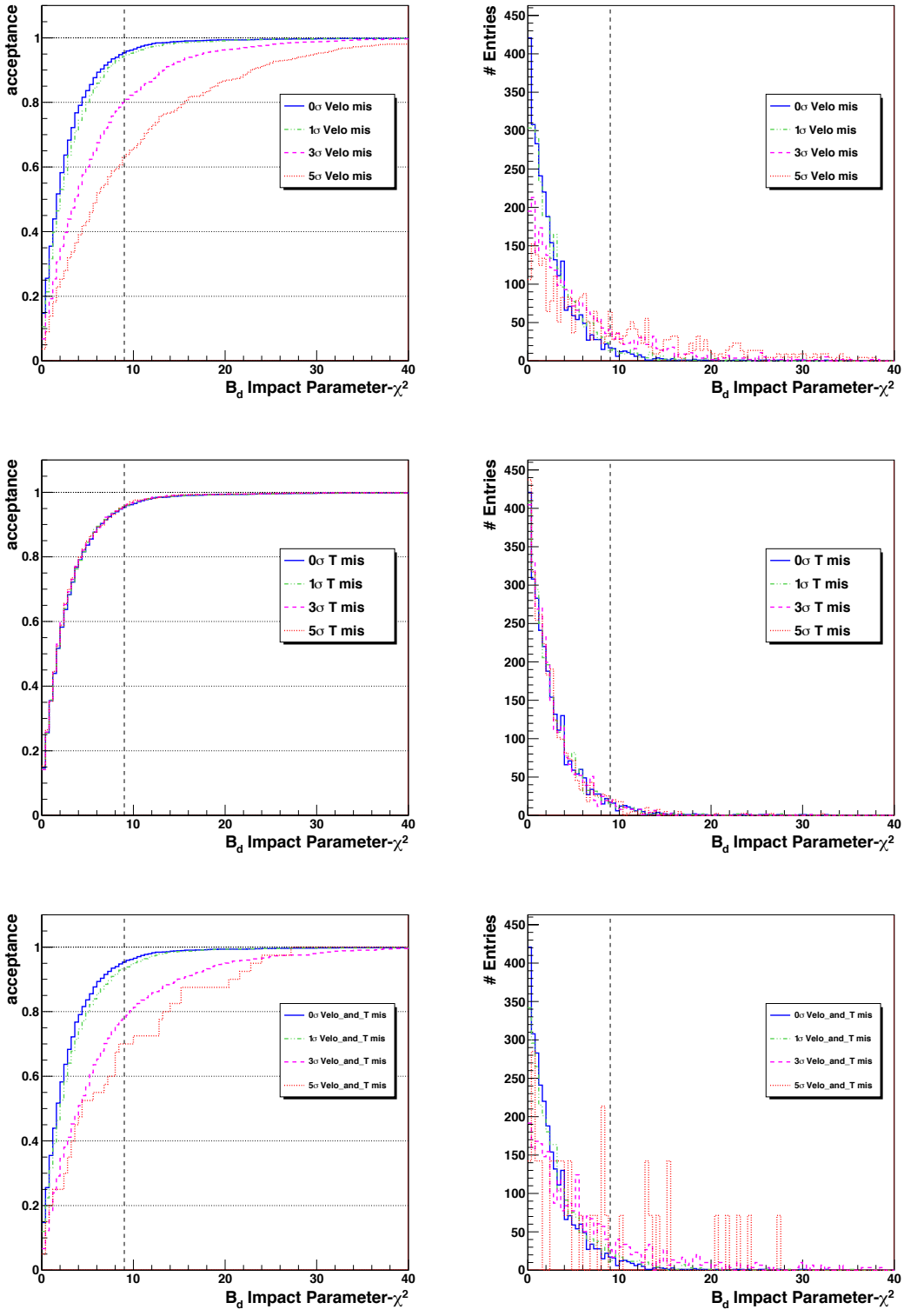

Figure 5.6: *Misalignment effects on the B_d Impact Parameter-χ^2 cut. The B_d Impact Parameter-χ^2 distributions are presented on the right-hand side and those on the left-hand side are the corresponding acceptance distributions. The top row is for the VELO misalignments, the middle row for T-station misalignments, and the bottom row for both combined. The chosen cut is a vertical dashed line.*

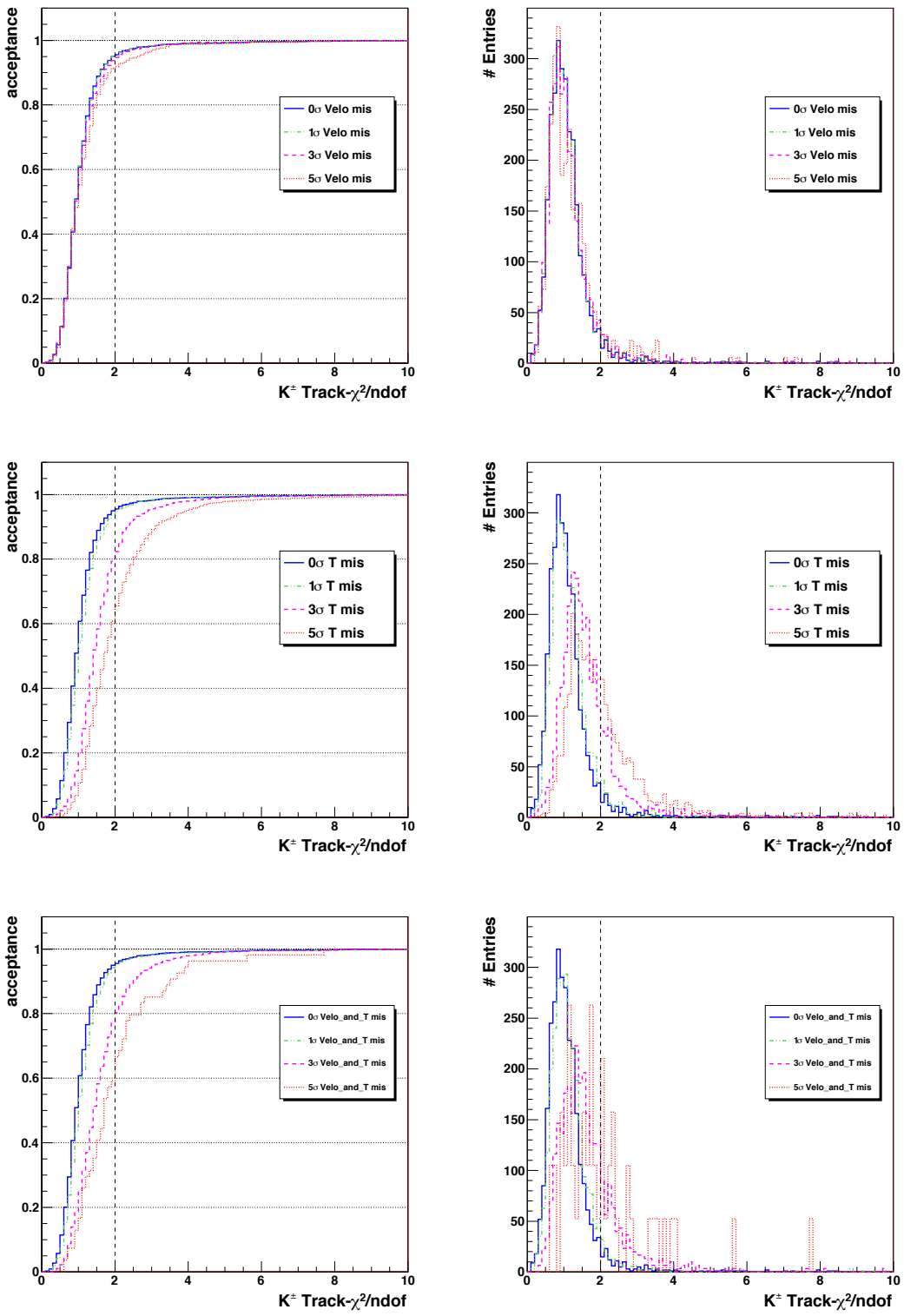

Figure 5.7: *Misalignment effects on the Kaon Track-χ^2/ndof cut. The Kaon Track-χ^2/ndof distributions are presented on the right-hand side and those on the left-hand side are the corresponding acceptance distributions. The top row is for the VELO misalignments, the middle row for T-station misalignments, and the bottom row for both combined. The chosen cut is a vertical dashed line.*

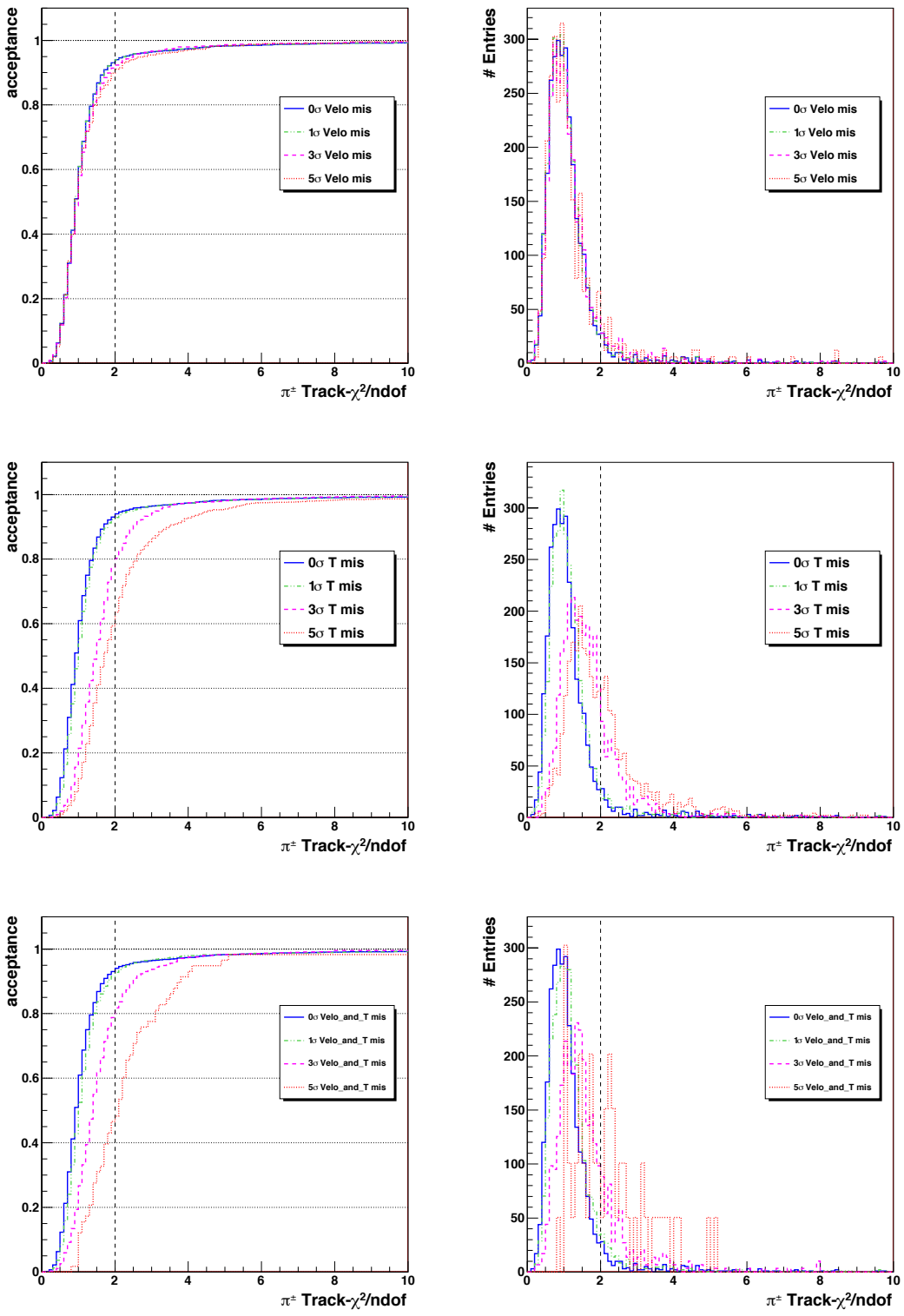

Figure 5.8: *Misalignment effects on the Pion Track-χ^2/ndof cut. The Pion Track-χ^2/ndof distributions are presented on the right-hand side and those on the left-hand side are the corresponding acceptance distributions. The top row is for the VELO misalignments, the middle row for T-station misalignments, and the bottom row for both combined. The chosen cut is a vertical dashed line.*

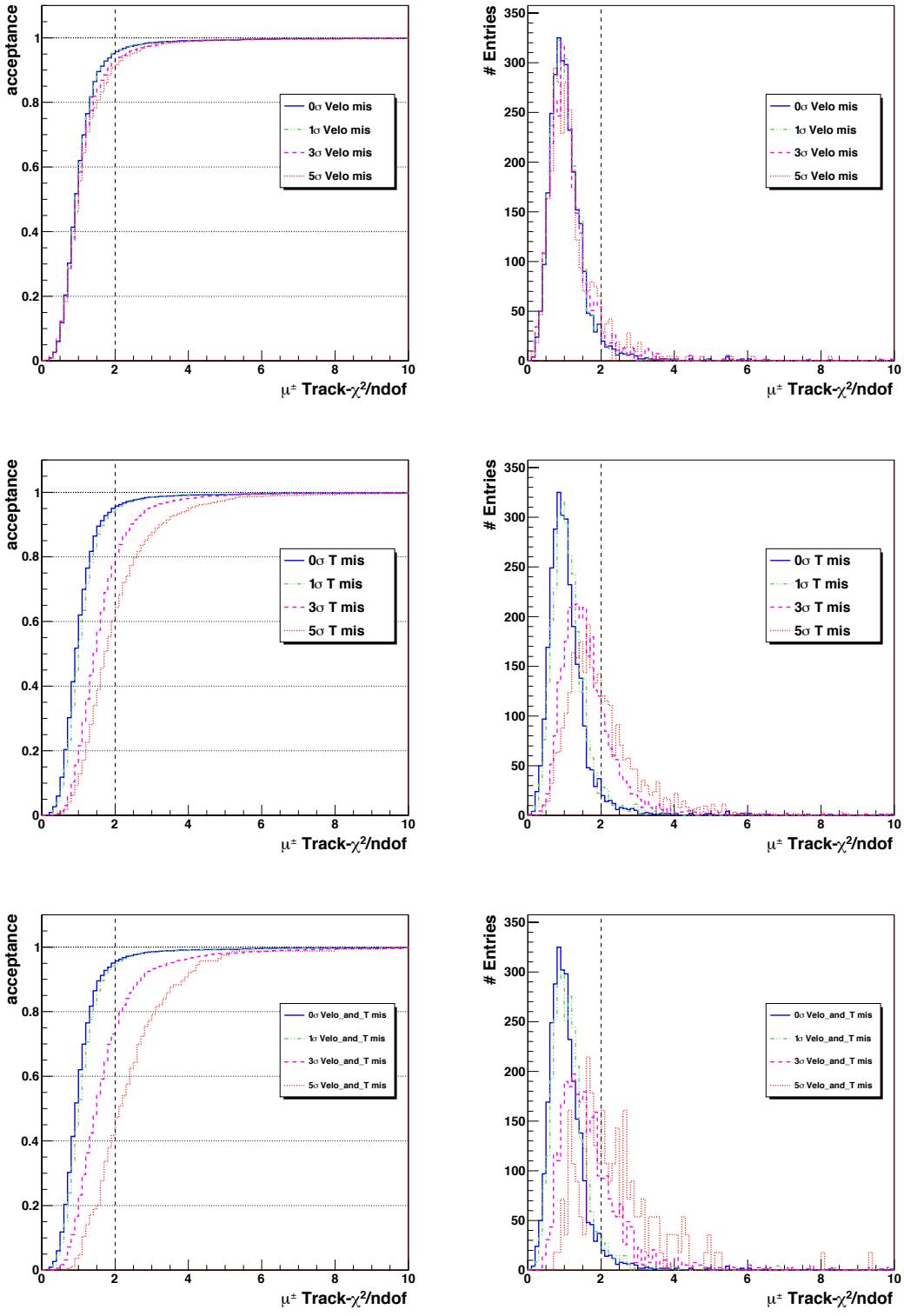

Figure 5.9: *Misalignment effects on the Muon Track-χ^2/ndof cut. The Muon Track-χ^2/ndof distributions are presented on the right-hand side and those on the left-hand side are the corresponding acceptance distributions. The top row is for the VELO misalignments, the middle row for T-station misalignments, and the bottom row for both combined. The chosen cut is a vertical dashed line.*

Misalignment scenario	Mass resolution [MeV/c^2]		
	VELO Mis.	T Mis.	VELO+T Mis.
0σ	15.5 ± 0.3	15.5 ± 0.3	15.5 ± 0.3
1σ	15.7 ± 0.3	15.6 ± 0.3	15.6 ± 0.3
3σ	16.7 ± 0.4	15.8 ± 0.3	16.0 ± 0.5
5σ	16.6 ± 0.7	15.7 ± 0.4	-

Table 5.8: *Misalignment effects on the B_d mass resolution. The available statistics are insufficient to perform the 5σ VELO+T misalignment mass fit.*

employed. The A_{FB} distributions were extracted using the unbinned method discussed in section 5.2.2. For the VELO misalignment, the T-station misalignment and the combined VELO and T-station misalignment cases 0σ, 1σ, 3σ and 5σ scenario were studied.

Since each of these misalignment scenarios consists of ten sub-samples of $6k$ generated events, ten A_{FB} distributions were extracted for each scenario. In order to increase the statistics only a very loose selection was applied. Table 5.9 presents the average number of selected events for each misalignment scenario obtained under these conditions, which corresponds to approximately 1 fb^{-1} each.

Figures 5.10, 5.11 and 5.12 are, respectively, the A_{FB} distributions obtained from the VELO, the T-station and the combined VELO and T-station misaligned data. Similarly to the method employed to extract the 1σ error presented in section 5.2.3, the 1σ error (green band) corresponds to the RMS of the entries of the ten A_{FB} distributions for each misalignment case. As shown in these figures any effect of detector misalignments on the A_{FB} distributions is not significant compared to the statistical error on these small samples.

The effects of the detector misalignments on the zero crossing point was quantified. From each of the A_{FB} distributions extracted from the misaligned data, their corresponding zero crossing point was directly obtained from the curve. Table 5.10 presents the values of the zero crossing point S_0 from all misalignment scenarios. The results obtained on these samples are given. The mean values all agree within the statistical errors. However, the different misalignments were all applied to the same sample and hence are correlated samples. At this point, it is not possible to judge if the difference in mean value is significant or not. Table 5.10 also contains the values scaled to 2 fb^{-1}, as the statistics vary between misalignment samples. These scaled values allow to see if a trend is observed on the S_0 uncertainty. No clear trend is observed. However, the

statistics are very limited in this study. Hence, further study with higher statistics is necessary to reduce the statistical error to a minimum and allow to extract the values of the systematic errors due to detector misalignments.

Misalignment scenario	Number of selected events		
	VELO Mis.	T Mis.	VELO+T Mis.
0σ	1858 ± 34	1858 ± 34	1858 ± 34
1σ	1840 ± 36	1856 ± 33	1844 ± 37
3σ	1632 ± 82	1860 ± 32	1672 ± 56
5σ	1430 ± 122	1882 ± 41	1356 ± 122

Table 5.9: *Average number of selected events from the ten sub-samples on each misalignment scenario by applying very loose cuts and no Particle Identification requirements in the $B_d \to K^*\mu^+\mu^-$ selection.*

5.4 Conclusion

This chapter has presented the analysis of the $B_d \to K^*\mu^+\mu^-$ decay. The $B_d \to K^*\mu^+\mu^-$ event selection was described as well as the simulated data employed and was used to evaluate the signal and background yields. The estimated signal yields from the DC06 and the MC09 data samples were, respectively, 4060^{+1080}_{-970} events/2 fb^{-1} and 4360^{+1160}_{-1040} events/2 fb^{-1}. The background yield was estimated from ($b \to \mu^-$, $\bar{b} \to \mu^+$) MC09 events, which is the main source of background for $B_d \to K^*\mu^+\mu^-$. The obtained background yield is 5300 ± 1800 events/2 fb^{-1}. Both the estimated signal and background yields are in agreement with the values obtained in previous studies.

The binned and unbinned methods of extraction of the forward backward asymmetry were defined. Both methods were employed to extract the A_{FB} distribution and its zero crossing point S_0. Using a data sample of 45.3 fb^{-1}, the extracted values of S_0 are 4.19 $\pm$ 0.08 GeV^2/c^4 and 4.12 $\pm$ 0.07 GeV^2/c^4 using the unbinned and the binned methods, respectively. The unbinned method gives direct access to the value of S_0, while the binned method may introduce a bias to the mean value of S_0 due to assumptions of fitting the data close to the crossing point. However, the bias is small and with its simplicity the binned method could be used for the earlier extraction of A_{FB} with real data obtained with the LHCb detector. The unbinned method was used to estimate the values of S_0 and its uncertainty, with data samples of 0.2 fb^{-1}, 2 fb^{-1} and 10 fb^{-1}.

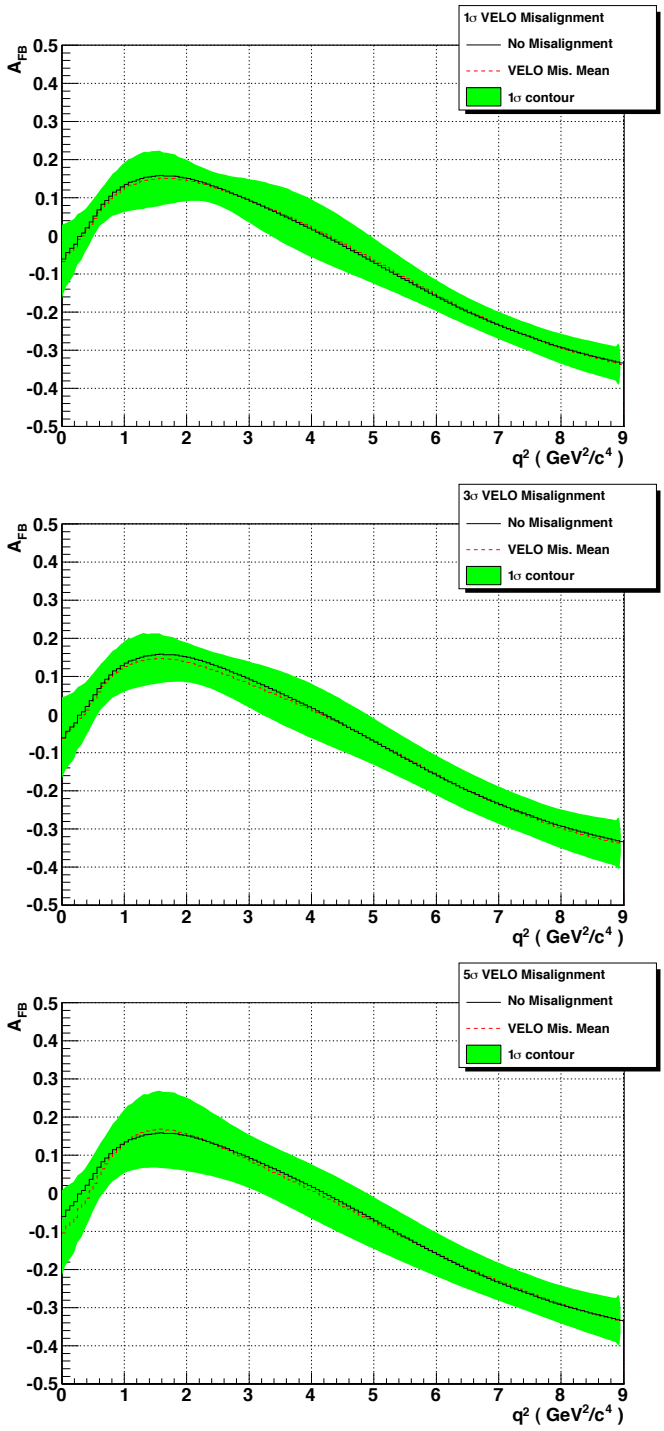

Figure 5.10: *A_{FB} distributions extracted from the VELO misaligned data of approximately 1* fb^{-1} *using the unbinned method. A- (top): The 1σ misalignment. B- (middle): The 3σ misalignment. C- (bottom): The 5σ misalignment. The average misaligned A_{FB} distribution is presented (red dashed line). The error band $\pm 1\sigma$ (green) and the average A_{FB} distribution obtained without misalignment (continuous line) are also shown.*

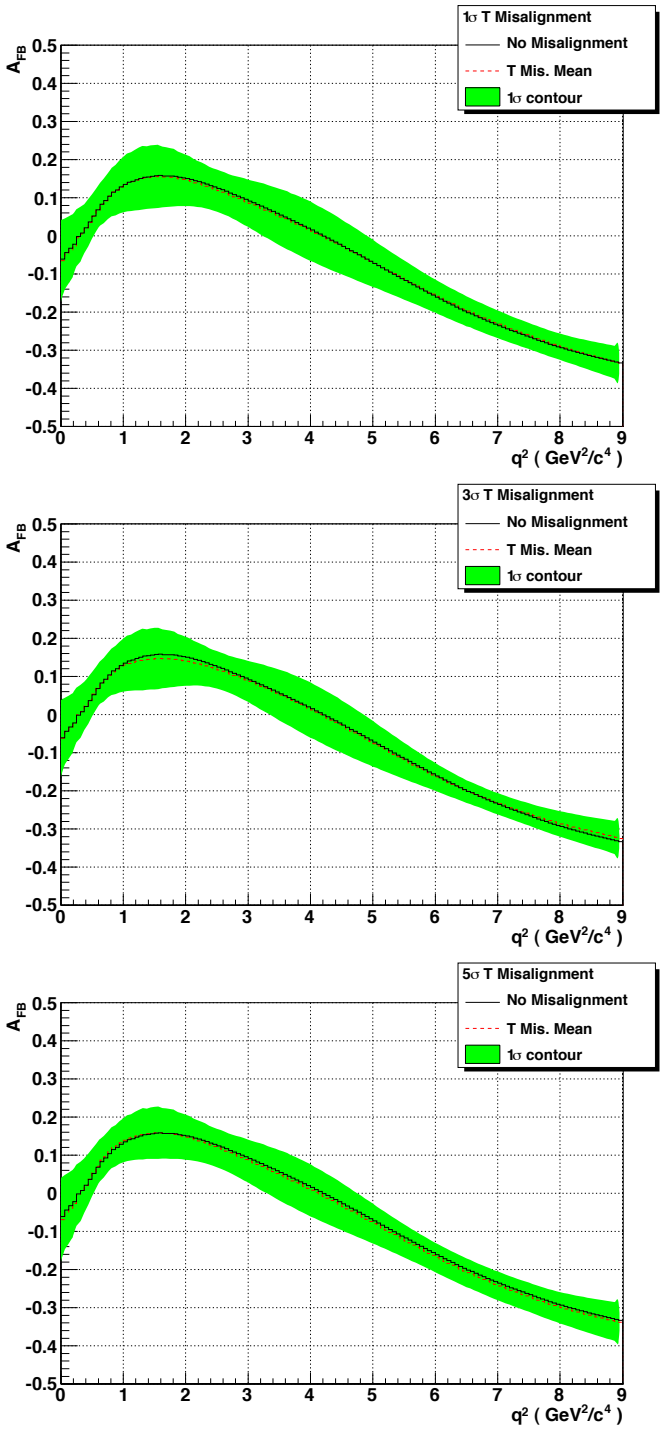

Figure 5.11: *A_{FB} distributions extracted from the T-station misaligned data of approximately 1 fb^{-1} using the unbinned method. A- (top): The 1σ misalignment. B- (middle): The 3σ misalignment. C- (bottom): The 5σ misalignment. The average misaligned A_{FB} distribution is presented (red dashed line). The error band $\pm 1\sigma$ (green) and the average A_{FB} distribution obtained without misalignment (continuous line) are also shown.*

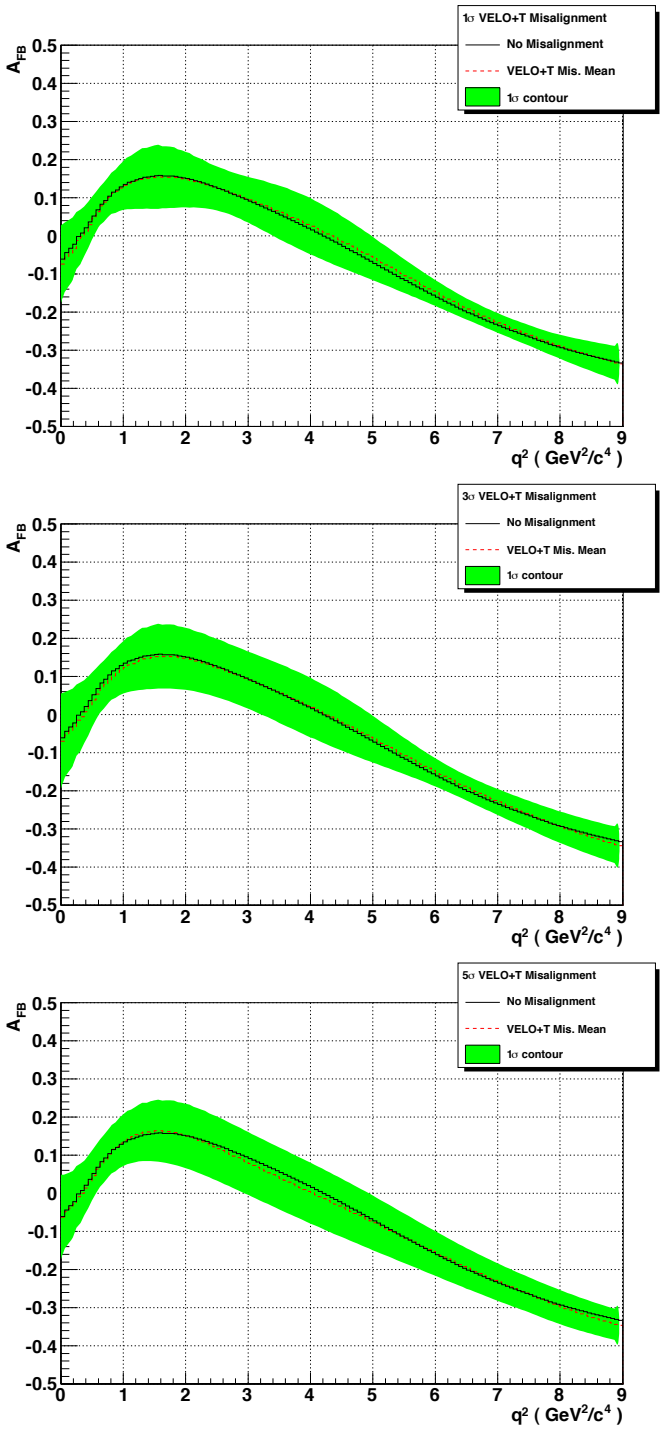

Figure 5.12: *A_{FB} distributions extracted from the combined VELO and T-station misaligned data of approximately 1* fb^{-1} *using the unbinned method. A- (top): The 1σ misalignment. B- (middle): The 3σ misalignment. C- (bottom): The 5σ misalignment. The average misaligned A_{FB} distribution is presented (red dashed line). The error band $\pm 1\sigma$ (green) and the average A_{FB} distribution obtained without misalignment (continuous line) are also shown.*

S_0 [GeV^2/c^4]				
Mis. Scenarios	Type	VELO Mis.	T Mis.	VELO+T Mis.
0σ (no mis.)	Result	$4.19\ ^{+0.69}_{-0.88}$	$4.19\ ^{+0.69}_{-0.88}$	$4.19\ ^{+0.69}_{-0.88}$
	Scaled to 2 fb^{-1}	4.19 ± 0.53	4.19 ± 0.53	4.19 ± 0.53
1σ	Result	$4.25\ ^{+0.69}_{-0.83}$	$4.13\ ^{+0.81}_{-0.88}$	$4.31\ ^{+0.69}_{-0.94}$
	Scaled to 2 fb^{-1}	4.25 ± 0.51	4.13 ± 0.57	4.31 ± 0.55
3σ	Result	$4.13\ ^{+0.75}_{-0.94}$	4.13 ± 0.75	$4.25\ ^{+0.75}_{-1.06}$
	Scaled to 2 fb^{-1}	4.13 ± 0.53	4.13 ± 0.50	4.25 ± 0.58
5σ	Result	$4.06\ ^{+0.81}_{-0.88}$	$4.13\ ^{+0.63}_{-0.81}$	$4.0\ ^{+0.94}_{-1.06}$
	Scaled to 2 fb^{-1}	4.06 ± 0.50	4.13 ± 0.49	4.00 ± 0.58

Table 5.10: *Values of the A_{FB} zero crossing point S_0 from the detector misaligned data. Their values scaled to 2* fb^{-1} *are presented.*

The obtained values of S_0 are, respectively, $4.0\ ^{+0.8}_{-1.4}$ GeV^2/c^4, 4.19 ± 0.38 GeV^2/c^4 and 4.19 ± 0.17 GeV^2/c^4.

In addition, the effects of detector misalignments on the $B_d \to K^*\mu^+\mu^-$ decay were quantified. The effects of the VELO misalignments, the T-station misalignments and the combined VELO and T-station misalignments were analysed. Their effects on the pattern recognition, the event selection, the B_d mass resolution and on the forward backward asymmetry and its zero crossing point were studied.

On the selection, it was found that the selection cut on the B_d Impact Parameter-χ^2, the Kaon, Pion and Muon Track-χ^2 are the most affected variables. The effects on the Impact Parameter-χ^2 are more driven by the VELO misalignment than the T-stations, which drive the effects on the Track-χ^2. As the current knowledge of misalignment obtained from data is $\approx 1.5\sigma$, no significant effect is expected on the selection of $B_d \to K^*\mu^+\mu^-$ events as well as the B_d mass resolution.

The effect of misalignments on the A_{FB} distribution was also considered, but the statistics used do not allow conclusions to be drawn on whether this will be significant in the LHCb data. Repeating the study with much higher statistics and more realistic misalignments is proposed in order to reduce the statistical error to a minimum and allow the extraction of the systematic errors due to detector misalignments for the first publication.

6 Conclusion

6.1 Summary

This thesis began by introducing the Standard Model (SM) theory of elementary particles with discussion on the electroweak and QCD components of the theory. Particular emphasis was placed on the rare B decay $B_d \to K^*\mu^+\mu^-$, which is one of the golden modes in the LHCb experiment.

The LHCb experiment, which started data taking at the end of 2009, will make precise measurements of CP violation and rare decays. The $B_d \to K^*\mu^+\mu^-$ decay is an important channel for indirect measurements of new physics phenomena, and observables that can be measured at LHCb were discussed. Recent experimental results from the B-factories and the Tevatron on the measurements of various observables, which are significant for $B_d \to K^*\mu^+\mu^-$ were also presented.

The LHCb detector and its six sub-detectors were described. The VELO is one of the tracking detectors of LHCb, provides the tracking coordinates close to the interaction point and is used to define the primary and secondary vertices. The VELO system was extensively described, since the work presented in this thesis was mainly focused on the VELO. The trigger and the online system were also presented. The main projects that comprise the LHCb software were described as they were used for the production and analysis of the $B_d \to K^*\mu^+\mu^-$ events.

The VELO silicon strip sensors must be operated under reversed bias. A reliable and secure high voltage system that can operate up to 500 V is therefore required for the VELO. A substantial programme of quality assurance tests were performed on both the hardware and software parts of the high voltage system. The noise spectra were measured at the module output and at the end of the detector cable installed in the Pit. A small excess of noise was observed in the range of 50 MHz to 80 MHz at the module output and also at 44 MHz and 53 MHz at the end of the detector cable installed in the LHCb Pit. This excess of noise is found to be suppressed to a negligible level when connecting a load emulating the hybrid.

Long term tests of the high voltage power supply at the defined voltage level, during

ramping and when the interlock signals are fired individually and globally did not show any spikes. Spikes up to 1 V were observed during short power glitches. In case of a power-cut, an uninterruptible power supply (UPS) is provided, and this was tested. The crate powers the modules temporarily and all channels are ramped down to 0 V with a ramping speed of 12 V/s.

The VELO high voltage has a reliable protection system both in hardware and in software for the VELO modules. All high voltage channels can be inhibited individually or globally by firing the interlock signal of the corresponding channel(s), which causes the corresponding channel(s) to power down at a speed of approximately 5 kV/s. The high voltage hardware and current limits of the modules can be changed as desired. The VELO power supplies are always operated in current trip mode. Under this mode, the channel that triggers a trip alarm shuts off directly.

The current-voltage characteristics of the VELO sensors taken during the module production and during the commissioning in December 2008, in June 2009 and in October 2009 were analysed. The leakage current of a number of sensors was found to increase on cooling to -25°C, contrary to expectation. This could be a consequence of stress in the modules and will be monitored. The evolution of currents over time for all data has shown no obvious increase in the number of high leakage current sensors. Approximately 8% of the sensors showed non-negligible leakage current increases compared to production. The increases are small enough not to affect their performance. The VELO high voltage system complies with the safety and the performance of the VELO sensors and is currently employed to bias the VELO sensors.

The upgrade of the LHC will require silicon strip detectors that are more radiation hard. P-type silicon sensors are one possible candidate for the upgraded LHC detectors. P-type detectors with four different isolation techniques before and after irradiation up to 10^{16} n_{eq}/cm^2 were characterised.

Before irradiation, the current-voltage and capacitance-voltage characteristics of ten detectors tested in Glasgow and 19 other detectors tested in Liverpool were analysed. The breakdown and full depletion voltages of each detector were identified. A breakdown voltage above 1000 V was observed within all categories of isolation employed, apart from Type 4†, which includes individual p-stops. The full depletion voltage of the detectors was not significantly different between isolation techniques, with an average of approximately 170 V.

After irradiation, five detectors were characterised. Their IV characteristics were taken and the breakdown voltages were identified. The charge collected was mea-

†See details in section 4.2.2.2, for the definition of the different types of isolation.

sured and the charge collection efficiency was compared. Approximately 30% of charge was collected for both fluences of 5×10^{15} n_{eq}/cm^2 and 10^{16} n_{eq}/cm^2, for bias voltages of 900 V and 1000 V respectively. At a fluence of 2×10^{15} n_{eq}/cm^2 the Type 1 detector, with p-spray, could be biased to a higher voltage than the Type 3 detector, with common p-stops, potentially due to the p-spray isolation technique and as a result it collected $\approx$ 15% more charge. The n-on-p detectors are a promising candidate for the LHCb upgrade as they provide a reasonable collected charge at fluences up to 10^{16} n_{eq}/cm^2. Moreover, they can be operated not fully depleted. As the replacement of the VELO sensors will be n-on-p detectors, operating the n-on-p VELO sensors at the maximum voltage of the current system of 500 V, after a fluence of $\approx$ 5×10^{14} n_{eq}/cm^2 corresponding to approximately 7 fb^{-1}, will ensure a collected charge of $\approx$ 65 %.

The analysis of the $B_d \to K^*\mu^+\mu^-$ decay was presented. The $B_d \to K^*\mu^+\mu^-$ event selection was described as well as the simulated data employed, which was used to evaluate the signal and background yields. The estimated signal yields from the DC06 and the MC09 data samples were, respectively, 4060^{+1080}_{-970} events/2 fb^{-1} and 4360^{+1160}_{-1040} events/2 fb^{-1}. The background yield was estimated from ($b \to \mu^-$, $\bar{b} \to \mu^+$) MC09 events, which is the main source of background for $B_d \to K^*\mu^+\mu^-$. The obtained background yield is 5300 $\pm$ 1800 events/2 fb^{-1}. Both the estimated signal and background yields are in agreement with the values obtained in previous studies.

The forward backward asymmetry (A_{FB}) is a particularly sensitive observable to New Physics contributions. The binned and unbinned method of extraction of the forward backward asymmetry were discussed. Both methods were employed to extract the A_{FB} distribution and its zero crossing point S_0. The unbinned method gives direct access to the value of S_0, while the binned method may introduce a bias to the mean value of S_0 due to assumptions of fitting the data close to the crossing point. However, the bias is small compared to the statistical error and, due to its simplicity, the binned method could be used for the earlier extraction of A_{FB} with real data obtained with the LHCb detector. The unbinned method was used to estimate the values of S_0 and its uncertainty, with data samples of 0.2 fb^{-1}, 2 fb^{-1} and 10 fb^{-1}. The obtained values of S_0 are, respectively, 4.0 $^{+0.8}_{-1.4}$ GeV^2/c^4, 4.19 $\pm$ 0.38 GeV^2/c^4 and 4.19 $\pm$ 0.17 GeV^2/c^4.

The effects of detector misalignments on the $B_d \to K^*\mu^+\mu^-$ decay were quantified. The effects of the VELO misalignments, the T-station misalignments and the combined VELO and T-station misalignments were analysed as a function of expected misalignment levels of 1σ, 3σ and 5σ. Their effects on the pattern recognition, the event selection, the B_d mass resolution and on the forward backward asymmetry and

its zero crossing point were studied.

On the selection, it was found that the selection cut on the B_d Impact Parameter-χ^2, the Kaon, Pion and Muon Track-χ^2 are the most affected variables. The effects on the Impact Parameter-χ^2 are more driven by the VELO misalignment than the T-stations, which drive the effects on the Track-χ^2. At the current knowledge of detector alignment a reduction of less than 10% from perfect alignment can be expected for the selection of $B_d \to K^*\mu^+\mu^-$ events.

The effect of misalignments on the A_{FB} distribution was also considered, but the statistics used do not allow conclusions to be drawn on whether this effect will be significant in the LHCb data. Repeating the study with much higher statistics and more realistic misalignments is proposed in order to reduce the statistical error to a level that will allow the extraction of the systematic errors due to detector misalignments for the first publication.

In summary this thesis has presented work in three areas. The design and characterisation of the high voltage system of the VELO has been shown. The qualification studies of p-type silicon sensors before and after proton and neutron irradiations have shown that they are promising candidates for the proposed upgrade of the LHC. Finally, the analysis of $B_d \to K^*\mu^+\mu^-$ simulation events has permitted the extraction of the forward backward asymmetry from fully reconstructed simulated data as well as its zero crossing points using the binned and unbinned methods. The VELO high voltage system has successfully supplied bias voltages to the VELO sensors and has made possible the reconstruction of the first tracks from data recorded with the LHCb VELO detector, as presented in figure 6.1.

6.2 Outlook

LHCb started regular data taking at the end of 2009, the LHCb collaboration has already started to analyse the data and is trying to fully understand the detector. In future years, as more data will be obtained, radiation damage to the VELO sensors will be an issue and will need to be monitored. Current-voltage characteristics are regularly taken in order to monitor the radiation effects on the sensors. Charge collection measurements at different voltages are an alternative method of monitoring this induced non-uniform radiation damage to the VELO sensors, which is also being used.

Radiation damage induces changes to the properties of the sensors. The replacement of the VELO sensors, with identical geometry to the current VELO, is foreseen with n-on-p silicon strip sensors. These sensors have already been shown to be a good

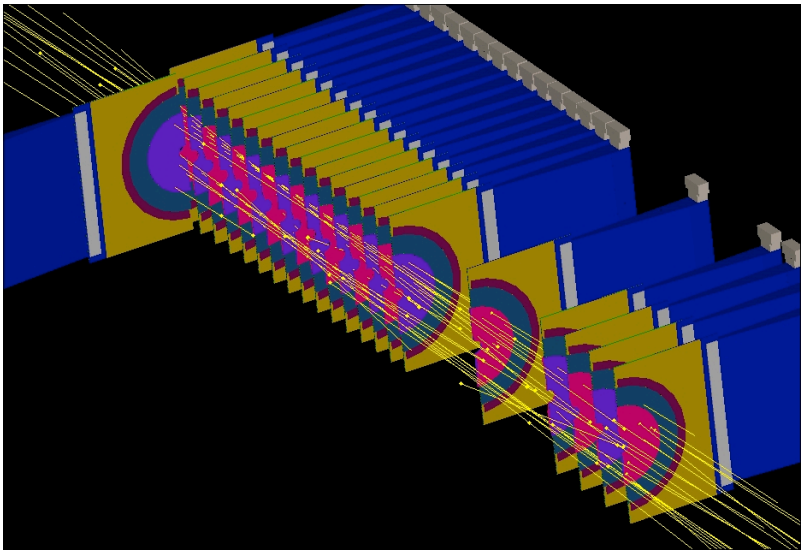

Figure 6.1: *Panoramix picture of the first tracks reconstructed from data recorded with the LHCb VELO detector. Reproduced from [140].*

candidate for a future luminosity upgrade of the LHC experiments (SLHC). Other alternative solutions are also possible for the upgrade, such as 3D detectors or Diamond which have shown good radiation hardness performance with the SLHC fluences of the order of 10^{16} $\mathrm{n_{eq}/cm^2}$.

As more data is collected, LHCb will be able to make measurements of the forward backward asymmetry A_{FB} and its zero crossing point S_0 using the $B_d \to K^*\mu^+\mu^-$ decay. The two methods presented in this thesis could both be used to extract A_{FB} and S_0, and have their respective advantages. The binned method, with its simplicity, could be used for the earlier extraction of the A_{FB} and S_0. On the other hand, the unbinned method, a more complex method, gives direct access to S_0 and might be more appropriate at higher integrated luminosities. Other variables sensitive to the contribution of New Physics phenomena, such as F_L and S_5, can also be extracted. In the longer term use of the full angular information in $B_d \to K^*\mu^+\mu^-$ can be made to maximise the sensitivity to a New Physics discovery.

Bibliography

[1] S.L. Glashow. Partial Symmetries of Weak Interactions. *Nucl. Phys. 22:579-588*, 1961.

[2] S. Weinberg. A Model of Leptons. *Phys. Lett., 19*, 1967.

[3] A. Salam and J.C. Ward. Electromagnetic and weak interactions. *Phys. Lett. 13:168 171*, 1964.

[4] S. Davidson. The Standard Model. *RAL-TR-2007-004*.

[5] M. Herrero. The Standard Model. *arXiv:hep-ph/9812242v1*, 1998.

[6] C. Amsler et al. Particle Data Group. *Phys. Lett. B667, 1*, 2008 and 2009 partial update for the 2010 edition.

[7] A. Salam. Elementary Particle Theory: Relativistic Groups and Analicity. *In Proceedings of The* 8^{th} *Nobel Symposium, Estocolmo*, 1968.

[8] M. E. Peskin and D. V. Schroeder. An Introduction to Quantum Field Theory. *Addison-Wesley*, 1995.

[9] Y. Fukuda et al. Evidence for oscillation of atmospheric neutrinos. *Phys. Rev. Lett., 81:1562-1567*, 1998.

[10] P. W. Higgs. Broken Symmetries and the masses of gauge bosons. *Phys. Rev. Lett., 13:508*, 1964.

[11] N. Cabibbo. Unitary Symmetry and Leptonic Decays. *Phys. Rev. Lett. 10:531-533*, 1963.

[12] I. Bigi and A. Sanda. CP Violation. *Nucl. Phys. B, 193:85-108*, 1981.

[13] Eds. P. Harrison and H. Quinn. The BaBar Physics Book. *SLAC report 504*, 1998.

[14] Eds. P. Ball, R. Fleischer, G.F. Tartarelli, P. Vikas and G. Wilkinson. B Decays at the LHC. *hep-ph/0003238*.

[15] M. Kobayashi and K. Maskawa. *Prog. Theor. Phys., 49:652*, 1973.

[16] T. Mannel. Effective field theories in flavour physics. *Springer Tracts in Modern Physics, 203:23-31*, 2004.

[17] M. Adinolfi et al. The tree-level determination of γ at LHCb. *LHCB-ROADMAP5-002*, 2009.

[18] A. Bates et al. Road map for charmless charged two-body B decays at LHCb. *LHCB-ROADMAP6-001*, 2009.

[19] G. Sterman et at. Handbook of Perturbative QCD. *Rev. Mod. Phys., 67:157*, 1995.

[20] C.J. Maxwell. Perturbative and non-perturbative QCD. *arXiv:hep-ph/0611120v1*, 2006.

[21] S.L. Glashow, J. Iliopoulos and L. Maiani. *Phys. Rev., D2:1285*, 1970.

[22] F.J. Hasert et al. Observation of neutrino-like interactions without muon or electron in the gargamelle neutrino experiment. *Phys. Lett. B 1, 46:138-140*, 1973.

[23] P. Bagnaia et al. Evidence for $Z^0 \rightarrow e^+e^-$ at the CERN $\bar{p}p$ collider. *Phys. Lett. B 129, 1-2:130-140*, 1983.

[24] P. Aarnio et al. Measurement of the mass and width of the Z0-particle from multihadronic final states produced in e+e- annihilations. *Phys. Lett. B 231, 4:539-547*, 1989.

[25] J. H. Christenson, J. W. Cronin, V. L. Fitch and R. Turlay. Evidence for the 2π Decay of the K_2^0 Meson. *Phys. Rev. Len. 13, 138-140* , 1964.

[26] Abulencia et al. Observation of $B_s^0 - \bar{B}_s^0$ Oscillations. *Phys. Rev. Lett. 97,24:8*, 2006.

[27] A. Zupanc. Mixing and CP violation in heavy meson decays from Belle. *Nucl. Phys. A, 827:466c-468c*, 2009.

[28] F. Marinho. Quality Assurance of the VELO Module and Analysis of the $B_d \to K^*\mu^+\mu^-$ Rare Decay on LHCb. *University of Glasgow. PhD Thesis CERN-THESIS-2009-002.*

[29] P. Koppenburg. Contribution to the Development of the LHCb Vertex Locator and Study of Rare Semileptonic Decays. *University of Lausanne. PhD Thesis CERN-THESIS-2002-010*, 2002.

[30] J. Dickens. A Study of the RICH Detector Performance and Search for New Physics in $B_d \to K^*\mu^+\mu^-$ Decays within the LHCb experiment. *University of Cambridge. PhD Thesis CERN-THESIS-2009-084*, 2008.

[31] R. Ammar et al. Evidence for penguin-diagram decays: First observation of $B \to K^*(892)\gamma$. *Phys. Rev. Lett. 71, 674-678*, 1993.

[32] D. E. Kaplan. Particle Physics Beyond the Standard Model. *Second CERN-Fermilab Hadron Collider Physics Summer School*, 2007.

[33] F. D. Steffen. Supersymmetric Dark Matter Candidates. *hep-ph/07111240.*

[34] K. G.Wilson andW. Zimmermann. Operator Product Expansion and Composite Field Operators in the General Framework of Quantum Field Theory. *Commun. Math. Phys., 24:87*, 1972.

[35] P. Koppenburg. Study of rare semileptonic B decays at LHCb. *LHCb-2002-017*, 2002.

[36] M. Gorbahn and U. Haisch. *Nucl. Phys. B, 713:291-332*, 2005.

[37] C. Bobeth, P. Gambino, M. Gorbahn and U. Haisch. *JHEP, 04:071*, 2004.

[38] M. Beneke, T. Fieldmann and D. Seidel. *Nucl. Phys. B, 612:25-58*, 2001.

[39] C. Bobeth, M. Misiak and J. Urban. Photonic penguins at two loops and m_t-dependence of BR $[BR \to X_s l^+ l]$. *Nucl. Phys. B, 574:291*, 2000.

[40] J. Dickens and al. Roadmap for the analysis of $B_d \to K^*\mu^+\mu^-$. *LHCB-PUB-2009-029*, 2009.

[41] W. Altmannshofer et al. Symmetries and asymmetries of $B \to K^* \mu^+ \mu^-$ decays in the Standard Model and beyond. *JHEP01 019*, 2009.

[42] A. Ali,P. Ball, L. T. Handoko and G. Hiller. *Phys. Rev., D61:074024*, 2000.

[43] A. Ali et al. A Comparative study of the decays B→(K,K*)l^+l^- in Standard Model and Supersymmetrie theories. *Phys. Rev. D 61:074024*, 2000.

[44] A. Bharucha and W. Reece. Constraining new physics with $B \to K^* \mu^+ \mu^-$ in the early LHC era. *IPPP/10/12, DCPT/10/24, IC/HEP/010-1, arXiv:1002.4310v2*, 2010.

[45] A. Ishikawa et al. Observation of $B \to K^* l^+ l^-$. *Phys. Rev. Lett., 91:261601*, 2003.

[46] B. Aubert et al. Evidence for the Rare Decay $B \to K^* l^+ l^-$ and Measurement of the $B \to K l^+ l^-$ Branching Fraction. *Phys. Rev. Lett., 91:221802*, 2003.

[47] T. Aaltonen et al. Search for the rare decays $B+ \to \mu^+ \mu^- K^+$, $B \to \mu^+ \mu^- K^*(892)$, and $B_s \to \mu^+ \mu^- \phi$ at CDF. *Phys. Rev. D,79:011104*, 2009.

[48] The Babar Collaboration. Direct CP, Lepton Flavor and Isospin Asymmetries in the Decays $B \to K^{(*)} l^+ l^-$. *Phys. Rev. Lett. 102, 091803*, 2009.

[49] B. Aubert et al. Angular distributions in the decay $B \to K^* l^+ l^-$. *Phys. Rev. D, 79:031102*, 2009.

[50] J. T. Wei et al. Measurement of the Differential Branching Fraction and Forward-Backward Asymmetry for $B \to K^{(*)} l^+ l^-$. *Phys. Rev. Lett., 103:171801*, 2009.

[51] The CDF Collaboration. Measurement of Forward-Backward Asymmetry in $B \to K^{(*)} \mu^+ \mu^-$ and First Observation of $B_s^0 \to \phi \mu^+ \mu^-$. *CDF note 10047, http://www-cdf.fnal.gov*, 2010.

[52] The Large Hadron Collider. http://lhc.web.cern.ch/lhc/, February 2009.

[53] L. Evans et al. The CERN Large Hadron Collider: Accelerator and Experiments. *JINST S08001*, 2008.

[54] The European Centre for Nuclear Reasearch. http://public.web.cern.ch/Public/Welcome.html, December 2008.

[55] The Linear Electron Collider. http://public.web.cern.ch/public/en/Research/LEP-en.html, December 2008.

[56] The Linear Accelerator LINAC2. http://linac2.home.cern.ch/linac2/, January 2008.

[57] The Proton Synchrotron Booster. http://ab-dep-op-psb.web.cern.ch/, April 2009.

[58] The Proton Synchrotron. http://public.web.cern.ch/public/en/Research/PS-en.html, December 2008.

[59] The Super Proton Synchrotron. http://public.web.cern.ch/public/en/Research/SPS-en.html, December 2008.

[60] G. A. et al. The ATLAS experiment at the CERN Large Hadron Collider. *JINST S08003*, 3, 2008.

[61] S. Chatrchyan et al. The CMS experiment at the CERN LHC. *JINST S08004*, 3, 2008.

[62] K. Aamodt et al. The ALICE experiment at the CERN LHC. *JINST S08002*, 3, 2008.

[63] Reoptimized LHCb Detector Design and Performance TDR. *CERN-LHCC-2003-030*.

[64] The LHCb Experiment Technical Proposal. *CERN-LHCC-98-004*.

[65] S. Viret, C. Parkes, M. Gersabeck. Alignment procedure of the LHCb vertex detector. *Nucl. Instrum. Meth. A 596:157-163*, 2008.

[66] The LHCb detector at LHC. *JINST S08005*, 3, 2008.

[67] The LHCb VELO Technical Design Report. *CERN-LHCC-2001-0011*.

[68] T. Bowcock et al. Performance of an irradiated $n^+ - on - n$ Hamamatsu prototype VELO detector. *LHCb-2001-039*.

[69] The ROSE collaboration. 3rd RD-48 status report. *CERN-LHCC-2000-009*.

[70] The LHCb Liverpool Home page. http://hep.ph.liv.ac.uk/lhcb/index.html, November 2006.

[71] The Beetle Manual Reference. *CERN-LHCb-2005-105.*

[72] G. Haefeli et al. The LHCb DAQ interface board TELL1. *Nucl. Instrum. Meth. A 560:494-502*, 2006.

[73] T. Szumlak and C. Parkes. Description of the Vetra Project and its Application for the VELO Detector. *Technical Report CERN-LHCb-2008-022*, May 2008.

[74] The LHCb Technical Design Report: RICH. *CERN-LHCC-2000-037.*

[75] T. Gys et al. First operation of a hybrid photon detector prototype with electrostatic cross-focussing and integrated silicon pixel readout. *Nucl. Instrum. Meth. A 449:48-59*, 2000.

[76] The LHCb Technical Design Report: Inner Tracker. *CERN-LHCC-2002-029.*

[77] The LHCb Technical Design Report: Outer Tracker. *CERN-LHCC-2001-024.*

[78] The LHCb Technical Design Report: Calorimeters. *CERN-LHCC-2000-036.*

[79] The LHCb Technical Design Report: Muon System. *CERN-LHCC-98-010.*

[80] LHCb Addendum to the Muon System Technical Design Report. *CERN-LHCC-2003-002.*

[81] The LHCb Technical Design Report: LHCb Trigger System. *CERN-LHCC-2003-031.*

[82] The LHCb Technical Design Report: Online System, Data Acquisition and Experiment Control. *CERN-LHCC-2001-040.*

[83] Addendum to the LHCb Online System Technical Design Report. *CERN-LHCC-2001-039.*

[84] G. Barrand et al. GAUDI - A software architecture and framework for building HEP data processing applications. *Comput. Phys. Commun., 140:45-55*, 2001.

[85] D. J. Lange. The EvtGen particle decay simulation package. *Nucl. Instrum. Meth. A 462:152-155*, 2001.

[86] S. Agostinelli et al. GEANT 4: simulation toolkit. *Nucl. Instrum. Meth. A 506:250-303*, 2003.

[87] N.A. Smith et al. VELO Interlock. *The CERN Engineering and Equipment Data Management Service Document No: 706629. https://edms.cern.ch.*

[88] J. Libby et al. The LHCb Vertex detector. *Nucl. Instrum. Meth. A 494:113-119*, 2002.

[89] M. Moll. Radiation Damage in Silicon Particle Detectors. *DESY-THESIS-1999-040*, 1999.

[90] G. Casse et al. Charge collection studies and annealing effects in heavily irradiated planar silicon strip sensors. *Nuclear Science Symposium and Medical Imaging Conference, 25-31 October 2009, Orlando, Florida, USA.*

[91] The ROSE Collaboration. 3^{rd} RD48 Status Report. *CERN/LHCC 2000-009*, 1999.

[92] T. Schulz, H. Feick, E. Fretwurst, G. Lindstrom, M. Moll, K.H. Mahlmann. Long term reverse annealing in silicon detectors. *IEEE Trans. Nucl. Sci. 41, 4:791 - 795*, 1994.

[93] B. Rakotomiaramanana et al. High Voltage Connectivity. *The CERN Engineering and Equipment Data Management Service Document No: 836439. https://edms.cern.ch.*

[94] T. Smith. Engineering drawings of K05 kapton hybrid. *The CERN Engineering and Equipment Data Management Service Document No: 598706. https://edms.cern.ch.*

[95] L. Eklund. PCB layout for counting house patch panel. *The CERN Engineering and Equipment Data Management Service Document No: 833525. https://edms.cern.ch.*

[96] A. Saavedra. LHCb VeLo High Voltage Patch Panel. *The CERN Engineering and Equipment Data Management Service Document No: 833526. https://edms.cern.ch.*

[97] ETM professional control PVSS. http://www.pvss.com.

[98] P. C. Burkimsher. JCOP Experience with a Commercial SCADA product, PVSS. *9th International Conference on Accelerator and Large Experimental Physics Control Systems, Korea*, October 2003.

[99] W. Salter. The LHC Experiments' Joint Controls Project (JCOP). *Computing in High Energy and Nuclear Physics CHEP'01, Beijing*, September 2001.

[100] P. Y. Duval et al. Guide for ECS FSM design in LHCb sub-detectors. *The CERN Engineering and Equipment Data Management Service Document No: 655828. https://edms.cern.ch.*

[101] ISEG. High Voltage Power Supply EHQ F607n-F Operator manual. http://www.iseg-hv.de.

[102] B. Rakotomiaramanana et al. VELO High Voltage Procedure. *The CERN Engineering and Equipment Data Management Service Document No: 9096687. https://edms.cern.ch.*

[103] S. Borghi, C. Parkes et al. First LHC induced tracks reconstructed in the LHCb VELO. *Nucl. Instrum. Meth. A 604:1-4*, 2009.

[104] The LHCb Collaboration. Expression of Interest for an LHCb Upgrade. *CERN-LHCb-2008-019*, 2008.

[105] S. Sze. Semiconductor Devices and Technology. *John Wiley and Sons, New York*, 1985.

[106] G. Lutz. Semiconductor Radiation Detector Physics. *Spring-Verlag, Berlin Heidelberg New York, first edition*, 1999.

[107] R. Wunstorf. Radiation Hardness of Silicon Detectors. *IEEE Trans. Nucl. Sci. 44, 3*, 1997.

[108] The RD50 Collaboration. RD50 Status Report 2005: Radiation hard semiconductor devices for very high Luminosity colliders. *CERN-LHCC-2005-037. LHCC-RD-009*, 2005.

[109] Y. Unno. Silicon Sensor Development for the ATLAS upgrade for SLHC. *Nucl. Instrum. Meth. A, 569:41-47*, 2006.

[110] I. Gorelov et al. Electrical Characteristics of Silicon Pixel Detectors. *Nucl. Instrum. Meth. A, 489:202-217*, 2002.

[111] S. Parker and C. Kenney. Charge compensation in irradiated semiconductor devices using high-resistivity field plates. *Nucl. Instrum. Meth. A, 465:101-107*, 2001.

[112] Y. Unno et al. Evaluation of P-stop Structure in the N-side of N-on-N Silicon Strip Detector. *IEEE Trans. Nucl. Sci. 45,401*, 1998.

[113] S. Braibant et al. Investigation of design parameters and choice of substrate resistivity and crystal orientation for the CMS silicon microstrip detector. *CMS-NOTE-2000-011*, 2000.

[114] S. Terada et al. Proton Irradiation on p-bulk Silicon Strip Detectors using 12 GeV PS at KEK. *Nucl. Instrum. Meth. A, 383:159-165*, 1996.

[115] M. Bruzzi et al. Radiation-hard Semiconductor Detectors for SuperLHC. *Nucl. Instrum. Meth. A, 541:189-201*, 2005.

[116] G. Casse et al. First Results on pn Charge Collection Efficiency of Heavily Irradiated Microstrip Sensors Fabricated on Oxygenated p-type Silicon. *Nucl. Instrum. Meth. A, 518:340-342*, 2004.

[117] G. Pellegrini et al. Tecnology Development of p-type Microstrip Detector with Radiation hard p-spray Isolation. *Nucl. Instrum. Meth. A, 566:360-365*, 2006.

[118] R. Marco-Hernandez et al. *IEEE Trans. Nucl. Sci. 56,3*, 2009.

[119] S. Eidelman et al. Passage of particles through matter. *Phys. Lett. B592, 1*, 2004.

[120] I. Mandic et al. Measurement of anomalously high charge collection efficiency in n^+p strip detectors irradiated by up to 10^{16} n_{eq}/cm^2. *Nucl. Instrum. Meth. A 603:263-267*, 2009.

[121] G. Casse. Radiation hardness of p-type detectors. *Nucl. Instrum. Meth. A 612:464-469*, 2010.

[122] The Gauss Project.
http://lhcb-release-area.web.cern.ch/LHCb-release-area/DOC/gauss/, 2010.

[123] The Boole Project.
http://lhcb-release-area.web.cern.ch/LHCb-release-area/DOC/boole/, 2010.

[124] The Brunel Project.
http://lhcb-release-area.web.cern.ch/LHCb-release-area/DOC/brunel/, 2010.

[125] T. Sjostrand, S. Mrenna and P. Skands. PYTHIA 6.4 Physics and Manual. *arXiv:hep-ph/0603175v2*, 2006.

[126] The DaVinci Project.
http://lhcb-release-area.web.cern.ch/LHCb-release-area/DOC/davinci/, 2010.

[127] M. Bebayoun and C. Jones. RICH Reconstruction and Particle Identification Using Ring Fit Methods: Application to the RICH2 Detector. *CERN-LHCb-2004-057*, 2004.

[128] M. Patel and H. Skottowe. A Cut Based Selection for $B_d \to K^{*0}\mu^+\mu^-$. *LHCb-2009-008*, 2009.

[129] J. Dickens et al. Selection of the Decay $B_d \to K^{*0}\mu^+\mu^-$ at LHCb. *CERN-LHCb-2007-038*, 2007.

[130] I. Belyaev et al. Python-based Physics Analysis Environment for LHCb. *CERN-LHCb-2004-089*, 2004.

[131] J. H. Lopes. Study of the rare $B_d^0 \to K^{*0}(K^+\pi^-)\mu^+\mu^-$ decay with the LHCb detector. *LHCb-2003-104*, 2003.

[132] F. Marinho, C. Parkes and S. Viret. A non-parametric method to estimate the Forward-Backward Asymmetry from the $B_d \to K^*\mu^+\mu^-$ decay at LHCb. *CERN-LHCb-2009-004*, 2009.

[133] E. Parzen. On estimation of a probability density function and mode. *Ann. Math. Statist., 33:1065-1076*, 1962.

[134] M. Beneke et al. Exclusive radiative and electroweak b $\to$ d and b $\to$ s penguin decays at NLO. *Eur. Phys. J. C41:173-188*, 2005.

[135] S. Borghi et al. First Spatial alignment of the LHCb VELO and analysis of beam absorber collision data. *Nucl. Instrum. Meth. A 618:108-120*, 2010.

[136] M. Gersabeck, J. Nardulli and E. Rodrigues. Impact of misalignments on the analysis of B decays. *CERN-LHCb-2008-012*, 2008.

[137] S. Borghi et al. Performance of the Tracking System at the LHCb Experiment. *35^{th} International Conference on High Energy Physics*, 2010.

[138] D. Hutchcroft. VELO Pattern Recognition. *CERN-LHCb-2007-013*, 2007.

[139] M. Needham. Performance of the LHCb track reconstruction software. *CERN-LHCb-2007-144*, 2007.

[140] C. Parkes et T. Szumlak. Private Communication. 2009.